Numerical Modelling of Bidirectional Dry Gas Face Seals

Joel Oroh Ojile

Degree Sought: PhD - Full Time

Cranfield University

School of Engineering

Department of Power & Propulsion Engineering

Cranfield University

School of Engineering

Department of Power & Propulsion Engineering

PhD THESIS

Academic Year 2009 - 2010

Joel Oroh Ojile

Numerical Modelling of Bidirectional Dry Gas Face Seals

Supervisor: Dr. Joao Amaral Teixeira

December 2009

This thesis is submitted in partial fulfillment of the requirements for the degree of Doctor of Philosophy

Abstract

The optimization of the geometrical parameters of the aerodynamic lift features and the analysis of the fluid flow in the seal interface are inter-twined. Any small changes in the geometrical parameters of the aerodynamic lift features significantly affect the performance of a non-contacting gas face seal.

For a gas face seal to function with optimum performance requires that the optimum geometrical parameters be identified. This can be achieved through a lengthy trial and error process, often heavily dependent on the designer's depth of insight, itself dependent on experience, or can be achieved through automated numerical methods.

The purpose of this research was to develop a reliable numerical model that can serve as a design tool for simulating the performance of both unidirectional and bidirectional dry gas face seals. This was achieved in three steps. The first approach consisted in developing a 2D numerical model that employed the Reynolds equation for seals operating at very low rotating speeds and low pressure differentials. In the second step a 3D-CFD model was assembled and the practicability of using CFD, in a seal design loop, for seals operating in wide range of operating conditions, was investigated. This model employed a commercial CFD package (ANSYS CFX version 11). For last approach both models were incorporated into an automatic optimization tool that can generate optimal seal geometries with a minimum of human intervention.

An extensive set of results from the analysis of dry gas face seals spanning across different operating conditions and geometrical seal face profiles, with the inclusion of convergent radial taper, are presented and discussed in this thesis. The results obtained from the Reynolds equation and 3D CFD models are compared and critically analysed. Results obtained with both models are validated against test data obtained from AESSEAL plc, the sponsor of this research. The 3D CFD model predictions showed a better agreement with the test data on the seal leakage than the Reynolds equation model. The leakage rates and fluid film thickness predictions illustrate how the 3D CFD model can be used for seal design while overcoming some of the shortcomings of the Reynolds equation based models. The major limitation of the 3D CFD model is that it is computationally expensive.

An automatic optimization tool which can be used for the design of dry gas face seals has been presented. The improvements achieved from the optimization of a spiral groove face seal utilising the automatic optimization tool are: 4.8% increase of opening force, 13.2% reduction of seal leakage, 20.7% increase of design efficiency parameter, 28.3% increase of axial film stiffness and 15.9% reduction of power consumption. A proposed new design of dry gas face seal capable of bidirectional operation has been presented. This type of seal outperformed the spiral groove face seal, in reverse rotation of the sealing shaft, in terms of opening force and positive axial film stiffness.

Acknowledgements

My sincere gratitude goes to Dr. Joao A. Teixeira, who acted as my academic supervisor.

I am very grateful to AESSEAL plc for its financial and technical support of this research. I wish to thank all the staff of AESSEAL plc and in particular Dr. Chris Carmody, Mr John Bright and also Nick Wills for being always available to answer my mechanical face seal related questions and providing me with test data.

I am also very grateful to Kevin Banks, now at Dresser-Rand, for the valuable discussions we had together on optimization.

I am indebted to Mr & Mrs Ambrose Alfred for being there for me as my only close family in the United Kingdom. A heartfelt thank you to all my friends with whom I have spent most of my time with at Cranfield University in particular, Emidio Giordano, Filipe Rosa and Chirath Assalaarachchi.

I want to mention as well my friends Samuel Oruerio, Isatu Kamara and Mr & Mrs Austin Egwu and all those with whom I have related with over the past four years.

Finally, this work would not have been possible without the loving support and encouragement of my whole family. I am very grateful to my brothers, Solomon and Godfrey for supporting me morally and financially, for always listening to my complaints and frustrations and invariably finding the right words to cheer me up. Sincere thanks also due to my sister Kome, for her unbroken encouragement and support. My nieces and my nephews are also appreciated for their love. I am also grateful to my cousin, Daniel Godwin for remembering me in his prayers and his moral support.

To the memory of my late mother, Mrs Felicia O. Ojile, for her love and sacrifice she made for me.

Contents

List of Figures

List of Tables

Nomenclature

Roman Symbols

$\bar{F}$	Load factor
$\dot{m}$	Seal leakage (kg/s)
a_g	Percentage of circumferential groove width
a_l	Percentage of circumferential land width
A_{cl}	Hydrostatic closing area (m^2)
A_{op}	Primary seal face area (m^2)
b	Seal dam width (m)
B_D	Balance diameter
B_r	Geometrical ratio
C_p	Specific heat capacity at constant pressure $(J/kg.K)$
c_k	The child in optimization process
F_F	Frictional force (N)
F_I	Inertia force (N)
F_s	Spring force (N)
F_{cl}	Seal closing force (N)
F_i	Individuals in front
F_{op}	Seal opening force (N)
h,h_f	Fluid film thickness or gap between the seal interface (m)
h_g	groove depth radius (m)

h_i Fluid film thickness at the seal ring inner radius (m)

h_o Fluid film thickness at the seal ring outer radius (m)

h_b Height of bottom block (m)

Hn mxn Halton generated results

k Boltzmann's constant taken as $1.380662x10^{-23}JK^{-1}$

k Thermal conductivity $(W/m.K)$

Kn Knudsen number

m number of sample points

M_D Molecular collision diameter (m)

N Rotational speed (rev/min)

n number of design variables (dimensions)

n_g Number of grooves

p Local pressure within the fluid film (N/m^2)

p_i Fluid pressure at the seal ring inner radius (N/m^2)

p_o Fluid pressure at the seal ring outer radius (N/m^2)

p_k The parent in optimization process

p_k^l The lower bound on the parent component in optimization process

p_k^u The upper bound on the parent component in optimization process

p_{rank} non-dominated rank

R Perfect gas constant $(J/kg.K)$

r Seal ring radius (m)

r_b Seal balance radius (m)

r_{gi} Seal groove inner radius (m)

r_{go} Seal groove outer radius (m)

r_i Seal ring inner radius (m)

r_k A uniformly sampled random number in optimization process

r_o Seal ring outer radius (m)

Re_c Rotational flow Reynolds number

Re_p Pressure flow Reynolds number

$step$ subsequence index number

T Sealed fluid temperature (K)

T_{fr} Frictional torque (Nm)

u_θ Circumferential velocity (m/s)

u_r Radial velocity (m/s)

u_z Axial velocity (m/s)

v Design Variable

$y(1)$ First objective function (a representative of the seal opening force)

$y(2)$ Second objective function (a representative of the seal leakage)

Greek Symbols

α Spiral angle (deg)

δ_k A small variation calculated from a polynomial distribution in optimization process

η Coefficient of Colomb friction

η_c Distribution index for crossover

η_m mutation distribution index

γ Groove - land width ratio

μ Dynamic viscosity $(kg.m^{-1}.s^{-1})$

ω Rotational speed or angular velocity of rotating shaft (rev/min)

ϕ Angle of radial taper $(radian)$

ρ Fluid density (kg/m^3)

ζ Molecular mean free path (m)

Superscripts

l Lower limit of design Variable

u Upper limit of design Variable

Subscripts

θ circumferential

b bottom block

c crossover

c rotational flow

cl closing

D Diameter

f fluid film

fr frictional

g groove

I inertia

i Row position of the number of sample points

j Column position of the number of sample points

m mutation

o outer

op opening

p pressure flow

r radial

s spring

sec sector

i inner

z axial

Other Symbols

Δp Pressure differential $p_o - p_i$ (N/m^2)

ΔR Seal face width (m)

$\prec_n$ crowded-comparison-operator

θ_{sec} Angle of the seal sector (deg)

Acronyms

CFD Computational Fluid Dynamics

$DGFS$ Dry Gas Face Seal

Chapter 1

Introduction

1.1 Project Overview

Dry gas face seals (DGFS) are gas-lubricated mechanical devices used for restricting leakage of fluids, wherever a rotating shaft penetrates a stationary housing that encloses pressurized fluid. These devices are used in rotating equipment such as gas compressors, pumps, gas turbines, steam turbines, turbochargers and mixers. They are widely used in the petroleum, petrochemical and aero industries. Dry gas face seals ensure that the leakage of expensive, toxic, corrosive, explosive or flammable fluids escaping into the atmosphere is eliminated or reduced to a barest minimum. Gases ranging from inert gases such as nitrogen to highly toxic gaseous mixtures of natural gas and hydrogen sulphide can be sealed utilizing the appropriate seal arrangements. The performance of seals therefore is a major area of concern for seal manufacturers as well as users. In order to reduce the design cycle time and enable the inclusion of numerical optimisation schemes, reliable numerical models are needed for analysing dry gas face seal performance.

Current environmental regulations impose stringent requirements on the safe operation as well as service longevity of seals. Economic and environmental advantages of dry gas face seals over wet seals have led to series of studies in order to improve the designs of dry gas face seals in terms of improving their reliability and the minimizing of leakage rates. The economic and environmental benefits of dry gas seals include:

- reduced gas leakage rates
- mechanically simple since they do not require elaborate oil circulation components and treatment facilities
- reduced rate of power consumption since no accessory oil circulation pumps and systems are required

- improved reliability since fewer ancillary components are employed, which translates into higher overall reliability and less plant downtime
- elimination of seal oil leakage into the plant thereby avoiding contamination of the sealed fluid and degradation of the plant

The numerical modelling of dry gas face seals is a complex task as the analysis must not only be able to represent the dynamics of the fluid-structure interaction of the seal rings, but must also provide detailed fluid flow analysis in the seal interface. The prediction of the fluid flow in the seal interface is certainly demanding and if a detailed analysis is required, to include the effects on the flow of the complex interaction with the geometric features of the faces, dams, grooves, feed slots and the effects of deformation of the faces, a computational fluid dynamics (CFD) prediction is required.

In order to analyse intricate face geometries and seals operating at high rotational speeds and pressures, special purpose solvers or 3D numerical codes that solve the full Navier-Stokes equations are required such that the effects of compressibility, turbulence, choking and discontinuities in the film thickness can be handled.

Despite the recent advances in dry gas face seal technology, computational fluid dynamics (CFD) which has been actively employed in studying ancillary rotating components such as bearings and labyrinth seals, has not been effectively used to evaluate dry gas face seal designs and very little work has been reported in the open literature. The main reason is that the size of the gap separating the seal faces is very small, of the order of micrometers, and this feature complicates significantly the numerical work.

Dry gas seals are classified into fixed clearance and surface-guided seals. The most common types of the former are the labyrinth, brush and visco seals. The latter can either be cylindrical surface guided or annular surface-guided. An example of the cylindrical surface-guided seal is the lip seal. The dry gas face seal is an example of annular surface guided seal.

Labyrinth seals are composed of many linear threads, often placed on both the stationary and rotating components, such that the sealed fluid flows through a convoluted and extensive path before exiting into the atmosphere. They are designed to ensure the presence of clearances that are very small between the tips of the labyrinth threads and the running surface. In some designs there are threads both on the outer and inner portions which interlock to produce a long path in order to slow the leakage.

Most turbomachinery seals are of the labyrinth type, a mature technology which has a number of disadvantages. Its design is based on increasing the seal gap as the diameter

increases, an approach that causes significant flow leakage and lower plant efficiency. Labyrinth seals tend to be multistage with a large degree of built-in redundancy, a feature which increases the overall weight of the plant. Maintenance requirements are high because of significant wear that may occur at the knife-edges that operate very close to the rotating parts.

Brush seals are occasionally used for inter-stage sealing of compressor and turbine assemblies but can only handle relatively low pressure ratios, i.e., pressure differential across the seal, and suffer from wear and fatigue problems. The pressure and temperature considerations limit their applicability to compressor and turbine inter-stages. They suffer from problems such as accelerated wear during transients and high heat generation due to rubbing interface. The brush wires are usually prone to high cycle fatigue and creep.

Dry gas face seals are much lighter than all other dry gas seals and due to their non-contacting nature, make them in principle, virtually maintenance free. The dry gas face seals are designed in a way that one of the seal faces is flexibly mounted with respect to the shaft or housing and is entirely supported and guided by the second seal face, one of which is sliding relative to the other. The pressure across the seal induces a thin film of fluid into the gap between the stationary ring and the rotating ring, provided that the fluid gap can be maintained small irrespective of the ring's diameter. Such design reduces the flow leakage considerably when compared with the labyrinth and brush seals.

1.1.1 Basic Concepts of Dry Gas Face Seals

A dry gas face seal comprises three basic components namely the primary elements, secondary seals and the ancillary parts as shown in Figure 1.1. The primary elements are made up of the primary and mating rings. The primary ring is held stationary and fixed to the seal housing but allowed to move axially. The mating ring is fixed to the shaft and rotates with it. Either one of the ring faces is etched with grooves whose depth is of the order of a few micrometers. The overall performance of the dry gas face seal depends mostly on the performance of the primary elements, the hydrodynamic behaviour of the intervening lubricating film and operating conditions.

The secondary seals are commonly made from various fluoroelastomers and usually close the leakage paths around the primary and the mating faces. For pusher-type seals, the secondary seals must move forward along the shaft to compensate for wear and vibration at the seal faces. For non-pusher-types, such as metal bellows units, vibration and wear are taken up internally in the bellows, and here the secondary seals are truly static. The ancillary parts are used for attaching, positioning and maintaining face-to-face contact of

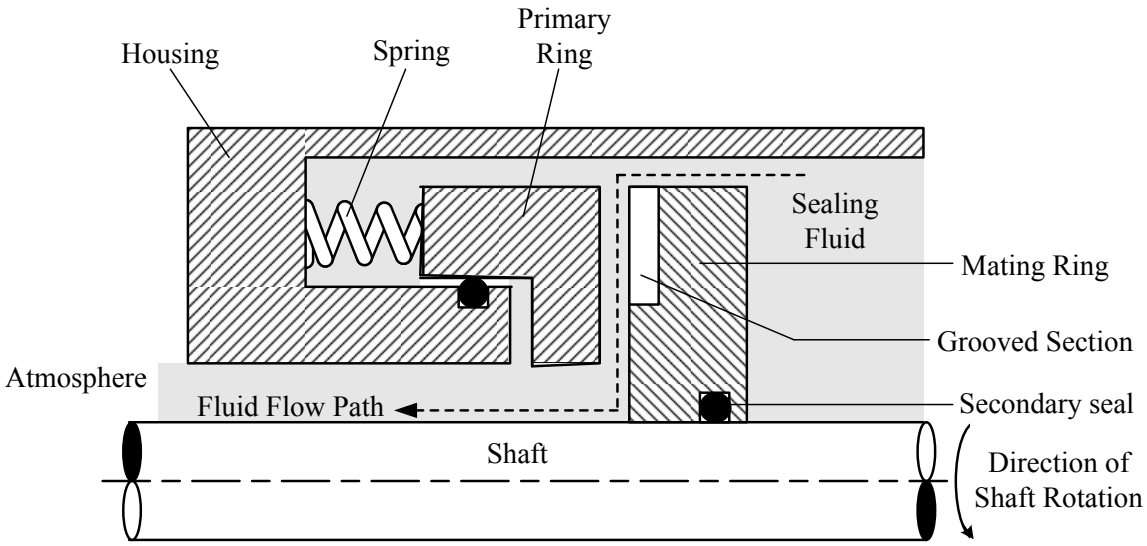

Figure 1.1 Schematic diagram of a non-contacting dry gas face seal

the seal. These ancillary parts may consist of a sleeve or housing for ease and precision of seal setting. Also the ancillary parts include springs that provide mechanical preloads to the seal faces, until hydraulic pressures take over. These are either a large single-coil spring, or a set of small coil springs or bellows. Other ancillary parts include series of drive pins, dents, notches or screws that transmit torque to both the primary and mating faces.

The operating principle of the dry gas face seal is that of a hydrostatic and hydrodynamic force balance. As gas enters the grooves, it is directed towards the centre. The sealing dam acts as a restriction to the gas flows, thereby raising the pressure upstream of the dam. This increased pressure causes the flexibly mounted primary ring to separate from the mating ring. Under static conditions, the primary and mating rings are held in contact as a result of the spring load acting on the primary ring. During normal operation, the running gap varies between $3-5\,\mu m$. Under pressurization, the forces exerted on the seal are hydrostatic and are always present whether the mating ring is stationary or rotating. Hydrodynamic forces are generated only upon rotation. The key factors responsible for the hydrodynamic forces are: the mating ring consisting of some grooves on its face and the primary ring being tapered in the radial direction. A typical operating range of dry gas face seals is given in Table 1.1.

1.1.2 Classification of Dry Gas Face Seals

Dry gas face seals are classified either by face lubrication, seal arrangement or direction of shaft rotation. Each of the classes is discussed below:

Table 1.1 Typical operating conditions for dry gas face seals (Saxena, 2003)

Operating Parameter	Imperial Unit	SI Unit
Maximum dynamic sealing pressure	6160 psig	42500 kPag
Maximum static sealing pressure	6160 psig	42500 kPag
Minimum operating temperature	(-) 242^oF	(-) 152^oC
Maximum shaft size	13.75 in.	350 mm
Maximum compressor operating speed	70000+ rpm	
Normal allowable radial movement	$\pm$0.024 in.	$\pm$0.06 mm
Maximum allowable axial movement (size dependent)	0.24 in.	6 mm
Maximum surface speed at seal balance diameter	590 fps	180 m/s

1.1.2.1 Face Lubrication

The three classes of face lubrication include boundary, mixed-film and full-film lubrication. In boundary lubrication, the seal faces are coated with layers that protect the surfaces. There is no fluid pressure build-up at all and the load is completely carried by the interacting asperities of the seal faces. In this type of lubrication, shear takes place in the boundary layers or at the interface of both layers. Whenever the boundary layers are damaged, direct contact between the asperities occurs and shear takes place at this interface or in the weaker asperities which results in material transfer from one surface to the other. This type of lubrication is experienced in dry gas face seals at start-up and shut-down.

In mixed-film lubrication, the fluid film thickness is of the same order as the surface roughness of the seal faces. Part of the load is carried by the fluid pressure while the remaining load is carried by the asperities of the seal faces. In this type of lubrication, shear takes place in both the fluid and the surface boundary. The wavy gas seals fall into the mixed-film lubrication classification. For conditions beyond the capability of boundary-lubricated seals, mixed-film lubrication offers a worthwhile improvement in capability.

In full-film lubrication also known as hydrodynamic lubrication, the faces are fully separated by fluid and the fluid film thickness is several times greater than the surface roughness of the seal faces. The separation of the seal faces is as a result of pressure build-up from the sealed fluid pressure differential or relative motion of the seal faces or the combination of both effects. In this type of lubrication, the load is entirely carried by the sealed fluid and all shearing takes place in the fluid. Almost all dry gas face seals run with full-film lubrication whenever the seal is fully operational hence they are regarded as non-contacting face seals. Full-film lubrication offers the highest sealing capability, and because the faces are separated by a full film, such seals offer long service lives. There are three types of dry gas face seals based on full-film lubrication: the hydrostatic, hydrodynamic and the hybrid type.

The hydrostatic seal generates its lift force by maintaining a constant fluid film that is created by the upstream and downstream pressure differential. The pressure differential is usually achieved by injecting lubricating fluid directly into a parallel plane seal interface. They are better suited to high pressure differentials. The hydrodynamic seals rely on the relative surface velocity between the rotating and the stationary rings, one of the ring faces having grooves, which establish a lift force that is required to maintain a certain clearance. This type of seals, operates efficiently at high surface velocities i.e., high shaft speed. The gap sizes of the hydrodynamic seals are always smaller than the ones of the hydrostatic seals. The hybrid seal combines the features of the other two (hydrostatic and hydrodynamic seals) which makes them more efficient. The hybrid types of seals are capable of generating both hydrostatic and hydrodynamic forces hence they are capable of supporting large loads. Also the flexibly mounted seal face is capable of dynamically tracking the second seal face when there are changes in operating conditions hence they have a high positive stiffness. Leakages from full-film lubricated seals are higher than from boundary and mixed-film lubrications.

1.1.2.2 Direction of Shaft Rotation

Dry gas face seals are classified into two groups according to their ability of generating hydrodynamic force with regards to the direction of rotation of the shaft. The hydrodynamic forces generated mainly depend on the nature of the seal face profiles. The grooves which make up the seal face profile generate the hydrodynamic force that allows the gas seal under operation to run without contact between the seal faces. They are of the unidirectional and bidirectional types respectively. The unidirectional types have grooves patterns designed in such a way that hydrodynamic forces can only be generated when the shaft is rotating in a particular direction. The seal faces may contact when the shaft rotates in the reverse direction. This happens since the grooves are ineffective and do not generate enough forces required to separate the seal faces in the reverse direction of shaft rotation. Examples of the unidirectional seals, single spiral and double spiral seals are shown in Figure 1.2 (a) and (d) respectively. The bidirectional types have their groove patterns designed in such a way that hydrodynamic forces can be generated on both directions of rotation of the shaft. In this type of seals, their designs usually have symmetrical groove patterns. Examples of the bidirectional seals, the radial groove and T-groove seals are shown in shown in Figure 1.2 (b), and (c) respectively.

The economic and environmental benefits of the bidirectional dry gas face seals are numerous. Some of their advantages over the unidirectional types include:

- Can support loads when unintentional reverse rotation that is caused by back pressure cannot be avoided as a result of suction valves failing to close or recycle valves failing

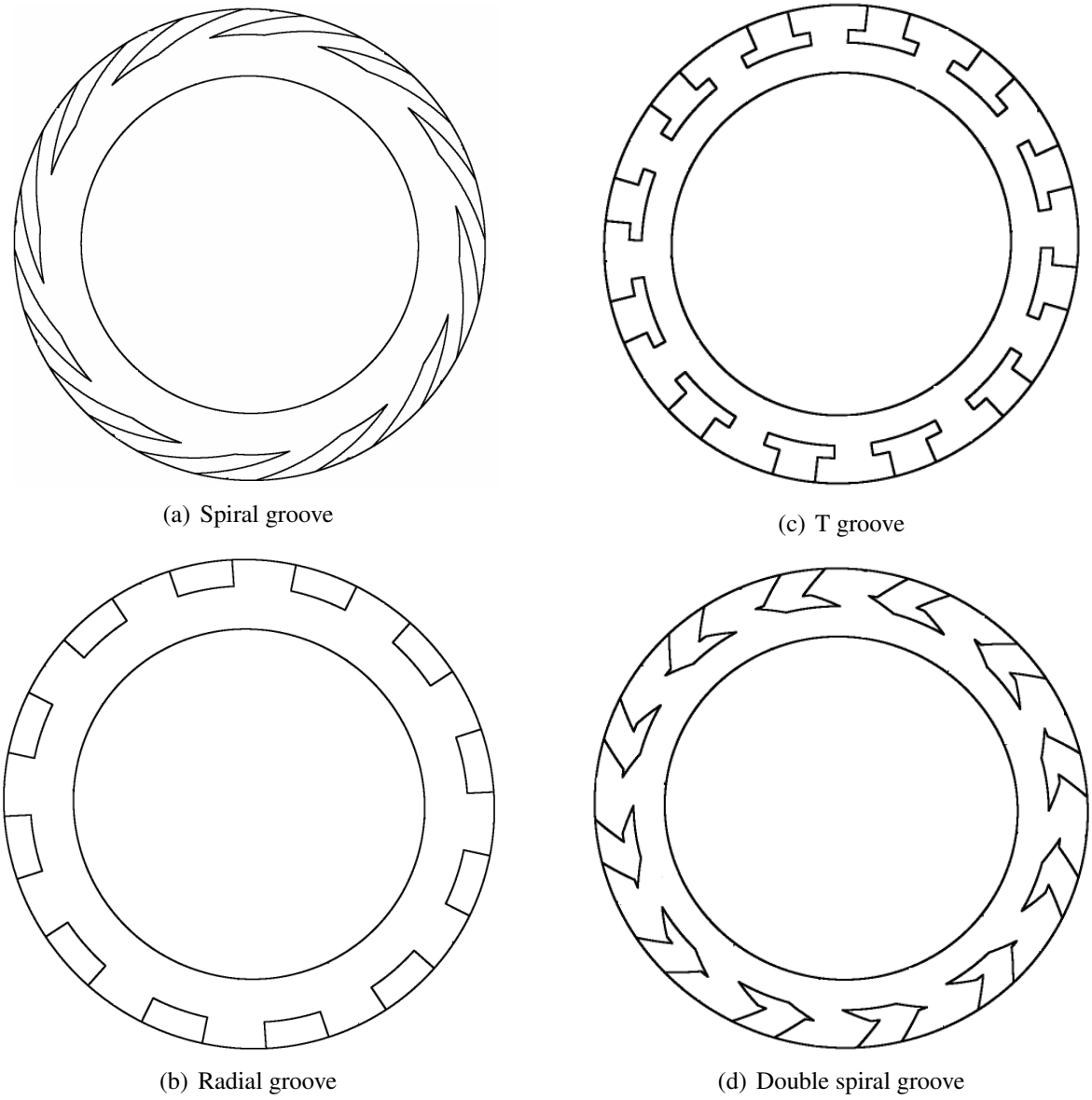

(a) Spiral groove

(c) T groove

(b) Radial groove

(d) Double spiral groove

Figure 1.2 Some geometrical seal face designs used in dry gas face seals

to open or malfunctioning of check valves.

- Reduce the problems associated with mounting two unidirectional seals unto the two ends of a shaft since it requires a high degree of acquaintance with these types of seal to be able to distinguish between the seal face profiles that will support load only on a particular direction of shaft rotation.
- Reduce the problem of providing different seal face profiles for unidirectional types of seals as spares.

1.1.2.3 Seal Arrangement

There are two aspects to seal arrangements. The first deals with fundamental arrangements of the basic parts and the second with various arrangements of complete seals. Fundamental

arrangements of the basic parts consider the location of the rotating element. Internal seals have their rotating element inside the seal housing and the sealed fluid at the outer diameter of the seal interface, therefore leakage is normally inwards towards the shaft. Centrifugal action in the fluid tends to oppose leakage across the seal interface. External seals are the opposite; the rotating element is outside the seal housing and the sealed fluid is at the internal diameter of the seal interface. Leakage is therefore normally outwards away from the shaft, with centrifugal action in the fluid tending to promote leakage, and hence encouraging the centrifuging of any solids in the fluid into the sealing interface. With these types of arrangement, there is direct leakage of the sealed fluid into the atmosphere. This is not always tolerable, for reasons of seal face life, fluid toxicity, fluid cost or environmental pollution.

To avoid this effect, multiple seals, either double or tandem depending on the particular circumstances, are used. When the service is such that the sealed fluid cannot be allowed to leak into the atmosphere (toxic or polluting) or must be kept out of the seal interface (abrasive solids in the fluid), a double seal offers a practical solution. The seal is then made up of two single seals mounted either back to back or face to face. The region between the seals is maintained at a pressure either greater or lower than the sealed fluid pressure with a barrier fluid. When the pressure between the seals is greater than the sealed fluid, the barrier fluid flows through the sealing interface into the sealed fluid. When the sealed fluid pressure is greater than the pressure between the two seals, the sealed fluid flows through the sealing interface into the barrier fluid. In seals employing this modus operandi the barrier fluid was invariably a liquid and a double seal with a liquid barrier was the only available solution for toxic, polluting, or abrasive pumped fluids.

This arrangement is complex however, and somewhat unreliable as a consequence, a circumstance that led to the development of better solutions for most services. The wet-lubrication systems that have been used in sealing centrifugal compressor technology are now been replaced by the dry gas systems where an inert gas is used as the barrier fluid which simplifies the sealing system considerably. Such designs are now used quite extensively in pumps handling toxic and polluting liquids, limited only by compatibility of the barrier gas with the pumped liquid.

The objective of a tandem seal is to provide a backup so failure of the main or primary seal does not result in gross leakage and the need to immediately shut down the plant. In services such as hydrocarbon or crude oil, safety and pollution requirements alone can warrant tandem seals to prevent even short-term gross leakages. A tandem seal has two or more single seals arranged in series, with each successive seal serving to backup the preceding seal. The most common arrangement has two seals, the inner acting as the primary, and

the outer as the secondary. Under normal conditions, the primary seal contains the sealed fluid, whereas the secondary seal runs at a pressure below the sealed pressure, usually atmospheric, in an inert buffer fluid. Leakage beyond a certain rate causes a pressure rise in the secondary seal lubrication system, a condition that is used to close off the lubrication system vent, and hence contain the primary seal leakage and sound an alarm. Figure 1.3 shows a number of dry gas face seal arrangements. The sketches illustrate complete seals with the mating ring marked in pink while the primary ring is shown in blue for all seal arrangements.

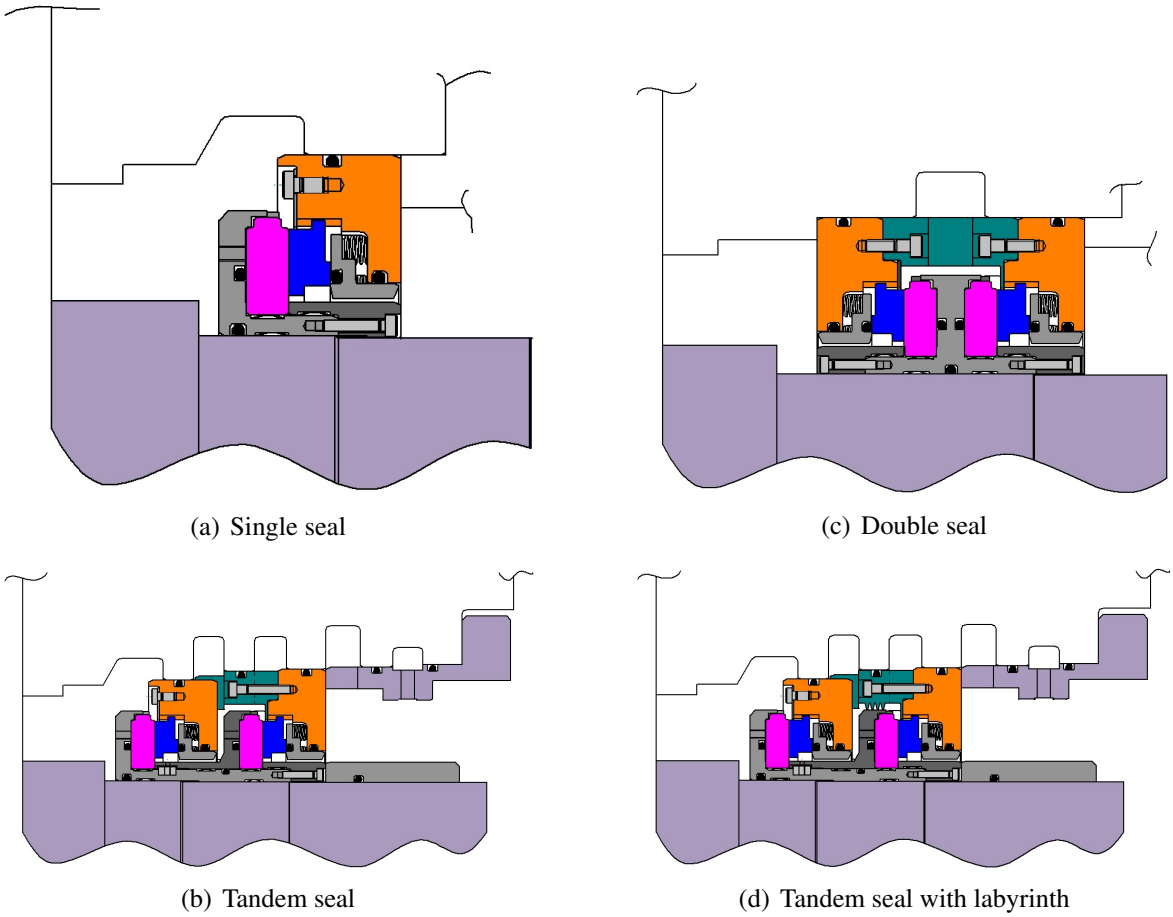

(a) Single seal

(c) Double seal

(b) Tandem seal

(d) Tandem seal with labyrinth

Figure 1.3 Dry gas face seals arrangement (courtesy of AESSEAL plc)

1.1.3 Materials Selection

The selection of materials for seal rings is an important aspect of seal design. It requires extensive tribological testing in order to identify suitable material combinations for a particular application. Specifically, sealing materials should have good mechanical and thermal shock resistance, appropriate wear characteristics and corrosion resistance, desirably a self lubrication property and a high modulus of elasticity. Carbon-graphite usually meets most of these requirements. Carbon-graphite is usually chosen in combination

Table 1.2 Dry gas seal face materials

Seal Part	Material
Mating ring	Tungsten-Carbide or Silicon-Carbide
Primary Ring	Special grade Carbon or Silicon-Carbide
O-Rings	Elastomers (Viton or Kalrez)
Sleeves, Discs, Retainer rings	Stainless Steel
Coil Springs	Stainless Steel

with some other compatible hard materials like tungsten or silicon carbide. Some other combinations of seal materials used are: carbon-graphite vs. stainless steel, tungsten carbide vs. tungsten carbide depending on the operating conditions that include the gas-film composition, contaminants in the gas stream, operating temperatures as well as process conditions. The most common materials used for making the seal parts are shown in Table 1.2.

1.1.4 Gas Seals Support Systems

The use of dry gas face seals requires a system designed for supplying a steady flow of sealing gas to the seal interface as the working fluid that occupies the running gap. These gas seal support systems are normally supplied by the compressor original equipment manufacturer (OEM) and they are mounted on the compressor base plate. There are two basic types of gas seal systems: differential pressure (ΔP) control and flow control. The differential control systems control the supply of seal gas to the seal interface by regulating the seal gas pressure to a pre-determined value usually 15 *psi* (1 Bar) above the sealing pressure. This is achieved through the use of a differential pressure control valve. The flow control systems control the supply of seal gas to the seal interface by regulating the seal gas flow through an orifice upstream of the seal. This is achieved through the use of a differential pressure control valve monitoring pressures on either side of the orifice. Figure 1.4, Figure 1.5 and Figure 1.6 show some of the gas seals support systems used for the different seal arrangements. The system shown in Figure 1.4 is for a single seal arrangement, that in Figure 1.5 is for a double seal arrangement while Figure 1.6 shows a support system for a tandem seal arrangement.

1.2 Research Motivation

The motivation for this research was threefold: the first objective was to review the understanding of the physics governing the fluid flow in thin fluid film lubrication within gas seal faces etched with grooves. The second goal consisted in the evaluation of CFD as an appropriate means to analyse the performance of dry gas face seal designs. The third aim

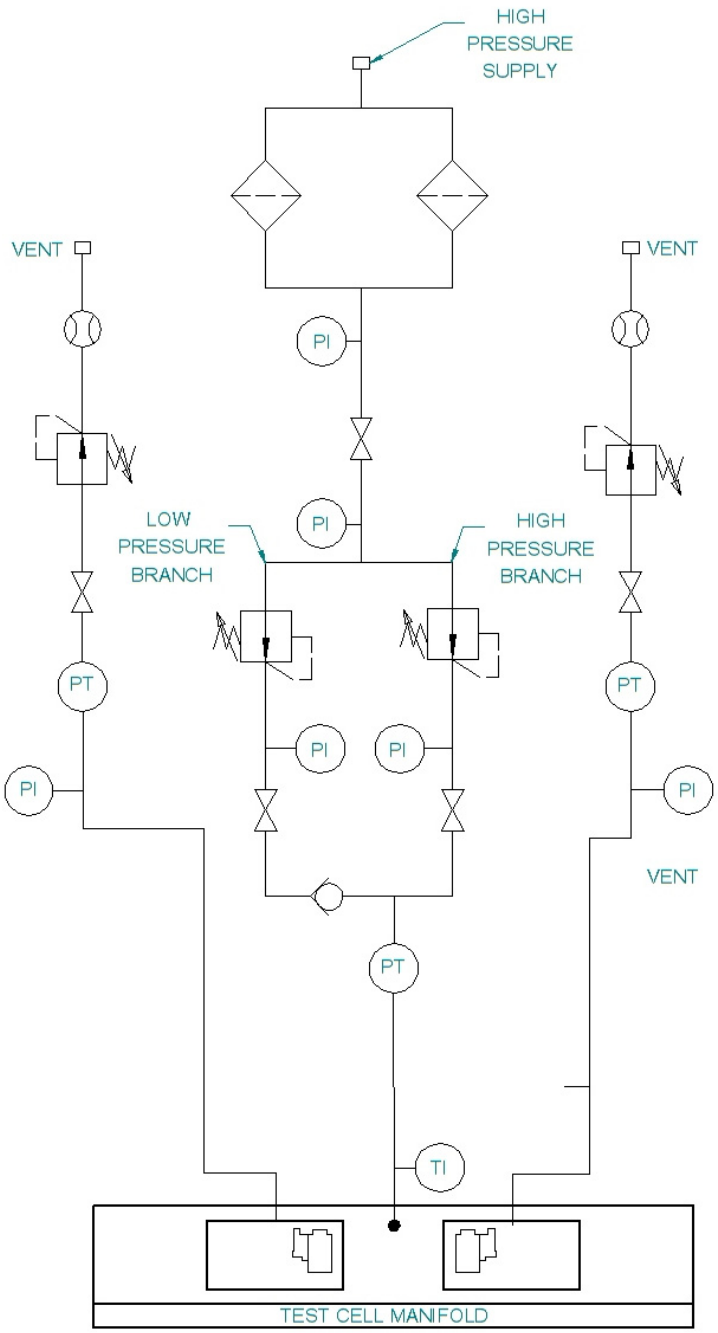

Figure 1.4 Seal support system for a single seal arrangement (courtesy of AESSEAL plc)

was to develop a method for AESSEAL plc, the company sponsoring the research, which could be used as a design tool for uni and bidirectional dry gas face seals operating at high pressure differentials and high rotating speeds.

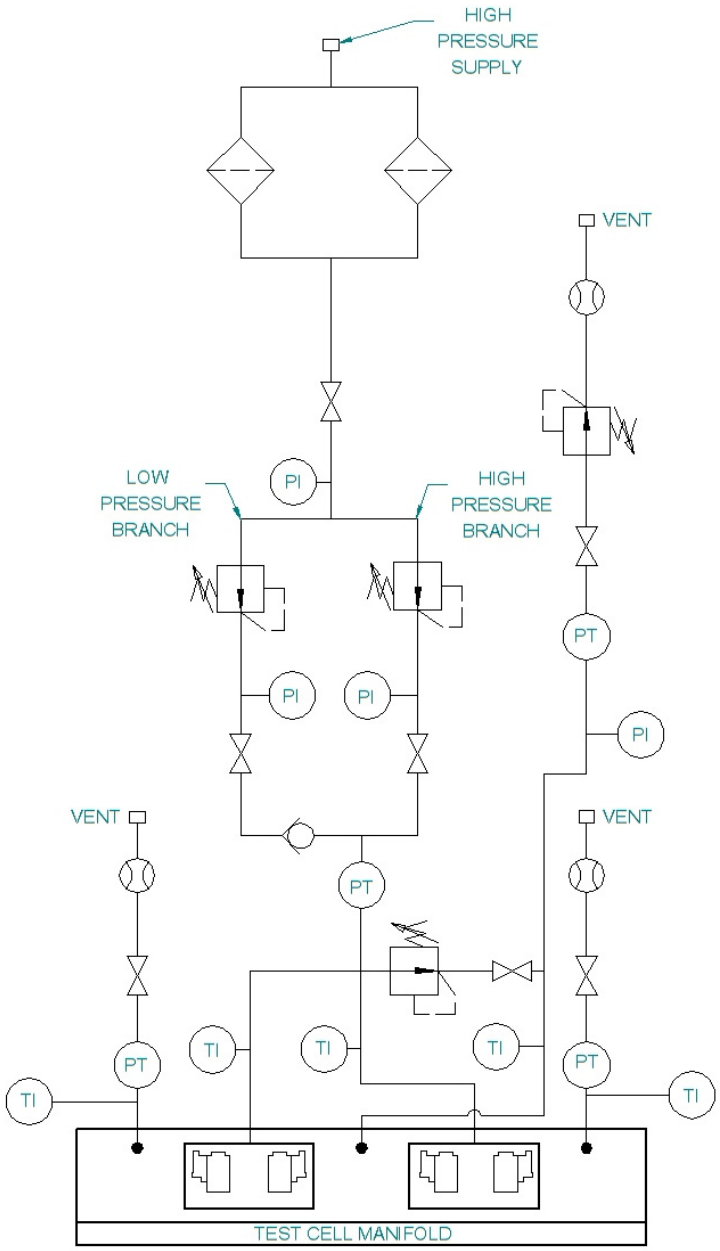

Figure 1.5 Seal support system for a double seal arrangement (courtesy of AESSEAL plc)

1.3 Scope of Research/Research Focus

The study involved three phases. The first phase consisted of the development of a 2D model that employed the Reynolds equation. This model neglected the effects of inertia and turbulence and used an isothermal condition for the fluid flow. This code was essentially developed to conduct parameterization studies for different geometrical face profiles of seals operating at very low operating conditions. It was also developed to show the limitations associated with the use of methods employing the Reynolds equations for analyzing seals operating at high pressure differentials and high rotating speeds and with

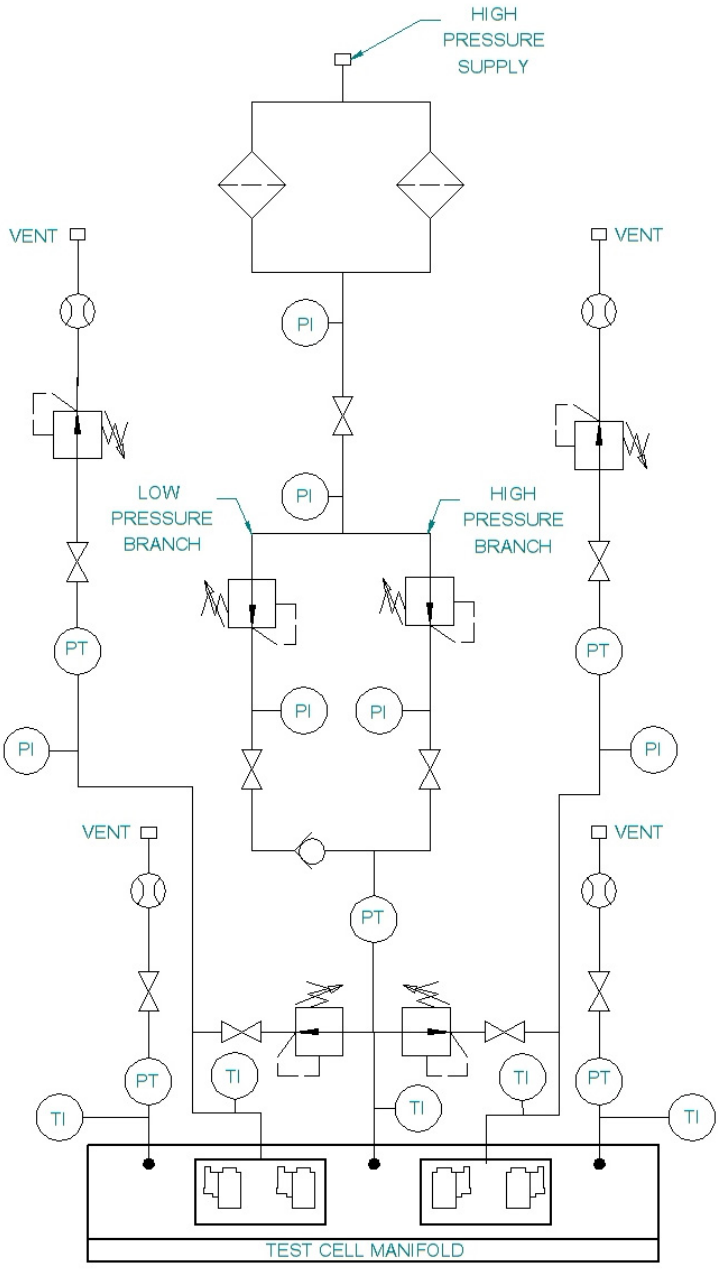

Figure 1.6 Seal support system for a tandem seal arrangement (courtesy of AESSEAL plc)

complex geometries.

The second phase investigated the application of a 3-dimensional commercial CFD package (ANSYS CFX) for the analysis of dry gas face seals. This model solves the full Navier-Stokes equation system: continuity momentum and energy equations. The limits of the applicability of the CFD as a modelling tool were identified. The 3D CFD model takes into account the effects of compressibility, laminar or turbulent flow regimes, and choked flow as well as non-isothermal conditions.

The last phase involved developing an optimization tool that can be coupled to either a

3D CFD package or a 2D model based on the Reynolds equation. This tool implements a low-discrepancy sequence technique for the sampling of points in the design space and makes use of approximate models (metamodels) in place of running a large number of CFD simulations. This approach produces good fitness functions from just a few CFD simulation runs and passes these fitness functions to an optimizer. The optimizer employs a Genetic Algorithm that is capable of dealing with both single and multi-objective functions. The optimization tool is used in obtaining the best possible solutions in the shortest time rather than depending directly on the results from CFD simulations runs, which is computationally expensive. With this numerical tool, optimal seal geometries with a minimum of human intervention can be generated.

This study covers the analysis of dry gas face seals operating at a wide range of operating conditions (maximum sealed fluid pressure of about 350 bars and 45000 shaft rpm) with fluid film thickness ranging from 3-10μm. A number of geometrical seal face profiles, including a proposed novel seal face design, where used in the study. Performance parameters such as opening force, leakage, axial stiffness and friction coefficient at various operating conditions were analysed and presented. Results obtained from the first and second phases were validated against experimental data obtained from the tests carried out at AESSEAL laboratory in Rotherham

1.4 Thesis Description

A succinct description of the contents of the thesis is presented below.

In Chapter 2 the relevant literature with respect to this research is presented and critically reviewed.

Chapter 3 presents the fundamentals of fluid sealing with regards to dry gas face seals. Most of the physics governing the flow between the seal face interface are covered in this chapter. Also presented in this chapter are the methodologies of the two developed numerical models. Detail descriptions of each model are covered in this chapter.

The results of a large number of seal performance investigations carried out for various operating conditions and geometrical seal face profiles are presented in Chapter 4. Also discussed in this chapter are the effects of reverse rotation and face deformation resulting from various geometrical seal face profiles. Chapter 4 also presents the comparative results between both 2 and 3D models as well as the validations of the numerical results against experimental data. An innovative bidirectional type of dry gas face seal developed as part of the study is also presented in this chapter.

Chapter 5 presents the automatic optimization tool that was assembled by the author and was used in this research for the optimisation of mechanical face seals provided the design variables and objective functions can be identified. It describes its methodologies as well as its practical applicability.

Chapter 6 presents a number of parametric studies and optimization of various dissimilar dry gas face seals. A spiral groove gas face seal was used for testing and validating the tool.

Finally Chapter 7 discusses the major findings of this research and presents suggestions for further work to be carried out in the future. A discussion of the novelty and impact of the research is presented in this chapter.

Chapter 2

Review of Dry Gas Face Seal Analysis

2.1 Introduction

The literature review is discussed under the following sub-headings; geometrical seal face profiles, numerical analysis, seal flow regimes and inertia effects, effects of face deformation, effects of surface roughness and numerical optimization. Detailed analyses of some of the papers considered very useful to this study are each evaluated and reported. Some of the papers used in this study were not cited in the thesis are listed in the bibliography.

2.2 Geometrical Seal Face Profiles

Geometrical seal face profiles play major roles in full-film and mixed-film lubrication in terms of generating the film pressure that is required to keep the seal faces apart. Among the widely studied geometrical seal face profiles are the spiral groove seals, radial and parallel groove seals, shrouded pocket seals and the micro-dimples seals. Others are the orifice controlled seals, radially tapered seals and the wavy seals. These geometrical seal face profiles either generate hydrodynamic forces or hydrostatic forces or in some designs both hydrodynamic and hydrostatic forces are generated. The hydrodynamic forces are generated as a result of the viscous shearing of the thin gas film between the rotating and the stationary seal faces, where one of them slides relative to the other. The hydrostatic forces are generated due to the pressure differentials that exist between the seal outer and inner ring diameters peripherals.

The different types of seals - spiral groove, radial and parallel groove, shrouded pocket, micro-dimples seals and orifice controlled seals are described in this section as mechanisms of film pressure generation. However, the forces generated by the wavy and radially tapered

seals are minute compared to the above seal face profiles; hence they are described under the section "effects of face deformation". Additionally, they are not considered in this section as studies have revealed that although they are not machined into seal faces, they can be developed during operation.

2.2.1 Spiral groove seals

This design has series of spirals consisting of elevated regions (land) and recessed regions (grooves) as well as a sealing dam as shown in Figure 2.1. The spiral grooves pattern located on either the rotating or stationary face utilizes the entire outer portion of the seal face. The sealing dam occupies the inner portion of the sealing face. The spiral groove seal generates axial film stiffness in three ways. Firstly, the spiral groove pattern pumps the gas inward, secondly, sealing dam restricting the flow and thirdly, the step bearings mechanism that is developed from the layout of the grooves and lands. The pressurized gas escapes inward over the dam towards the inner diameter (ID) of the seal faces. The generated pressures have areas of higher pressure as well as areas of lower pressure. High-pressure areas on the spiral groove design overlie each other (Sedy, 1980). Waviness is usually developed on the seal faces when the high-pressure areas are wide apart. The difference may become significant when one of the seal faces is made of carbon with a low modulus of elasticity. Waviness formation increases when the film gap decreases due to the increase of film pressure generation which when not properly controlled, can lead to face contact. The waviness formation can be reduced in spiral groove seal by increasing the number of grooves and also by using similar seal face materials that have high modulus of elasticity.

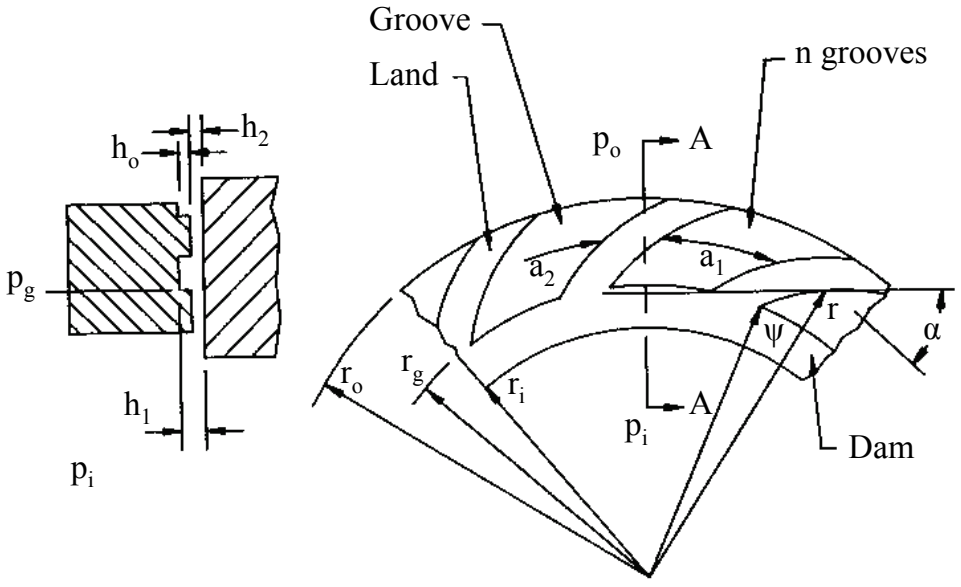

Figure 2.1 Spiral groove face seal (Lebeck, 1991)

In Figure 2.1, p_o, p_i and p_g are the fluid pressure at the seal face outer, inner and groove diameters, respectively. In this figure, r_o, r_g and r_i are the seal face outer, groove and inner radii, respectively while a_1 and a_2 are the circumferential widths of the groove and land, respectively. Also in Figure 2.1, $h_1 = h_o + h_2$ is the total fluid film thickness, h_2 is the minimum film thickness without the groove depth, h_o is the groove depth, ψ is the angular coordinate, r is the radial coordinate and α is the spiral angle.

The well known spiral groove profile was presented by Muijderman (1967) who stated that the best spiral groove profile is that of a spiral that gives a constant tangent angle (logarithmic spiral) as given in Equation (2.1). He (ibid) provided a detailed analysis of the spiral groove bearing using the Reynolds equation. Additionally, Muijderman (1967) reported that the groove to land width ratio γ and film thickness ratio H given in Equations (2.2) and (2.3) respectively, have some significant effect on the spiral groove bearings performance.

$$r = r_g e^{\psi \tan \alpha} \tag{2.1}$$

$$\gamma = \frac{a_2}{a_1} \tag{2.2}$$

$$H = \frac{h_2}{h_1} \tag{2.3}$$

Cheng et al. (1968) compared the performance of the spiral-groove face seal to that of a shrouded pocket seal. They (ibid) observed that for a seal that is primarily hydrostatic (i.e., having a significant pressure ratio), it is better to locate the grooves on the high-pressure side in order to cause greater leakage thereby enhancing stiffness. Cheng et al. (1968) maintained that the shrouded pocket seal produced similar performances as the spiral groove seal although the spiral groove depth used in their comparison was twice that of the depth of the shrouded pocket seal. The shallower the grooves, the higher the stiffness that will be generated by the spiral groove seal (Sedy, 1980).

Zheng and Berard (2001) presented a double spiral groove seal that can generate more angular film stiffness (about three times more) than the conventional spiral groove. This increased angular stiffness is vital for successful operation of large diameter seals that are vulnerable to large face coning resulting from high speed. As a result of more angular stiffness being generated, the stationary seal face could have more power to adapt to the deflection of the rotating face. The seal face consists of a pair of spiral groove sections positioned at the midsection of the sealing dam of the rotating face as shown in Figure 2.2(b). The spiral grooves are aligned in such a manner that the outer spirals pump the fluid outward while the inner spirals pump the fluid inward. The inner and outer spiral grooves are fed through one set of deep middle feeding grooves located at the stationary face as shown in

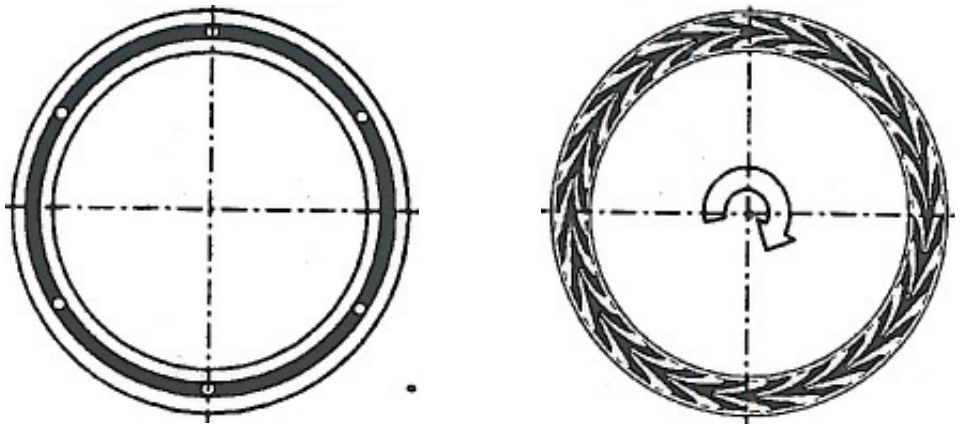

(a) Stator face (b) Rotor face

Figure 2.2 Double spiral groove face seal (Zheng and Berard, 2001)

Figure 2.2(a). These feeding grooves are connected to high-pressure gas through restricted orifices. The feeding holes that lead the high pressure into the middle feeding grooves are designed to restrict the effects on the feeding groove pressure when film thickness is large. Zheng and Berard (2001) maintained that since the fluid enters from the centre of the sealing dam, face coning would never prevent sealing fluid from getting into the seal interface; thereby making the double spiral groove seal more reliable to use in large diameter and high speed applications.

2.2.2 Radial and Parallel Groove Seals

These types of seals have almost the same features as the spiral groove face seal. The only difference between the radial and spiral groove seal is that the radial groove face profile are designed in such a way that the groove depth is constant along a radial line (Basu, 1992). In the parallel groove face profile, the groove depth is constant along a line parallel to the mid-section radial line (Basu, 1992). These seals generate their stiffness in two ways: restriction of the fluid flow by the sealing dam that is located at the seal ring inner diameter (ID) section and the step bearing mechanism formed by the layout of the grooves and lands. Figure 2.3(a) shows the schematic diagram of the radial groove while Figure 2.3(b) shows the comparison between the radial groove and parallel groove.

Some authors ((Basu, 1992) and (Shellef and Johnson, 1992)) have reported on the work on seals having radial and parallel groove features. These authors employed the Reynolds equation in optimizing the geometrical profiles. Based on the rationale of the groove profiles being used in a parametric analysis study, the papers regarding to radial and parallel groove seals are discussed under the section, “numerical optimization”.

Kowalski and Basu (1995) studied the limitation of the spiral groove gas face seal in terms

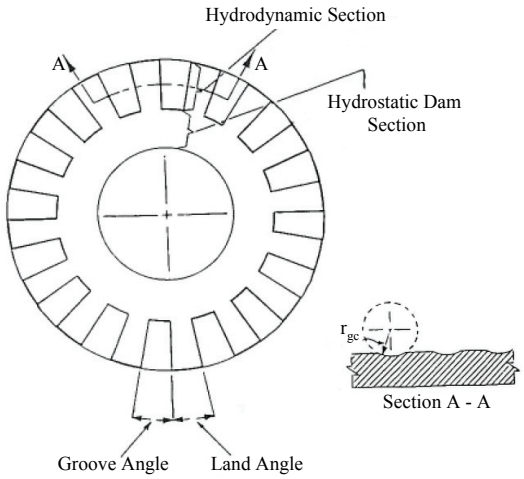

(a) Schematic diagram of a radial groove face seal

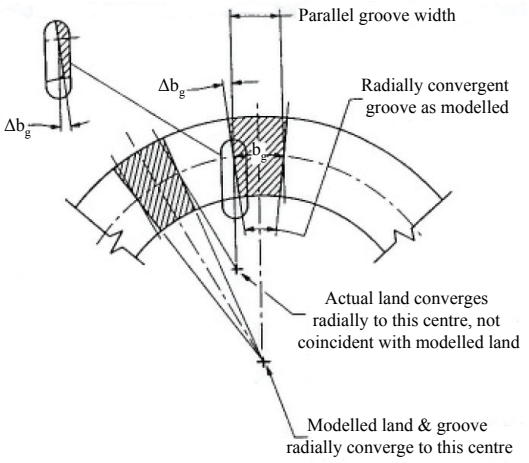

(b) Comparison between parallel and radial groove geometries

Figure 2.3 Radial and Parallel groove face seals (Basu, 1992)

of reverse rotation of the sealing shaft, comparing the axial film stiffness of the spiral groove with the radial groove seals for both directions of shaft rotations. They (ibid) reported that the spiral groove seal generates more positive stiffness than the radial groove seal in forward rotation due to the fact that the radial grooves lack the inward pumping capabilities. In reverse rotation, the radial-groove generates the same stiffness as the one generated in the forward direction, while the spiral-groove loses its positive stiffness and becomes negative beyond a threshold speed of about -1200 rpm. Their (ibid) research indicates that by proper optimization of the spiral groove, the threshold speed where its stiffness becomes negative may be delayed. However, this is at the expense of reducing the stiffness in the forward rotation. Additionally it was stated that by proper optimization of the radial groove, the radial groove can generate the same amount of positive stiffness as the spiral groove in forward rotation.

2.2.3 Shrouded Pad Seals

These types of seals shown in Figure 2.4 generate pressure between the faces by means of their mutual rotation and by pressure generating systems utilizing a 'pump-restrictor' principle. The Rayleigh pockets scoop up the gas, raising its pressure, while the land around the pockets restricts the gas flow. The pressure is generated at certain speeds and therefore depends on the efficiency of the pumping pattern and flow restrictor. The shrouded gas seal ensures higher positive film stiffness and stability at higher generated pressure. The shrouded pad pattern needs a radial groove and an annular groove to feed the gas to the pockets and also to equalize the pressure around the pads. The pressurized gas escapes in three directions over all three dams surrounding the pockets. Unless the dams are very wide, they provide much less restriction than a single width dam on a spiral groove pattern. If the

dams are wide, they occupy too much area and less grooved area is available for pressure generating pads. They generate some areas of higher pressure and other areas with lower pressure. High-pressure areas on the shrouded pad design are wide apart; consequently this makes them more vulnerable to the formation of waviness when compared with the spiral groove seal (Sedy, 1980). Reducing the distance between the high-pressure areas in the shrouded-pad design requires elongated pads and thus a waviness problem is hard to avoid in shrouded pad seals.

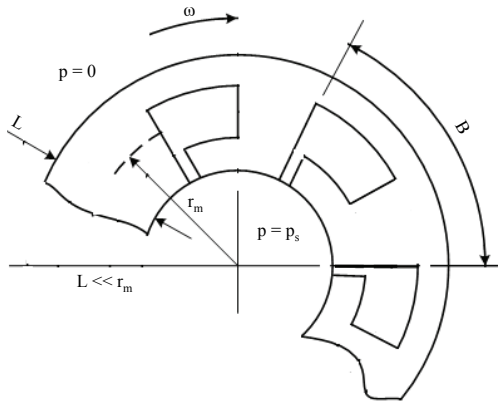

(a) Segmented pocket face seal

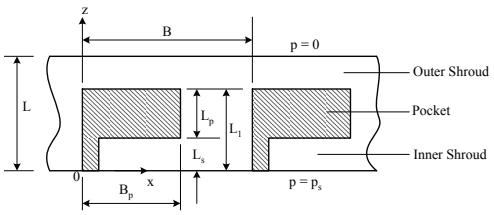

(b) Element of seal

Figure 2.4 Segmented shrouded face seal (Walowit and Pinkus, 1982)

2.2.4 Micro Dimples Seals

These seals have regular hemispherical micro structures (dimples) that are evenly distributed on one of the seal surfaces. These micro structures can be made by laser surface texturing (LST) that entails creation of an array of micro dimples on the seal surface by a material ablation process with a pulsed laser beam (Etsion and Burstein, 1996). There are two types of design, the partial micro-dimple seal and the full micro-dimple seal. In the former design, the micro dimples occupy only a specified part of the sealing dam width usually located at the high pressure section (typically at the outer diameter) leaving the remaining part of the sealing dam width untextured. The latter design consists of micro dimples spread over the entire face of the sealing dam width. The textured segment provides an equivalent larger gap that result in converging clearance in the direction of pressure drop and thereby resulting in hydrostatic pressure build-up.

A schematic illustration of the partial micro-dimple mechanical face seal is shown in Figure 2.5. The textured part adjacent to the high pressure boundary at the outer diameter, d_o stretches from the dimples diameter d_p to d_o as shown in Figure 2.5(a). Micro-dimples seal are usually treated as a collection of radial dimples columns as shown in Figure 2.5(b). This is based on the assumption that mechanical face seals have negligible seal curvature

whereby the ratio of the inner seal diameter to outer seal diameter, d_i/d_o is close to unity (about 0.9). Each column is considered to have a length l equal to the radial width of the sealing dam and a micro-dimple seal length b that is equal to $(d_p - d_o)/2$. A spherical segment with a base radius, r_p (as shown in Figure 2.5(d)) and depth h_p is used to model each of the micro dimples (Kligerman and Etsion, 2001). The micro dimples are spread evenly over the sealing dam with an area density, S_p, which represents the percentage of the seal face between d_p and d_o that is occupied by the dimples. Each micro dimple is located at the centre of an imaginary square cell of sides $2r \times 2r$ where, $r = \frac{r_p}{2}\sqrt{\frac{\pi}{S_p}}$.

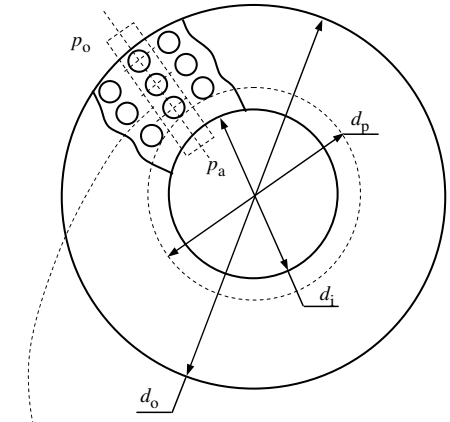

(a) Schematic of a partial LST mechanical seal

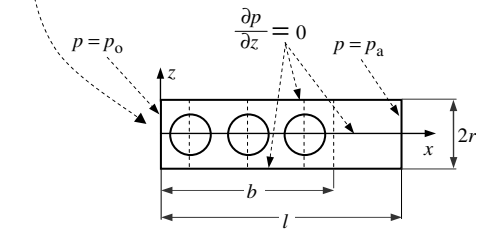

(b) radial dimples column and boundary conditions

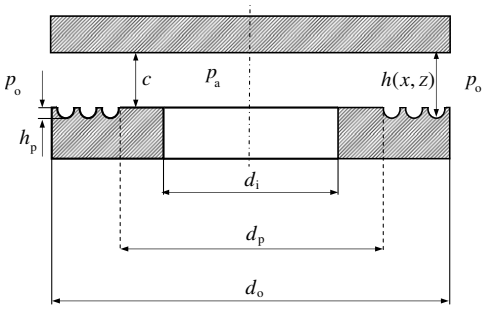

(c) Film thickness variation

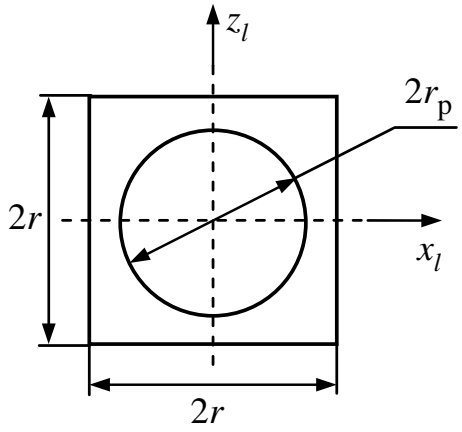

(d) individual cell with a single dimple

Figure 2.5 Geometry of a laser surface textured seal having micro dimple structures (Feldman, Kligerman and Etsion, 2006)

Etsion and Burstein (1996) demonstrated the first model for mechanical seals with regular micro surface structure that showed a substantial improvement in seal performance in terms of film pressure generation. These features were first applied to seals whose sealing fluids were liquid. Kligerman and Etsion (2001) demonstrated that the hydrodynamic effects generated by micro-dimple seal in liquids are as well applicable to gas lubricated high speed seals. The main difference between the micro dimple seal used for incompressible fluid and the one used for compressible fluid is that the ratio of the optimum dimple depth to dimple diameter of the incompressible fluid application is larger than the compressible fluid

application. The micro-dimple seal is advantageous in terms of reducing frictional torque and increasing seal operating pressure limit. The results of experiments carried out by Etsion and Halperin (2002) indicate that the partial micro-dimple seal can significantly reduce the friction torque of high pressure liquid seals thereby boosting the seal operating pressure limit. Additionally, McNikel et al. (2004) showed experimentally in a test carried out at $12000\,rpm$ that a micro-dimple seal can also substantially reduce friction torque and face temperature and have the capabilities of generating hydrodynamic forces. When the micro-dimple seal was compared with an untextured seal at the same operating conditions, it was observed that the micro-dimple seal was more stable during operation than the untextured seal.

Etsion (2004) referring to the work of Hoppermann and Kordt (2002) states that texturing just one surface reduces the friction by 40% compared to a standard non-textured case. Etsion (2004) also reported that texturing both mating surfaces would increase the friction by 100% when compared to a standard non-textured case. Etsion (2004) also reported that texturing one of the seal faces would improve the hydrodynamic pressure generation, reduce friction and increase axial stiffness. The different methods of texturing described in the text include electron beam texturing, etching techniques and laser surface texturing. It was reported that laser surface texturing was the best method because of its speed, positive environmental impact and its excellent control of the shape and size of the grooves. This allows realization of optimum designs. Etsion (2004) also highlights that the partial micro-dimple seal is more advantageous than the full micro-dimple seal. This is mainly because the full micro-dimple seal has poor performance in terms of hydrostatic pressure generation at high pressures. As such, in micro-dimples, a high stiffness of the fluid film is observed below a clearance value of $1\,\mu m$ and a high friction torque of about $5\,Nm$ will indicate the beginning of severe face contact for a micro dimple seal.

2.2.5 Orifice controlled Seal

This type of seal, shown in Figure 2.6, requires the by supplying the seal interface with a source of pressure through some type of restrictor such that the pressure at the supply point becomes larger as the film thickness decreases, thus generating load support and positive stiffness. Lebeck (1991), reviewing the work of Laurenson and O'Donoghue (1978), stated that there were three types of orifice controlled seals capable of generating hydrostatic load. These seals were classified as capillary controlled, orifice controlled and slot feed controlled types. Lebeck (1991) proposes that the orifice controlled is better than the others as it gives higher positive stiffness and lower leakage. It was assumed (ibid) that the source of the controlled pressure to the seal face is the sealed pressure itself, although it was stated that some designs may encourage the use of higher pressure taken from a separate source.

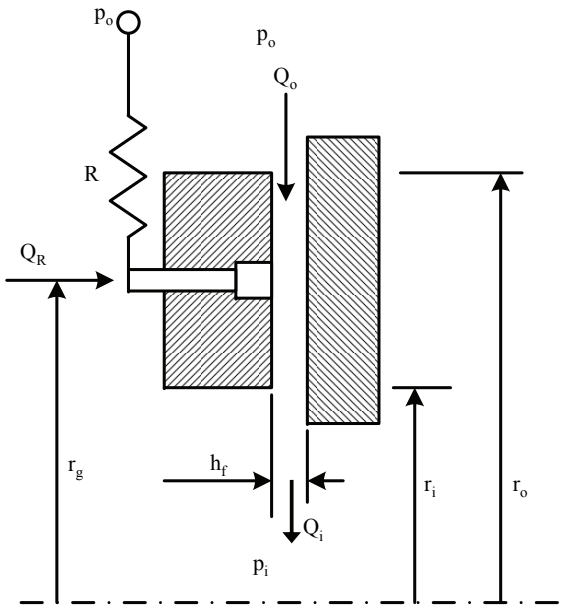

Figure 2.6 Hydrostatic, orifice control face seal (Lebeck, 1991)

A set of flow equations were derived (Equations (2.4) to (2.6)) for leakage associated with orifice controlled seal (Lebeck, 1991). These sets of equations are only applicable to incompressible flow but can be modified for compressible flow. In deriving the sets of equations, it was assumed that the fluid flow from the outside-pressurized side of the seal to the point of the groove radius r_g, and also from the groove radius to the inside radius r_i, assuming that the inside pressure p_i is less than the sealed fluid pressure.

$$Q_o = \frac{\pi(r_o + r_g)}{r_o - r_g} \frac{h^3}{12\mu} (p_o - p_g) \tag{2.4}$$

$$Q_i = \frac{\pi(r_g + r_i)}{r_g - r_i} \frac{h^3}{12\mu} p_g \tag{2.5}$$

$$Q_R = Q_i - Q_o \tag{2.6}$$

2.3 Numerical Analysis

The analysis of dry gas face seals comprises of fluid lubrication analysis, face deformation and heat transfer analysis as well as dynamic analysis. The solutions of the fluid lubrication analysis serve as inputs to the face deformation and heat transfer analysis as well as dynamic analysis. The fluid lubrication analysis is used in analysing the fluid flow in the seal interface to obtain the pressure distribution and seal leakage. Other performances parameters obtained from the fluid lubrication analysis are the opening force and axial stiffness as well as power consumption (frictional torque). The dynamic analysis is usually carried out to ascertain whether the gas film is stiff enough to enable the stator to track the rotating rotor in case of

axial runout. The face deformation and heat transfer analysis is employed in determining the amount of face deformation that occurs in seal operation.

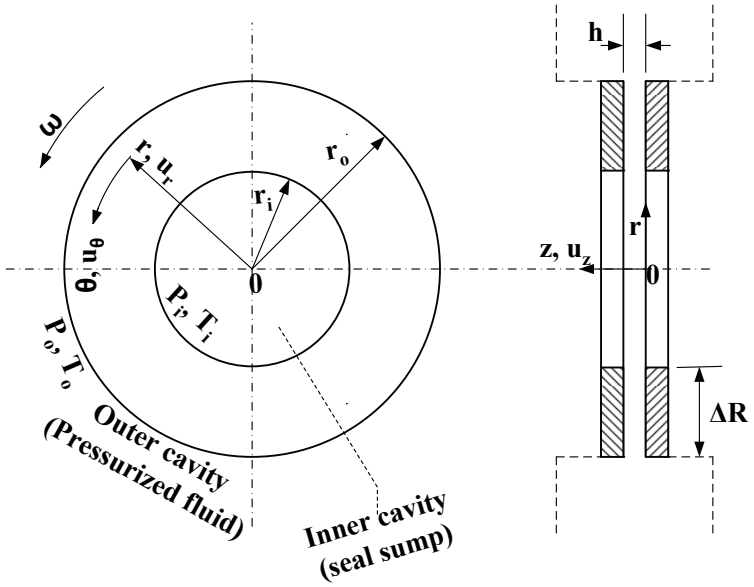

Figure 2.7 Two narrowly spaced parallel plain surfaces - one rotating relative to the other

The compressible Navier-Stokes equations set, which includes the continuity equation, are the equations that govern compressible fluids (gases) between narrowly spaced annular disks such as dry gas face seals. Using Figure 2.7 as a reference, the radial, circumferential and axial components of the compressible Navier-Stokes equations are presented in Equations (2.8), (2.9) and (2.10) respectively. Equation (2.7) represents the continuity equation. The z axis is aligned with the thin direction of the lubrication film as shown in Figure 2.7. The fourth term on the left hand-side of Equation (2.8) is the centrifugal inertia term and the remaining terms on the left hand-side of Equations (2.8), (2.9) and (2.10) are the convective inertia terms. The first terms in the right hand-side of Equations (2.8), (2.9) and (2.10) are the pressure gradient force terms. The second terms in the right hand-sides of Equations (2.8), (2.9) and (2.10) are the viscous friction force terms and the last terms on the right hand-sides of Equations (2.8), (2.9) and (2.10) are the gravitational forces. These last terms are negligible compared to the other terms.

$$\frac{1}{r}\frac{\partial}{\partial r}(r\rho u_r)+\frac{1}{r}\frac{\partial(\rho u_\theta)}{\partial\theta}+\frac{\partial(\rho u_z)}{\partial z}=0 \tag{2.7}$$

$$\begin{aligned} &u_r\frac{\partial(\rho u_r)}{\partial r}+\frac{u_\theta}{r}\frac{\partial(\rho u_r)}{\partial\theta}+u_z\frac{\partial(\rho u_r)}{\partial z}-\frac{\rho u_\theta^2}{r}=-\frac{\partial p}{\partial r}\\ &+\mu\left[\frac{1}{r}\frac{\partial}{\partial r}\left(r\frac{\partial u_r}{\partial r}\right)+\frac{1}{r^2}\frac{\partial^2 u_r}{\partial\theta^2}+\frac{\partial^2 u_r}{\partial z^2}-\frac{u_r}{r^2}-\frac{2}{r^2}\frac{\partial u_\theta}{\partial\theta}\right]+\rho g_r \end{aligned} \tag{2.8}$$

$$u_r\frac{\partial(\rho u_\theta)}{\partial r}+\frac{u_\theta}{r}\frac{\partial(\rho u_\theta)}{\partial\theta}+u_z\frac{\partial(\rho u_\theta)}{\partial z}+\frac{\rho u_r u_\theta}{r}=-\frac{1}{r}\frac{\partial p}{\partial\theta}$$
$$+\mu\left[\frac{1}{r}\frac{\partial}{\partial r}\left(r\frac{\partial u_\theta}{\partial r}\right)+\frac{1}{r^2}\frac{\partial^2 u_\theta}{\partial\theta^2}+\frac{\partial^2 u_\theta}{\partial z^2}+\frac{2}{r^2}\frac{\partial u_r}{\partial\theta}-\frac{u_\theta}{r^2}\right]+\rho g_\theta \tag{2.9}$$

$$u_r\frac{\partial(\rho u_z)}{\partial r}+\frac{u_\theta}{r}\frac{\partial(\rho u_z)}{\partial\theta}+u_z\frac{\partial(\rho u_z)}{\partial z}=-\frac{\partial p}{\partial z}+\mu\left[\frac{1}{r}\frac{\partial}{\partial r}\left(r\frac{\partial u_z}{\partial r}\right)+\frac{1}{r^2}\frac{\partial^2 u_z}{\partial\theta^2}+\frac{\partial^2 u_z}{\partial z^2}\right]+\rho g_z \tag{2.10}$$

2.3.1 Reynolds Equations Based Methods

The Reynolds equation given in Equation (2.11) is the fundamental equation for the study of thin full-film lubrication. It is derived from the Navier-Stokes and continuity equations. In deriving the Reynolds equation, some terms such as the inertia terms and turbulence effects are neglected. As a result of the mentioned assumptions, using the Reynolds equation for the analysis of seals operating at high rotating speeds and high pressure differential is limited. This equation is used in solving for the pressure distributions and flow fields in the seal face interface. The pressure distributions as well as the flow characteristics control the performance and dynamic behaviour of liquid and dry gas face seals. Detailed derivation of the Reynolds equation is given in Lebeck (1991) and therefore need not be stated here. The assumptions considered in deriving the equation are given below.

1. A steady state condition is imposed thus $\frac{\partial(\,)}{\partial t}=0$. This assumption will not have a significant impact on the seal performance, provided one of the surfaces is relatively flat relative to the other (Lebeck, 1991).
2. The velocity gradients of u_r and u_θ with respect to z are much larger than all other velocity gradients. The fluid flow in the seal interface is assumed to be laminar. This is an appropriate simplification given that in lubrication problems, the film thickness is very small (of the order of micrometers) relative to other dimensions of length. Thus $\frac{\partial^2(\,)}{\partial r^2}\ll\frac{\partial^2(\,)}{\partial z^2}$ and $\frac{\partial^2(\,)}{\partial\theta^2}\ll\frac{\partial^2(\,)}{\partial z^2}$.
3. There is no pressure gradient across the seal interface hence $\frac{\partial p}{\partial z}=0$.
4. The gravitational forces are very small compared to other forces present in mechanical seals hence they are neglected provided the fluid is fully enclosed. Thus $\rho\, g_r=\rho\, g_\theta=\rho\, g_z=0$.
5. The effect of surface roughness on fluid flow is negligible provided the minimum film thickness is several times greater than the magnitude of the surface roughness.
6. The fluid is assumed to be a perfect gas hence $p=\rho\, RT$.

$$\frac{1}{r}\frac{\partial}{\partial\theta}(\rho h^3\frac{\partial p}{\partial\theta})+\frac{\partial}{\partial r}(r\rho h^3\frac{\partial p}{\partial r})=6\mu r\omega\frac{\partial}{\partial\theta}(\rho h)+12\mu r\frac{\partial}{\partial t}(\rho h) \tag{2.11}$$

The first and the second terms on the left hand-side of Equation (2.11) are the circumferential-direction and radial-direction pressure flow terms respectively. The first term on the right hand-side of Equation (2.11) is the tangential shear flow and is always regarded as the "wedge film" or hydrodynamic term. The last term on the right hand-side of Equation (2.11) is the flow due to wall motion, normal to the radial flow, and is regarded as the squeeze film term. The wedge term represents the pressure build up because of the geometrical face profiles while the squeeze film term represents the pressure build up because of film thickness changing with time. The r and θ variables are the radial and circumferential polar coordinates respectively, p is the local pressure within the fluid film, ρ and μ are the density and dynamic viscosity of the lubricant, respectively. Also, h denotes the film thickness and ω is the angular velocity of the rotating seal face. The Reynolds equation is discretized in two ways, either with the finite difference method or with the finite element method. The latter method is very flexible in treating curved physical boundaries hence it is preferable to the finite difference method for modelling complex groove geometries.

The fluid flow in the seal interface has been analysed in the past mainly as a 2-dimensional problem. This has been done by either employing the Reynolds equation, or subsequent modifications of the Reynolds equation, to include the effects of turbulence. The fluid film thickness is part of the Reynolds equation and it is expressed as a function of the minimum axial distance separating the sealing rings apart. It can also be expressed as a function of radial taper, circumferential waviness as well as surface roughness to include the effects of face deformation and surface roughness. Discussed below are some of the papers that employed the Reynolds equation in their analysis. Some of them will be discussed under the section "numerical optimization" hence, they will not be discussed in this section.

van Odyck and Venner (2003) investigated the laminar flow of a compressible medium in a thin film containing rectangular slot geometry. They employed the Reynolds equation and Stokes equation in their analysis. The authors reported that there are differences in the load capacities obtained from the solutions of the Reynolds and Stokes equations; additionally they reported that the Stokes solution was able to predict the compressibility of the medium that can lead to cross-film pressure dependence. The Reynolds equation failed to predict the compressibility of the fluid thereby limiting its validity. van Odyck and Venner (2003) also concluded that despite the fact that there are local differences in the pressure at the edges of the rectangular slot; the solutions of the two methods in terms of load carrying capacity are in excellent agreement.

Guardino et al. (2004) investigated both incompressible and compressible flows in air riding seals having a Rayleigh step geometry on the stationary wall. They solved the full Navier-Stokes equations for the fluid flow in the seal interface and also used the Reynolds equation for their analysis. They considered different two-dimensional roughnesses in the form of sinusoidal waves on the stationary wall. These authors showed that surface roughness produced observable effects on the streamline patterns, which resulted in widespread recirculation regions, mostly when the ratio of the roughness amplitude to the clearance is large. Guardino et al. (2004) also reported that the solutions of the Navier-Stokes and Reynolds equations were in good agreement at low values of the ratio of the roughness amplitude to the clearance. At higher values of the ratio of roughness amplitude to clearance, they further described that the solutions of the Reynolds equation underestimate the load carrying capacity when compared to the Navier-Stokes solutions. They detailed that the differences observed between the Reynolds equation and Navier-Stokes solutions are more pronounced for incompressible flow than the ones of compressible flow.

Almqvist and Larsson (2004) examined the limits of the validity of the Reynolds equation for lubricant film flows through a parallel slider having a 2D edge surface roughness placed on the stationary surface. The authors considered Newtonian, non-Newtonian, piezoviscous and compressible fluids in their study. They indicated that the Reynolds equation was a good approximation with an error of less than 3% in the maximum pressure and in the pressure difference across the fluid film when the film thickness to wave length ratio is of order 10^{-2} or less. They also reported that when the film thickness to wave length ratio is of order 10^{-1}, the variations between the Reynolds and the full Navier-Stokes solutions increased to about 8% in the maximum pressure and increased to about 30% in the pressure difference across the fluid film. The comparison made by these authors dealt with the local pressure extremum in relation to the load carrying capacity. Almqvist and Larsson (2004) concluded that despite the fact that the error in the pressure field may be large, the included effect in the terms of load carrying capacity may be minute and can therefore be considered as negligible.

Feldman, Kligerman, Etsion and Haber (2006) employed a finite difference algorithm in discretizing the compressible Reynolds equation which was used in solving for the fluid flow in the seal interface of a micro dimples seal. A single dimple was considered in their analysis. The geometrical parameters used in their study are: dimple diameter $2r_p = 100\,\mu m$, the dimple depth h_p ranges from $5\,\mu m$ to $50\,\mu m$ and the clearance c ranges from $1\,\mu m$ to $5\,\mu m$. The dimensionless dimple depth ε ranges from 0.05 to 0.5 while the dimensionless dimple diameter δ ranges from 0.01 to 0.05. The dynamic viscosity μ of air used was $18.21 \times 10^{-6}\,Pa\,s$ at 20^oC, and the pressure drop across the dimples strip was considered to be $0.1\,MPa$. The authors compared the solutions of the Reynolds equation with the Navier-Stokes equations solutions for the same problem. Feldman, Kligerman,

Etsion and Haber (2006) showed that the maximum comparative difference in the pressure distribution between the solutions of the two methods occurred in the midsection of the dimple.

There exist significant pressure variations across the fluid film thickness close to the leading and trailing edges of the dimple where the film thickness gradient is discontinuous as reported by Feldman et al. (2006b). They stated that the local differences mentioned above only have little effect on the load carrying capacity. It was also identified that for clearances, c, that are 3% or less of the dimple diameter, the load capacity predicted by the Reynolds equation is valid over the entire range of practical dimple depth and pressure ratios. Large clearances as large as 5% of the dimple diameter and pressure ratios of about 2.5, the error in terms of load capacity predicted by the Reynolds equation may reach 15% were also reported. Feldman, Kligerman, Etsion and Haber (2006) showed that employing the Reynolds equation in seal analysis would yields realistic load capacity predictions for a wide range of reasonable clearances and pressures. They also accounted for higher clearances, indicating that the use of the Reynolds equation would only offer a rough approximation of the load carrying capacity. Feldman, Kligerman, Etsion and Haber (2006) concluded that since the Reynolds equation underestimates the load for the range of parameters considered, the Reynolds equation can safely be used for hydrostatic seals with micro dimples.

2.3.2 Navier - Stokes Equations Based Methods

The prediction of the fluid flow in the seal interface is undoubtedly complex. Therefore if a detailed analysis is required to include the effects on the flow of the complex interaction with the geometric features of the faces, dams, grooves, feed slots and the effects of deformation of the faces, then a computational fluid dynamics (CFD) prediction is required. In order to analyse complex face geometry and seals operating at high rotational speeds and pressures, special purpose solvers or 3D numerical codes that solve the full Navier-Stokes equations are required such that the effects of inertia, compressibility, turbulence, choking and discontinuities in the film thickness can be handled.

Despite the recent advances in dry gas face seal technology, computational fluid dynamics (CFD) which has been actively employed in studying rotating components such as bearings and labyrinth seals, has not been effectively used to evaluate dry gas seal designs and very little work has been reported in published papers. The main reason being that the size of the gap separating the seal faces is very small, which is of the order of micrometers, and this feature complicates significantly the numerical work.

To date, only a few papers, (Wu and Clark (2000), Kudriavtsev et al. (2001), Leefe (2002),

Zheng (2005), Luan and Khonsari (2006) and feng Zhang et al. (2006)) have addressed the use of commercial CFD models for analysing mechanical face seals. A few of these (Leefe (2002), Luan and Khonsari (2006) and feng Zhang et al. (2006)) employed incompressible fluids while others (Wu and Clark (2000), Kudriavtsev et al. (2001) and Zheng (2005)) made use of compressible fluids in their research. All focussed their attention on seals operating within the range of sealed fluid pressure of a maximum of $40\,bars$ and a shaft speed of $30000\,rpm$. Most of them (Kudriavtsev et al. (2001), Leefe (2002) and feng Zhang et al. (2006)) did not considered flows at a very thin fluid film thickness since their simulations stopped at $5\,\mu m$ except Wu and Clark (2000) and Zheng (2005). Dry gas face seals typically operate between $3-5\,\mu m$. Some of them (Wu and Clark (2000), Kudriavtsev et al. (2001), Leefe (2002) and feng Zhang et al. (2006)) used the commercial CFD package for solving the full Navier-Stokes equations for the fluid flow in the interface while Luan and Khonsari (2006) solved the Navier-Stokes equations for fluid flow between the seal gland and sealing rings outer surfaces. Therefore, in this section, the key findings of papers that analysed mechanical face seals performances by solving the full Navier-Stokes equations using commercial CFD packages will be discussed.

Wu and Clark (2000) carried out a CFD analysis for studying and examining stationary and rotating spiral groove seal rings in terms of pressure development and fluid flow in the seal interface of a twin hybrid gas lubricated mechanical face seal. They employed a commercial CFD package, Fluent in solving the full Navier-Stokes equations. The spiral grooves were located at the midsection of the sealing dam. The seal they considered had two dams, one located at the seal ring outer diameter section and the other sealing dam located at the seal ring inner diameter section. A barrier gas was injected through a series of holes equally spaced circumferentially within the floating stationary ring during operation.

The gas film thickness between the stationary and rotating faces was assumed to be $1.9\,\mu m$ for a seal operating at $3600\,rpm$. A constant pressure boundary condition of $0.446\,MPa$ was used to represent the incoming flow of barrier gas through the annular inlet surface. The temperature of the boundaries representing the seal faces was assumed to vary linearly from 32^oC at the ID to 49^oC at the OD. The temperature of the annular inlet was also assigned a radially dependent value equivalent to that imposed on the seal ring boundaries. $r_i = 0.0262\,m$, $r_o = 0.0382\,m$, $r_g = 0.0342\,m$ and $\Phi = \pi/6$ is the angular extent of the single cyclic geometric segment.

The results indicated that there is no difference in terms of pressure generation and fluid flow when the hydrodynamic lift features were positioned on either the rotating or stationary face. It was also reported that the computed scalar variables (pressure and density) of the flow within the seal interface, as well as the hydrodynamic seal face features, were all found

to be everywhere unchanged with axial position (Wu and Clark, 2000). They (ibid) deduced that their results showed strong evidence for the validity of the thin-film lubrication theory and associated assumptions used in the development of the simplified governing equations. The results obtained for pressure and density, as well as those representing the flow velocity field, suggested that the development of hydrodynamic pressure by the spiral grooves arise via boundary-driven pumping and compression of gas against the sealing dams at the inner and outer diameter sections of the seal. Additionally, the circumferential component of the velocity dominated nearly everywhere in the flow field, particularly within the radial range of the spiral grooves. Wu and Clark (2000) also noted that valuable physical characteristics of the flow can be revealed by the behaviour of all velocity components comprising of the radial, axial and circumferential components of the velocities.

Kudriavtsev et al. (2001) employed a full 3D Navier-Stokes equations solver (CFD-ACE+) in studying the flow patterns inside an inward pumping spiral groove seal. In their computational domain, the grooved patterns were etched on the stationary ring. The compressible laminar and $k-\varepsilon$ turbulent flow models were used. The gas properties they considered followed the Sutherland's formula of viscosity. The effects of groove angle/rotation alignment were taken into account by changing sign of the rotating speed from positive to negative. In their study, a diverging groove layout as shown in Figure 2.8(a) was employed. The groove inlet was located at the high pressure end while the sealing dam at the low pressure side. A segment of the seal face was modelled. The geometrical dimensions of the model were: seal ring inner radius r_i, $0.0184\,m$, seal ring outer radius r_o, $0.05\,m$, fluid film thickness h_f, $10\,\mu m$ and groove depth h_g, $500\,\mu m$. In addition, the operating parameters considered were: rotating speed ω, $25000\,rpm$, sealed fluid pressure p_o, $0.45\,MPa$ and the seal ring inner pressure p_i, $0.1\,MPa$.

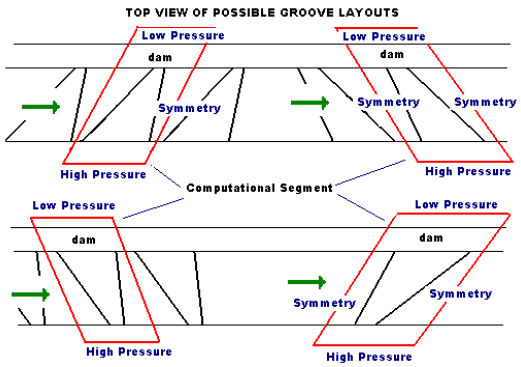

(a) Groove Layouts Row 1: converging groove; Row 2: diverging groove Column 1: opposite rotation; column 2: aligned with rotation

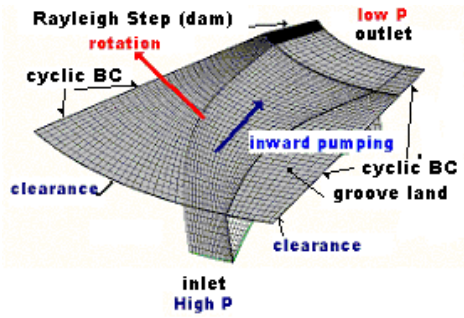

(b) A diverging groove layout of a spiral groove seal section

Figure 2.8 A computational domain of a spiral groove seal (Kudriavtsev et al., 2001)

Kudriavtsev et al. (2001) demonstrated the feasibility of using the full Navier-Stokes equations for analysing the performances of the fluid flow in the seal interface of a spiral groove gas face seal configurations. It was demonstrated that the inward pumping spiral groove creates a positive pressure gradient as a result of the pressure differential between the seal ring diameters as well as fluid been entrained into the groove area by mechanical pumping action of the rotating shaft. They reported that the pumping characteristics were most critical and strongly depended on the rotational speed, direction of rotation, groove depth, orientation and shape, groove to dam ratio and liquid/gas properties. The complex 3D nature of the flow in the seal interface, which highlights the limitations of the narrow groove theory and Reynolds equations, was also identified. They compared the performance of two alternative designs at realistic operating conditions. Kudriavtsev et al. (2001) concluded that groove layout and direction of rotation can significantly impact leakage flow.

Leefe (2002) performed the analysis of a spiral groove seal used in a high - speed cryogenic turbopump and parallel plain face seal. The author used a commercial CFD package, CFX-4, in solving the 3D Navier-Stokes equations for the fluid flow in the seal interface. This was used in optimizing the seal face geometry as well as evaluating the seal performance for several known combinations of operating speed and pressure. The isothermal flow assumption was made and a low Reynolds number $k-\varepsilon$ turbulence model was employed in cases where the flow was presumed to be turbulent. Cryogenic fluid - LOx (an incompressible fluid) was used as the sealing fluid. The maximum speed and sealing fluid pressure employed were $30000\,rpm$ and $3.4\,MPa$ respectively. The effects of cavitation were neglected. The number of grooves chosen was between 10 and 20, where the land to groove ratio was fixed to a value of 1, the groove depth was between 10 and $100\,\mu m$ and the groove angle between 30^o and 60^o. The seal ring inner and outer radii were $0.0375\,m$ and $0.0435\,m$ respectively.

Leefe (2002) clearly distinguished between the application p-v rating and tribological p-v rating with regards to non-contacting seals. The application p-v rating was defined as the severity of the duty in terms of the product of the sliding speed and sealed pressure. This is compared to the tribological p-v which represents the friction and wears demand in terms of the product of the sliding speed and mean contact pressure. This study determined that non-contacting seals are indicative of application p-v duty, which could be very high and limited by the ability of the sealing elements to withstand the sealed pressure in order to maintain the design clearance; whereas the tribological p-v can be low and typically sufficient to withstand rubbing contact in the early stages of the start-up transient.

Curves of opening force against parallel fluid film thickness and parallel fluid film thickness against leakages were also established in this study (Leefe, 2002). The opening force curves

were generated by running CFD simulations at different fluid film thickness. In this study, four fluid film thicknesses, which lie between 5 and 40 μm were considered. The opening forces obtained at these different values of the fluid film thicknesses were plotted against the respective fluid film thicknesses. The opening force curve was approximated with a quadratic interpolation. In order to obtain the equilibrium fluid film thickness, the closing force was also plotted against the fluid film thicknesses. The point of intersection of the opening force and closing force curves was used in obtaining the equilibrium fluid film thickness. The equilibrium fluid film thickness is used in estimating the seal leakage from the equivalent curve of leakage and fluid film thickness.

It was predicted by Leefe (2002) that fluid film thickness increases with speed at a constant sealed pressure. He (ibid) also observed that given a constant speed, as the sealed pressure decreased, the film thickness increased - despite the decrease in opening force. This may be due to the fact that the opening force balances with the closing load, which also decreases with sealed pressure, thereby making the film thickness quite insensitive to the operating conditions. It was also pointed out that the proportional change in fluid film thickness per unit coning was low, about 5% less than when coning angle was not applied, and provided the shaft speed is high. The results indicated that for a plain face seal in non-contacting operation, the leakage rate has a cubic dependence on film thickness while for a spiral groove face seal, the leakage rate depends on the film thickness by a power of approximately 1.56, both operating at the same sealed pressure and speed. It was concluded that the lower power dependence in the spiral groove seal is an indication of spiral groove face seal generating less leakage as compared with plain face seals. These results were not validated against experimental data.

For the optimization process, five design variables were used. They include the groove angle, groove depth, number of grooves, dam width and film thickness. Each of the design variables have lower and upper limit values respectively. The performance parameters (response surfaces) include opening force, leakage and torque. A systematic variation of the design variables was achieved using the factorial experimental design technique in investigating the response surfaces. This technique was used in specifying ways in which combination of the design variables (geometrical parameters) were varied, not just one at a time, so that the maximum information were extracted from the few CFD runs that were carried out. The optimum parameters obtained from the optimization process are: groove angle of 45^o, 15 numbers of grooves, and groove depth of 32.5 μm and seal dam width of 0.00125 m.

Luan and Khonsari (2006) employed a commercial CFD package for solving the flow between the seal gland and rings outer surfaces. The flow fields inside the seal chamber

and the seal rings outer surfaces were produced by the influx of flush fluid (barrier fluid) into the seal chamber for the cooling of the seal rings. All the rotating speeds considered were less than 7200 rpm and were treated as laminar flows. They deduced from their results that the thickness of the dense streamlines adjacent to the rotating ring varies approximately linearly with the flush rate. They concluded that cooling is not necessarily improved if the flush rate is increased beyond a certain rate as some of the flush will exit directly without offering much cooling effect on the rings.

2.4 Seal Flow Regimes and Inertia Effects

The appropriate equations used for seal analysis mainly depend on the flow regimes and the effect of inertia. There are two possible seal flow regimes which are based on the Reynolds number and the Knudsen number respectively. The Reynolds number is used in characterizing the flow into either laminar, transition or fully turbulent flow regimes. The Knudsen number is used in classifying the flow into either the continuum or non-continuum flow. Discussed in this section are the effect of turbulence, continuum and non-continuum flow and the effect of inertia.

2.4.1 Effect of Turbulence

In ideal situations, some seals may operate with a large pressure gradient and without rotating velocity; while others may operate with relatively high rotating speed and zero pressure gradients. The former can be described as radial Poiseuille flow (Pressure driven flow) and the latter as pure Couette flow (shear flow). In practice, dry gas face seals operate with both pressure gradient and rotating speed, hence the fluid flow in the sealing interface is a combined circumferential Couette flow and radial Poiseuille flow. When dry gas seals operate with a high pressure gradient and high rotation speed, the fluid flow may become non-laminar (turbulent).

The Reynolds number which determines the flow regime depends on the rotating speed, fluid density, characteristic length and fluid viscosity. The fluid viscosity is assumed to be essentially constant if the temperature change in the fluid flow is minimal and there is no contact between the seal faces. The fluid flow can be characterized into three flow regimes according to the critical Reynolds number. One of these regimes is the laminar condition where the Reynolds number is less than the critical Reynolds number, while in the other, the fully turbulent regime, the Reynolds number is greater than the critical Reynolds number. A transition condition lies between the laminar and the fully turbulent regimes and this corresponds to the behaviour of the flow as it begins to exhibit some randomness.

The transition point in terms of the Reynolds number for the radial Poiseuille flow Re_p is defined as shown in Equation (2.12). For flow between narrowly spaced plates and coaxial annular disks the hydraulic diameter is $D = 2h$ as reported by Zuk (1976).

$$Re_p = \frac{\rho u_r D}{\mu} \tag{2.12}$$

Whenever there is a relative rotation of the seal surfaces, turbulence can be induced by the rotational effect. The factor that is responsible for the turbulent nature of the flow may be attributed to the rotational flow component of the velocity which, always acts in the circumferential direction or shear flow direction (Zuk, 1976). For narrow gaps (close clearances, where the boundary layers maybe separated or merged), the critical rotational Reynolds number at the point of transition appears to be the simple Couette flow transition Reynolds number. The Couette flow Reynolds number Re_c is defined in Equation (2.13).

$$Re_c = \frac{\rho \omega r h}{\mu} \tag{2.13}$$

Patel and Head (1969) are among the researchers who have based their studies on pure Poiseuille flows. Their findings indicate that in measured skin friction of flow in a channel, the flow is laminar when Re_p is less than 1300 and the flow is turbulent when Re_p is greater than 2800. Bassani and Piccigallo (1992) reported that the flow will become turbulent when Re_p is greater than 2300.

Other researchers have based their studies on pure Couette flows with interesting findings. Robertson (1959) measured the friction factor for turbulent plane-Couette flow and reported that the flow would be laminar when Re_c was less than 1300 and fully turbulent when Re_c was greater than 3000. Robertson (1959) obtained his Couette's data via an outer rotating cylinder with a small clearance and observed that the Taylor vortices only have minimal effects on the flow. Frêne (1977) experimental study observed that thin film fluid flows become turbulent when $Re_{c,min}$ is greater than 800 and $Re_{c,max}$ is less than 5000, but greater than 4100, with $Re_{c,min}$ and $Re_{c,max}$ as the minimum and maximum values of the Couette Reynolds number in thin film. In his theoretical work, Frêne (1977) observed that the fluid flow was not laminar when Re_c was greater than 1000 and the flow was turbulent when it was greater than 2000, which raised some doubts over his experimental results. Souchet (1991) as reported by Brunetière et al. (2002) recommended that the flow will be laminar when Re_c is less than 900 and will be fully turbulent when Re_c is greater than 1600. Yasuna and Hughes (1994) assumed that turbulence appears when Re_c is greater than 3000. They were interested in the axial dynamic behaviour for both laminar and turbulent thin film fluid flow. They pointed out that their study was limited by the fact that no attempt was made to

resolve the transition from laminar regime to turbulence. Lin and Yao (1996) noted that the flow in the interface of a face seal will be turbulent when Re_c is greater than 1000.

It has been reported that in pure Poiseuille flows, a flow that was initially turbulent at the entrance region could revert to laminar flow at a lower radius and subsequently a higher Reynolds number. Murphy et al. (1983), Mutama and Iacovides (1993), and Singh et al. (1999) contended that the acceleration of the fluid could lead to a decrease in the turbulence level. Mutama and Iacovides (1993) reported that the appearance of such reverse transition depends on an acceleration parameter, K_r as defined in Equation (2.14); where β in Equation (2.14) is the seal faces total coning. Mutama and Iacovides (1993) also stated that reverse transition occurs for values of K_r ranging from 10^{-7} to 10^{-6}. This implies that the fluid flow in a pure Poiseuille flow cannot be turbulent if the rotor of the seal is motionless.

$$K_r = \frac{1}{Re_p}\left(\frac{h}{r} + \beta\right) \tag{2.14}$$

Based on the above rationale, Debuchy et al. (1998) studied the flow between a stationary and rotating disc with and without a superimposed radial inflow. The rotation of one of the disks led to a turbulent flow. Their results showed that when the accelerated inward flow was superimposed on the circumferential Couette flow, the turbulence level was not decreased. Debuchy et al. (1998) reported that even if the acceleration parameter K_r was large enough for a reverse transition, the fluid acceleration in the radial direction was unable to remove turbulence produced by the circumferential motion.

When both circumferential shear flow and radial pressure flow exist, (as in a dry gas face seal), Brunetière (2005) noted that the parameter that characterized the flow into regimes is the Couette flow Reynolds number. He based his argument on the basis that the net flow of the combined shear flow and radial pressure flow is a spiral flow. Brunetière (2005) stated that the fluid flow would be laminar when Re_c is less than 900 and the flow will be fully turbulent when Re_c is greater than 1360 and within these two limits is the transition regime.

When a high pressure gradient and high rotating speed exist, it is necessary to include the effect of the pressure flow in determining the critical Reynolds number. The critical Reynolds number for a combined rotational flow Re_c and pressure flow Reynolds number Re_p is determined from a flow factor α_f proposed by Brunetière et al. (2002) and defined in Equation (2.15). The flow factor shows that transition to turbulence is dependent on both the rotational flow Reynolds number and pressure flow Reynolds number. When the flow factor is greater than 1, Brunetière et al. (2002) note that the flow is fully turbulent, when it is less than $900/1600$, the flow is laminar and between $900/1600$ and 1, the flow is in the transition regime. They (ibid) demonstrated that the limits of the flow regime are defined by

ellipses of the same eccentricity.

$$\alpha_f = \sqrt{\left(\frac{Re_c}{1600}\right)^2 + \left(\frac{Re_p}{2300}\right)^2} \tag{2.15}$$

The studies of turbulence in lubricant film started in the 1960s as a result of the increase in operating requirements of bearings which were later applied to mechanical seals. During this period, several authors developed several turbulence models for thin fluid films. The first lubricant film turbulence model was developed by Constantinescu (1962) using the concept of mixing length. Other models were later proposed by Ng (1964), Ng and Pan (1965) and Elrod and Ng (1967). Their theories were based on the empirical law of Reichardt. Elrod and Ng (1967) developed a model which is a nonlinear eddy-viscosity model as opposed to the original model of Ng and Pan (1965) that offers the advantage of correctly describing both Couette and Poiseuille flows. The bulk flow model was initiated by Hirs (1973) and only the averaged velocity of the fluid in the cross-film directions was considered which limits its use, thereby not giving access to the fluid velocity in the whole film.

For flow very close to the wall, Elrod and Ng (1967) used the Reichardt's formula to determine the turbulent viscosity as given in Equation (2.16).

$$\frac{\varepsilon_R}{\nu} = \kappa\left(Z\sqrt{\tau^*} - \delta_l^+ \tanh\frac{Z\sqrt{\tau^*}}{\delta_l^+}\right) \tag{2.16}$$

Where κ is the Karman constant and equal to 0.4 and δ_l^+ is a viscous length scale which they considered to be 10.7. Z (expressed as $Z = min\left(\frac{z-H_2}{h}, \frac{H_1-z}{h}\right)$) and τ^* (expressed as $\tau^* = \frac{h^2 \mid \tau \mid}{\mu\,\nu}$) are the dimensionless distance from the nearest wall and shear stress respectively. Where h is the axial distance between the stationary ring (H_2) and the rotating ring (H_1), both distances taken from a reference point respectively. Also τ is the shear stress, ν is the fluid kinematic viscosity and z is the axial distance.

To ensure that the turbulent viscosity does not vanish when the shear stress is zero, they (ibid) forced an increasing monotonous evolution of the viscosity in each half channel as given in Equation (2.17).

$$\frac{\varepsilon_W}{\nu}(z) = max\left[\frac{\varepsilon_R}{\nu}(z')\right], \ \forall z' \prec z \tag{2.17}$$

In the core region, Elrod and Ng (1967) proposed the use of a modified Clauser formula given in Equation (2.18) that is adapted to lubrication. Where V_{XM} and V_{YM} are the

components of the maximum velocity across the film. In order to consider both the wall and core regions, they used a turbulent viscosity ε_M that is a minimum of ε_W and ε_C ($\varepsilon_M = min(\varepsilon_W,\ \varepsilon_C)$). Where ε_W, ε_R and ε_C are the wall turbulent diffusivity, Reichardt turbulent diffusivity and Clauser turbulent diffusivity respectively.

$$\varepsilon_C = \frac{1}{56}\sqrt{\left[\int_{H_2}^{H_1}(\bar{V}_x(z) - V_{XM})\,dz\right]^2 + \left[\int_{H_2}^{H_1}(\bar{V}_y(z) - V_{YM})\,dz\right]^2} \tag{2.18}$$

Brunetière (2005) asserted that δ_l^+ cannot be considered a constant for low Reynolds numbers, therefore to improve the accuracy of the Elrod and Ng (1967) turbulence model at this low Reynolds numbers, the δ_l^+ must be modified as given in Equation (2.19). He (ibid) reported that at high Reynolds numbers, δ_l^+ approaches an asymptote that is equal to the value of the δ_l^+ used in Elrod and Ng (1967) model. Re_m is the Reynolds number based on the maximal velocity.

$$\delta_l^+ = 10.7 + 1054\,(Re_m - 640)^{-0.877} \tag{2.19}$$

The transition to turbulence has been modelled by several researchers using an interpolation factor δ_ε to balance the transitional flows and turbulent viscosity. Szeri (1998) considered that the interpolation factor evolves gradually from 0 for laminar zone to 1 for fully turbulent zone. He (ibid) used a power law of Ng and Pan (1965) in the transitional zone to determine the interpolation factor δ_ε as given in Equation (2.20).

$$\begin{cases} \delta_\varepsilon = 0, & \text{if } \alpha < \alpha_l; \\ \delta_\varepsilon = f(\alpha), & \text{if } \alpha_l \leq \alpha \leq \alpha_t; \\ \delta_\varepsilon = 1, & \text{if } \alpha > \alpha_t \end{cases} \tag{2.20}$$

Where

$$f(\alpha) = 1 - \left(\frac{\alpha_t - \alpha}{\alpha_t - \alpha_l}\right)^{1/8}$$

Brunetière et al. (2002) also observed that the interpolation law used by Szeri (1998) lead to sharp variations near the turbulent limit, so numerical convergence was difficult to attain. To avoid these abrupt variations, they used a sinus law of Elrod and Ng (1967) given in Equation (2.21) that evolved smoothly from 0 to 1.

$$f(\alpha) = \frac{\left[1 - \cos\left(\dfrac{\alpha_l - \alpha}{\alpha_l - \alpha_t}\pi\right)\right]}{2} \tag{2.21}$$

Brunetière et al. (2002) friction factor was compared with Reichardt's experimental data and that of Missimer and Thomas (1983) and their results were close. Brunetière et al. (2002) therefore concluded that the Elrod and Ng (1967) model was probably not as accurate for low Reynolds numbers as for high Reynolds numbers. They used the transition Reynolds numbers of Missimer and Thomas (1983) and Patel and Head (1969) in carrying out their comparisons.

Brunetière (2005) later modified the sinus law given in Equation (2.22) to the one given in Equation (2.23). The power coefficient, 0.6, allows fully turbulent behaviour to be approached more quickly.

$$f(Re) = \frac{\left[1 - \cos\left(\frac{Re_l - Re}{Re_l - Re_t}\pi\right)\right]}{2} \tag{2.22}$$

$$f(Re_c) = \frac{1 - \cos\left[\left(\frac{900 - Re_c}{900 - 1360}\right)^{0.6}\pi\right]}{2} \tag{2.23}$$

In addition Brunetière (2005), while studying hydrostatic seals, indicated that there were four regimes of flow between plane rotating and stationary disks. The experimental work that initially identified the four regions which depend on the Reynolds number and the gap ratio, (h/r) was carried out by Daily and Neece (1960) who studied the flow in an enclosed rotating disk. The four regions are as follows:

I. Laminar with merged boundary layers
II. Laminar with separated boundary layers
III. Turbulent with merged boundary layers
IV. Turbulent with separated boundary layers.

These four regimes are shown in Figure 2.9. Brunetière (2005) pointed out that hydrostatic seals whose gap ratio varies from 10^{-4} to 10^{-3} operate in regimes I and III. He deduced that the boundaries of each zone occurred at the intersection of friction laws experimentally determined by Daily and Neece (1960). He (ibid) concluded that the friction law of regime I is the same as in laminar plane Couette flow. Brunetière (2005) also defined the friction factor C_{fC} for the turbulent flow in regime III as a function of the gap ratio as given in Equation (2.24). He showed that if the gap ratio is replaced by its limiting values, the computed friction factor is very close to those of plane Couette flow as summarized in Equation (2.25).

$$C_{fC} = 0.0297\left(\frac{h}{r}\right)^{1/12} Re_c^{-0.25} \tag{2.24}$$

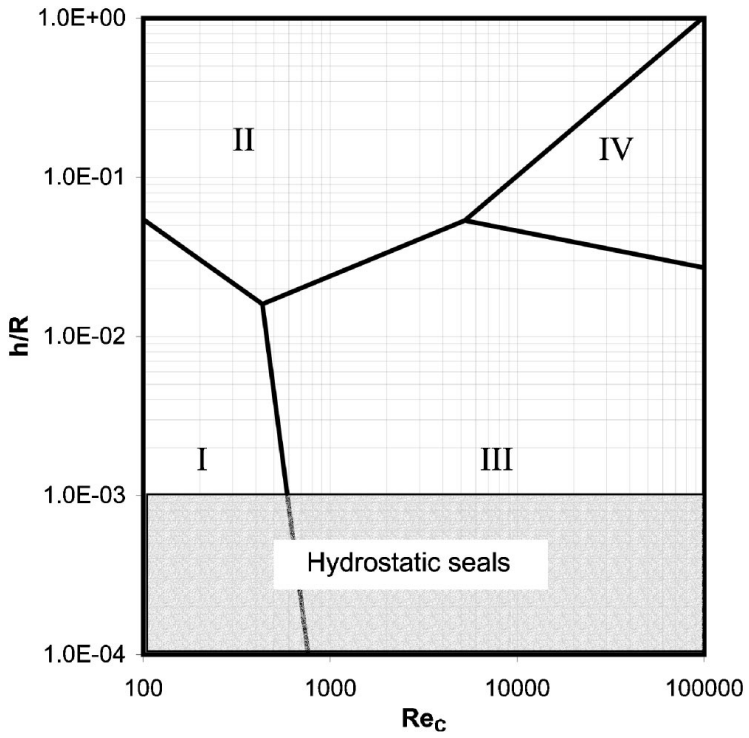

Figure 2.9 Regimes of flow between a rotating and a stationary disk (Brunetière, 2005)

$$C_{fC}(10^{-4}) = 0.0138\,Re_c^{-0.25} < 0.0159\,Re_c^{-0.25} < C_{fC}(10^{-3}) = 0.0168\,Re_c^{-0.25} \qquad (2.25)$$

In fluid flow, there are different sizes of turbulent eddies. The largest eddies obtain their energy from the mean flow by a process known as vortex stretching. The characteristic velocity and length of the largest eddies are of the same magnitude as the mean flow velocity and length scales. The largest eddies Reynolds' numbers are formed by combining these eddy scales with the kinematic-viscosity that is always large in all turbulent flows, thereby the largest eddies are mainly dominated by inertia effects, and viscous effects are minimal. The largest eddies essentially inviscid and their angular momentum is preserved during vortex stretching. This effect caused the rotation rate to increase and the radii of their cross-sections to decrease. The process produces motions at smaller transverse length scales and smaller time scales. The stretching work done by the mean flow on the largest eddies provides the energy that maintains the turbulence.

Smallest eddies are themselves stretched strongly by largest eddies and weakly by the mean flow. Kinetic energy is transferred from the largest eddies to progressively smaller and smaller eddies in a process called energy cascading. The smallest eddies Reynolds numbers is less than or equal to 1 based on their characteristic velocity and length scales. The length scales are of the order of 0 to $0.1\,mm$ and the fluctuating properties of typical turbulent engineering flows contain energy across a wide range of frequencies of around $10\,kHz$,

(Versteeg and Malalasekra, 1996). Within this region, work is performed against the action of viscous stresses and since the effects of viscosity become very important, the energy associated with the eddy motion is dissipated and converted into thermal energy, which results in increased energy losses.

As a result of the thin film gap associated with dry gas seals, the length scale of the largest eddies exhibits the same properties as the smallest eddies of a typical engineering turbulent flow. Thus their turbulent flows are dictated mainly by viscosity and the convection and diffusion of turbulence properties are often neglected. In the past, this made it possible to specify the influence of turbulence on the mean flow by simply using the mixing length as proposed by Prandtl. Although, the eddy-viscosity formulation is simple to implement as a result of determining only the ε_M, it is not really suitable for seals that have complex geometries. Flows that have the characteristics of sudden change of mean strain rate, significant streamline curvature, rotation and stratification, secondary flows in ducts and turbomachinery, and boundary layer separation and reattachment cannot be predicted correctly using the zero-equation models. In dry gas seals, where there are grooves on one of the sealing faces and the shaft rotating at high speed, the zero-equation turbulence models may not be appropriate in modelling the flow in the seal interface because of the above mentioned limitations. In order to cater for the limitations associated with the eddy-viscosity model, higher order turbulence models that do not require the use of wall functions, are required to model the fluid flow in the seal interface in dry gas seals that operate in the transition and fully turbulent regimes.

Some of the higher order turbulence models are: Spalart-Allmaras (one-equation model), two-equation models such as $k-\varepsilon$, $k-\omega$ and the $k-\omega$ SST (Shear-Stress Transport), Reynolds Stress model and the Large-eddy Simulation model. The $k-\omega$ SST and Reynolds Stress models do not require the use of wall functions hence making them more suitable for dry gas face seal simulations. Detailed comparisons of all the turbulence models for various cases are reported in Bardina et al. (1997). The benefits of the SST model over the other models, as applied to dry gas seals simulations, are discussed in the next paragraph.

The $k-\omega$ SST turbulence model of Menter (1994) and Menter and Rumsey (1994), combines the $k-\omega$ model of Wilcox (1988) and Wilcox (1993) with a high Reynolds number $k-\varepsilon$ model. It combines the positive features of both models. The $k-\omega$ method is utilized in the sublayer of the boundary layer since it needs no damping function. The $k-\omega$ approach is also utilized in the logarithmic part of the boundary layer in view of the fact that it is superior to the $k-\varepsilon$ approach in adverse pressure flows and in compressible flows. The $k-\varepsilon$ approach is employed in the wake region in the boundary layer since the $k-\omega$ model is strongly sensitive to the free stream value (Menter, 1992). The $k-\varepsilon$

approach is also used in the free shear layers since it represents a fair agreement in accuracy for wakes, jets and mixing layers. One definite characteristic of the $k-\omega$ SST model is the modified turbulent eddy-viscosity which enhances the accuracy of predicting flows with strong adverse pressure gradients and pressure-induced boundary layer separation. The modification accounts for the transport of the turbulent shear stress hence it is employed in this research for transitional and fully turbulent regimes.

2.4.2 Continuum and Non-Continuum Flow

For an ideal gas modelled as rigid spheres, the mean free path of the molecules ζ can be related to the temperature, T and the fluid pressure, p as defined in Equation (2.26). Here k is the Boltzmann's constant taken as $1.380662 \times 10^{-23} JK^{-1}$ and M_D is the collision diameter of the molecules (m). The collision diameter of an air molecule has been determined to be $9.69 \times 10^{-7} mm$ (Loschmidt, 1995).

$$\zeta = \frac{kT}{\sqrt{2}\pi M_D^2 p} \tag{2.26}$$

The ratio of the mean free path, ζ to the characteristic dimension of the flow geometry, h is referred to as the Knudsen number Kn and defined in Equation (2.27).

$$Kn = \frac{\zeta}{h} \tag{2.27}$$

The value of the Knudsen number determines the extent of rarefaction of the gas and the validity of the continuum flow assumption. Like the Reynolds number and Mach number, the Knudsen number can be used for flow regime characterization. There are four flow regimes based on the order of the Knudsen number. These include the continuum flow, slip flow, transition flow, and free molecular flow. The classical demarcation of the regimes is given below:

1. If $Kn < 0.01$, the flow is in the continuum flow regime
2. If $0.01 < Kn < 0.1$, the flow is in the slip flow regime
3. If $0.1 < Kn < 3$, the flow is in the transition flow regime
4. If $Kn \geq 3$, the flow is in the free molecular regime.

Assuming that the seal is operating at standard pressure and temperature ($p = 1\,bar$ and $T = 25^oC$) and using Equation (2.26), the mean free path of the sealing fluid (air) is approximately 9.74×10^{-9}. The results of the computed Knudsen number employing

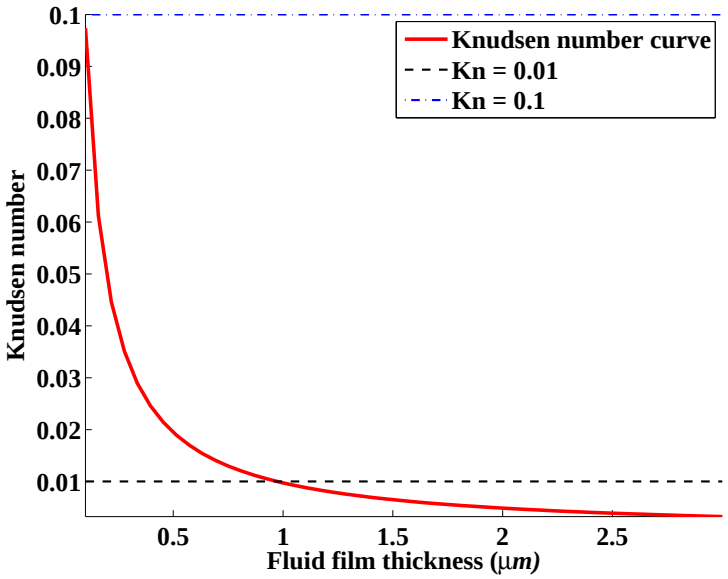

Figure 2.10 Knudsen number as a function of fluid film thickness

Equation (2.27), are shown in Figure 2.10 for a fluid film thickness as the characteristic length ranging from 0.1 to 3 μm. It is observed from the results shown in Figure 2.10 that for fluid film thicknesses less than 1 μm, the seal operates in the slip flow regime while for fluid film thicknesses greater than or equal to 1 μm, the seal operates in the continuum flow regime.

The continuum assumption considered in the Navier-Stokes equations is only valid when the molecules average free path is smaller than the characteristic dimension of the flow domain. The characteristic dimension in seal analysis is the fluid film thickness. In the event that this condition is violated, the fluid will no longer be under local thermodynamic equilibrium and thus, it will be impracticable to apply the linear relationship between the shear stress and rate of shear strain. Velocity profiles, boundary wall shear stresses, mass flow rates and differences in pressure will then be influenced by non-continuum effects. Also the conventional no-slip boundary condition always used on the solid-gas interface will begin to break down before the linear stress-strain relationship becomes unacceptable (Gad et al., 2006).

In the continuum regimes, the continuum hypothesis is appropriate and the flow can be analyzed using the Navier-Stokes equation with conventional no-slip boundary conditions. In the slip-flow regime, rarefaction effects begin to dominates the flow, and the Navier-Stokes equations may only be employed provided tangential slip-velocity boundary conditions are applied along the walls of the flow domain (Gad et al., 2006). In the transition-flow regime, the continuum assumption of the Navier-Stokes equations begins to breakdown and alternative simulation techniques must be adopted. A good example is the particle based DSMC (Direct Simulation Monte Carlo) approach. For the free molecular regime,

the continuum approach breaks down completely and the flow regime is regarded as free molecular flow.

Barber and Emerson (2002) reported that in order to consider the non-continuum effects in the slip-flow regime ($Kn \leq 0.1$), the Navier-Stokes equations are solved in conjunction with the tangential slip-velocity boundary conditions given in Equation (2.28). In this equation, u_t is the tangential slip-velocity at the wall, τ_t is the shear stress at the wall and β is the slip coefficient. The slip coefficient can be related to the mean free path of the molecules as given in Equation (2.29).

$$\tau_t = \beta\, u_t \tag{2.28}$$

$$\beta = \frac{\mu}{\left(\dfrac{2-\sigma_{TMAC}}{\sigma_{TMAC}}\right)\zeta} \tag{2.29}$$

In Equation (2.29), σ_{TMAC} is the tangential momentum accommodation coefficient (TMAC). The tangential momentum accommodation coefficient is included in Equation (2.29) in order to account for the reduction in the momentum of gas molecules colliding with the wall as reported by Schaaf and Chambre (1961). For perfectly smooth surfaces, the angles of incidence and reflection are identical. Hence, the molecules preserve their tangential momentum. This is referred to as specula reflection and results in perfect slip at the boundary ($\sigma_{TMAC} \rightarrow 0$). On the contrary, where the surface is extremely rough, the molecules are reflected at random angles and lose, on average, their entire tangential momentum. This situation is known as diffusive reflection ($\sigma_{TMAC} = 1$). The crystalline surfaces found in silicon micro-machined components often exhibit sub-unity tangential momentum accommodation, with σ_{TMAC} typically ranging from 0.8 to 1.0 (Arkilic et al., 1997). Combining Equations (2.28) and (2.29) gives the tangential slip-velocity at the wall as given in Equation (2.30).

$$u_t = \frac{2-\sigma_{TMAC}}{\sigma_{TMAC}}\,\frac{\zeta}{\mu}\,\tau_t \tag{2.30}$$

For including the effects of rarefaction in the Reynolds equation, Polycarpou and Etsion (1998) studied the static sealing performance of gas mechanical seals by solving the combined problems of contacting nominally flat rough surfaces and pressure-induced flow through the seal interface. The effect of rarefaction was considered by multiplying the pressure gradient given in Equation (2.31) with an average pressure flow factor Φ defined in Equation (2.33). The authors integrated the velocity, V given in Equation (2.31) along with the pressure flow factor with respect to the sealing gap, h to obtain the mass flow rate per

unit length of the seal circumference q as shown in Equation (2.32).

$$V = \frac{1}{2\mu}\frac{\partial p}{\partial r}\left(y^2 - yh - \lambda_p h\right) \tag{2.31}$$

$$q = \Phi\rho\int_0^h V\,dy = \frac{\rho h^3}{12\mu}\Phi\frac{\partial p}{\partial r}\left(1+\frac{6\lambda_p}{h}\right) \tag{2.32}$$

$$\Phi = 1 + g\left(\frac{1}{h^*}\right)^2\left(1 - \frac{f^2}{g}\frac{1}{\gamma+1}\right) \tag{2.33}$$

where

$$f = 3 - \frac{6a_\Phi Kn}{1+6a_\Phi Kn}$$

$$g = 3 - \frac{12a_\Phi Kn}{1+6a_\Phi Kn}$$

Where ρ is the fluid density, λ_p is the mean free path of the fluid at pressure p, μ is the viscosity, r and y are the radial and normal coordinates, respectively. Also, γ is the Peklenik number (a roughness anisotropy index), f and g are rarefaction coefficients that are functions of the Knudsen number, Kn, and h^* the dimensionless face separation defined as h/σ. a_Φ is the accommodation coefficient which was reported that it is always taken as unity.

The geometry of the sealing interface considered has the following dimensions: r_i is $0.010\,m$ and r_o is $0.012\,m$. One of the seal ring materials was made from high carbon chromium steel and the other made of resin-bonded carbon. The authors considered three different surface roughnesses, σ of 0.040, 0.055 and $0.070\,\mu m$ respectively. They also considered three different Knudsen number Kn of 0.544, 0.395 and 0.311 respectively. The operating conditions considered are: viscosity, $\mu = 2\times10^{-5}\,Pa\,s$ at $T = 25^oC$, $\lambda_a\,p_a$ was $6.8\times10^{-3}\,mPa$ and the system pressure of $p_i = 0.59\,MPa$ and $p_o = p_a = p_{atm} = 0.101\,MPa$.

The authors reported that in all the cases they considered, their model predictions were lower than the experimental results they were compared with but stated that their results were within the same order of magnitude as the experimental results. They concluded that as Knudsen number increases, there is an increase in the dimensionless leakage. Also, they showed that at very low leakages associated with high face loading, the effect of the Knudsen number on the leakage is large, while the effects of the pressure and surface roughness reduce.

Ruan (2000) developed a computational tool for analysing the spiral groove gas seal with the consideration of the effect of slip flow. The author used the Finite element method (Galerkin)

in discretizing the Reynolds equation that was employed in analysing seals operating at slow speed ($\leq 500\,rpm$) and low pressure ($\leq 0.303\,MPa$) condition. This was used in studying the effect of slip flow by introducing a Poiseuille flow factor q_p into the Reynolds equation given in Equation (2.34). The Poiseuille flow factor given in Equation (2.35) was approximated by a power series (presented by Fukui and Kaneko (1990)) and it is a function of the inverse Knudsen number, D given in Equation (2.36).

$$\nabla.\left(q_p \frac{\rho h^3}{12\mu}\nabla p - \frac{r\omega}{2}\rho h e_\theta\right) = 0 \tag{2.34}$$

$$q_p = c_o + \frac{c_1}{D} + \frac{c_2}{D^2} + \frac{c_3}{D^3} \tag{2.35}$$

$$D = \frac{1}{Kn} = \frac{h p}{\mu\sqrt{\frac{\pi}{2}R_{gas}T_a}} \tag{2.36}$$

Where T_a is ambient temperature, R_{gas} is the gas constant, c_0, c_1, c_2, and c_3 are constant coefficients given in Fukui and Kaneko (1990). e_θ is a unit vector in the positive θ direction. The spiral groove geometry considered has the following dimensions: r_i is $0.030\,m$, r_o is $0.042\,m$, h_g is $2.5\,\mu m$, n_g is 12, γ is 1, $\delta = ((r_g - r_i)/(r_o - r_i))$ is 0.4 and $\alpha = 20^o$. The operating conditions considered are: B is 0.8, F_{spring} was $75\,N$, $T = 300\,K$ and air was considered as the sealed fluid. Three different fluid film thicknesses ($h = 0.6$, 0.9 and $1.2\,\mu m$) were considered and the effects of surface roughness was neglected based on the fact that the film thickness is much greater than the surface roughness ($h \gg 3\,\sigma$).

The author observed that slip flow can significantly affect the seal lift-off speed, leakage, gas film stiffness and the seal operating characteristics at slow speed (($\leq 500\,rpm$) and ($\leq 0.303\,MPa$)). They reported that without the consideration of the slip flow effect, the lift-off speed, the corresponding leakage rate, and the film stiffness would be underestimated by as much as 20%, 31%, and 7.3% respectively for a given lift-off film thickness at near ambient pressure conditions. They concluded that the slip flow would be significant when the Knudsen number is greater than or equal to 0.05 and its effect would reduce the viscous pumping thereby leading to loss of load carrying capacities.

Generally, gas film seals operate in the continuum flow regime, where the gas is very dense; that is, the molecular mean free path is very small compared with the film thickness. Non-continuum flow can occur in gas face seals in two ways: firstly, the seal operates in a vacuum environment and secondly, the gas is very less dense and operates at zero pressure differentials with the seal ring inner diameter pressure at atmospheric conditions and the gap between the seal rings is not greater than $1\,\mu m$. Gases such as Helium, Neon and Hydrogen having a large molecular mean free path, can easily operate in the slip-flow regime (Hsing

and Malanoski, 1969).

2.4.3 Effects of Inertia

Dry gas face seals are generally characterized by Reynolds numbers that lead not only to a turbulent flow regime but also characterize flow regimes where fluid inertia becomes significant. The flow restriction through the seal interface is not entirely viscous as modelled using the Reynolds equation. As a result of high pressure gradients, grooved geometries and sometimes large operating film thickness found in dry gas face seals, fluid inertia that is neglected in the Reynolds equation becomes significant. The fluid inertia produces steep pressure drops at flow restrictions, or sudden contractions in the path of the flow. The sudden contractions around the vicinity of the grooves, at the dam and land regions, as well as fluid entering into the groove seal from the high-pressure fluid at the outer periphery, convert the pressure to velocity head. The fluid inertia consists mainly of the convective and centrifugal terms in the momentum equations. The centrifugal forces generally retard the flow and Shapiro et al. (1984) reported that neglecting the centrifugal terms in analysing mechanical seals would not be more than 10% on the predicted leakage rates.

The magnitude of the convective inertia terms and the centrifugal inertia terms can be evaluated using the reduced Poiseuille Reynolds number Re^*_{po} defined in Equation (2.37) and reduced Couette Reynolds number Re^*_{co} defined in Equation (2.38), respectively (Brunetière and Tournerie, 2006). When $Re^*_{po} \ll 1$, the convective inertia terms are negligible and $Re^*_{co} \ll 1$, the centrifugal inertia terms are negligible (Brunetière and Tournerie (2006) and Frêne et al. (2006)).

$$Re^*_{po} = Re_{po}\frac{h}{r_o} \tag{2.37}$$

$$Re^*_{co} = \frac{Re^2_{co}}{Re_{po}}\frac{h}{r_o} \tag{2.38}$$

In order to incorporate the fluid inertia in the Reynolds equation, Brunetière and Tournerie (2006) presented a theoretical model for axisymetric laminar or turbulent radial flows that considered the effects of inertia. Their model was based on the assumptions proposed by Constantinescu and Galetuse (1982). They simplified the Navier-Stokes and continuity equations to obtain a modified incompressible Reynolds equation. It was shown that inertia effects can be neglected when the reduced Poiseuille Reynolds number is lower than 0.075 but becomes significant when its value reaches 0.25. They reported that the temperature field in the fluid film is only weakly influenced by inertia and that the preswirl velocity of the fluid at the inlet does not affect the seal behaviour for a speed range of 500 rpm to $3000\,rpm$. In order to accurately model the flow in the seal interface to include the fluid

inertia, the full Navier-Stokes equations must be solved (Frêne et al., 2006).

2.5 Effects of Face Deformation

2.5.1 Radial Taper

Non-parallel surfaces can be developed in the faces of seals in two ways. They can be deliberately machined as a radial taper or can be caused by face distortions during operation. Distortions of the primary seal faces are inherently present in face seals of the gas film. Inherent distortions include radial and axial displacements due to the centrifugal force and are especially important under high rotational speeds.

Another common face distortion is thermal coning, which is caused by an axial thermal gradient along the shaft. The shaft's hotter end causes a differential shaft radial displacement which results in the face coning. Some other causes of face distortions include: pressure - due to high pressure drops and improper seal balance diameter, mechanical effects, asymmetry of rotating seal seat and tolerance build up due to fabrication and assembly. Generally, for internally pressurized seals, the distortions cause seal faces to diverge. In order to overcome this effect, most seals are externally pressurized from the seal face's outer diameter. The external pressurization of the seal from the seal face's outer diameter will distort the seal face to converge in the direction of the leakage flow path. This results in positive stiffness that is beneficial to seal performances unlike the divergent taper that starve the gap of the fluid film thereby reducing the opening force.

For seal faces that are not parallel, the pressure gradients are dependent on film thickness. A negative deformation indicates a diverging film whilst a positive deformation indicates a converging film in the leakage-flow path. Importantly, for the convergent film, a decrease in film thickness results in greater area (larger opening force) under the pressure gradient curve; thus, the convergent film has a positive stiffness. Conversely, a divergent film has negative film stiffness. This indicates that for a divergent film, a decrease in film thickness (which always occurs dynamically) can cause a decrease in opening force.

Young and Lebeck (1982) reported that large convergent initial tapers can result in high initial leakage in balanced seals and small initial leakage in unbalanced seals. They (ibid) showed that wear progresses across the face and may take a long time prior to the seal lapping its flat so as to reduce leakage. They recommended a small convergent radial taper for balanced seals, in the order of $100\,\mu m$, to ensure minimum leakage at start off. Leakage begins to significantly increase when the hydrostatic load support becomes large enough that the seal lifts off completely. The point of complete lift off occurs when the fluid pressure

load support equals the applied load. The just-lifting-off fluid support is attained when the inside film thickness is just equal to the contact film thickness.

Lebeck (1991) reported that radial taper can be induced on seal faces in two ways. The faces are either machined to include radial taper or developed during operations as a result of deflections, changes in pressures and temperatures. The likelihood of radial taper being induced during operation makes them uncontrolled. Interestingly, if properly controlled, radial taper plays a major role in seal performance by generating hydrostatic load support. There are two types of radial tapers: convergent and divergent radial tapers. Convergent radial taper occurs when the outside film thickness is greater than the inside film thickness while the converse results in divergent radial taper. In practice, divergent radial taper reduces leakage and starves the interface of fluid whilst convergent radial taper enhances lubrication in the sealing interface.

Thermal radial taper which is induced as a result of changes in temperature can be evaluated by determining the thermal rotation coefficient, that is, the ratio of radial taper to seal power. Its value is mainly determined by the shape of the cross sections, coefficient of thermal expansion and thermal conductivity. Most seal designs, whether inside or outside pressurized, often have a positive thermal rotation coefficient. An outside pressurized seal has a convergent radial taper -with positive fluid film stiffness - when the thermal rotation coefficient is positive. Whereas, an inside pressurized seal has a divergent radial taper - with negative fluid film stiffness - when thermal rotation coefficient is positive. This is equivalent to an outside pressurized seal with negative thermal rotation coefficient. The pressure caused radial taper that mainly occurs due to changes in pressure can be evaluated by determining the pressure rotation coefficient. This is related to the inside and outside fluid film thickness and changes in pressure as shown in Equation (2.39) for balanced seals (Lebeck, 1991). A positive pressure rotation coefficient K_p induces a convergent radial taper while a negative K_p induces a divergent radial taper.

$$h_o = h_i + K_p \left(p_o - p_i\right) \Delta r \tag{2.39}$$

Lebeck (1991) also discussed that a negative pressure rotation coefficient can balance a positive thermal rotation coefficient in order to minimize initial leakage. The author noted that after wear-in has taken place, the seal then operates with radially parallel faces, and thereby no further consequences of pressure caused taper will result pending a change in operating conditions. Also, the author reported that in the event that a seal is shut down and re-pressurized, the seal will be subjected to have a net convergent radial taper as a result of wear-in at a higher pressure. Hence there is a possibility that under re-pressurization, the seal may leak unnecessarily at some pressure lower than the earlier maximum operating

pressure.

2.5.2 Waviness

Experiments and theories have shown that waviness on the faces of seals can improve the lubrication conditions. Pape (1968), Stanghan-Batch (1971) and Lebeck (1981) agreed that waviness on the faces of seals usually developed during operation.

Mayer (1969) provided test data and detail analysis of a circular groove thermo hydrodynamic seal. It was deduced that the grooves ensure that fluid came in contact across a significant radial fraction of the face and also provide some circulation and cooling (ibid). The seal becomes wavy when there is circumferentially non-uniform cooling. Trytek (1983) provided detail analysis of seals having hydropads. The hydropads ensure that a significant fraction of the interface contacts fluid and produces some cooling (ibid). These hydropads are etched in the soft faces that are sufficiently deep so that no normal amount of wear can remove them. Further, hydropads do not provide any hydrodynamic load support because of their large depth but reduce heat generation and power consumption (Mayer (1969); Trytek (1983)). They act to enhance parallel sliding load support and greatly affect the balance ratio.

Lebeck (1981) reported that one of the causes of this waviness is drive forces acting on the seal rings. In spite of considerable research on wavy seals, it appears that no deliberately wavy seal exists except those created from geometrical features such as hydropads (deep pocket grooves), circular thermo hydrodynamic groove seal and radial slits seals. The waviness is caused by pressure and thermal-caused distortion.

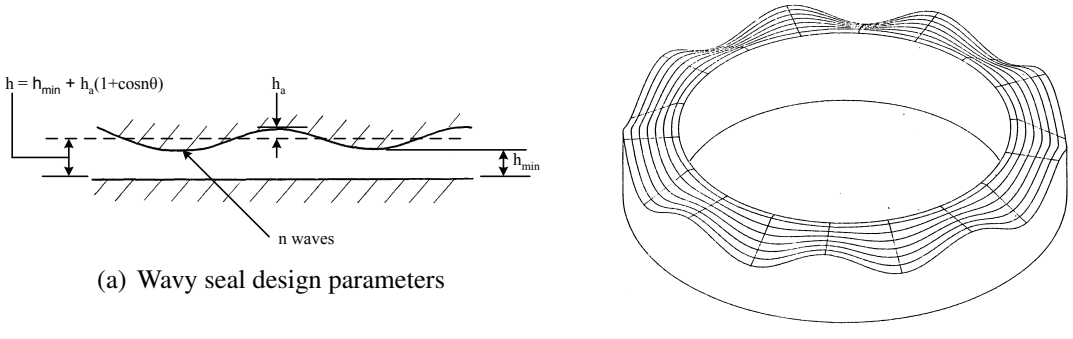

(a) Wavy seal design parameters

(b) Wavy-tilt seal face

Figure 2.11 Wavy seal (Lebeck, 1981)

Lebeck (1991) noted that radial slit seals ensure that fluid is present across the entire face width. Relatively high leakage must be acceptable in order to use this type of seal. Low direct cooling is provided as a result of the slits being narrow. The author also reported

that there are two types of waviness, the radially parallel waviness, where the surface stays radially parallel throughout the period of the wave, and the wavy tilt dam. The later has more advantages over the former due to its design of having a sealing dam that produces a hydrostatic stiffness as well as producing hydrodynamic load support.

When waviness is deliberately machined on seal faces, there are two variables that one can easily control in order to achieve good seal performance. The first variable is the waviness amplitude. In order to obtain hydrodynamic lift, one must have waviness amplitude of the order of the minimum film thickness which must be slightly greater than the contact height (taken at three standard deviations of roughness). For just touching condition, the minimum film thickness is equal to the contact height. Larger amplitudes than this simply cause more leakage and provide no benefit. The second variable is the number of waves. When used, it must be based on the stiffness of the rings and they must be capable of maintaining the needed waviness under load. The author reported that theories have shown that it is very difficult to control the net waviness when number of waves is small. At low pressures, one may have complete separation and excessive leakage, and at high pressures, one may have small waves. It is much easier to impose a large number of waves to make it moderately stiff.

2.6 Effects of Surface Roughness

Surface roughness can be classified into two groups: initial or as-manufactured roughness and operating surface roughness. The operating surface roughness as it name indicates, develops during seal operation. It depends upon the seal material themselves as well as the type of abrasive particles presents. As-manufactured surface roughness can be reduced to minimum by lapping the seal faces but the operating surface roughness is not easily controlled. Lebeck et al. (1978) observed in a survey of several seal faces that surface roughness varies greatly from one sealing situation to another. In some cases, extremely large surface roughness can prevent hydrodynamic effects. Large surface roughness is detrimental to seal performance as it increases leakage, friction coefficient as well as wear rates thereby reducing seal life.

Christensen and Tonder (1971) proposed isotropic models that have been applied to the mixed friction cases where some roughness interference occurs. These were used as a first approximation to actual seal roughness. Isotropic roughness in its simplest term represents a mathematically ideal case in which flow resistance and roughness statistics are equal in all directions. Christensen (1972) defined the total film thickness H including rough surfaces as given in Equation (2.40). Here, $h(r, \theta)$ is the nominal film thickness which varies due to waviness and radial taper, $h_s(\xi)$ is the random part of the film thickness due to

surface roughness and ξ is some random variable. A polynomial approximation was used in describing the surface roughness as given in Equation (2.41) for $-\sigma \leq h_s \sigma$.

$$H = h(r, \theta) + h_s(\xi) \tag{2.40}$$

$$f(h_s) = \frac{35}{32\sigma^7}\left(\sigma^2 - h_s^2\right)^3 \tag{2.41}$$

The peak roughness amplitude, (σ), corresponds to three standard deviations. It was assumed that the roughness distribution remains constant with time and coordinate r and θ. It was also assumed that the roughness occurs on one surface only. The Reynolds and flow equations which were originally developed by Christensen and Tonder (1971); was modified by Lebeck (1981) and included isotropic surface roughness in polar coordinates. These equations, have been applied by Lebeck (1981) to the analysis of hydrodynamic lubrication for wavy contacting face seals, where part of the load was supported by hydrodynamic pressure distributions and the remaining part supported by asperity pressure distributions. Lebeck et al. (1978) reported that the surface roughness can lead to conservative predictions of hydrodynamic load support when applied to a face seal. The formulation of the modified Reynolds equation to include the effects of surface roughness has been detailed in Lebeck (1981).

Patir and Cheng (1978) argued that the effect of surface roughness cannot be neglected in the mixed lubrication regime where $h/\sigma \leq 3$. Furthermore, Etsion and Front (1994) calculated that for a typical SiC/Carbon face material pair, its composite roughness is about $0.1\,\mu m$. For seals operating at the full-film lubrication, a representation of non-contacting gas seal frequently has a minimum film thickness greater than $1\,\mu m$ thereby h/σ is always greater than 3. This shows that the effect of surface roughness can be neglected when analysing non-contacting dry gas seals.

2.7 Numerical Optimization

The optimization of leakage or fluid opening force is one of the greatest challenges in the design of dry gas face seals. This optimization would usually be at the expense of one another. The benefit of seals having minimal leakage, while maintaining maximized fluid opening force is that contact between the seal rings faces would be avoided during operation. It is essential therefore that this issue not be undermined since it improves the seal performance as well as ensuring sizeable cost savings to the users. The most viable solution depends on functions that directly depend on some geometrical parameters that need to be varied. These geometrical parameters may include the groove depth, groove angle, number of grooves, the dam width, and ratio of land to groove.

The parametric analysis has been the general method employed in the optimization of the geometrical face profiles of mechanical face seals. In this approach, one design variable is varied at a time while the other design variables are fixed. The optimum design variable is attained one at a time without the interaction of varying all the design variables at the same time. Discussed below is some of the research that used the parametric analysis approach.

Walowit and Pinkus (1982) carried out the design and optimization of a shrouded pocket seal by employing the incompressible Reynolds equation. They performed a detailed parametric analysis to find the optimum geometrical parameters as well as the performance parameters that are of prime interest to seal optimization. The design variables with reference to Figure 2.4 considered in their studied are: Radial extent of inner shroud, L_s; Aspect ratio, (L/B); Radial extent of pocket, L_p; Circumferential extent of pocket, B_p and Step height, (h_1/h_2), where h_1 is the pocket film thickness and h_2 is the minimum film thickness. The low and high speed considered are $100\,rpm$ and $10000\,rpm$, respectively and low and high pressure considered are $0.0345\,MPa$ and $0.6895\,MPa$, respectively. The performance parameters considered are: adequate film thickness with regards to opening force, leakage and stability with regards to stiffness.

Walowit and Pinkus (1982) also suggested that for seals operating at high speed and low pressure, the optimization represented a compromise between the conflicting effects of the hydrodynamic and squeeze forces, as well as between the objectives of highest load capacity and least leakage. The authors (ibid) also reported that for seals operating at low speed and high pressures, the dominant force and leakage are those given by hydrostatic load and hydrostatic leakage, while for low values of pressures, the dominant quantities are those produced by both hydrodynamic and squeeze-film terms. Additionally, Walowit and Pinkus (1982) research indicated that the contribution of the hydrostatic forces to stiffness was insignificant and that the hydrodynamic stiffness term is the dominant element in all cases considered. They (ibid) also reported that the hydrostatic forces varied little with changes in the various geometrical seal parameters, both hydrostatic forces and hydrostatic stiffness could be left out of any considerations in optimization of seal dimensions.

Salant and Homiller (1992) analysed the flow field within a lubricant film (water) of a mechanical seal having shallow groove (depths on the order of microns) patterns that extended across the entire seal face length. They (ibid) employed the Reynolds equation by considering the effect of cavitation. Two groove patterns were considered. The oblique and the spiral groove. They considered the upstream pumping seal whereby the groove patterns pump the buffer fluid toward the sealed fluid. The sealed fluid is located at the seal outer diameter (OD) and the buffer fluid at a lower pressure to the sealed fluid pressure located at the seal inner diameter.

The film thickness profile for the oblique groove curve used in their study is defined in Equation (2.42) and the equation defining the oblique curve is given in Equation (2.43). Also, the film thickness for the spiral groove curve is defined in Equation (2.44), here h_1 is the coning parameter, h_2 is the groove depth parameter, h_{av} is the average film thickness, α is the parameter describing the groove slope and N is the number of grooves. P_c is the cavitation pressure, P_s is the sealed pressure at OD and P is the fluid pressure. Also, $\hat{r}$ is dimensionless radial coordinate, r/r_i, θ and r are the circumferential and tangential coordinates respectively.

$$\hat{h} = 1.0 + h_1 \left[\hat{r} - \frac{(1+\hat{r}_o)}{2} \right] + h_2 \cos \left[N\theta - 2\pi\alpha \frac{(\hat{r}-1)}{(\hat{r}_o - 1)} \right] \tag{2.42}$$

$$N\theta - 2\pi\alpha \frac{(\hat{r}-1)}{(\hat{r}_o - 1)} = constant \tag{2.43}$$

$$\hat{h} = 1.0 + h_1 \left[\hat{r} - \frac{(1+\hat{r}_o)}{2} \right] + h_2 \cos \left[N\theta - 2\pi\alpha \frac{\ln(\hat{r})}{\ln(\hat{r}_o)} \right] \tag{2.44}$$

Salant and Homiller (1992) analysis was primarily to evaluate the reduction or elimination of leakage resulting from the groove patterns where they compared leakage to an equivalent plain-faced seal (without grooves) having the same minimum film thickness. They defined a leakage rate ratio Q_r as the ratio of the grooved seal leakage to that of an equivalent plain-faced seal. This implies that when the leakage rate ratio is less than 1, the grooved seal is more effective in sealing than the equivalent plain-faced seal. Their analysis was based on the following: speed, groove slope, groove depth, coning, number of grooves, radius ratio as well as comparison of the two grooved patterns.

Salant and Homiller (1992) therefore maintained that under static conditions and at dimensionless rotational speed Λ (where $\Lambda = (6\mu\ \omega r_i^2)/((P_s - P_c)h_{av}^2)$) less than 60, the plain-faced seal is a more effective sealing device than the grooved seal, but grooved seal becomes more effective when the speed becomes greater than 60. At these higher speeds, the grooved seal is about 34% more effective than the plain-faced seals. It was also noted that as Λ increased, the magnitude of the slope of the Q_r vs Λ curve decreased. They (ibid) reported that the cause of the above effect was as a result of cavitation region been developed as Λ increased hence the cavitation hinders the pumping ability of the grooves.

In evaluating the effect of groove slope on the leakage rate, they considered the groove slope parameter (α) in two ways: when the groove slope was negative and the other when it was positive. They reported that when it is negative, the grooves were oriented such that they tended to pump the fluid from the OD towards the ID. They reported that for all values of speeds, the negative groove slope produces higher leakage than the plain-faced seal. They

reported that for the positive groove slope ($\alpha \geq 1$), sealing was enhanced at speeds (Λ) greater than the critical speed (approximately 55-60). They reported that the larger the magnitude of α, the lower the leakage rate ratio.

In evaluating the effect of groove depth on the leakage rate, Salant and Homiller (1992) reported that for values of h_2 equal to 0.1 and lower, the grooved seal was less effective than a plain-faced seal at all speeds. Also when h_2 was greater than or equal to 0.3, the grooved seal was more effective than a plain-faced seal at speeds higher than a critical value. At higher speeds above the critical speed value, the larger the value of h_2, the lower the leakage rate. They (ibid) noted that at lower speeds where the grooved seal was less effective than the plain-faced seal, the larger the value of h_2, the higher the leakage rate ratio. In evaluating the effect of coning on the leakage rate, they reported that positive values of h_1 corresponded to convergence of the fluid film from OD to ID and negative values of h_1 correspond to divergence of the fluid film from OD to ID. Salant and Homiller (1992) described that at speeds above the critical speed, positive coning increases the effectiveness of the grooved seal while negative coning decreases the effectiveness of the groove seal.

In evaluating the effect of the number of grooves on the leakage rate, Salant and Homiller (1992) again indicate that when $N = 3$, the grooved seal was less effective than the plain-faced seal irrespective of the operating speed. Where $N \geq 10$, the grooved seal was more effective than the plain-faced seal provided the critical speed was exceeded. They also highlighted that when $\Lambda > 120$, there was only a slight difference in leakage when $N = 30$ and $N = 50$. In evaluating the effect of radius ratio, $\hat{r}_o$ on the leakage rate, Salant and Homiller (1992) identified that the larger the radius ratio, the more effective the grooved seal at high speed. It was also noted that the larger the radius ratio, the lower the critical speed. At speeds below the critical speed, the grooved seal was less effective than the plain-faced seal and the larger the radius ratio, the less effective the groove seal. The authors reported that there was no large difference between the results of the oblique and spiral grooves.

Basu (1992) carried out a parametric study analysis on both radial and parallel round-bottom groove shaped gas face seals. The author's objective was to compare the performances of radial and parallel grooved geometries with finite difference and finite element discretization methods on the compressible Reynolds equation without inertia effects. In one of his cases, Basu (1992) discretized the Reynolds equation for the radial groove with finite difference method and in another case, he used the finite element method for both the radial and parallel grooved geometries. Basu (1992) also distinguished the radial grooved geometry from the parallel grooved in that the radial groove geometry has a groove depth that is constant along a radial line whereas for the parallel groove, its groove depth is constant along a line parallel

to the mid-section radial line. Basu (1992) highlighted that the finite difference method cannot be used for the parallel grooved geometry since in the conventional finite difference formulation in polar coordinates, the grid lines should be either radial or circumferential lines.

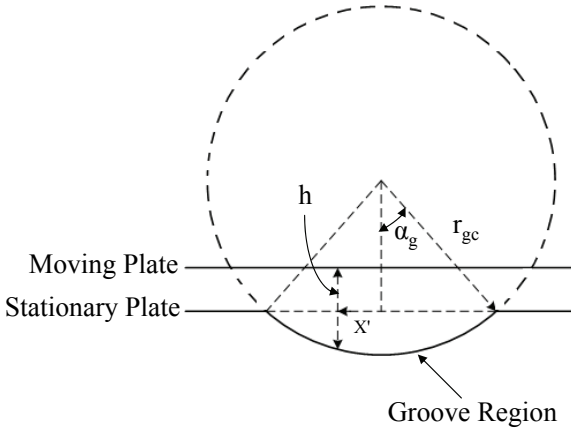

Figure 2.12 Film thickness variation - circumferential direction (Basu, 1992)

Basu (1992) also considered only one sector, which consists of a pair of land and groove for his analysis. Basu (1992) divided the domain into two parts in order to solve for the pressure distributions, one part as the hydrodynamic section while the other part as the hydrostatic section as shown in Figure 2.3(a). He used the 2D Reynolds equation for the hydrodynamic section and 1D Reynolds equation for the hydrostatic section. Basu (1992) iteratively determined the pressure at the junction of the hydrodynamic and hydrostatic sections by matching the leakage through both sections. Basu (1992) presented that the film thickness variation in the radial direction comes from the coning that is caused by the face distortions due to pressure, thermal and centrifugal effects, or intentional lapping on the harder face. The film thickness variation in the circumferential direction originated from the presence of the grooves. He approximated the film thickness variation over the hydrodynamic section in the land region as given in Equation (2.45) and for the groove region as given in Equation (2.46). Here x' is measured from the mid-section radial line of the groove along the mid-circumferential line in either direction as shown in Figure 2.12. At the hydrostatic section, he assumed the film thickness variation as the same as the film thickness variation at the land region of the hydrodynamic section.

$$h(r,\theta) = h_i + \beta(r - r_i) \tag{2.45}$$

$$h(r,\theta) = h_i + \beta(r - r_i) + r_{gc}\left[\cos\left(\sin^{-1}\frac{x'}{r_{gc}}\right) - \cos\alpha_g\right] \tag{2.46}$$

Basu (1992) went on to describe the hydrodynamic effectiveness as the ratio of excess

opening force generated due to hydrodynamic action over the corresponding hydrostatic force (in the absence of any motion) to hydrostatic force. He pointed out that the higher the compressibility number Λ (as defined in Equation (2.47)), the higher will be the hydrodynamic effectiveness. Additionally, Basu (1992) concluded that for design optimization, the radial groove approximation can be used for the parallel groove design since both yield approximately the same opening force irrespective of the discretization method employed. He showed that the finite difference method is faster in terms of computer usage time than the finite element method.

$$\Lambda = \frac{6\mu\omega r_o^2}{P_o h_i^2} \tag{2.47}$$

Shellef and Johnson (1992) analyzed and optimized the geometrical parameters of a bidirectional radial groove gas face seal using the dimensionless form of the compressible Reynolds equation. The controlling parameters were identified as five geometrical parameters and one dynamic parameter as the compressibility number, Λ defined as $\Lambda = (6\,\mu\,\omega\,r_m\,[w_g - w_l]\,r_m)/(p_o\,h_o^2)$. The five geometrical parameters are: radial length ratio Lr defined as $Lr = w_g/(w_g + w_l)$, clearance ratio Cr defined as $Cr = h_o/h_M$ where, h_o and h_M are the minimum and maximum gap, respectively. The other three geometrical parameters are: span ratio Sr defined as $Sr = (r_g - r_i)/(r_o + r_i)$, aspect ratio Ar defined as $Ar = r_m\,(w_g + w_l)/(r_o - r_g)$ and curvature number Cn defined as $Cn = (r_o - r_i)/r_i$. w_g and w_l are the angular groove length and angular land length respectively.

In their parametric analysis study, Shellef and Johnson (1992) considered the film stiffness as the performance parameter to obtain an optimum length ratio of 0.45. They stated that the length ratio was quite independent of the other controlling parameters. They (ibid) reported that the optimum clearance ratio was dependent on the compressibility number. Additionally, they stated that for compressibility numbers in the range of 10 to 50, the optimum clearance ratio equals to 0.35 and as the compressibility number increased, optimum clearance ratio decreased. Shellef and Johnson (1992) also reported that as stiffness was maximized, span ratio decreased to small values. The optimum aspect ratio they obtained was about 4.0. They reported that the radial span, the optimum aspect ratio as well as a selected span ratio fully defined the number of grooves required. They (ibid) reported that the radial span which defines the curvature number was usually fixed within the physical design envelope and could not be optimized, but the aspect ratio was under the designer's control and was most readily varied by changing the circumferential sector length.

Liu et al. (2004) compared four different geometrical spiral groove gas face seal layouts

in terms of seal performances comprising of opening force, film stiffness, and seal leakage and power consumption. The different layouts considered were the down stream pumping, upstream pumping, herringbone and the down-up-stream pumping as shown in Figure 2.13. These authors employed the compressible Reynolds equation which was discretized with the finite element method. The authors concluded that the order of maximum opening force for the seal face layout are: the herringbone, downstream, down-up-stream and the least being the upstream. They also noted that the order of maximum leakage for the seal face layout are: downstream, down-up-stream, herringbone, and the least is the upstream. Also, the order of maximum stiffness for the seal face layout is: down stream, herringbone, down-up-stream and the least been the upstream. The order of maximum power consumption for the seal face layout is: upstream, herringbone, down stream and the least is down-up-stream.

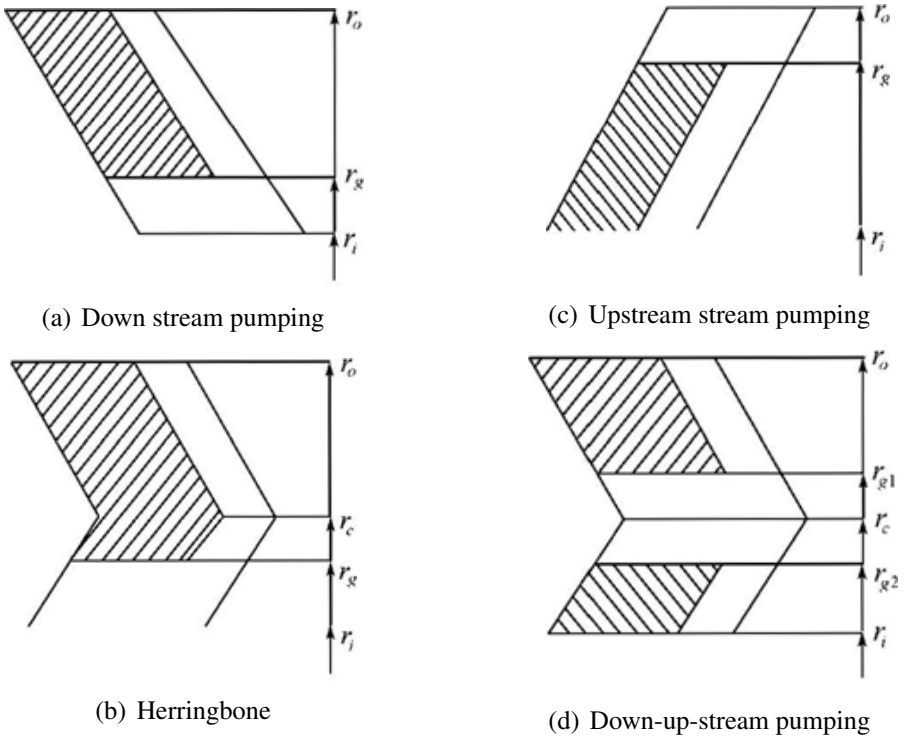

(a) Down stream pumping

(c) Upstream stream pumping

(b) Herringbone

(d) Down-up-stream pumping

Figure 2.13 Layout of different spiral groove faces (Liu et al., 2004)

The second part of their study was a parametric analysis study which considered the down stream spiral groove gas face seal as the seal face layout. The geometrical dimensions of their base case considered were: $r_o = 0.08795\,m$, $r_i = 0.07005\,m$, $r_g = 0.07875\,m$, $\alpha = 75^o$, groove-to-land width ratio of 1, $h_g = 5\,\mu m$ and $h_o = 5.6\,\mu m$. The operating conditions considered were: $p_o = 0.6\,MPa$, $p_i = 0.1\,MPa$, $\omega = 12000\,rpm$ and gas temperature was 100^oC. The spiral angle was varied from 10^o to 80^o, number of grooves from 5 to 50, groove-to-land width ratio from 0.25 to 5, groove radius from $0.071\,m$ to $0.087\,m$ and groove depth from $2\,\mu m$ to $20\,\mu m$. Their analysis was based on opening force and film stiffness

without the consideration of seal leakage. Their optimum geometrical parameters in terms of opening force were: $(r_o - r_g)/(r_g - r_i) = 2.0$, spiral angle was 67^o, groove-to-land width ratio was 1.0 and h_g/h_o was 1.0. In terms of the film stiffness, the optimum geometrical parameters were $(r_o - r_g)/(r_g - r_i) = 2.0$, spiral angle was 62^o, groove-to-land width ratio was 2.0 and h_g/h_o was 2.0. They reported that when the number of grooves exceeded 30, there were no changes in the seal performance. From the results presented by the authors, it shows that a compromise has to be made in choosing the optimum parameters since the results from the two performance parameters considered are different.

Feldman, Kligerman and Etsion (2006) presented a theoretical model for studying the effect of partial micro dimples on hydrostatic seal. They carried out a detailed parametric analysis to obtain the optimum micro dimples parameters for maximum seal efficiency that was based on the ratio of load carrying capacity P_{av} to gas leakage Q. They employed the finite difference method using a non-uniform grid in discretizing the compressible Reynolds equation in laminar flow condition. They solved the discretized Reynolds equation with the successive over-relaxation Gauss-Seidel iterative method. They also compared their results to a Rayleigh step in terms of providing load capacity.

The design parameters considered by the authors were: texture portion or step location γ, area density S_p and dimensionless dimple diameter δ defined as $\delta = (2r_p)/c$. The typical case they considered were: number of dimples equal to 7, $\gamma = 0.7$, $S_p = 0.65$, $\delta = 100$ and the dimensionless pressure P_o with reference to the outer ring diameter and defined as p_o/p_a was assigned a value of 2. The dimensionless dimple depth was defined as $\varepsilon = h_p/c$.

They observed that the performance of a partial micro dimples seal operating as hydrostatic gas seal is mainly dependent on the dimples area density S_p, and it is not affected by the dimple diameter, $2r_p$. They reported that the actual depth of the dimples has very little effect on the performance of the seal thereby they suggested that a dimple depth that is five to ten times the nominal seal clearance is sufficient for a micro dimples seal design.

Feldman, Kligerman and Etsion (2006) reported that a textured portion value of 0.7 provides the maximum load capacity over a wide range of micro dimple seal parameters and operating conditions. The authors concluded that the lubricant leakage through a partial micro dimples seal and the loads generated by this type of seal are significantly less than that of a corresponding equivalent radial step seal. The leakage for the partial micro dimples seal was about 30% less than that of a corresponding equivalent radial step seal. Also the partial micro dimples seal generates loads that are about 40 to 50% less than the loads generated by radial step seal.

They noted that an efficiency parameter can be defined and maximized for an optimum seal

design that minimizes the risks from face contact and provides good sealing properties. A textured portion γ value of 0.5 for a partial micro dimples seal and a radial step seal was attained as the optimum value when the maximum efficiency parameter was considered as the performance parameter for their optimization. For this optimum value of γ, the maximum efficiency parameter value of the partial micro dimples seal was about 20% less than the value of the corresponding equivalent radial step seal.

Feldman et al. (2007) performed a detailed dimensionless analysis of the texturing parameters of a partial micro dimples seal to achieved maximum gas film stiffness with minimum gas leakage. They employed the compressible Reynolds equation for solving for the fluid flow in the seal interface. The authors considered the main dimensionless parameters affecting the hydrostatic pressure distribution. The main dimensionless parameters are: the dimple area density S_p which represents the percentage of textured seal face area between d_o and d_p, the dimensionless dimple depth ε, the dimensionless dimple diameter and the textured portion $\gamma = b/l$. They fixed the value of the dimple density S_p to 0.65 for high load carrying capacity in order to maintained the validity of the Reynolds equation. The other three dimensionless parameters were varied. The dimensionless high pressure used was assigned a value of 2.0.

The authors reported that it is more practical to maximize the design efficiency parameter defined as the ratio of the axial stiffness K to the seal leakage Q rather than the ratio of load carrying capacity P_{av} to seal leakage as defined by Feldman, Kligerman and Etsion (2006). They supported their claim that maximizing the K/Q rather than the P_{av}/Q will expand the maximization of P_{av}/Q from an ideal steady-state case to a real life application involving disturbances of the seal clearance thereby providing a more stable seal operation. The optimum geometrical parameters obtained over a wide range of partial micro dimples parameters and operating conditions in terms of maximum film stiffness and design efficiency parameter are: a textured portion value of $\gamma = 0.7$ and dimensionless dimple depth value of $\varepsilon = 1.4$.

Quite a few researchers have employed other optimization methods whereby all the design variables can be varied at the same time to obtain the optimum geometrical parameters. The few researchers that consider this approach are discussed below. Zhou et al. (2007) employed the complex method of nonlinear constrained optimization in obtaining the optimum geometrical parameters of a spiral groove face seal. The authors considered the opening force as the design objective while a permissible leakage rate was set as a design constraint. They proved that the geometrical parameters which affect the design objective comprise α, n_g, h_g, the ratio of circumferential width of spiral groove to that of a periodic weir and groove γ, and $\bar{R}_g$ where, $\bar{R}_g = (r_g - r_i)/(r_o - r_i)$. In their optimization,

they used a fixed film thickness of $3\,\mu m$, $r_i = 0.020\,m$ and $r_o = 0.030\,m$. The rotating speed considered in their study was $500\,rad/s$ while the pressure differential was not mentioned which may be presumed to be zero pressure differential. The ranges of the design variables were: $0 \leq \alpha \leq 1.736\,rad$, $8 \leq n_g \leq 20$, $0.5 \leq h_g \leq 20\,\mu m$, $0.1 \leq \gamma \leq 0.9$ and $0.1 \leq \bar{R}_g \leq 0.9$. The value of the objective function was evaluated with the incompressible Reynolds equation that was discretized with the finite element method. The optimum values they obtained from their optimization were: $\alpha = 0.14\,rad$, $n_g = 12$, $h_g = 6.2\,\mu m$, $\gamma = 0.7$ and $\bar{R}_g = 0.6$.

2.8 Chapter Summary

Surface texturing improves the mechanism of film pressure generation significantly. The widely used hydrodynamic lifting generating features are to be found in spiral groove seals, radial and parallel groove seals, shrouded pockets seals, micro-dimples seal and orifice-controlled seals. The spiral groove is the most used hydrodynamic lifting generating features in non-contacting gas face seal designs as widely reported in the open literature. It has a good tracking capability as a result of its higher film stiffness at close film thickness. Due to its asymmetric nature, it lacks the capability of generating lift upon reverse rotation of the shaft. This makes it not suitable for bidirectional application. The radial and parallel groove, the shrouded pockets and the micro-dimples hydrodynamic lifting generating features generate the same lift both in forward and reverse rotations as a result of their symmetric groove patterns. These make them suitable for bidirectional application. However the lift produced by these groove patterns is less than the lift produced by the spiral groove seal in the forward rotation. These seals are also less effective in terms of reducing leakage compared to the spiral groove seal. It has been reported in the open literature that the orifice-controlled seal main function is to increase the supply of fluid to the seal interface.

Depending on the design of seals having grooves, placing the groove at the high pressure section of the seal improves the stability of the seal and also improves fluid entrainment into the seal interface. With large diameter seals, placing the grooves at the high pressure section would increase the seal coning thereby reducing the angular stiffness. To improve the angular stiffness of large diameter seals, it is recommended to use double spiral grooves located at the midsection of the sealing dam and the grooves fed with sealing fluid with orifice-controlled slots. Etching grooves on both seal rings increases the frictional torque.

Based on the papers reported in the open literature, the bulk of the work carried out on mechanical face seals employed the Reynolds equation for analysing the fluid flow in the seal interface. Some authors considered the effects of turbulence by subsequent modification of the Reynolds equation to include the eddy viscosity zero-equation turbulence model.

The finite element and finite difference methods of discretization of the Reynolds equation methods are comparable in terms of efficiency and solution time on condition that the same number of nodes and a direct matrix solver (Gaussian elimination technique) are used. When seals operate at high operating conditions, the flow no longer remains laminar and becomes turbulent. Then the effect of inertia, neglected in the Reynolds equation, becomes important. In order to analyse seals that operate at these high operating conditions to a high degree of accuracy, the effects of inertia and turbulence as well as compressibility and choking have to be considered. The Reynolds equation is then not applicable and a full compressible Navier-Stokes equations solver with two-equation turbulence model is thus needed. Only a few papers have been reported in the open literature that considered the analysis of non-contacting gas face seals using the full compressible Navier-Stokes equations solver.

Seals operating at high operating conditions are characterized by convective and centrifugal inertia effects, and turbulence. The centrifugal effect due to rotation of the seal can produced a reverse flow thereby starving the seal interface of the sealing fluid. It has detrimental effects on the seal performance as it reduces the load carrying capacity. The convective inertia effects are beneficial to the seal since it increase the load carrying capacity. For non-contacting gas face seals such as mixers and agitators that run on slow speed and operate at low pressure conditions, the possibility of neglecting the slip flow effects is inevitable. The slip effect is significant when the Knudsen number is 0.01. The condition of low speed and low pressure does exist in seal applications where the pressure is near ambient and speed is barely enough to lift the faces. Analysis of non-contacting gas face seals that require extended period of slow rolling must therefore include the effects of slip flow.

Radial taper can be intentionally machined on seal faces and can be develop during operation. Radial convergent taper is beneficial to the generation of lift while divergent radial taper tends to starve the seal interface of fluid. Seals exposed to this condition do not generate any useful lift that can keep the seal interfaces apart during operation. Waviness in non-contacting gas face seals is difficult to control since this situation develops during operation. Seal ring faces that have low modulus of elasticity, such as carbon, increase the formation of waviness during operation. To reduce the formation of waviness during operation, the non-contacting gas face seals should be design in a manner that the areas of higher pressures should not be farther apart. The effects of radial taper, usually referred to as coning, are more significant than the effects of waviness.

Optimization of the geometrical parameters of the hydrodynamic lifting generating features and the analysis of the fluid flow in the seal interface are intertwined. Any little change in the geometrical parameters of the hydrodynamic lifting generating features significantly affects the performance of the non-contacting gas face seals. For a non-contacting gas face seal to

function properly, the optimum geometrical parameters as well as the appropriate equations that govern thin film flow to include the effects of inertia, turbulence, compressibility as well as choking must be used. Most of the papers reported in the open literature used the parametric analysis approach in optimizing the geometrical parameters of the hydrodynamic features and employed the Reynolds equation in determining the performance parameters. In this approach, the design variables are varied one at a time to obtain the optimum performance parameters. There is no interaction among the design variables since only one design variable is varied at a given time; the other design variables been kept constant. In this approach, a compromise has to be made in choosing the optimum geometrical and performance parameters. Only very few papers attempted to use the standard optimizers with the Reynolds equation for optimizing mechanical face seals. It has been reported that with automated optimization of the geometrical parameters of the hydrodynamic lifting generating features, the performance characteristics of seals can be improved. In optimization of the geometrical parameters of the hydrodynamic lifting generating features, the pressure differentials should not be considered but the effects of rotational speed must be considered. When an unsteady condition is considered, the squeeze-film terms should also be considered.

Chapter 3

Presentation and Development of Numerical Methods

3.1 Introduction

This chapter is divided into two parts - fundamentals of seal design and research methodology. The first part presents the basic principles governing dry gas face seals. It covers seal operating regimes, physics of compressible flow and concept of choking, seal pressure balancing and performance parameters. The second part of the chapter presents a detailed description of the research methodology. Two models were developed - a Reynolds equation based code and 3D CFD models. The Reynolds equation model solves the compressible Reynolds equation. In this model, the fluid film thickness is defined analytically and included in the Reynolds equation. This code developed by the author is based on FORTRAN and MATLAB languages. The 3D CFD model employed a commercial CFD package (ANSYS CFX version 11) in solving the full Navier-Stokes equation for the fluid flow in the seal interface. The 3D CFD model eliminates the film thickness discontinuity problems associated with the Reynolds equation model. It also considered the effects of inertia and turbulence that were neglected in the Reynolds equation model. Both models assumed steady state conditions for the fluid flow in the seal interface.

3.2 Fundamentals of Seal Design

3.2.1 Seal Operating Regimes

Seals may operate in different lubrication regimes depending on the type of seal, the sealed fluid and the application. The different lubrication regimes that can exist in a dry gas face seal are best explained using a plot of friction coefficient against seal duty parameter. The

duty parameter G, defined in Equation (3.1), is a dimensionless parameter that is an indicator of the operating conditions and which depicts the seal lubrication mode. In Equation (3.1), μ is the dynamic viscosity, ω is the sealing shaft rotational speed, r is the seal radius, $\Delta r = r_o - r_i$, is the seal face radial length, F_c is the seal closing force, r_o and r_i are the seal outer and inner radii, respectively. The duty parameter is essentially an inverse measure of the severity of the operating conditions. High values of the duty parameter typically indicate full-film lubrication mode while low values signify mixed or boundary lubrication modes. The friction coefficient is expressed as the ratio of the tangential friction force to the normal applied force (closing force).

$$G = \frac{\mu\,\omega\,r\,\Delta r}{F_c} \tag{3.1}$$

Figure 3.1 shows the variation in friction coefficient of a seal from start-up under a load (e.g., spring force and pressure) in the boundary lubricating regime to steady-state operating speed in the full-film lubricating regime. The mechanism for achieving full-film operation could be an external pressurization source, or it could be self-generated by hydrodynamic lubrication or combination of both. At start-up, the seal faces are in solid-to-solid contact and the seal runner (mating ring) begins to turn under essentially dry conditions and follows the path AB. When sufficient lubricant is available, the lubricant is quickly drawn in between the surfaces sliding together (either by the mechanisms of capillary or forced pumping) and the seal goes directly into the thin-film (or mixed film) regime, following the path ABC. When the speed reaches the value equivalent to point C, the seal enters the full-film regime. The seal operates in this regime and at point D, compressibility effects begin to set in and the effects of inertia become significant. It continues up to point E where transition from laminar flows start and the flow becomes fully turbulent at point F. A critical look at Figure 3.1 will show that if a fluid film is not present, the seal would be forced to operate dry at a speed corresponding to point A. The resulting temperature rise could be extreme because of the high friction being generated.

The region on the right-hand side of the second dashed vertical line in Figure 3.1 represents the full-film lubrication regime as shown in Figure 3.2(c). This is the region of thick film lubrication, where the surface asperities are completely separated by a fluid film thickness that no solid-to-solid contact can occur and the theory of hydrodynamic lubrication is applicable. At sufficiently large values of seal duty parameter, turbulent flow may occur (transition occurs at point E and becomes fully turbulent beyond point F) as shown in Figure 3.1. The friction here rises significantly and increases at a more rapid rate with speed than when the flow regime is laminar.

To the left-hand side of the second dashed vertical line in Figure 3.2 are the regions of boundary (Figure 3.2(a)) and mixed film lubrication (Figure 3.2(b)) respectively. As can

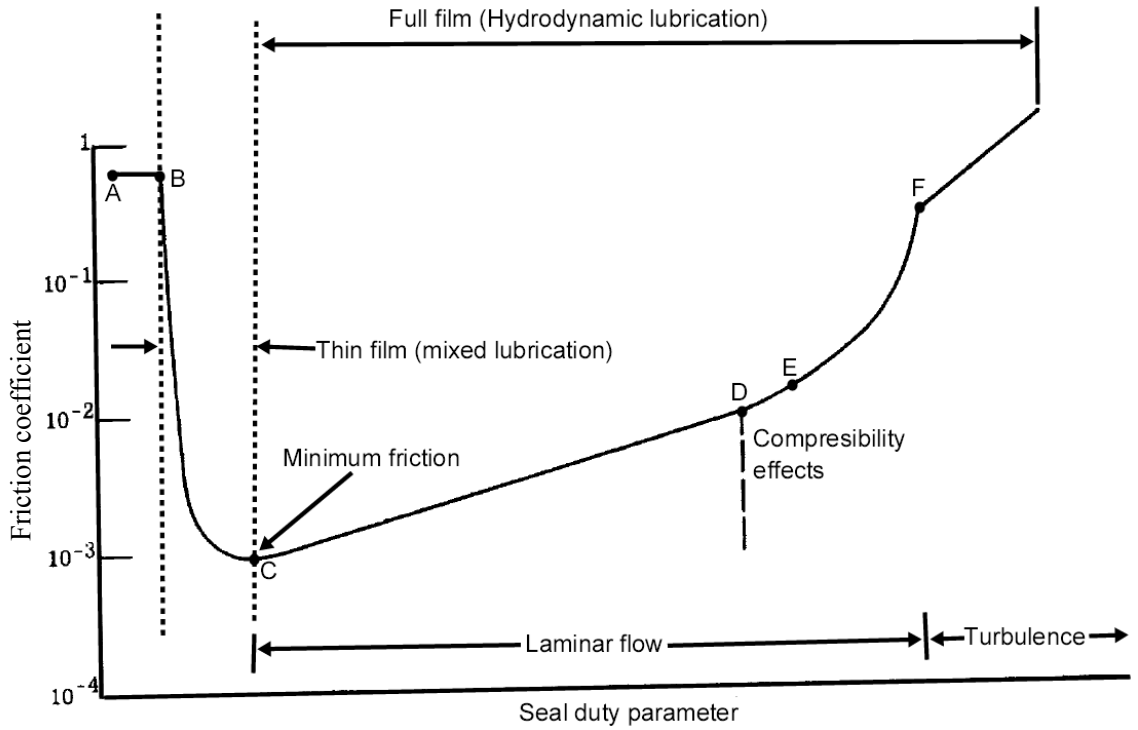

Figure 3.1 Friction coefficient as a function of seal duty parameter for gas lubrication (Zuk, 1976)

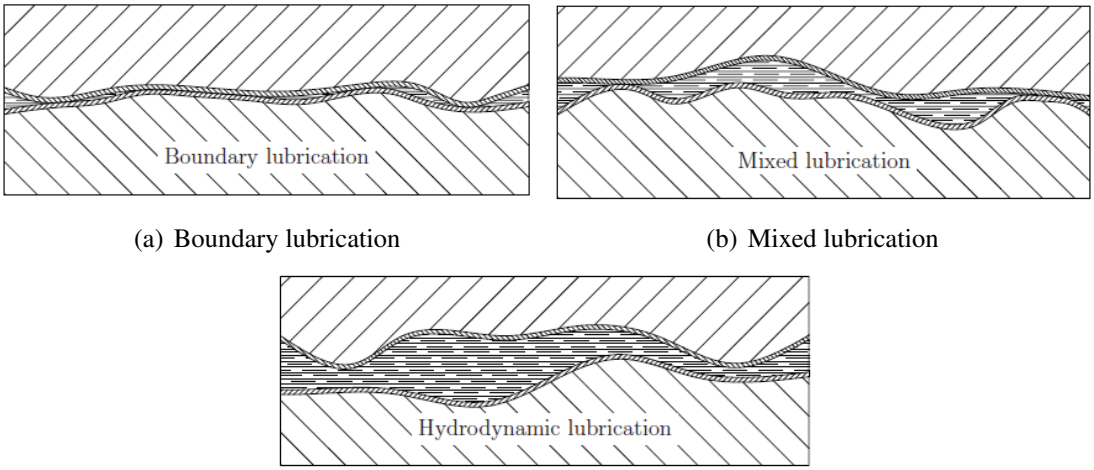

(a) Boundary lubrication

(b) Mixed lubrication

(c) Full-film lubrication

Figure 3.2 Dry gas face seal lubrication mode (Lubbinge, 1999)

be seen in Figure 3.2(a), the film thickness in the boundary lubrication is so thin that asperities make contact through the fluid film. The mixed film regime is one that combines hydrodynamic and boundary lubrication. This is also the regime where elastohydrodynamic effects may not be neglected. Friction coefficients in the boundary and thin-film regimes are empirically determined. In Figure 3.2, the thin lubrication film layer on the seal surfaces is used for protecting the seal surfaces against wear in the event of face contact.

In full-film fluid lubrication, the asperities do not contact, only bulk lubricant physical properties are important. In boundary and thin-film lubrication, the solid properties together with surface physics and chemistry of the sealing ring materials are of primary importance since there is solid-to-solid contact by asperities. Lubricant chemical properties are liable to influence the type of damage that occurs. The lubricating regimes can be associated with seal-face loading and speed. The full-film lubricating regime is characterized by the fluid film thickness being several times greater than the seal rings surface roughness. The mixed film regime has the film thickness of the same order as the surface roughness. In the boundary regime, asperity contact characterizes the interface.

The value of friction coefficient of gases is almost the same value as that obtained from a solid sliding on a solid at low seal duty parameters as a result of gases being poor boundary lubricants. Also gases have a much lower viscosity compared with liquids; thereby their friction forces in the full-film lubricating regime are less than those of liquids by one or two orders of magnitude. In order for a gas seal to operate safely in this regime, incorporation of lift geometries to the seal faces is usually required. Operating gaps are inherently smaller for gas film seals (due to the low viscosity); hence, these seals are more sensitive to face distortion. This, coupled with the poor boundary lubricating properties of gases, means that stable self-induced hydrodynamic operation is unlikely in gas film seals when there are no lift generating geometries. Compressibility effects become important before turbulence occurs and for large gaps and sufficiently high pressures or speeds, turbulent flow may occur (Zuk, 1976).

Fluid film lubrication implies the existence of an interposed full film of fluid that physically separates the mating surfaces of the seal. The four generally recognised modes of full-film lubrication in dry gas face seals are categorized as follows:

1. Hydrodynamic - the load-carrying capacity is achieved as a result of a relative tangential motion between the uneven sealing surfaces.
2. Hydrostatic - the load carrying capacity is achieved as a result of frictional pressure drop in the seal interface through external pressurization.
3. Squeeze film - the load carrying capacity is achieved as a result of the flexible seal face moving relative to the stationary face normal to the direction of the fluid flow in the interface.
4. Hybrid operation - the load carrying capacity is achieved by a combination of two or more of the preceding modes of full-film lubrication.

3.2.2 Physics of Compressible Flow and Concept of Choking

In compressible flow, density is a dependent variable and the equations are nonlinear and this makes them difficult to solve. The pressure appears both in a dynamic and thermodynamic state unlike in the incompressible flow where the constant-density assumption is made and the equations are simpler to solve. The momentum equation is interrelated to the energy equation. Another equation that is required is the equation of state. The physics of the flow are also different and more complex.

For thin films, the standard lubrication assumption of isothermal surfaces can be made even for gases provided the flow rates are kept low. Isothermal assumption is usually made because gas lubricant films are very thin and are in contact with relatively large masses of the sealing faces. At higher flow rates, an adiabatic or polytropic equation of state may be more relevant. This isothermal or polytropic equation of state enables a relation to be found which eliminates consideration of temperature in solving the set of equation hence the energy equations is not always considered. The polytropic equation of state is:

$$\frac{p}{\rho^{\gamma}} \tag{3.2}$$

The gas film theory, as well as gas dynamics is based on the principle that at any point in time and space the flow is in thermodynamic equilibrium and the perfect-gas law applies. Compressible flows are characterized by the local change in density in the film. As a result of the isothermal assumption that is usually made, the density change results primarily from changes in pressures as predicted by the perfect-gas laws. The viscosities of gases increase slowly with temperature, as opposed to the rather rapid decrease that liquids exhibit.

Incompressible flow in long narrow spaces is characterized by a linear pressure drop and a velocity profile that does not change in the flow direction assuming the flow is laminar. This can be seen by examining the continuity equation for a parallel flow between two plates:

$$\frac{\partial u}{\partial x} = 0 \tag{3.3}$$

The continuity equation for the same case but for a compressible fluid is:

$$\frac{\partial \rho u}{\partial x} = \rho \frac{\partial u}{\partial x} + u \frac{\partial \rho}{\partial x} \tag{3.4}$$

From the equation of state, pressure is directly proportional to density; that is, as the pressure drops, the density also decreases, and the velocity is no longer constant in the

flow direction but rather increases. Thus the term "quasi-fully-developed flow" is employed in compressible viscous flow and the flow is characterized by a parabolic pressure drop across the radial leakage path. A gas has a large specific volume associated with a pressure drop. For a certain pressure drop across a seal, the less dense the sealed fluid, the lower the resultant mass flow rate.

Compressible flow and choking will occur as a consequence of the static pressure drops through the seal face in order to overcome flow friction. The pressure drop increases the specific volume of the fluid. Assuming that the area change is negligible, the mean velocity must increase as the specific volume increases in order to maintain the same mass flow rate at each section of the leakage path. As the friction causes the velocity to increase, the fluid momentum change also becomes important. In order to accelerate the fluid to a greater velocity, a force is required which can be attained only through an additional pressure drop. This results in a still greater increase in specific volume. This process will continue until the end of the leakage path or until the fluid attains the choking condition. Choking occurs when the Mach number is unity at the exit (i.e., exit velocity is sonic). Should the Mach number reach unity somewhere along the leakage path interior, it is expected that behaviour similar to duct flow will occur. For duct flow it has been shown that the flow process will adjust itself until the point at which the Mach number reaches unity is shifted to the exit of the leakage passage. The mass flow rate of the fluid is the maximum which can be handled for a given inlet density and passage cross-sectional area. This flow process is known classically as the Fanno line flow.

The velocity head loss at the entrance is negligible in subsonic viscous flow compared to the total seal pressure drop; under choked conditions the entrance velocity head loss is no longer negligible. This gives rise to pressure loss at the entrance. Also under choked flow conditions, the exit pressure at the seal ring inner diameter is larger than the atmospheric or sump pressure and increases with fluid film thickness. The pressure decreases to atmospheric pressure through expansion waves in the outer cavity. The expansions that take place at the outer cavity do not have significant effect on the axial force balance on the seal nose piece (Zuk, 1976).

3.2.3 Seal Pressure-Balancing Fundamentals

One of the main objectives in fluid-film, face-seal design is to ensure that the face loading is reasonably low so that high heat generation and high wear are prevented. Conversely, in order to avert excessive leakage, close clearance must be preserved at all operating conditions. In order to achieve optimum face loading, seals are generally designed to have a hydraulic loading area as well as sealing interface area. The sealed fluid acts on the

hydraulic loading area in order to generate hydrostatic closing forces along with the spring load to keep the sealing faces together. The sealed fluid acts on the sealing interface which tends to open the seal faces. The hydraulic area is the area between the outside diameter of the sealing face (d_o) and the balance diameter (d_b). The factor that basically determines if a seal is balanced or unbalanced is the relationship between the hydraulic loading area and the sealing interface area. The forces acting on the seal rings as well as the geometrical dimensions are shown in Figure 3.3. Shown in Figure 3.3 is a balanced pusher seal that has a sealing interface area larger than the hydraulic loading area which is attained by machining a step in the shaft or sleeve. In an unbalanced seal, the sealing interface area is smaller than the hydraulic loading area.

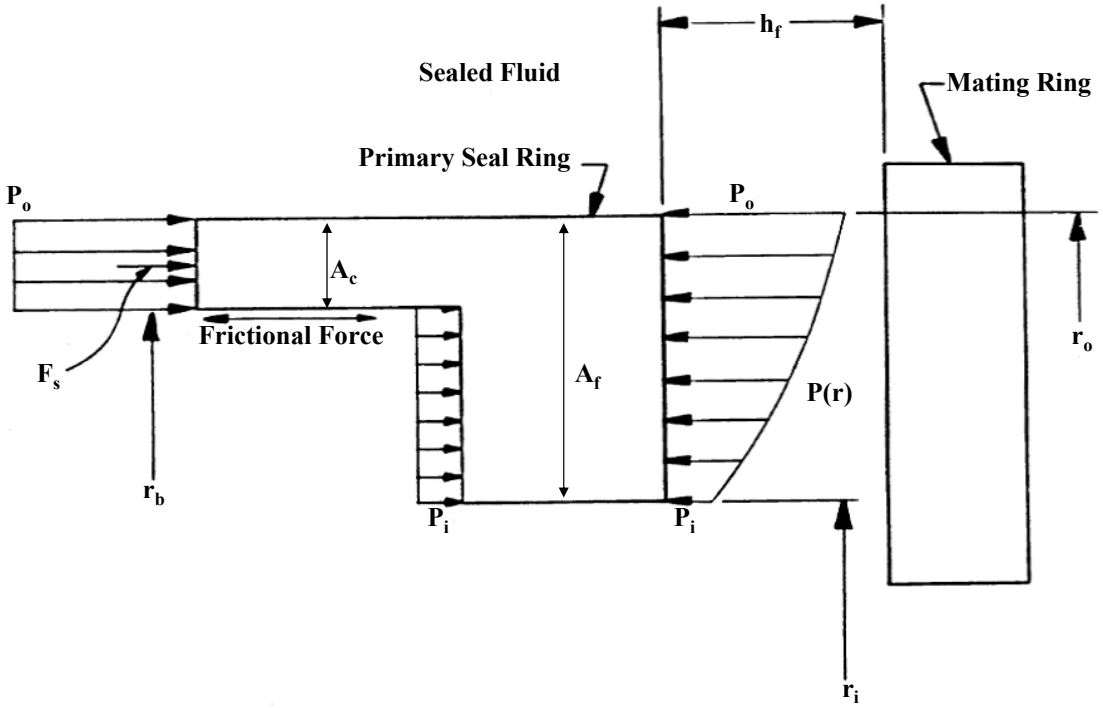

Figure 3.3 Forces acting on seal ring faces

A general term used by seal designers in balancing seals is the geometric balance ratio typically known as balance ratio B_r. For an externally pressurized seal that is internally mounted, the balance ratio is expressed as in Equation (3.5) and for an internally pressurized seal that is externally mounted, the balance ratio is defined in Equation (3.6).

$$B_r = \frac{\frac{1}{4}\pi\left(d_o^2 - d_b^2\right)}{\frac{1}{4}\pi\left(d_o^2 - d_i^2\right)} \tag{3.5}$$

$$B_r = \frac{\frac{1}{4}\pi\left(d_b^2 - d_i^2\right)}{\frac{1}{4}\pi\left(d_o^2 - d_i^2\right)} \tag{3.6}$$

For a seal that is balanced, the balance ratio is usually less than one. Most of the available balanced seals usually have balance ratios that vary between 0.65 and 0.85 (Wallace, 1992). For unbalanced seals, the balance ratios are usually equal to or greater than 1. The balance ratio for unbalanced seals is usually about 1.2 and the degree of unbalance mostly depends on the clearance between the seal face inner circumference and the shaft (Wallace, 1992). Balanced seals are mostly used for sealing applications that have high sealed fluid pressure while unbalanced seals are used for low fluid pressure applications. Seals having high balance ratios ($B_r = 0.85$) are less prone to blow open and are considered to be more stable in the action of hydrostatic pressure between the faces, other than at the expense of higher face loading (Wallace, 1992). Seals having lower balance ratios ($B_r = 0.65$), have lower face loadings therefore lower heat generated, but can be hydraulically unstable at higher pressures (Wallace, 1992).

The closing force usually comprises the hydraulic load F_h, spring load F_s, frictional forces F_F and inertia forces F_I as expressed in Equation (3.7). The frictional forces come from the secondary seals such as O-rings while the inertia forces are due to the anti-rotation lugs such as torque pins that rub on the seal housing. A balanced seal behaves like two seals in terms of hydraulic loading, that is, one is internally pressurized while the other is externally pressurized. The hydraulic closing force can be attained by superposition of the two as expressed in Equation (3.8).

$$F_c = F_h + F_s \pm (F_F + F_I) \tag{3.7}$$

$$F_h = \frac{1}{4}\pi \left(d_o^2 - d_b^2\right) p_o + \frac{1}{4}\pi \left(d_b^2 - d_i^2\right) p_a = A_f \left[B_r\, p_o + (1 - B_r)\, p_a\right] = A_f \left(B_r \Delta p + p_a\right) \tag{3.8}$$

The spring load is defined as the product of the face pressure due to the spring p_s and the sealing interface area. Characteristic values of face pressure due to the spring are in the range of 0.1 to 0.3MPa, although in some designs, the value might be as low as 0.02MPa or as high as 0.5MPa. In order to design the seal to resist vacuum loads, the spring load is usually selected to be greater than $\frac{1}{4}\pi \left(d_h^2 - d_b^2\right)(p_a - p_o)$, where d_h is the outer diameter of stationary secondary seal. Also, if the stator is clamped, the spring load is selected to be greater than $\frac{1}{4}\pi \left(d_o^2 - d_b^2\right)(p_a - p_o)$ (Wallace, 1992).

The closing force in a dry gas face seal is easily predicted. For simple geometries (such as parallel plain face seals with radial taper), the seal opening force can be evaluated analytically. For more involved geometries (such as found in grooved dry gas seals); numerical methods are needed to determine the seal opening force. The net closing force is the resulting difference between the opening force and closing force as expressed in Equation (3.9).

$$F_{net} = F_c - F_o \tag{3.9}$$

Another key parameter that is employed for seal pressure-balancing is the load factor $\bar{F}$ expressed in Equation (3.10). It is defined as the ratio of the opening force F_o to the sealed pressure differential Δp force acting over the sealing interface area A_f.

$$\bar{F} = \frac{F_o}{A_f \Delta p} \tag{3.10}$$

For a seal to be balanced, the opening force will be equal to the hydraulic load provided the magnitude of the spring load is sufficient to overcome any axial friction that may arise from the dynamic secondary seal and the dynamic effects of any face misalignments. Equating the opening force to the closing force and substitution of Equation (3.8) into Equation (3.10), shows that the load factor is equal to the balance ratio as illustrated in Equation (3.11). It was assumed in the expression given in Equation (3.11) that p_a is negligible compared to the sealed fluid pressure and that the seal is sealing to atmosphere ($p_a = 1\,bar$). Once the load factor is known, the seal balance diameter d_b can be computed from Equation (3.12). The basic consideration in designing a pressure-balanced seal is the selection of the balance diameter. This diameter determines the hydraulic closing force. By properly positioning the balance diameter, the closing force can be equal to the seal opening force or, at least theoretically, to any degree of face loading.

$$\bar{F} = \frac{A_f \left(B_r \Delta p + p_a\right)}{A_f \Delta p} = B_r \tag{3.11}$$

$$d_b = \sqrt{\bar{F}\left(d_o^2 - d_i^2\right) + d_i^2} \tag{3.12}$$

3.2.4 Mechanisms of Film Pressure Generation

The mechanism of load generation in grooved seal can best be described with a step bearing configuration shown in Figure 3.4. The main assumptions are: $h_1 \ll L_1$ and $h_2 \ll L_2$ where $h_1 = h_f$, $h_2 = h_f + h_g$, $L_1 = r_g - r_i$ and $L_2 = r_o - r_g$. Here, h_1 is the same as the fluid film thickness h_f, h_2 is the total fluid film thickness at the groove region consisting of the fluid film thickness h_f and groove depth h_g. Also, L_1 is the radial length of the land region, L_2 is the radial length of the groove region while r_g is the radius at the beginning of the groove, r_i and r_o are the radii at the seal inner and outer diameters, respectively. The flow is assumed to be viscous, one-dimensional laminar flow. One of the surfaces rotates at a constant speed about the z-axis with a velocity u in a direction parallel with the surfaces as shown in Figure 3.4. The local flow velocity u in the film varies uniformly from zero at the stationary surface to u at the moving surface.

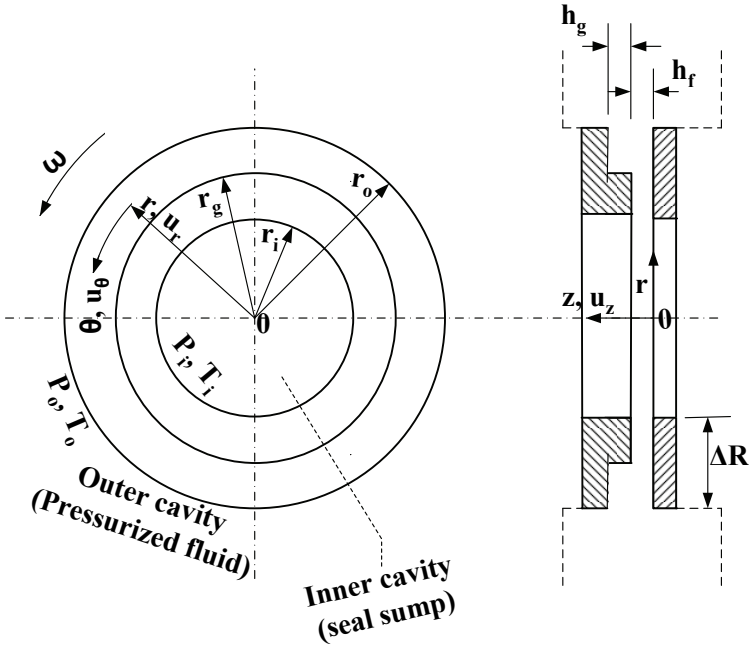

Figure 3.4 Model of a Rayleigh step seal face

The total flow crossing any radius of the seal shown in Figure 3.4 must be a constant and equal to the total leakage Q_r defined in Equation (3.13).

$$Q_r = 2\pi r \int_0^h u\,dz = \frac{\rho\,\omega^2\,\pi\,r^2\,h^3}{20\,\mu} - \frac{\pi\,r\,h^3}{6\,\mu}\,\frac{\partial p}{\partial r} \tag{3.13}$$

Integrating Equation (3.13) with respect to r between r_i and r yields the pressure distributions given in Equation (3.14).

$$p = p_i + \frac{3\,\rho\,\omega^2}{20}\left(r^2 - r_i^2\right) - \frac{6\,\mu\,Q_r}{\pi\,h^3}\ln\frac{r}{r_i} \tag{3.14}$$

Assuming that general Couette flow governs the flow along flow passages in the land and groove regions, and employing Equation (3.14), gives the continuity equation for the leakage rate at the land (Q_l) and groove (Q_g) regions, respectively. The leakage rate for the land and groove regions are expressed in Equations (3.15) and (3.18).

$$Q_l = \frac{\pi\,h_2^3}{6\,\mu\,\ln\left(\dfrac{r_o}{r_g}\right)}\left\{\frac{3\,\rho\,\omega^2\,L_2}{20}\,(r_o + r_g) + p_g - p_o\right\} \tag{3.15}$$

$$Q_g = \frac{\pi\,h_1^3}{6\,\mu\,\ln\left(\dfrac{r_g}{r_i}\right)}\left\{\frac{3\,\rho\,\omega^2\,L_1}{20}\,(r_g + r_i) + p_i - p_g\right\} \tag{3.16}$$

For the condition of continuity to hold, the leakage in the land and groove must both be equal. The peak pressure at the beginning of the step, p_g is found by equating Equations (3.15) and (3.18) together and the resulting p_g is given in Equation (3.17).

$$\begin{aligned} p_g = {} & 3\,h_1^3\,\rho\,\omega^2\,L_1\,\ln\left(\frac{r_o}{r_g}\right)\,(r_g + r_i)\,C_1 \\ & - 3\,h_2^3\,\rho\,\omega^2\,L_2\,\ln\left(\frac{r_g}{r_i}\right)\,(r_o + r_g)\,C_1 \\ & + 20\left(p_i\,h_1^3\,\ln\left(\frac{r_o}{r_g}\right) + p_o\,h_2^3\,\ln\left(\frac{r_g}{r_i}\right)\right)C_1 \end{aligned} \tag{3.17}$$

$$C_1 = \frac{1}{20\left(h_1^3\,\ln\left(\frac{r_o}{r_g}\right) + h_2^3\,\ln\left(\frac{r_g}{r_i}\right)\right)}$$

When this pressure is known and then substituted into Equation (3.14), the entire pressure distributions across the land and the groove are known. The opening force can be found by integrating the pressure distributions over the seal face area and the resulting opening force is defined in Equation (3.18).

$$\begin{aligned} F_o = {} & -p_i\,\pi\left(r_i^2 - r_o^2\right) - \frac{3\,\mu\,Q_l}{h_1^3}\left(r_i^2 - r_o^2\right) \\ & + \frac{3\,\pi\,\rho\,\omega^2}{40}\left(r_i^4 - r_o^4\right) - \frac{3\,\pi\,\rho\,\omega^2\,r_i^2\,r_o^2}{20} - \frac{6\,\mu\,Q_l}{h_1^3}\,r_o^2\,\ln\left(\frac{r_o}{r_i}\right) \end{aligned} \tag{3.18}$$

As can be seen from Equation (3.18), the opening force is a function of the fluid film thickness and groove depth. If the groove depth and the film thickness are changed, the opening force would decreased or increased respectively. This is the mechanism that all grooved seals such as the spiral and radial grooved seals use as their mechanism of film pressure generations.

3.2.5 Performance Parameters

3.2.5.1 Pressure Distributions

This is the most important parameter in seal analysis. When the pressure distribution is known, all other parameters can be solved for. It is usually found by solving numerically either the Reynolds equation or the full Navier-Stokes depending on the choice of numerical method chosen.

3.2.5.2 Seal Leakage

Leakage is one of the significant performance parameters of a dry gas face seal and must be obtained as one of the results of the modelling effort. The seal leakage is obtained from the mean velocity at any radial cross section. The mean velocity u_m is defined in Equation (3.19) and the seal leakage is given in Equation (3.20). The radial velocity u_r in Equation (3.19) is obtained from the numerical integration of either the Reynolds equation or the full Navier-Stokes equations. The desired information of the seal leakage is always expressed in "Standard Cubic Feet per Minute" (SCFM) which is the volumetric flow rate of a gas corrected to "standardized" conditions of pressure, temperature and relative humidity. It corresponds to a precise mass flow rate at a common base.

$$u_m = \frac{1}{h}\int_0^h u_r\, dz \tag{3.19}$$

$$\dot{m} = 2\pi r h \rho\, u_m \tag{3.20}$$

3.2.5.3 Seal Opening Force

Since there is a pressure drop when fluid flows, the integrated effects yield a net force. This force is called the opening force and it is obtained by integrating the fluid pressure over the total surface (sealing interface) over which it is acting. The opening force F_o is computed from the pressure distribution as expressed in Equation (3.21).

$$F_o = \int_A p\, dA = \int_0^{2\pi}\int_{r_i}^{r_o} p\, r\, dr\, d\theta \tag{3.21}$$

3.2.5.4 Axial Film Stiffness

This is an important parameter for maintaining positive surface separation when the seal is operating under severe conditions, such as high sealed-fluid pressure differentials and/or speeds. The axial film stiffness is defined as given in Equation (3.22). A positive value of the stiffness will indicate that the seal nose piece can dynamically track the run-out motion of the rotating face. A negative value of the axial stiffness is detrimental to the seal performance.

$$K_z = -\frac{dF_o}{dh} \tag{3.22}$$

3.2.5.5 Power Consumption

The friction in the seal interface is due to the viscous shearing of the fluid film in the interface and can be described by the Newton's law of viscous shear and the solid sliding contact governed by Amonton's law. The Newton's law of viscous shear states that the friction force per unit area is proportional to the shear rate while the Amonton's law states that friction force is proportional to the normal load. The frictional force as a result of the viscous shearing F_{film} is defined in Equation (3.23) and the friction force due to solid sliding contact F_{solid} is expressed in Equation (3.24).

$$F_{film} = \frac{\mu\,\omega\,r\,A_f}{h} \tag{3.23}$$

$$F_{solid} = \mu_f\,F_{mech} \tag{3.24}$$

Where μ_f is the friction coefficient of the face material in contact, F_{mech} is mechanically supported load, h is the effective film thickness and A_f is the area of the sealing interface. The total friction force F_f is the addition of F_{film} and F_{solid}. The frictional torque T_q is the product of the total frictional force F_f and the seal mean radius r_m. In full-film lubrication mode, the mechanically supported load is zero since there is no contact but in boundary and mixed-film lubrication mode, the mechanically supported load has to be included. The power absorbed or consumed q_{absorb} in dry gas face seals is computed by multiplying the frictional torque by the rotational speed of the shaft as given in Equation (3.25).

$$q_{absorb} = T_q\,\omega \tag{3.25}$$

3.2.5.6 Film Temperature Rise

As a result of viscous shearing of the fluid film in the sealing interface, heat is generated resulting in a film temperature rise ΔT. It is advantageous to determine the temperature rise in order to evaluate the temperature that the sealing face materials can withstand. The approach adopted in predicting the film temperature rise is by equating the heat generated q_{absorb} from the viscous shearing of the fluid film to the heated dissipated by convection. The heat dissipated by convection q_{cov} is given in Equation (3.26) where h_c is the heat transfer coefficient.

$$q_{cov} = h_c A_f\,\Delta T \tag{3.26}$$

$$h_c = 0.133\,Re_D^{2/3}\,Pr^{1/3}\,\frac{k_f}{D} \tag{3.27}$$

The heat transfer coefficient is computed from Becker's correlation (Becker, 1963) given in Equation (3.27). It is assumed that the temperature distribution is uniform along both sealing rings. In Equation (3.27), k_f is the thermal conductivity of the fluid, Pr is the Prandtl number of the fluid expressed as $Pr = \frac{C_p \mu}{k_f}$ and Re_D is the Reynolds number based on the outer diameter D of the seal. The Reynolds number is defined as $Re_D = \frac{\rho \omega D^2}{2\mu}$. The temperature rise is thus calculated as shown in Equation (3.28).

$$\Delta T = \frac{q_{absorb}}{h_c A_f} \tag{3.28}$$

3.2.5.7 Design Efficiency Parameter

The main objective of a good seal is to minimize leakage while maintaining a reasonable fluid gap such that face contact can be avoided. To achieve this objective, some performance measures have to be taken into account during seal analysis. These performance measures consist of the opening force, leakage, axial film stiffness and power consumption already described. Seals are usually designed to have maximum opening force, minimum leakage, maximum positive axial film stiffness and minimum power consumption. Some researchers (Feldman, Kligerman and Etsion (2006), Feldman et al. (2007) and Zhou et al. (2007)) have pioneered the use of a design efficiency parameter E_p as a performance measure that represents the overall seal performance parameters (opening force, leakage, axial film stiffness and power consumption). The higher the value of the design efficiency parameter the better the performance of the seal in terms of minimizing leakage and avoiding face contact.

$$E_p = \frac{F_o}{\dot{m}} \tag{3.29}$$

$$E_p = \frac{K_z}{\dot{m}} \tag{3.30}$$

The design efficiency parameter has been defined in different ways by different authors. Feldman, Kligerman and Etsion (2006) and Zhou et al. (2007) defined the design efficiency parameter as the ratio of opening force to leakage (Equation (3.29)), while Feldman et al. (2007) defined it as the ratio of stiffness to leakage (Equation (3.30)). Zhou et al. (2007) referred to the design efficiency parameter as aggregating evaluating indicator. Axial film stiffness is usually preferred to the opening force since a good seal must have a positive stiffness such that one of its faces will be able to dynamically track the run out motion of the other face when it is subjected to disturbances. Computing the stiffness is expensive since a single computation of stiffness will requires several calculations of the opening forces at different fluid film thicknesses for a single combination of seal geometrical parameters

and operating conditions. Based on the above reasoning, this study considered the design efficiency parameter as the ratio of opening force to seal leakage.

3.3 Research Methodology

Dry gas face seal design is a systems design problem that comprises the phenomena of lubrication theory, mechanical distortion, heat transfer, dynamics and surface roughness effects. These phenomena are interactive and they are all important in seal design. The lubrication theory describes or explains the major phenomena that mostly influence the seal design. The seal system can be described by the fluid-film lubrication analysis, face deformation analysis and instability analysis as illustrated in Figure 3.5.

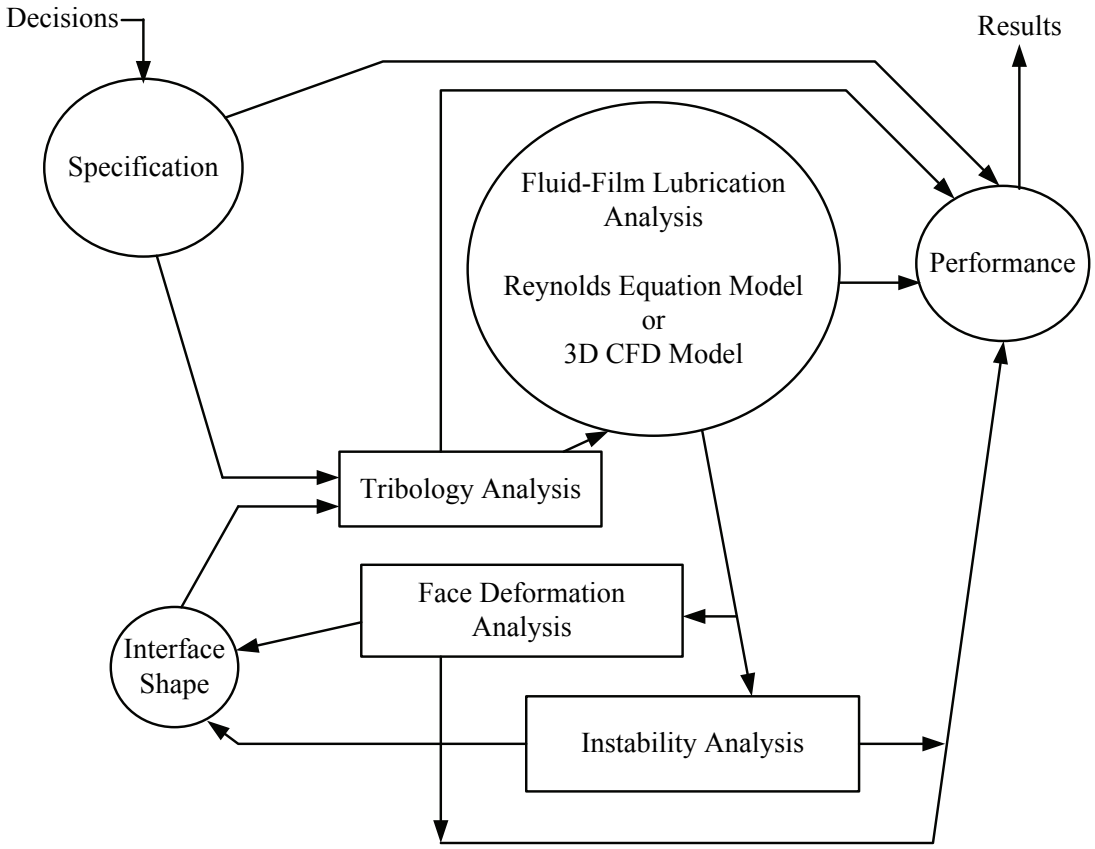

Figure 3.5 Schematic diagram of dry gas face seal system analysis

The first step in the design cycle is the specification. It comprises the given seal fluid environment which includes temperature and chemistry as well as speed and pressure. It also includes the selection of materials, which are of fundamental importance to the tribological performance of the sliding faces as well as the secondary seals and other ancillary components. It also contains all of the design selections and choices of the precise geometric definition and manufacturing process.

The interface shape is the geometrical seal face profile of the seal defined both as a function of the radial and angular position. The interface shape is essential to the seal performance. Some interface shapes promote hydrodynamic lubrication, some of them are capable of generating hydrostatic loads while others may virtually eliminate most fluid pressure load support and cause boundary lubrication to occur. Some interface shapes will produce excessive leakage while some will give only the smallest leakage. A variety of interface shapes have been discussed in Chapter 2 under sections "geometrical seal face profiles" and "the effects of face deformation" on pages 17 and 49 respectively. Several of these shapes may exist simultaneously in the same seal. Some are intentionally machined on the seal faces while some such as radial taper and waviness may occur during operation. Interface shape may change with time, rapidly or slowly. It certainly changes with wear. Whatever the cause of the interface shape, if it can be defined at some instant, then it is possible to predict how the seal is performing at that instant. The shape of the interface itself depends on the lubrication phenomenon that is dependent on the shape itself. Thus the problem becomes highly interactive. But definition of the shape and the prediction of performance based on it is a key step in the solution of the seal systems problem.

Knowing the specification and interface shape, the principles of tribology and application of the lubrication theory, the fluid pressure distribution for a full-film lubrication regime can be predicted. Also, the contact load support that does exist in mixed-film lubrication regime at start-up and shut-down can be estimated. Depending on the choice of numerical analysis method to be discussed in sections "Reynolds equation model" and "3D CFD model", the Reynolds equation or the full Navier-Stokes equations are solved for the fluid flow in the shape interface. The tribological behaviour may depend on the materials chosen as well as the chemical environment. It is important to recognise that while tribology is a key link in the seal system, tribology alone is insufficient to understand what is happening in the seal interface.

Seal performance may be influenced by some factors resulting in an increase in temperature in the seal rings. One of the factors may be related to the tribological condition of the seal where the shape interface may become a boundary lubrication condition resulting from seal face contact due to divergent radial taper in the event the temperature is too high. Another factor is that many materials are simply not tolerant of high levels of temperature and may be destroyed by operation at elevated temperature while the last factor is the nonuniform heating of the seal rings. Most of the heat is generated by sliding friction at the seal interface itself. Any imbalances in the moments on the ring about a circumferential axis, as well as nonuniform temperature distribution, produce face distortions in the form of coning. These distortions influence the shape interface as well as the very pressure distribution that is causing them in the first place - thus the interactive nature of the seal systems problem.

The prediction of the stresses and deflections of the seal rings can be achieved by the face deformation analysis. This analysis usually employs a finite element analysis method. The face deformation analysis is used to find the exact pattern of distortion for a given set of loads. The stresses in relation to the strength of the materials must be considered to be able to carry out a performance assessment of the seal. The face deformation analysis can help in minimizing any detrimental effects resulting from distortions. This is achieved by checking whether the distortions do not considerably affect the fluid-film performance. Modifying the exterior geometry of the seal rings as well as making some variations in the seal ring materials can reduce distortions.

There are several instances during seal operation when the running equilibrium is disturbed. The running equilibrium might be disturbed such as the pressure may suddenly change, a large particle been trapped in between the faces, secondary o-ring moves, and shaft moves axially or shifts radially. Whenever this happens, the seal faces may either return to the equilibrium state or start oscillating. The instability analysis (usually referred to as dynamic analysis) is carried out to ensure acceptable dynamic response to external excitations. This is achieved by checking the dynamic response and varying the seal ring mass and inertia properties to assured acceptable response. The dynamic response is the ability of the flexible stationary seal ring to track the run out motion of the rotating seal ring.

The performance of the seal can be assessed given the mechanical and fluid pressure distributions and the leakage predicted from the tribological and lubrication analysis. An estimate of wear rate as well as frictional heating can be obtained by using the fraction of load supported by mechanical fluid pressure distributions. Leakage is a direct result of the solution of either the "Reynolds equation model" or "3D CFD model". Using the solutions from the tribological and lubrication analysis, materials, and chemical information, and the temperature distribution, some assessment of the seal's materials behaviour can be made. Using the results of the deformation analysis, the structural integrity of the seal can be evaluated. Also using the results of the instability analysis, the stability of the seal can be evaluated.

In this study the lubrication analysis is considered by assuming a steady state condition. The dynamic analysis is not considered based on the assumption of the steady state condition. The face deformation analysis is also not considered but its effect on seal performance in terms of coning is included in the lubrication analysis model. Discussed in the subsequent sections are the Reynolds equation model, the 3D CFD model and the design approach used in this study.

3.3.1 Reynolds Equation Model

This model solves the 2-dimensional form of the Reynolds equation in the radial and circumferential directions. Leakage, radial pressure distributions as well as fluid load support are the main output from the model. The pressure distribution obtained serves as an input to any structural analysis package for the analysis of seal ring deflections. The assumptions considered in this model include: the flow is laminar, isothermal film temperature, fluid inertia is negligible in the radial and circumferential directions, and seal fluid is ideal gas and no angular misalignment hence dynamic analysis (squeeze film) is not considered.

3.3.1.1 Discretization

The finite difference discretization is not directly applied to the Reynolds equation (Equation (2.11) on page 28), rather, the mass flow rates for the radial and circumferential components are numerically integrated over the control area around each finite difference grid point (i, j) as shown in Figure 3.6. The perimeter of the control area extends halfway between the grid point and its four neighbouring points. The grid of points may go around the entire seal, or if periodic, it may be for one period only. The grid is for a constant meshing space.

The numerical solution is initiated by considering a flow balance on the control volume. The mass flows at the control volume boundaries are given in Equations (3.31)), (3.32)), (3.33)) and (3.34)) respectively.

$$\dot{m}_{\theta\ i-1/2,j} = \left(-\frac{\rho h^3}{12\mu r}\frac{\partial p}{\partial \theta} + \frac{\rho r \omega h}{2} \right)_{i-1/2,j} \Delta r \tag{3.31}$$

$$\dot{m}_{\theta\ i+1/2,j} = \left(-\frac{\rho h^3}{12\mu r}\frac{\partial p}{\partial \theta} + \frac{\rho r \omega h}{2} \right)_{i+1/2,j} \Delta r \tag{3.32}$$

$$\dot{m}_{r\ i,j-1/2} = \left(-\frac{\rho h^3}{12\mu}\frac{\partial p}{\partial r} r\Delta\theta \right)_{i,j-1/2} \tag{3.33}$$

$$\dot{m}_{r\ i,j+1/2} = \left(-\frac{\rho h^3}{12\mu}\frac{\partial p}{\partial r} r\Delta\theta \right)_{i,j+1/2} \tag{3.34}$$

The sum of these mass flows (Equations (3.31)), (3.32)), (3.33)) and (3.34))) must be equal

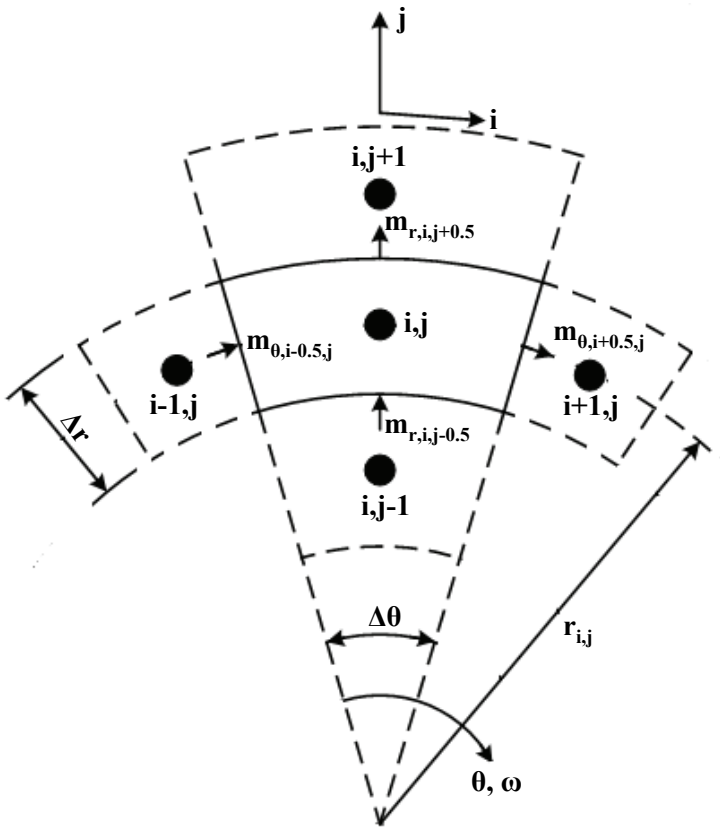

Figure 3.6 Finite-difference control volume used for the Reynolds equation model

to the time rate of change of the mass in the control volume as given in Equation (3.35).

$$\dot{m}_{\theta\ i-1/2,j} - \dot{m}_{\theta\ i+1/2,j} + \dot{m}_{r\ i,j-1/2} - \dot{m}_{r\ i,j+1/2} = \frac{\partial}{\partial t}\left(\rho h r \Delta r \Delta\theta\right)_{i,j} \tag{3.35}$$

In this model, the gas is assumed to be a perfect gas and isothermal ($\rho = \frac{p}{RT}$) and the squeeze film terms are negligible ($\frac{\partial h}{\partial t} = 0$) and Equation (3.35) can be represented as shown in Equation (3.36).

$$\begin{aligned}\left(-\frac{ph^3}{12\mu\, rRT}\frac{\partial p}{\partial\theta} + \frac{pr\omega h}{2RT}\right)_{i-1/2,j}\Delta r + \left(\frac{ph^3}{12\mu\, rRT}\frac{\partial p}{\partial\theta} + \frac{pr\omega h}{2RT}\right)_{i+1/2,j}\Delta r \\ -\left(\frac{ph^3}{12\mu RT}\frac{\partial p}{\partial r}r\right)_{i,j-1/2}\Delta\theta + \left(\frac{ph^3}{12\mu RT}\frac{\partial p}{\partial r}r\right)_{i,j+1/2}\Delta\theta - \left(\frac{\partial p}{\partial t}hr\right)_{i,j}\Delta r\Delta\theta = 0\end{aligned} \tag{3.36}$$

Equation (3.36) is a set of nonlinear algebraic equations and the nonlinear term is the pressure. This set of equations can only be solved by first linearizing the equation. One of the best methods of linearizing these equations is the Newton method. For the Newton method to be applied, it is best to start with a slightly different form of the Reynolds equation. Equation (3.31) is rewritten as shown in Equation (3.37).

$$\dot{m}_{\theta\ i-1/2,j} = \rho_{\theta\ i-1/2,j}\left[-\frac{h^3_{i-1/2,j}}{12\mu r_{i,j}}\frac{\partial p}{\partial \theta}\mid_{i-1/2,j} + \frac{r_{i,j}\omega h_{i-1/2,j}}{2}\right]\Delta r \tag{3.37}$$

Where the pressure gradient at the control volume edge is expressed in the conventional way as given in Equation (3.38).

$$\frac{\partial p}{\partial \theta}\mid_{i-1/2,j} = \frac{p_{i,j} - p_{i-1,j}}{\Delta\theta} \tag{3.38}$$

The film thickness (h) and the pressure gradient are evaluated at the control volume boundary, which is a point one-half way between nodes. The density at the control volume edge is taken as the average density or using the assumption that the fluid is a perfect and isothermal gas, the density becomes as shown in Equation (3.39).

$$\rho_{i-1/2,j} = \frac{\rho_{i-1,j} + \rho_{i,j}}{2} = \frac{p_{i-1,j} + p_{i,j}}{2RT} \tag{3.39}$$

Using Equations (3.38) and (3.39), Equation (3.37) yields Equation (3.40).

$$\dot{m}_{\theta\ i-1/2,j} = \frac{p_{i-1,j} + p_{i,j}}{2RT}\left[-\frac{h^3_{i-1/2,j}}{12\mu r_{i,j}}\left(\frac{p_{i,j} - p_{i-1,j}}{\Delta\theta}\right) + \frac{r_{i,j}\omega h_{i-1/2,j}}{2}\right]\Delta r \tag{3.40}$$

Similar equations can also be developed for mass flow at the other three sides of the control volume. With this method, the solution to steady-state under consideration can be obtained directly. It is also considered that the squeeze film effects are negligible. Since the flow is considered as a steady-state, there will not be pressure changes with time ($\frac{\partial p}{\partial t} = 0$). With these conditions the mass flow for each control volume has to sum up to zero as given in Equation (3.41).

$$\dot{m}_{\theta\ i-1/2,j} - \dot{m}_{\theta\ i+1/2,j} + \dot{m}_{r\ i,j-1/2} - \dot{m}_{r\ i,j+1/2} = 0 \tag{3.41}$$

Substitution of Equation (3.40) and similar equations for the other flows into Equation (3.41)

yields Equation (3.42)

$$\begin{aligned} F[p] = F_{i,j} &= 0 \\ &= \left(p_{i-1,j} + p_{i,j}\right)\left[a_{i-1/2,j}(p_{i,j} - p_{i-1,j})h^3_{i-1/2,j} + b_{i-1/2,j}h_{i-1/2,j}\right] \\ &\quad -(p_{i,j} + p_{i+1,j})[a_{i+1/2,j}(p_{i+1,j} - p_{i,j})h^3_{i+1/2,j} + b_{i+1/2,j}h_{i+1/2,j}] \\ &\quad +(p_{i,j-1} + p_{i,j})[a_{i,j-1/2}(p_{i,j} - p_{i,j-1/2})h^3_{i,j-1/2}] \\ &\quad -(p_{i,j} + p_{i,j+1})[a_{i,j+1/2}(p_{i,j+1} - p_{i,j})h^3_{i,j+1/2}] \end{aligned} \tag{3.42}$$

Where

$$a_{i-1/2,j} = a_{i+1/2,j} = -\frac{1}{2RT}\frac{1}{12\mu r_{i,j}}\frac{\Delta r}{\Delta\theta}$$

$$b_{i-1/2,j} = b_{i+1/2,j} = \left(\frac{1}{2RT}\frac{r_{i,j}\omega}{2}\right)\Delta r$$

$$a_{i,j-1/2} = -\frac{1}{2RT}\frac{1}{12\mu}\left(r_{i,j} - \frac{\Delta r}{2}\right)\frac{\Delta\theta}{\Delta r}$$

$$a_{i,j+1/2} = -\frac{1}{2RT}\frac{1}{12\mu}\left(r_{i,j} + \frac{\Delta r}{2}\right)\frac{\Delta\theta}{\Delta r}$$

3.3.1.2 Computational Domain

Only one sector, consisting of a pair of land, groove and hydrostatic dam is considered for the analysis. As a result of periodicity, the other sectors will have identical pressure distributions. The grids created by this model (shown in Figure 3.7) are of constant mesh spacing in the radial and circumferential coordinates. The grids spacing were computed using Equations (3.43) and (3.44).

$$\Delta r = \frac{r_o - r_i}{j_{max} - 1} \tag{3.43}$$

$$\Delta\theta = \frac{2\pi}{n(i_{max} - 1)} \tag{3.44}$$

In Equation (3.43), Δr represents the radial incremental change and j_{max} represents the maximum number of nodes in the radial direction. In Equation (3.44), $\Delta\theta$ is the circumferential incremental change, i_{max} represents the maximum number of nodes in the

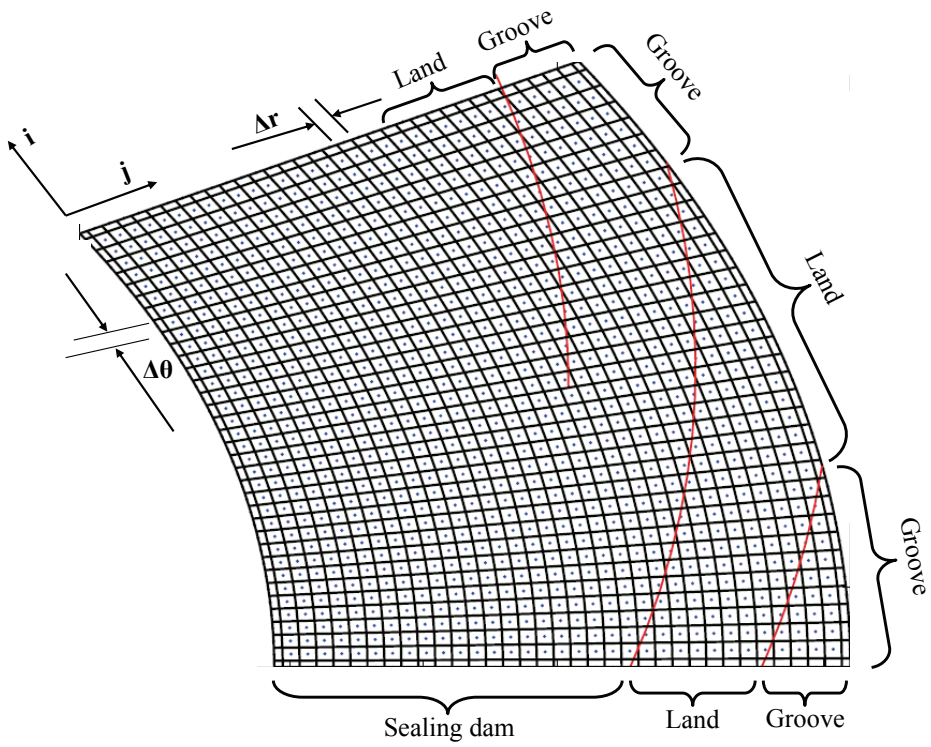

Figure 3.7 The grid layout used for the Reynolds equation model

circumferential direction and n is the number of grooves.

3.3.1.3 Boundary Conditions

In the numerical model, the operating conditions that are ascribed to the boundaries are: the sealed fluid temperature and pressure, the rotational speed of either the pump or compressor shaft and the sump pressure usually taken as the ambient pressure. The spiral angle of the grooves, groove-to-land width ratio, dam width, groove depth, sector angle, inner and outer seal ring diameters are taken as geometrical parameters and are taken into account when creating the grid. Given below are the possible boundary conditions. The rotational speed, sealed fluid temperature and the fluid film thickness are implemented directly into the discretized compressible Reynolds equation.

Pressure Inlet

For external pressurized:

$$p(\theta, r = r_o) = p_o$$

For inside pressurized:

$$p(\theta, r = r_i) = p_i$$

Pressure Outlet

For external pressurized:

$$p(\theta, r = r_i) = p_i$$

For inside pressurized:

$$p(\theta, r = r_o) = p_o$$

Periodic (Cyclic) Boundary Conditions

$$p(\Gamma) \mid_{AD} = p(\Gamma) \mid_{BC}$$

$$\vec{m}.\hat{n} \mid_{AD} = \vec{m}.\hat{n} \mid_{BC}$$

Where the two periodic boundaries of the sector are *AD* that corresponds to "Periodic Boundary - 2" and *BC* that corresponds to "Periodic Boundary - 1" as shown in Figure 3.8 respectively. The periodic boundaries simply mean that the normal mass flow rate per unit length out of boundary *AD* is equal to the normal mass flow rate per unit length into *BC* point by point.

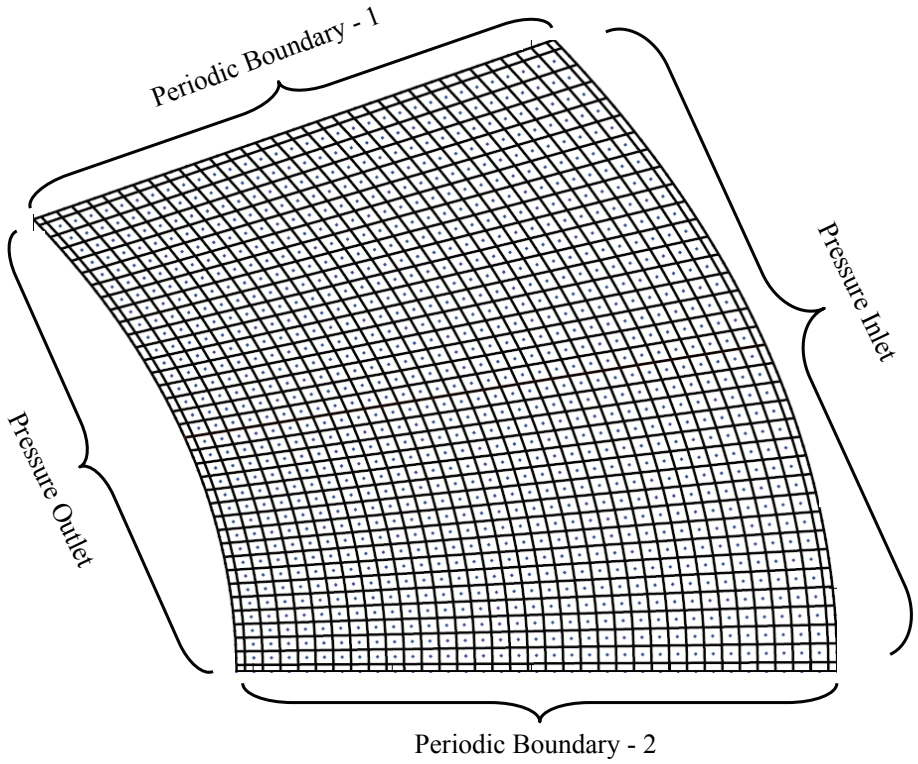

Figure 3.8 Boundary conditions used for the Reynolds equation model

3.3.1.4 Numerical Solution

Equation (3.42) represents an entire set of equations, one for each unknown pressure point in the grid. A solution to the problem of interest can only occur when a set of values of p causes all such equations to have a zero residual as shown in Equation (3.45).

$$F[p] = [0] \tag{3.45}$$

In order to find solution to these nonlinear equations, the Newton method is employed. It is observed that there maybe some set of value p^n that represents an estimate for the solution as shown in Equation (3.46)

$$F[p^n] \neq [0] \tag{3.46}$$

Using the Newton method approach, it can be shown that one can calculate a set of corrections Δp to the proceeding estimate using the matrix equation given in Equation (3.47) .

$$F'[p][\Delta p] = -F[p^n] \tag{3.47}$$

Equation (3.47) represents a set of simultaneous linear equations that can be solved for the pressure correction terms Δp. The new estimate of the solution is thus given in Equation (3.48).

$$[p^{n+1}] = [p^n] + [\Delta p] \tag{3.48}$$

The process of creating F' and solving Equation (3.47) and updating the estimate using Equation (3.48) is repeated until the condition of Equation (3.45) is approximated to the accuracy needed. This procedure is similar to the well known Newton method for solving for a root of a single nonlinear equation.

In order to derive an expression for F', Equation (3.42) is partially differentiated with respect to each pressure $p_{i,j}$ resulting in the partial differential equations as given in Equation (3.49). Examining Equation (3.42) will show that only five partial derivatives will exist since finite differencing scheme in 2-dimensions is adopted in this model. The five partial derivatives

are shown in Equations (3.50), (3.51), (3.52), (3.53) and (3.54) respectively.

$$[F'_{ij}] = \begin{bmatrix} \frac{\partial F_1}{\partial p_1} & \frac{\partial F_1}{\partial p_2} & \frac{\partial F_1}{\partial p_3} & \cdots \\ \frac{\partial F_2}{\partial p_1} & \frac{\partial F_2}{\partial p_2} & & \\ \frac{\partial F_3}{\partial p_1} & & & \\ \vdots & & & \end{bmatrix} = \begin{bmatrix} \ddots & \ddots & \ddots & \ddots & 0 \\ \ddots & \ddots & \ddots & \ddots & \ddots \\ \ddots & \ddots & \frac{\partial F_{ij}}{\partial p_{ij}} & \ddots & \ddots \\ \ddots & \ddots & \ddots & \ddots & \ddots \\ 0 & \ddots & \ddots & \ddots & \ddots \end{bmatrix} \tag{3.49}$$

$$\begin{aligned} \frac{\partial F_{i,j}}{\partial p_{i,j}} = {} & (p_{i-1,j}+p_{i,j})(a_{i-1/2,j}h^3_{i-1/2,j}) + [a_{i-1/2,j}(p_{i,j}-p_{i-1,j})h^3_{i-1/2,j} + b_{i-1/2,j}h_{i-1/2,j}] \\ & -(p_{i,j}+p_{i+1,j})(-a_{i+1/2,j}h^3_{i+1/2,j}) - [a_{i+1/2,j}(p_{i+1,j}-p_{i,j})h^3_{i+1/2,j} + b_{i+1/2,j}h_{i+1/2,j}] \\ & +(p_{i,j-1}+p_{i,j})(a_{i,j-1/2}h^3_{i,j-1/2}) + [a_{i,j-1/2}(p_{i,j}-p_{i,j-1/2})h^3_{i,j-1/2}] \\ & -(p_{i,j}+p_{i,j+1})(-a_{i,j+1/2}h^3_{i,j+1/2}) - [a_{i,j+1/2}(p_{i,j+1}-p_{i,j})h^3_{i,j+1/2}] \end{aligned} \tag{3.50}$$

$$\frac{\partial F_{i,j}}{\partial p_{i-1,j}} = -(p_{i-1,j}+p_{i,j})(a_{i-1/2,j}h^3_{i-1/2,j}) + [a_{i-1/2,j}(p_{i,j}-p_{i-1,j})h^3_{i-1/2,j} + b_{i-1/2,j}h_{i-1/2,j}] \tag{3.51}$$

$$\frac{\partial F_{i,j}}{\partial p_{i+1,j}} = -(p_{i,j}+p_{i+1,j})(a_{i+1/2,j}h^3_{i+1/2,j}) - [a_{i+1/2,j}(p_{i+1,j}-p_{i,j})h^3_{i+1/2,j} + b_{i+1/2,j}h_{i+1/2,j}] \tag{3.52}$$

$$\frac{\partial F_{i,j}}{\partial p_{i,j-1}} = -(p_{i,j-1}+p_{i,j})(a_{i,j-1/2}h^3_{i,j-1/2}) + [a_{i,j-1/2}(p_{i,j}-p_{i,j-1/2})h^3_{i,j-1/2}] \tag{3.53}$$

$$\frac{\partial F_{i,j}}{\partial p_{i,j+1}} = -(p_{i,j}+p_{i,j+1})(a_{i,j+1/2}h^3_{i,j+1/2}) - [a_{i,j+1/2}(p_{i,j+1}-p_{i,j})h^3_{i,j+1/2}] \tag{3.54}$$

It can be seen that all the derivatives in Equation (3.49) can be numerically evaluated using a current estimate of the pressure; the errors shown on the right-hand side of Equation (3.47) are given by Equation (3.42). The final form of Equation (3.47) takes on the matrix form

given in Equation (3.55).

$$\begin{bmatrix} \ddots & \ddots & \ddots & \ddots & 0 \\ \ddots & \ddots & \ddots & \ddots & \ddots \\ \ddots & \ddots & \frac{\partial F_{ij}}{\partial p_{ij}} & \ddots & \ddots \\ \ddots & \ddots & \ddots & \ddots & \ddots \\ 0 & \ddots & \ddots & \ddots & \ddots \end{bmatrix} \begin{bmatrix} \vdots \\ \vdots \\ \Delta p_{ij} \\ \vdots \\ \vdots \end{bmatrix} = \begin{bmatrix} \vdots \\ \vdots \\ -F_{ij} \\ \vdots \\ \vdots \end{bmatrix} \tag{3.55}$$

The coefficient matrix must be re-evaluated for each iteration since the values of the derivatives change with pressure. These sets of equations are solved with the Gaussian elimination method.

For a design purpose, it is assumed that one will choose a fluid film thickness, h_f as an assumed value and it must be chosen as a realistic height that includes one-half the average roughness height. At this height, the seal must operate in a condition where the seal faces do not touch one another from the imperfections resulting from radial and circumferential distortions and roughness. The procedures of obtaining solutions are shown in Figure 3.9.

The groove can take any profile set by the designers. The most popular profile used for designing seal faces is the spiral profile proposed by Muijderman (1967) and the equation for generating the spiral curves has been given in Equation (2.1) on page 19. As a result of the saw tooth nature of the pressure in the assumed derivation of the Reynolds equation for a spiral groove seal, the radius given in Equation (2.1) does not predict the actual seal leakage and the load support. To correct this effect, Muijderman (1967) gives a correction term that modifies the groove radius to achieve an effective groove radius, r_{eff} as given in Equation (3.56), here ω is the angular velocity of the rotating shaft, $\dot{m}$ is the seal leakage, a_2 is the groove width, a_1 is the land width, h_g is the grove depth, r_o is the seal ring outer radius, ρ is the gas density and k is the number of grooves.

$$r_{eff} = r_g \exp\left[-\frac{\pi}{2k}\left(1-\frac{\alpha}{90}\right)\tan\alpha\frac{2}{1+\gamma}\frac{1-H^3}{1+H^3}F_r\right] \tag{3.56}$$

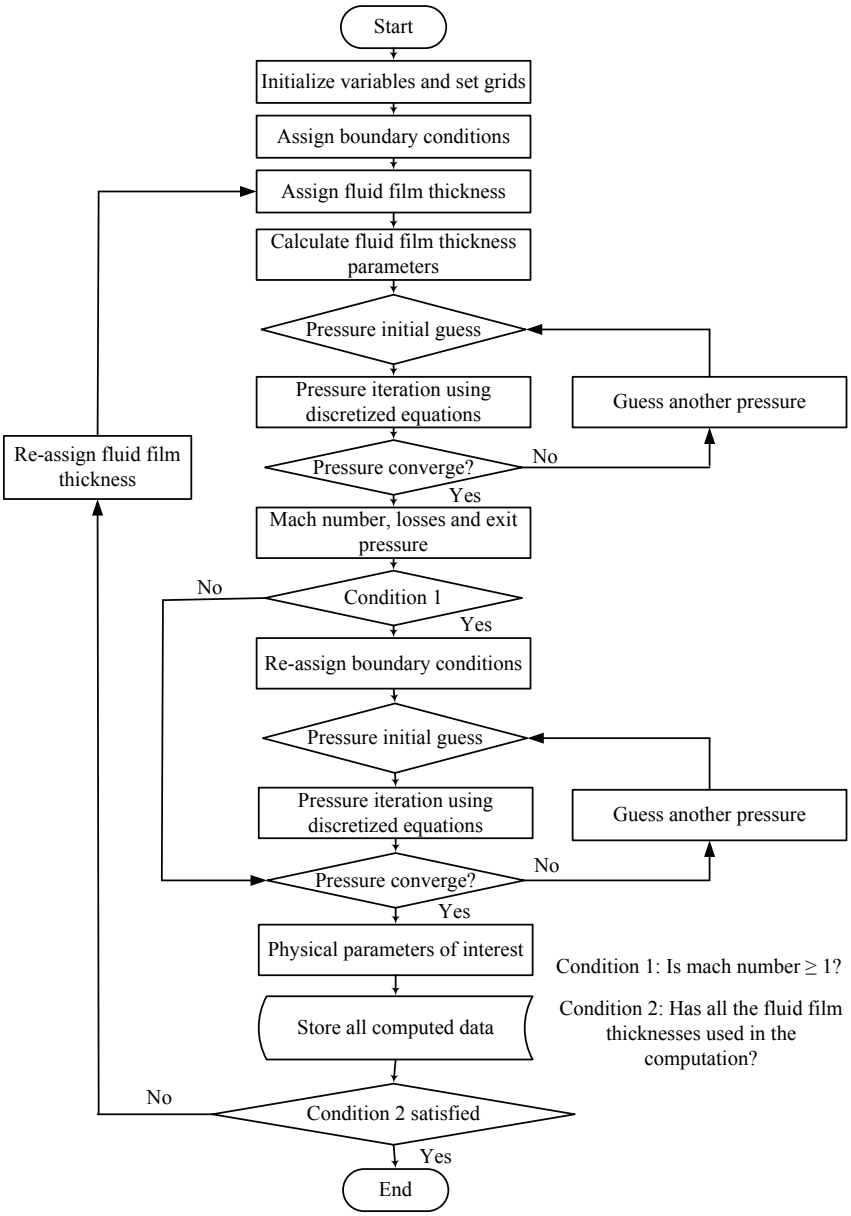

Figure 3.9 Flow chart of the Reynolds equation model

In Equation (3.56),

$$F_r = \frac{A_1 \cot\alpha}{A_1 \cot\alpha + C_1}$$

$$A_1 = -\gamma(1-H)\left(1+\gamma H^3\right) + S\gamma\cot\alpha\left(1-H^3\right)$$

$$C_1 = \gamma H^3 \cot\alpha(1+\gamma)(1-H) + S\left(\gamma + H^3 + H^3\cos^2\alpha(1+\gamma)\right)$$

$$S = \frac{-2\dot{m}(1+\gamma)}{r_o\omega(h_f+h_g)\rho 2\pi r_o} = \frac{-\dot{m}(1+\gamma)}{\pi r_o^2\omega(h_f+h_g)\rho(r_o)}$$

$$H = \frac{h_f}{h_f+h_g}$$

$$\gamma = \frac{a_2}{a_1}$$

The nominal fluid film thickness in the absence of surface roughness is defined in Equation (3.57). The first term on the right-hand side of Equation (3.57) represents the minimum fluid film thickness, the second term on the right hand side of Equation (3.57) represents the groove depth. The third term on the right-hand side of Equation (3.57) represents the face coning as a result of face deformation while the last term on the right hand side of Equation (3.57) represents the waviness. For the dam and land regions of the seal face, the groove depth is zero and if the faces are assumed parallel, the face coning will be zero. Also, if waviness is neglected, then the last term on the right hand side of Equation (3.57) reduces to zero.

$$h = h_f + h_g + (r - r_i)\tan\phi + h_n \cos(n\,\theta) \tag{3.57}$$

The total fluid film thickness H, when surface roughness is included, is defined in Equation (3.58). The first term on the right hand side of Equation (3.58) represents the nominal film thickness h while the second term on the right hand side of Equation (3.58) accounts for the random portion of the total film thickness h_s resulting from the effect of surface roughness.

$$H = h + h_s(\xi) \tag{3.58}$$

For the consideration of the surface roughness effects, the approach of Lebeck (1981) that modified the Reynolds equation in a dimensionless form (Equation (3.59)), by including the peak roughness amplitude, is adopted. The flow rates in the radial and circumferential directions with regards to the modification are given in Equations (3.60) and (3.61) respectively. The dimensionless forms are given by $\bar{r} = r/r_o$ is the dimensionless radial coordinate, $\bar{h} = h/\sigma$ is the dimensionless film thickness, $\bar{p} = (p\,\sigma^2)/(r_o^2\,\mu\,\omega)$ is the dimensionless fluid pressure, $\bar{H} = H/\sigma$ is the dimensionless total film thickness, $\bar{Q} = Q/(r_o^2\,\sigma\,\omega)$ is the dimensionless leakage, σ is the peak roughness amplitude and b is the fraction of area occupied by the fluid pressure.

$$\frac{1}{\bar{r}}\frac{\partial}{\partial\theta}\left(\rho\,E(\bar{H}^3)\,b\frac{\partial\bar{p}}{\partial\theta}\right) + \frac{\partial}{\partial\bar{r}}\left(\bar{r}\,\rho\,E(\bar{H}^3)\,b\frac{\partial\bar{p}}{\partial\bar{r}}\right) = 6\,\bar{r}\frac{\partial}{\partial\theta}\left(\rho\,E(\bar{H})\,b\right) \tag{3.59}$$

$$\bar{Q}_\theta = \left(-\frac{E(H^3)}{12\,\bar{r}}\,\frac{\partial\bar{p}}{\partial\theta} + \frac{\bar{r}E(\bar{H})}{2}\right) b \tag{3.60}$$

$$\bar{Q}_r = \left(-\frac{E(H^3)}{12}\,\frac{\partial\bar{p}}{\partial\bar{r}}\right) b \tag{3.61}$$

The expectancy operator $E()$ in Equations (3.59) to (3.61) is expressed as shown in Equation (3.62). The lower limit a of the integration in Equation (3.62) is expressed as $a = -\sigma$ when $h > \sigma$ and $a = -h$ when $h \leq \sigma$. Also in Equation (3.62), h_s is the random portion of the total film thickness while $f(h_s)$ is the roughness distribution function. In the event that the fluid film thickness is very much greater than the peak roughness amplitude ($h/\sigma \gg 3$), then the expectancy operator is defined as shown in Equation (3.63).

$$E() = \int_a^{\sigma} () f(h_s)\, dh_s \tag{3.62}$$

$$\begin{aligned} E(\bar{H}) &= \bar{h} \\ E(\bar{H}^3) &= \bar{h}^3 + \frac{\bar{h}}{3} \\ b &= 1.0 \end{aligned} \tag{3.63}$$

Also, when the fluid film thickness is less than or equal to the peak roughness amplitude, i.e., in the mixed-film lubrication regime, the expectancy operator is defined as shown in Equation (3.64).

$$\begin{aligned} E(\bar{H}) &= \frac{35}{32}\left[\frac{1}{8} + \frac{16}{35}\bar{h} + \frac{1}{2}\bar{h}^2 - \frac{1}{4}\bar{h}^4 + \frac{1}{10}\bar{h}^6 - \frac{1}{56}\bar{h}^8\right] \\ E(\bar{H}^3) &= \frac{35}{32}\left[\frac{1}{40} + \frac{16}{105}\bar{h} + \frac{3}{8}\bar{h}^2 + \frac{16}{35}\bar{h}^3 + \frac{1}{4}\bar{h}^4 - \frac{1}{20}\bar{h}^6 + \frac{3}{280}\bar{h}^8 - \frac{1}{840}\bar{h}^{10}\right] \\ b &= \frac{1}{32}\left[16 + 35\bar{h} - 35\bar{h}^3 + 21\bar{h}^5 - 5\bar{h}^7\right] \end{aligned} \tag{3.64}$$

The leakages at the seal outer and inner rings diameter are defined as expressed in Equations (3.65) and (3.66) respectively. The tangential fluid friction shear stress is defined in Equation (3.67).

$$\bar{Q}_i = \int_0^{2\pi} -\frac{E(\bar{H}^3)}{12} \left.\frac{\partial \bar{p}}{\partial \bar{r}}\right|_{\bar{r}_i} \bar{r}_i\, d\theta \tag{3.65}$$

$$\bar{Q}_o = \int_0^{2\pi} -\frac{E(\bar{H}^3)}{12} \left.\frac{\partial \bar{p}}{\partial \bar{r}}\right|_{\bar{r}_o} \bar{r}_o\, d\theta \tag{3.66}$$

$$\tau = \mu\, r\, \omega E\left(\frac{1}{H}\right) + \frac{1}{2r}\frac{\partial p}{\partial \theta} E(H) \tag{3.67}$$

An effective friction radius r_f that is based on the assumption that the friction shear stress

at the face is uniform is used instead of the mean radius. The effective friction radius is defined in Equation (3.68) and it gives a better approximation than using the mean radius. Equation (3.69) defined the total fluid friction force.

$$r_f = \frac{2}{3}\frac{\left(r_o^3 - r_i^3\right)}{\left(r_o^2 - r_i^2\right)} \tag{3.68}$$

$$\bar{F}_f = \frac{n}{\bar{r}_f}\iint \bar{r}^2 \left[\bar{r}E\left(\frac{1}{\bar{H}}\right) + \frac{1}{2\,\bar{r}}\frac{\partial \bar{p}}{\partial \theta}E(\bar{H})\right] b\,d\bar{r}\,d\theta \tag{3.69}$$

In order to evaluate the total fluid friction force as defined in Equation (3.69), two additional expectancy functions are required which are given in Equations (3.70) and (3.71) when $\bar{h} \leq 1$ and $\bar{h} > 1$ respectively.

$$E\left(\frac{1}{\bar{H}}\right) = \frac{35}{32}\left[\left(1-\bar{h}^2\right)^3 \ln\frac{\bar{h}+1}{\bar{\Delta}} - \frac{11}{12} + \frac{11}{5}\bar{h} + \frac{23}{4}\bar{h}^2 - \frac{8}{3}\bar{h}^3 - \frac{27}{4}\bar{h}^4 + \bar{h}^5 + \frac{147}{60}\bar{h}^6\right] \tag{3.70}$$

$$E\left(\frac{1}{\bar{H}}\right) = \frac{35}{32}\left[\left(1-\bar{h}^2\right)^3 \ln\frac{\bar{h}+1}{\bar{h}-1} + \frac{66}{15}\bar{h} - \frac{16}{3}\bar{h}^3 + 2\bar{h}^5\right] \tag{3.71}$$

The lower and upper limits for the expectancy integral in Equation (3.62), used for deriving Equation (3.69) are $-h+\Delta$ and σ respectively. Δ is a small nonzero positive number used for limiting the value of $E(1/H)$ so that viscous friction doesn't go to infinity as the film thickness tends to zero. A reasonable value for Δ is obtained by setting the maximum viscous shear stress equal to the shear strength of asperities (p_s). The dimensionless factor $\bar{\Delta}$ is defined in Equation (3.72).

$$\bar{\Delta} = \frac{1}{\bar{p}_s}\frac{\sigma}{r_o} \tag{3.72}$$

The hydrodynamic and asperity pressure distributions are both used in computing the dimensionless total load support $\bar{W}$ as expressed in Equation (3.73). The relationship between the dimensionless total load support and load support W is $\bar{W} = (W\,\sigma^2)/(r_o^4\,\omega\,\mu)$. In Equation (3.73), $\bar{p}$ is the dimensionless asperity pressure and defined as $\bar{p} = (p_m\,\sigma^2)/(r_o^2\,\omega\,\mu)$ and p_m is the asperity contact pressure that is equal to the compressive strength of the sealing face materials. $\bar{p}_s$ is the dimensionless shear strength defined as $\bar{p}_s = (p_s\,\sigma^2)/(r_o^2\,\omega\,\mu)$, h_n is the nth harmonic waviness and n is the number of the harmonic or number of waves around the seal face.

$$\bar{W} = \int_0^{2\pi}\int_{\bar{r}_i}^{\bar{r}_o} \left[\bar{p} - \bar{p}_m(1-b)\right]\bar{r}\,d\bar{r}\,d\theta \tag{3.73}$$

3.3.1.5 Capabilities of the Reynolds Equation Model and its Limitations

The different geometrical seal face profiles that can be modelled with this model are shown in Figure 3.10. A graphical user interface was developed with MATLAB to reduce the difficulties of entering the input and making plots. The source code is written in FORTRAN and run in MATLAB. A flow chart showing the various procedures of the source code is shown in Figure 3.9.

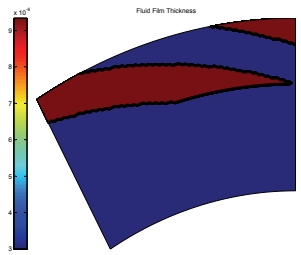

(a) spiral groove with a single dam located at ring inner diameter

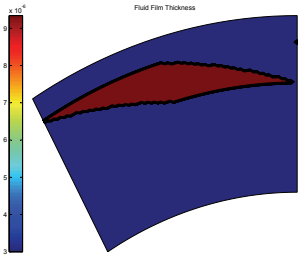

(b) spiral groove with two dams located at ring outer and inner diameters

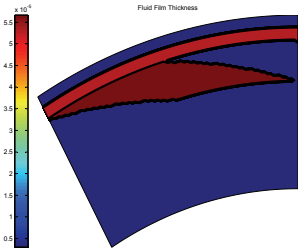

(c) spiral groove with two dams located at ring outer and inner diameters and with a rectangular recess

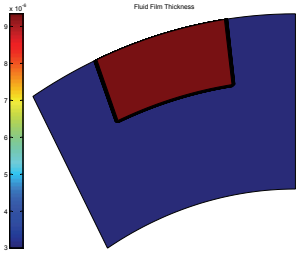

(d) radial groove with a single dam located at ring inner diameter

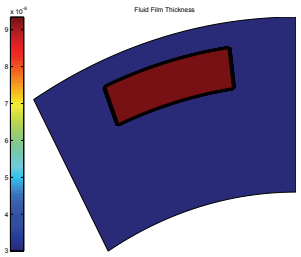

(e) radial groove with two dams located at ring outer and inner diameters

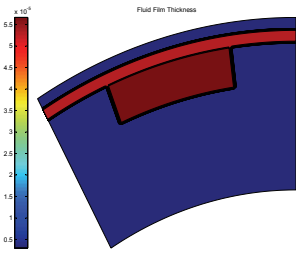

(f) radial groove with two dams located at ring outer and inner diameters and with a rectangular recess

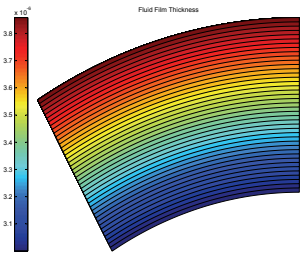

(g) plain seal with convergent radial taper

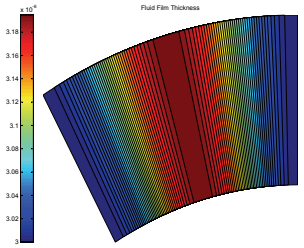

(h) plain seal with circumferential waves

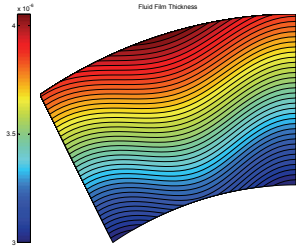

(i) plain seal with convergent radial taper and circumferential waves

Figure 3.10 Different seal face profiles incorporated in the Reynolds equation model

The effect of radial taper can be included in the model for geometrical seal profiles shown in Figure 3.10 (a), (b), (c), (d), (e) and (f) but if one decided to analyze seal rings that are parallel, then the value of the radial taper has to be set to zero. The effect of surface roughness can also be included when entering the input values in the model. The model

cannot handle the effects of inertia and turbulence in the flow since the Reynolds equation does not take such effects into account.

3.3.2 3D CFD Model

This model is 3-dimensional and solves the full compressible Navier-Stokes equations taken into account the effects of inertia and turbulence. The 3D CFD model can be used to model complex geometrical seal face profiles unlike the Reynolds equation, when used for complex geometrical seal face profiles, result in discontinuities in fluid film thickness across the groove to land regions. The 3D CFD model is time consuming with respect to computer usage time.

3.3.2.1 Solution Domain

Figure 3.11 shows a generic seal geometry which is a representative of spiral grooved face seal designs with sealed pressure at the outer diameter. The seal face can take the shape of any of the seal face profiles shown in Figure 1.2 on page 7. All seal face profiles employed the same working principles. The carbon-graphite seal ring (primary ring) is mounted on a metal retainer while the mating ring having the etched grooves is rigidly clamped to the shaft. The retainer may be bellows-mounted or have a multi-spring arrangement that provides the pre-start up axial closing force and flexible mounting. A pusher seal is used for effecting secondary sealing. Most of the seal geometrical details are not relevant to the CFD simulations. The solution domain corresponds to the wetted area indicated by the red lines in Figure 3.11(b) with the main characteristic dimensions for the solution domain listed in Table 3.1. For clarity, the solution domain is reproduced in Figure 3.12 as a three-dimensional view, with distances in the axial direction having been exaggerated significantly for clarity.

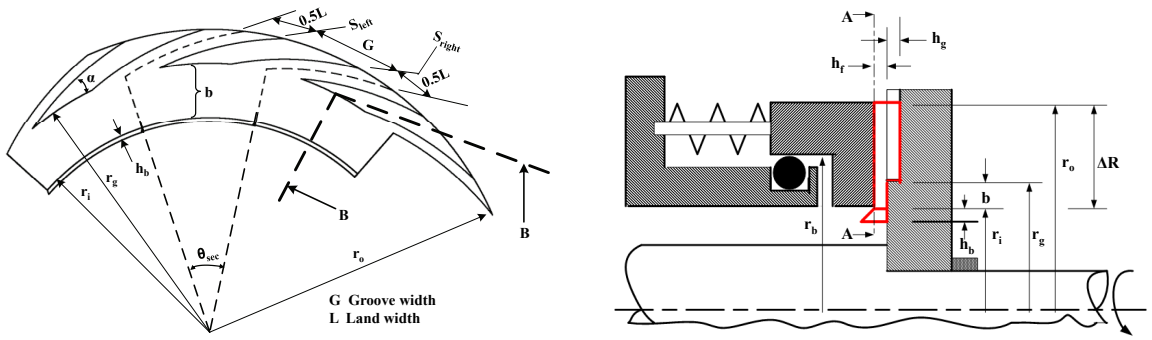

(a) Section "A-A" - Spiral groove

(b) Section "B-B"

Figure 3.11 Sectional views of the seal face geometry showing the extent of the computational domain

There are three categories of the geometrical parameters. These are the fixed, independent and the dependent parameters. The fixed parameters cannot be varied. They are dictated by either the compressor or pump manufacturers. The independent parameters can be varied in the optimization process while the dependent parameters rely on the values of the independent parameters.

Table 3.1 Categorization of Geometrical parameters

Geometrical Parameters	Type of Parameter
r_i	Fixed
r_o	Dependent
r_g	Dependent
a_g	Independent
$a_l = 1 - a_g$	Dependent
$\gamma = \frac{a_g}{a_l}$	Dependent
$s_{left} = \frac{a_l}{2}$	Dependent
$s_{right} = s_{left} + a_g$	Dependent
h_f	Independent
h_g	Independent
ΔR	Fixed
n_g	Independent
θ	Dependent
α	Independent
$b = r_g - r_i$	Independent
$h_b = 0.024\Delta R$	Dependent
ϕ	Fixed

The groove profile is defined by a logarithmic profile proposed by Muijderman (1967) as shown in Equation (2.1) on page 19. When $0^o < \alpha < 90^o$, the groove profile represents a spiral groove seal and when $\alpha = 90^o$, the groove profile represents a radial groove seal. The coning angle (radial taper) ϕ is also included in Table 3.1 in addition to the geometrical parameters to cater for modelling the effects of face deformation. The coning angle is defined in terms of the fluid film thickness (at the seal ring inner and outer diameters) and the seal face width. It is defined as shown in Equation (3.74).

$$\phi = \frac{h - h_i}{r - r_i} \tag{3.74}$$

A negative coning angle will indicate a divergent taper in the leakage flow path and a positive coning angle will indicate a convergent taper. Only a sector of the seal face is modelled as defined in Equation (3.75) in order to reduce the high aspect ratio associated with the seal

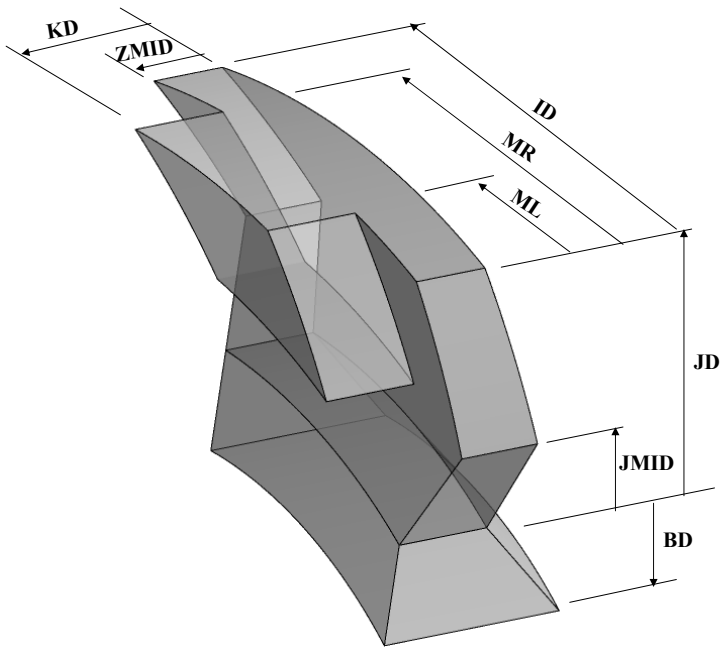

Figure 3.12 Computational domain with exaggerated fluid film thickness showing the meshing parameters

modelling as a result of very thin fluid film thickness in the order of microns.

$$\theta_{sec} = \frac{360^o}{n_g} \tag{3.75}$$

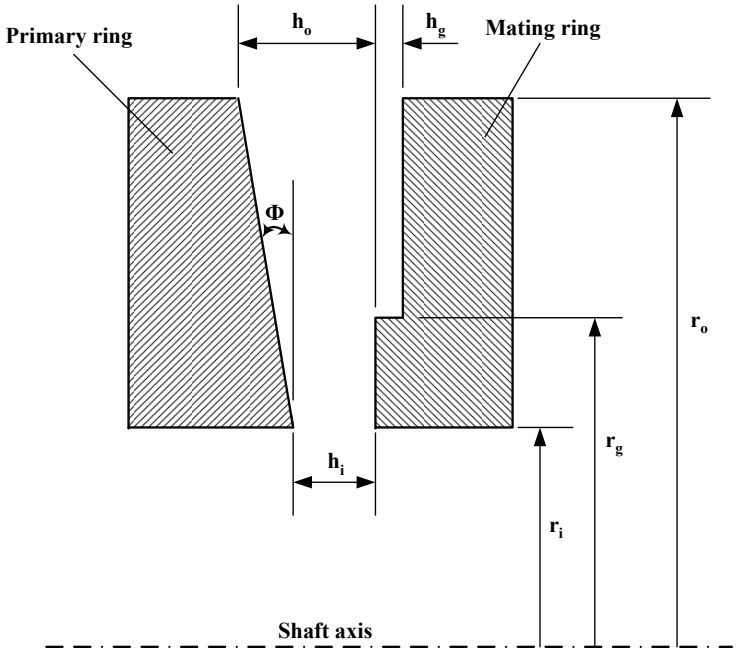

Figure 3.13 Flow between two narrowly spaced disks having radial convergent taper

3.3.2.2 Grid Generation

The computational domain was constructed with the grid generator software ANSYS Gambit (Gambit 2.3.16) with a user-specified subroutine. The user-specified subroutine is a Perl script that generates a journal file required by Gambit for generating the mesh. The geometrical parameters (Table 3.1) as well as geometrical seal face profile are specified in the user-specified subroutine. Also specified in the user-specified subroutine are the coning angle and meshing parameters (number and spacing of nodes along particular edges as given in Table 3.2). This avoids the need to spend effort constructing separate grids for each combination of geometrical and meshing parameter, and it is particularly useful in speeding up the model development phase in which suitable mesh density and grid spacing issues are explored. The user-specified subroutine also speeds up the optimization process when the design variables are varied.

In order to model the effects of choking, an additional block (referred to in this context as exit block) is attached to the seal ring inner diameter section of the main seal block. The exit block has a diverging geometrical profile so that the fluid flow will be sonic at the seal ring inner diameter to supersonic at the exit block discharge at atmospheric pressure. This is how the pressure jump at the seal ring inner diameter is handled. The Mach number of the fluid leaving the exit block may increase to about 4 depending on the value that the solver can handle. At the exit block, the seal pressure expands to atmospheric pressure and the expansion does not affect the seal's performance (Zuk, 1976). The exit block may have a face length of about 2.3 to 4.6% of the main seal face length depending on the available radial distance between the sealing shaft and the seal ring inner diameter.

Table 3.2 Meshing parameters

Meshing Parameters	Description
ID	Total number of grids in the circumferential direction
JD	Total number of grids in the radial direction
KD	Total number of grids in the axial direction
$ML = s_{left}.ID$	Number of grids at the beginning of groove width
$ML = s_{right}.ID$	Number of grids at the end of groove width
$JMID = \frac{b}{\Delta R}.JD$	Number of grids at the beginning of groove radius
$ZMID$	Number of grids at the beginning of groove depth
$BD = \frac{h_b}{\Delta R}.JD$	Number of grids on the height of the exit block

The computational domain is constructed as a topology of hexahedral blocks. In order to allocate a reasonable number of nodes in the axial direction while maintaining a reasonable mesh aspect ratio, large numbers of nodes were assigned to the radial and circumferential directions. Structured meshes are constructed with this method.

3.3.2.3 Boundary Conditions

A schematic drawing showing all the boundaries is presented in Figure 3.14. There are two walls (one rotating and the other stationary), two periodic boundaries for each of the main seal block and the exit block, an inlet specified on the main seal block, an outlet specified on the exit block and a fluid-fluid interface between the main seal block and exit block. The whole domain was set as rotating and assigned the value of the rotating shaft speed. The Reynolds number is computed analytically before specifying the boundary conditions using the formulas given in Equations (2.12), (2.13) and (2.15). If the computed Reynolds number is in the transition or fully turbulent regime, then a shear stress transport turbulence model (SST) with transition is chosen, otherwise, the flow is treated as a laminar flow.

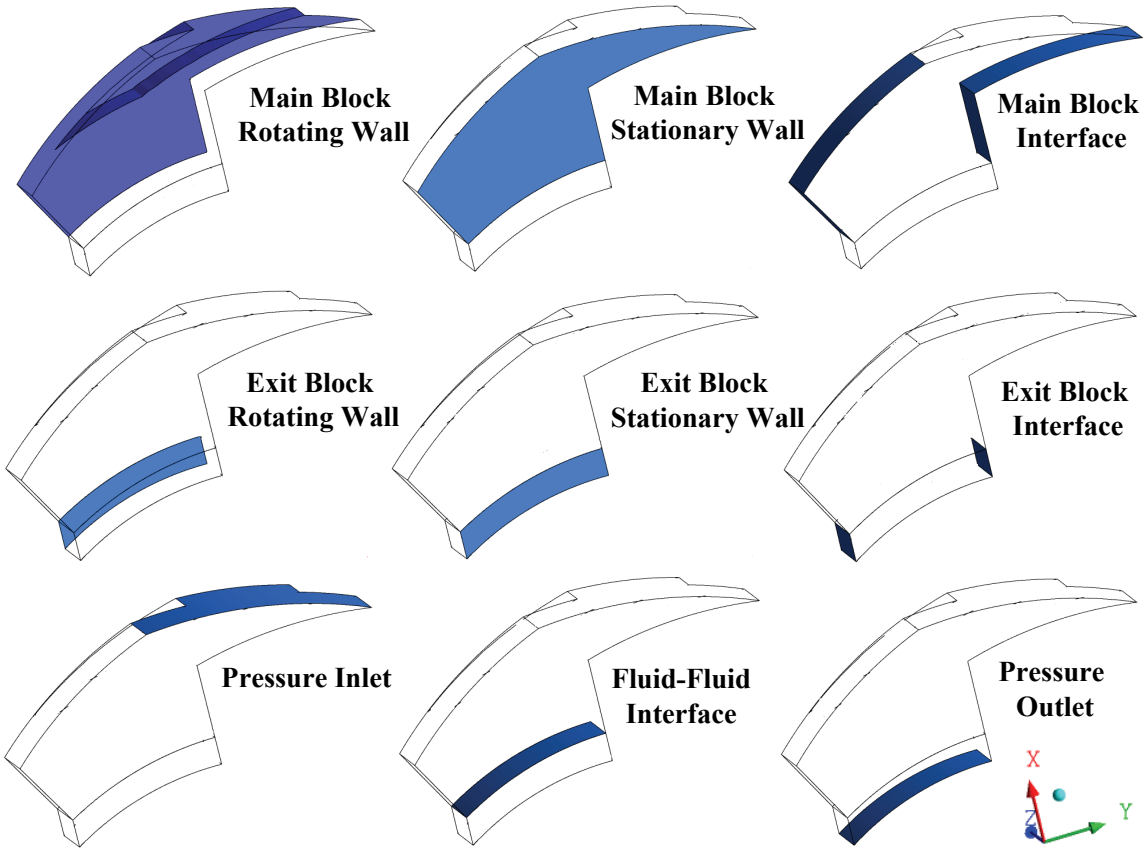

Figure 3.14 3D CFD model boundary conditions

The inlet is defined as pressure inlet and a total pressure corresponding to the sealed fluid pressure and having a direction normal to the Inlet boundary is assigned. A static

temperature corresponding to the sealed fluid temperature is also assigned to the inlet. If the flow is turbulent, then a 5% turbulence intensity is assigned to the inlet. An externally pressurized seal is considered in this study hence the fluid flow radially inwards. The sealed fluid pressure and temperature are defined as parametric inputs. The outlet is defined as pressure outlet and a static pressure corresponding to atmospheric pressure is assigned when the flow is subsonic (i.e. Mach number less than 1). While this assumption is as expected approximate, it provides a framework for the solutions and has no bearing on the simulation output which is concerned with relative, the pressure "deltas", rather than absolute values.

The appropriate tangential velocity (given by $r\omega$ at radius r) is assigned to the cell faces having the grooves. The angular velocity is derived from the shaft speed which is also assigned as a parametric input. The stationary cell faces (fixed wall) are fixed by setting the axial, radial and tangential velocities to zero. This is achieved in ANSYS CFX v11 by setting the fixed wall to "counter rotating wall". The no-slip condition and adiabatic walls are imposed on both walls. This is assigned to the main seal block and the exit block walls respectively. The periodic boundaries are the remaining two surfaces forming boundaries in the circumferential direction. They are set as rotational periodic boundaries for the main seal block so that the solution variables at corresponding cell faces at each boundary are forced to be equal.

3.3.2.4 Numerical Solutions

ANSYS CFX Solver (version 11) is used in these simulations. The Favre-averaged Navier-Stokes equations, which include the momentum, total energy and continuity equations are numerically integrated. The domain is considered as a rotating frame with constant angular velocity. The effects of rotations (Coriolis and centrifugal forces) are accounted for by adding these two forces to the momentum equations. In the energy equation, total enthalpy was replaced with rothalpy, to include the effects of rotation. Steady state computations were employed and ideal gas (i.e. air) was used throughout the simulations. Either laminar or turbulent conditions are considered depending on the Reynolds number obtained from the analytical calculation performed before setting the boundary conditions.

A residual target with rms value of 1×10^{-7} is used as the convergence criteria. A high resolution scheme was chosen in discretizing the Favre-averaged Navier-Stokes equations. In each simulation, 800 is used as the maximum number of iterations. After the 800 simulations is reached and it is observed that a good convergence is not attained, then the simulation can be re-run by taking a higher value of maximum number of iterations and the results already obtained are used as initial conditions.

Many of the cases studied involve, the same structure, with changes only in minor physical geometry and operating conditions. A representative value for the number of cells used is in the range of 3 million for one-twelfth sector of a seal face. A typical run took approximately 3 hours on a parallel modern compute end node, running on a 16 processors, and about 24 hours on a serial cluster grid running on a single processor.

3.3.2.5 Post Processing

A user-subroutine is used to output information of particular relevance in this study on completion of the final iteration. In particular, total mass flow is calculated across the pressure boundary at the inlet and the pressure boundary at the outlet, and multiplied by the number of grooves to give two measures of seal leakage, and hence a means of checking mass balance. Also the absolute pressure is integrated over each of the faces to obtain the axial force. The resulting axial force on the seal face is multiplied by the number of grooves to give seal opening force. The tangential force at each seal ring surface cell face is multiplied by the radial location of the cell centre and a cumulative sum formed to represent the torque.

3.3.3 Design Approach

1. Establish required operating conditions, suitable configuration, and generic seal ring material types.
2. Determine principal geometrical parameters and constraints and fix seal face parameters where possible. Determine limits for parameters to be varied in design optimization.
3. Carry out numerical simulation of the fluid flow in the seal interface by employing either the Reynolds equation model or 3D CFD model. Use the Reynolds equation model or 3D CFD model solutions with the optimization tool to be described in Chapter 5 for optimization of the seal geometry with respect to opening force and seal leakage.
4. With the optimized face design, for several identified combinations of operating speed and sealed fluid pressure, use 3D CFD model or Reynolds equation model to establish curves of opening force versus fluid film thickness, and curves of leakage versus fluid film thickness, and determine operating film thickness by obtaining a balance between calculated opening force and known closing force, determined by sealed pressure and balance ratio.
5. Use 3D CFD model or Reynolds equation model to calculate the leakage and power consumption at each operating condition and check the compatibility of the predicted

performance with the modelling assumptions and performance requirements. Refine design and/or modelling assumptions as necessary.

6. Use 3D CFD model or Reynolds equation model to determine the sensitivity of leakage and film thickness to film radial taper caused by seal face conning and reverse rotation rotation of sealing shaft.
7. Using finite element analysis (FEA), estimate impact of various thermal and mechanical factors (including seal face pressure distribution from Step 4 on seal face conning). Seal rings are designed in such a way that the net film taper is minimized.
8. From tribological tests, finalize selection of seal ring materials and with the use of finite element analysis, estimate the predicted net film taper at selected operating conditions.
9. Using the 3D CFD model or Reynolds equation model generated sensitivity analysis of Step 6, estimate seal performance at these operating conditions.
10. Validate design by seal testing.

The frame work covers Step 2 through Step 6, and Step 9 through Step 10. Step 1 is provided by the funding company, AESSEAL. Step 7 and Step 8 will be carried out by AESSEAL staff using the pressure distributions obtained from Step 4 as input to the FEA analyses.

3.4 Chapter Summary

The fundamentals of seal design as well as the research methodology adopted in this study have been presented. The fundamentals of seal design have been presented together with a description of the seal operating regimes, physics of compressible flow and concepts of choking, seal pressure-balancing and appropriate seal performance parameters. The research methodology employed two numerical models (a Reynolds equation formulation coded by the author and a commercial 3D CFD models) and design approach. The two numerical models assumed steady state conditions and air as the sealing fluid used in both models.

The seal operating regimes consist of boundary lubrication, mixed-film lubrication and full-film lubrication. In boundary lubrication, the asperities makes contact, in mixed-film lubrication, the film thickness is of the same order as surface roughness while in full-film lubrication, the film thickness is several times greater than surface roughness. The mixed-film and boundary lubrication regimes occurred in dry gas face seal at seal start-up and shut-down, while full-film lubrication regime is attained when the seal reached a steady state operating condition. Dry gas face seals are characterized with compressible flows as a result of local change in density in the fluid film. Choking occurs in dry gas face seal as

a consequence of static pressure drops through the seal interface face in order to overcome flow friction.

One of the main objectives in seal design is to ensure that the face loading is reasonably low that excessive leakage is avoided and high heat generation and high wear can be prevented by preserving an adequate clearance at all operating conditions. In order to achieve the optimum face loading, dry gas face seals are designed as pressure-balanced seals, having a balance ratio that is less than one. The balance ratio usually lies between 0.65 and 0.85. Seals with balance ratio around 0.85 have high face loading and are usually stable, less prone to blow open but likely to face contact. Seals with low balance ratio around 0.65 have low face loading and are prone to blow open and hydraulically unstable at higher pressures although have lower heat generation.

Dry gas face seal design can be represented as a system design problem that comprises lubrication theory, mechanical distortion, heat transfer and dynamics phenomena. These phenomena can best be analysed using lubrication analysis, face deformation analysis and instability analysis. The lubrication analysis covers the lubrication theory phenomenon; the face deformation covers the mechanical distortion and heat transfer phenomena while the instability analysis covers the dynamics phenomenon. The lubrication analysis solves for the fluid pressure distributions in the seal interface as well as leakage and other performance parameters (opening and closing forces, axial stiffness, design efficiency parameter and fluid film temperature rise). The face deformation analysis employs the finite element method in determining the pattern of distortion for a given set of loads. These distortions are formed from any imbalances in the moments on the seal rings about a circumferential axis and nonuniform temperature distributions in the seal faces. The instability analysis is carried out to ensure acceptable dynamic response to external excitations from sudden pressure changes, secondary O-rings movement, and shaft moving axially or shifting radially. These phenomena are interactive and they are all important in seal design. The solutions from the lubrication analysis serve as inputs to the face deformation and instability analyses and the results from the face deformation and instability analyses can be further used to improve the solution of the lubrication analysis. Thus, the phenomena in seal system design problems are interactive and they are all important. However the prediction of the lubrication phenomena is the starting point in the design of the seal and the determining factor in the performance of the device.

In seal design, the specification of the problem needs to be known a priori and an idea of the seal interface shape needs to be established. The specification comprises the given seal fluid environment, which include temperature and chemistry, as well as speed and pressure. It also includes the selection of materials, the secondary seals and other ancillary components. It

also contains all of the design selections and choices of the precise geometric definition and manufacturing process. The seal interface shape is the nominal gap between the seal faces. The seal interface shape is a function of the angular and radial positions of the seal. While some of the seal interface shapes (radial taper and waviness) develop during operation, the bulk of the seal interface shapes are intentionally machined on the seal faces to enhance the seal performance. Whatever the cause of the seal interface shape, if it can be defined at some operating condition, then it is possible to predict the seal performance at that regime. The very shape of the seal interface itself depends on the lubrication phenomenon that is dependent on the seal interface shape itself. Thus the seal system design problem is highly interactive. Therefore, the definition of the seal interface shape and the prediction of the seal performance based on the interface shape is a key step in the solution of the seal systems problem.

The Reynolds equation model account for the effects of surface roughness and face deformation (radial taper and waviness) but inherently neglects the effects of inertia and turbulence. It assumed isothermal condition, continuum flow and also considered choking and entrance loss effects. The Reynolds equation model is fast in terms of computer usage time but it is associated with problems of fluid film thickness discontinuities at the groove-land interface and groove-dam interface for the case of complex groove geometries. The 3D CFD model took account of the effects of choking, and inertia as well as turbulence. It is capable of handling complex geometries but it is computationally expensive as a result of the need to keep the mesh aspect ratio below a value of 200. The effect of waviness as a means of face deformation was not considered in this model.

Chapter 4

Application of Numerical Models and a Comparison with Experimental Data

4.1 Introduction

This chapter presents and discusses the results obtained with the numerical models presented in Chapter 3. The geometrical face profiles considered in this study comprise plain face seal, orifice controlled seal, spiral groove, radial groove, T-groove, double spiral groove and a novel seal. If not otherwise stated, the dimensions of the geometrical parameters considered in this study are the ones stated in Table 4.1. In order to examine effects of radial taper on seal performance, two cases were investigated. First of the cases considered the seal faces to be parallel i.e. no coning angle (zero radial taper) was utilised in constructing the computational domain. The second case used a coning angle, $0.0001\,rad$, in constructing the computational domain. In the second case, the seal faces are not parallel. The geometrical seal face profiles employed for the study of the radial taper effects on seal performance are plain face seal, spiral groove face seal and radial groove face seal. To investigate surface roughness effects on seal performance, a peak surface roughness amplitude, $0.1\,\mu m$ was used. The plain face seal and the Reynolds equation model were employed for examining the effects of surface roughness on seal performance.

Various operating conditions such as sealed fluid pressure, sealed fluid temperature, shaft rotating speed and fluid film thickness were varied. The ranges of operating conditions considered are: sealed fluid pressure from $1\,bar$ to $350\,bar$, rotating speed from $1\,rpm$ to $40000\,rpm$ and sealed fluid temperature from 23.9^oC to 400^oC. The fluid film thickness is considered as an operating condition and not as a set parameter of the seal. This is because when either the sealed fluid pressure, rotating speed or sealed fluid temperature are varied, the fluid film thickness also varies. The variation enables the calculation of the opening force as a function of the fluid film thickness for a particular operating condition and hence

Table 4.1 Generic seal geometrical parameters dimensions used for most of the analysis

Parameter	Description	Value
r_m	Seal mean radius	$65.2\,mm$
r_o	Seal outer radius	$76\,mm$
r_i	Seal inner radius	$54.4\,mm$
r_g	Seal groove radius	$67.75\,mm$
h_g	Groove depth	$6.5\,\mu m$
α	Groove angle	$15\,deg$
n_g	Number of grooves	12
γ	Groove-to-land width ratio	0.5
ϕ	Coning angle	$4.0728 \times 10^{-5}\,rad$

to evaluate the gas film stiffness. As a consequence of considering the fluid film thickness as operating condition, a number of meshes were created with different film thickness (ranging from $3 - 10\,\mu m$). These were employed in the simulations where the geometrical parameters of a given seal were maintained constant together with the appropriate operating conditions for each of the cases considered.

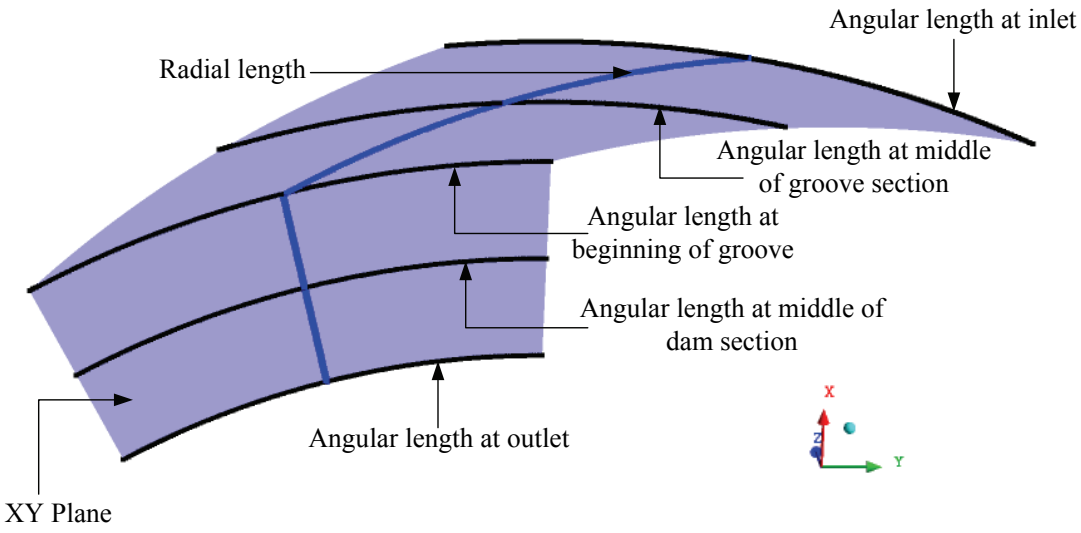

Figure 4.1 Radial and angular lengths passing through an XY plane at the middle of the fluid film thickness

Figure 4.1 shows the seal face radial and angular lines used for plotting the pressure distributions in this study. Both lines pass through an XY plane which is located at the middle of the fluid film thickness. The radial length is located at the centre of the angular length of the seal sector and the angular lengths are positioned at five different locations on

the XY plane. The five different locations are the seal outer diameter, middle of the groove section, beginning of the groove section which corresponds to the groove radius, middle of the dam section and the seal inner diameter.

Some of the results obtained from the numerical models were compared with test data obtained from AESSEAL plc, the sponsors of this research.

4.2 Comparison of Reynolds Equation Model with 3D CFD Model and Validation against Test Data

A spiral groove face seal with the dimensions of the geometrical parameters given in Table 4.1 was employed for this analysis. A balance ratio, 0.78, was used for balancing the seal. A spring force, $100N$ and atmospheric pressure at the seal ring inner diameter were used in Equation (3.7) on page 72 for computing the closing force.

Table 4.2 Comparison of numerical models results with experimental data

Case	Shaft Speed (rpm)	Gas Temperature (^oC)	Gas Pressure (bar)	Gas Leakage $(kg/s) \times 10^{-4}$			
				Experimental		Numerical	
				Non-drive end	Drive end	3D-CFD	2D Model
1	5052	23.9	36.52	5.367	5.428	5.542	9.324
2	10104	48.9	36.52	9.758	9.758	8.569	11.535
3	5052	23.9	31.52	N/A[1]	N/A	3.406	6.706
4	10104	48.9	31.52	N/A	N/A	6.458	8.666
5	40000	120.0	200.00	N/A	N/A	68.060	134.799

The experimental data and results obtained from the Reynolds equation and 3D CFD models for five flow conditions are presented in Table 4.2, Figures 4.2 and 4.3. The experimental data were obtained from test conducted at AESSEAL plc, Rotherham, UK. The dashed blue lines in Figure 4.2 a and c, and Figure 4.3 a, c, and e, are used in indicating the points where the opening force - fluid film thickness curve is equal to the seal closing force for a specified balance ratio ($B_r = 0.78$). The equilibrium fluid film thickness is the point where the opening force - fluid film thickness curve is equal to the closing force. Also, in Figure 4.2 b and d, and Figure 4.3 b, d, and f, the dashed blue lines indicate the points where the leakage - fluid film thickness curve is equal to the equilibrium fluid film thickness. The seal leakage is determined at the point where the leakage - fluid film thickness curve is equal to the equilibrium fluid film thickness. Some of the convergence plots of the numerical simulations employing the 3D CFD model for this analysis are shown in Figures A.1, A.2 and A.3 in Appendix A.

[1]Test data not available

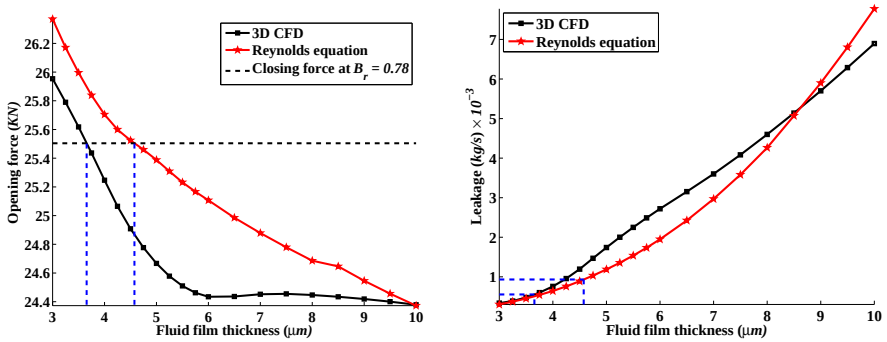

(a) Opening force for "Case 1"

(b) Seal leakage for "Case 1"

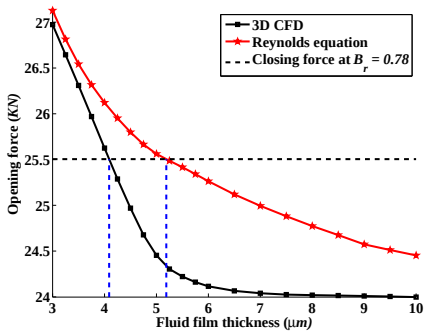

(c) Opening force for "Case 2"

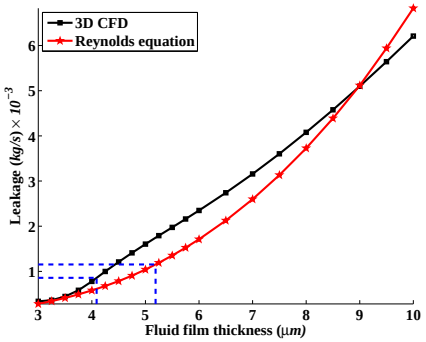

(d) Seal leakage for "Case 2"

Figure 4.2 Comparisons of results of 3D CFD model and Reynolds equation model at different operating conditions employing spiral groove gas face seal

The CFD model seal leakage prediction is about 3% more than the test data while the Reynolds equation model over predict the seal leakage with about 74% when compared with the test data for "case 1". The CFD model under predict the seal leakage with about 12% when compared with the test data while the Reynolds equation model over predict the seal leakage with about 18% when compared with the same test data for "case 2". The results show that the output of the 3D CFD model is closer to the test data than the predictions obtained with the Reynolds equation model.

The reason for the difference in results between the CFD model and Reynolds equation model is due to the assumptions made in the formulation of the Reynolds equation model. Also, the causes of the differences between the CFD model results and test data is that during seal operation, the seal faces are not parallel. Instabilities arising from sudden changes in pressure and speed as well as coning resulting from pressure and temperature variations in the seal faces are the main causes of seal faces not been parallel during seal operation. Although a coning angle of $4.0728 \times 10^{-5}\,rad$ was utilised for the effects of face deformation, the actual coning angle is unknown. This can be determined from a face deformation analysis employing Finite Element Analysis.

For cases 1 to 4, on both the opening forces (Figure 4.2, a and c, and Figure 4.3, a and c) and

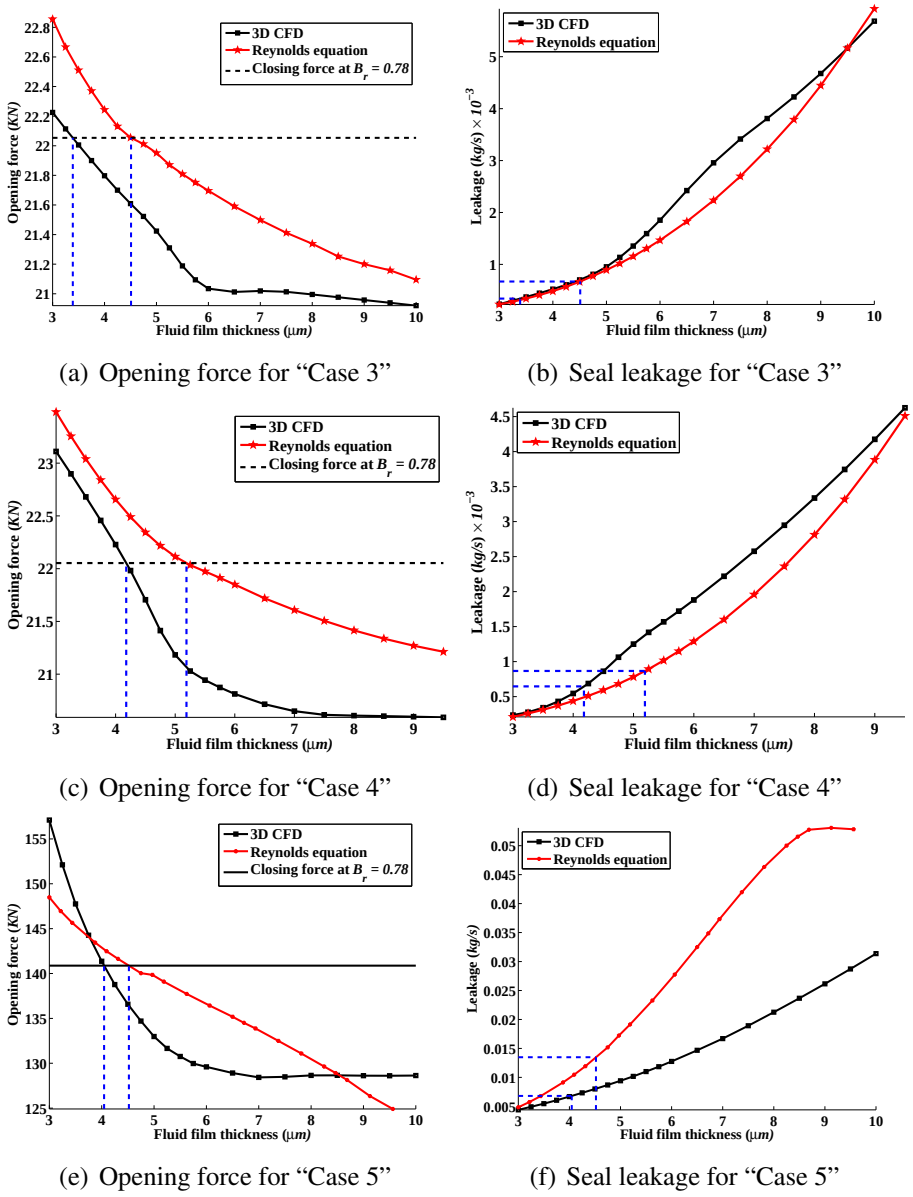

(a) Opening force for "Case 3"

(b) Seal leakage for "Case 3"

(c) Opening force for "Case 4"

(d) Seal leakage for "Case 4"

(e) Opening force for "Case 5"

(f) Seal leakage for "Case 5"

Figure 4.3 Comparisons of results of 3D CFD model and Reynolds equation model at different operating conditions employing spiral groove gas face seal - continuation

leakages (Figure 4.2, b and d), the Reynolds model predicts results that have similar trends to the CFD model predictions, the only difference being in the absolute values. However, for high operating condition (Figure 4.3, e and f) the results of the two models are markedly different.

Although the Reynolds equation model has a much faster run time when compared to CFD, it can only be used for approximate analysis provided the operating conditions, rpm and pressure, are low such that the effects of the convective and centrifugal inertias can be neglected. Accurate estimates of the seal performance therefore require a high fidelity model such as CFD to accurately estimate the fluid flow within the seal interface. The reduction in

the opening force with fluid thickness as seen in the CFD model (Figure 4.2, a and c, and Figure 4.3, a, c and e) by comparison to the corresponding Reynolds model cases, is as a result of the inclusion of the inertia terms.

4.3 Seal Pressure Balancing

Seals are always pressure balanced whereby a proper balance of the opening and closing forces must be achieved with a leakage gap that has a tolerable mass leakage. The gap must be small enough so that the leakage is minimal, but must be large enough so that power dissipation due to shear in the film, and face deformation, are tolerable. Thus the design of the sealing gap is especially vital to seal performance and therefore the pressure distribution in the gap and the mass leakage through the gap must be analyzed. In order to evaluate the gap size and thereby determine the mass leakage, a balance ratio must be chosen prior to the simulation and this will be used in computing the closing force (given in Eq. (3.7)) that will be balanced with the opening force obtained from integration of the pressure distribution over the seal face area.

Figure 4.4 shows the results of opening and closing forces as well as leakage as a function of fluid film thickness at operating conditions of sealed fluid pressure of $200\,bar$, rotating speed of $40000\,rpm$ and sealed fluid temperature of 120^oC. Figure 4.4(a) shows that the opening force greatly depends on the fluid film thickness and the geometrical parameters listed in Table 4.1. Several deductions can be made from Figure 4.4. The opening force decreases as the fluid film thickness increases. This is evidence that the seal possesses high gas film stiffness. In addition the leakage increases with increase in fluid film thickness.

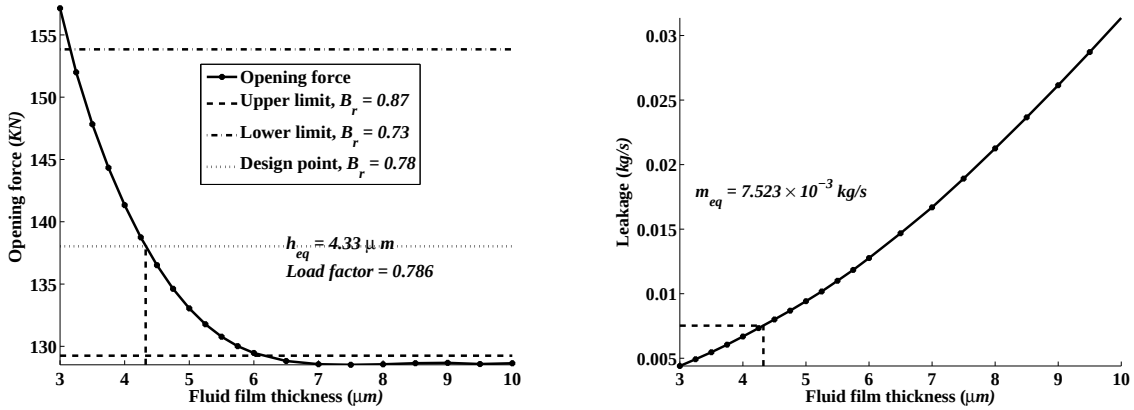

(a) Opening & Closing forces (b) Seal leakage

Figure 4.4 Seal performance characteristics as a function of fluid film thickness for pressure balancing using spiral groove gas face seal

From Figure 4.4(a), it shows that a seal may operate successfully within a range of operating

conditions and beyond the upper and lower limits of the balance ratios, the seal may either blow open when the balance ratio is below the lower limit or may contact when the balance ratio exceeds the upper limit. This is shown with the two dotted lines that cut across the force curve in Figure 4.4(a).

The seal can be balanced when the load factor is equal or almost equal to the design balance ratio. A balance ratio of 0.78 is chosen to balance this seal at a fluid film thickness of $4.33\,\mu m$ as shown in Figure 4.4(a) considered as the design point. The computed load factor is 0.786 which amounts to a percentage difference of 0.73% compared to the chosen balance ratio. Since the percentage difference is quite small, one could conclude that the estimated fluid film thickness is close enough in predicting the seal operation at the design balance ratio. When the seal is running with the design balance ratio and the operating conditions are within the range of the lower and upper limits, the seal may experience some instability while performing its function. Off-design operation of dry gas face seals is generally undesirable. It is not advisable to use a particular seal with a fixed geometric balance ratio for a wide range of operating conditions.

From the pressure plot shown in Figure 4.5, there is a strong evidence of hydrodynamic effects both in the radial and circumferential directions which is indicative that the seal has high gas film stiffness. The lower the fluid film thickness, the stronger the hydrodynamic effects resulting in the generation of a higher opening force. At the beginning of the spiral groove radius, as shown in Figure 4.5(a), there exists a marked pressure peak which is indicative of the presence of hydrodynamic effects. This fact is also in evidence when the pressure versus angular position is plotted, Figure 4.5(b).

If the results shown in Figure 4.5(a) are viewed independently, it can be observed that the pressure distributions are not in fact strictly linear. The linear observation is largely a function of the overall scale of the graph where the small changes in pressure at the inlet are insufficient to make the curve appear nonlinear. Similarly, the graph scale makes the inlet pressure appear constant but when the results are scrutinized separately, it can be seen that the values do differ. Again at the outlet, the values do differ and choked flow was observed on the $5.5\,\mu m$ and $10\,\mu m$ cases respectively.

4.4 Seal Performance as a Function of Varying Operating Conditions

4.4.1 Influence of Rotation Velocity

Figure 4.6 shows the behaviour of the opening force as well as leakage as function of fluid film thickness at operating conditions of sealed fluid pressure of $100\,bar$, fluid temperature

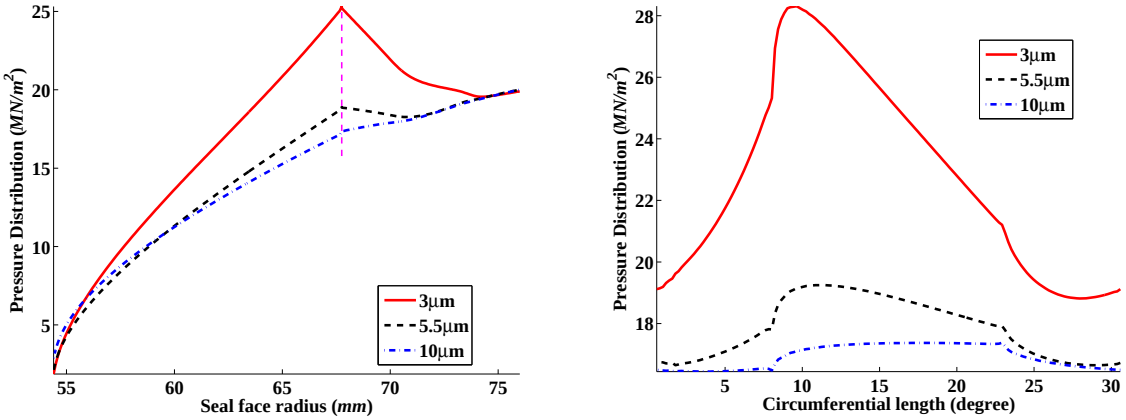

(a) Radial length (b) Angular length

Figure 4.5 Pressure distribution as a function of seal face length for pressure balancing using spiral groove gas face seal

of 120^oC and rotating speed ranging from $10000\,rpm$ to $40000\,rpm$. Figure 4.6(a) shows that the higher the rotating speed, the higher the gas film stiffness that will be achieved at the sealed fluid pressure. Also the equilibrium fluid film thickness increases with rotating speed at constant sealed pressure when the seal is balanced with a specific balance ratio (0.80 used in this analysis). Figure 4.6(b) in turn shows that the higher the speed, the more leakage that will result. It also shows that at moderate speed, say $10000\,rpm$, the gas film stiffness is quite low, as indicated by the gradient of the opening force curve, Figure 4.6(a). This implies that at this rotational speed the seal grooves will have a reduced impact on the seal performance in terms of hydrodynamic pressure generation as will be noticed by reference to Figure 4.7. This figure describes the variation in pressure in the domain as function of the radial distance with varying rotating velocity, Figure 4.7(a), and with angular position, Figure 4.7(b).

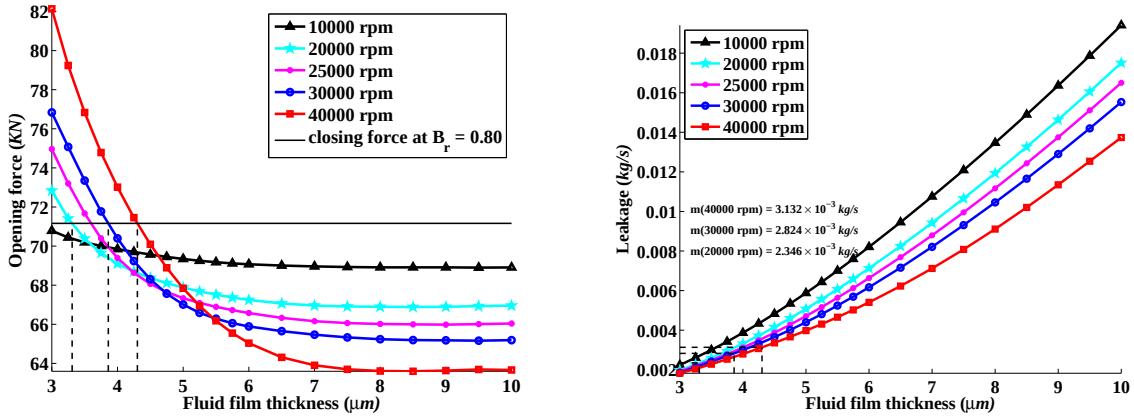

(a) Opening force (b) Seal leakage

Figure 4.6 Seal performance characteristics as a function of fluid film thickness operating at different speeds

All the cases described in this section are turbulent, and therefore the turbulence effects are modelled as are convective inertia phenomena and the choking condition. Therefore the variation observed in Figure 4.6 is due to the rotational term in the Navier-Stokes equations accounting for the centrifugal inertia, $\frac{\rho u_\theta^2}{r}$ and the significance effects of the hydrodynamic wedge. At high operating speed, the net flow may acquire a substantial swirling component.

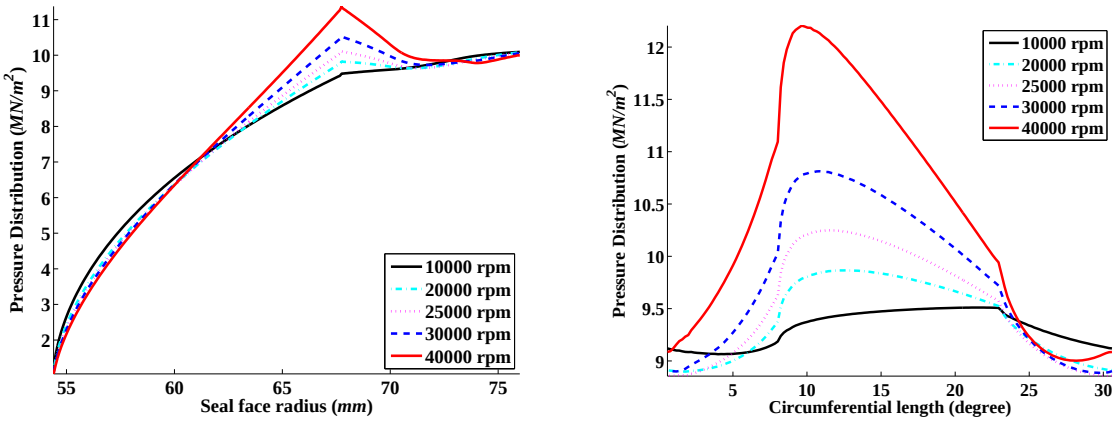

(a) Radial length at beginning of groove from seal ring inner diameter

(b) Angular length at beginning of groove from seal ring inner diameter

Figure 4.7 Pressure distribution as a function of seal face length operating at different speeds obtained at the centre of a fluid film thickness, 4 μm

4.4.2 Influence of Surrounding Fluid Pressure

Figure 4.8 shows the variation of opening force as well as leakage as a function of fluid film thickness when operating at a sealed fluid pressure ranging from 100 bar to 350 bar. The rotating speed is fixed at 20000 rpm while the fluid temperature is 120^oC. Figure 4.8(a) shows that the higher the sealed fluid pressure, the higher the closing and opening forces that will be produced.

The gas film stiffness does not depend on the sealed fluid pressure as can be clearly seen from Figure 4.8(a) as all cases have the same gradient. An analysis of Figure 4.8(b), shows that as the sealed fluid pressure increases the leakage is seen to rise. The pressure distributions for the different cases of sealed fluid pressure are shown in Figure 4.9. The results show that increasing the sealed fluid pressure does not affect the hydrodynamic pressure generated by the groove at what is a reasonable high rotating speed, 20000 rpm, Figure 4.9, both plots. The sealed fluid pressure provides the hydrostatic force that supports the bulk of the loads. Since all of the cases follow the same trend it is clear that the sealed fluid pressure only generates hydrostatic forces and not hydrodynamic forces.

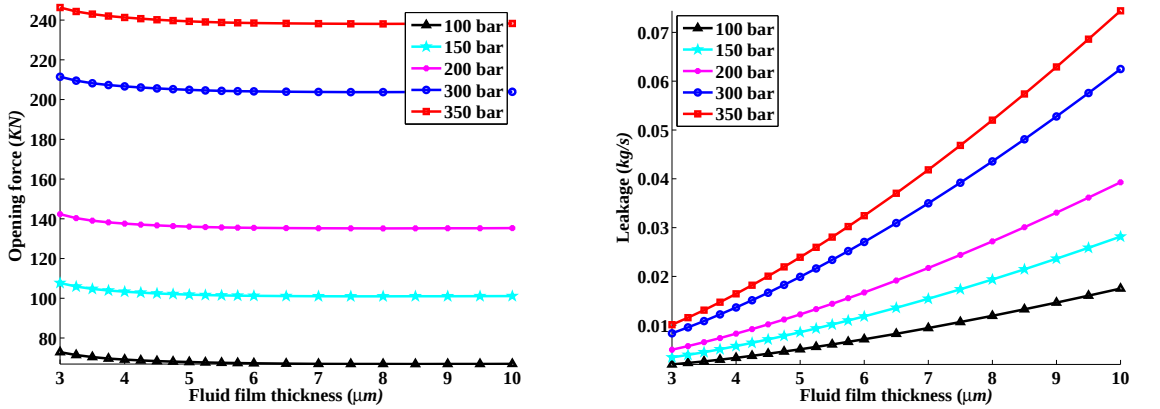

(a) Opening force

(b) Seal leakage

Figure 4.8 Seal performance characteristics as a function of fluid film thickness operating at different pressures

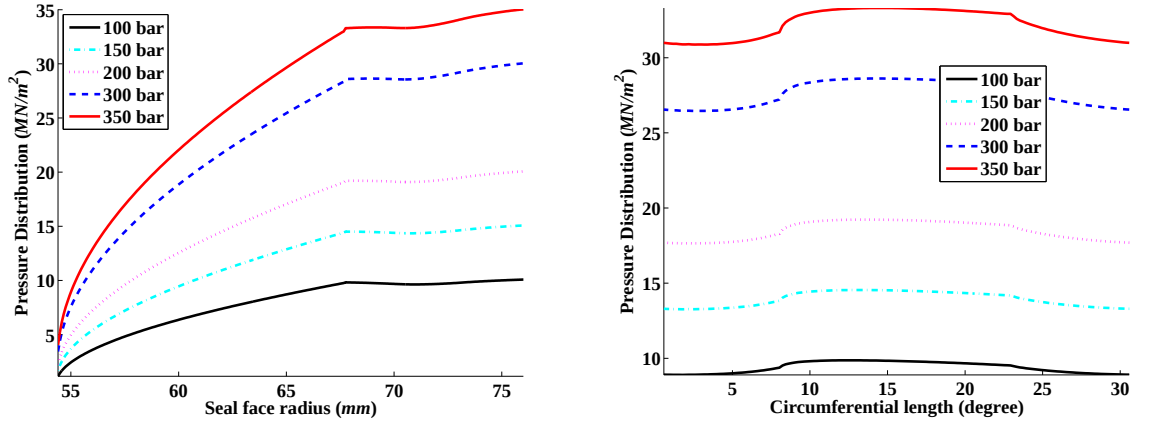

(a) Radial length at beginning of groove from seal ring inner diameter

(b) Angular length at beginning of groove from seal ring inner diameter

Figure 4.9 Pressure distribution as a function of seal face length operating at different pressures obtained at the centre of a fluid film thickness, 4 μm

4.4.3 Influence of Surrounding Fluid Temperature

Figure 4.10 shows the variation of the opening force as well as leakage as a function of fluid film thickness at operating conditions of sealed fluid temperature ranging from 120^oC to 400^oC and a sealed fluid pressure of $100\,bar$ and rotating speed of $20000\,rpm$. Below at a fluid film thickness of about $4\,\mu m$, Figure 4.10(a), the opening forces for all cases considered are essentially equivalent. Beyond this point, the higher the sealed fluid temperature, the less opening force is generated as shown in Figure 4.10(a). Also, for the leakage plotted in Figure 4.10(b), when the sealed fluid temperature increases a reduction in leakage is observed. As the gas temperature is raised, the velocity of the molecules increases which results in an increase in viscosity and hence a reduction in the leakage flow. This is accounted for by a Sutherland's law relationship within the CFD.

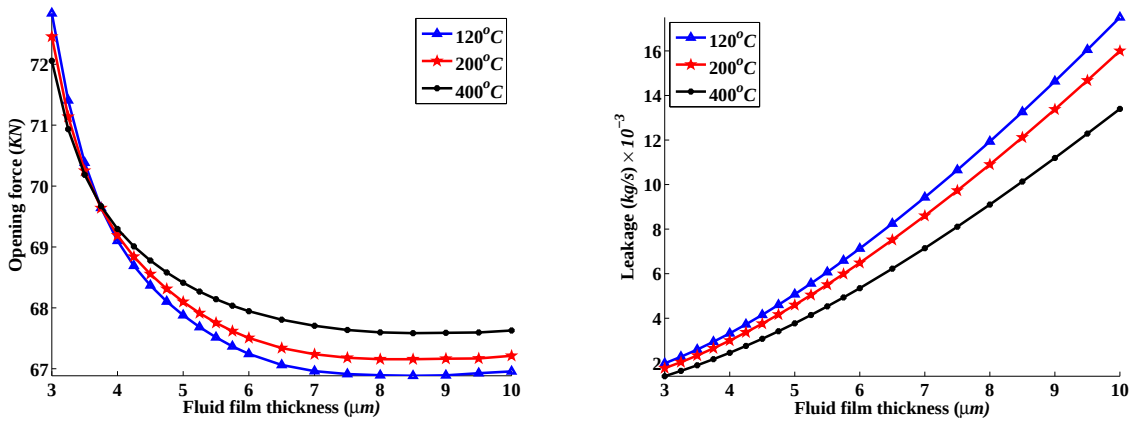

(a) Opening force

(b) Seal leakage

Figure 4.10 Seal performance characteristics as a function of fluid film thickness operating at different temperatures

An analysis of both plots in Figure 4.11 suggests that there is no variation of pressure distribution in the radial direction when the sealed temperature is varied, Figure 4.11(a), while in the circumferential direction, Figure 4.11(b), a slight variation of pressure distribution is observable. This shows that temperature variations in the circumferential direction of the seal interface can generate a certain amount of circumferential waviness that may be responsible for the generation of very small hydrodynamic force.

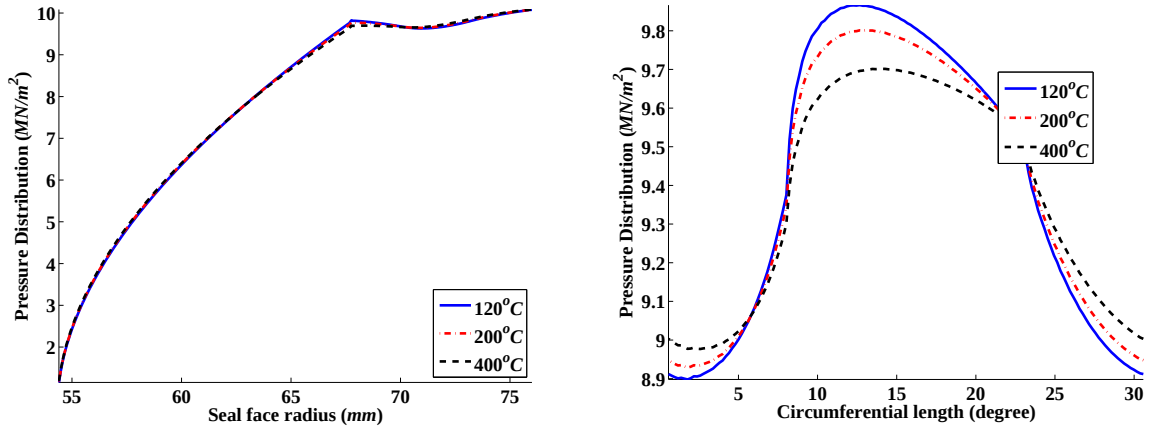

(a) Radial length at beginning of groove from seal ring inner diameter

(b) Angular length at beginning of groove from seal ring inner diameter

Figure 4.11 Pressure distribution as a function of seal face length operating at different temperatures obtained at the centre of a fluid film thickness, 4 μm

4.5 Evaluations of the Contributions of Hydrostatic and Hydrodynamic Forces to Seal Performance

In order to evaluate the contributions of the hydrostatic and hydrodynamic forces to the opening forces, three cases have been chosen for this analysis. The first case employed high pressure differential and a very low rotating speed. The sealed fluid pressure is $200\,bar$ and the rotating speed, $20\,rpm$. The second case considered a very low pressure differential and a high rotating speed whereby the sealed fluid pressure is $6\,bar$ and a rotating speed of $20000\,rpm$. The third case is a combination of high pressure differential and high rotating speed whereby the sealed fluid pressure is $200\,bar$ and the rotating speed $20000\,rpm$. The sealed fluid temperature used for all three cases was 120^oC. All cases used the dimensions of the geometrical parameters stated in Table 4.1. The 3D CFD model was employed for this analysis. The results obtained from this analysis are shown in Figure 4.12 for seal opening force (Figure 4.12(a) and (b)), seal leakage (Figure 4.12(c) and (d)) and design efficiency parameter (Figure 4.12(e) and (f)).

Selecting a fluid film thickness, $4\,\mu m$, for comparison purpose, the ratio of the reduced Couette Reynolds number to reduced Poiseuille Reynolds number is very much less than 1, about 2.02×10^{-5} for the high pressure and low rotating speed case. This shows that the flow is dominated by convective inertia terms and the effects of centrifugal inertia terms are negligible. The ratio of the reduced Couette Reynolds number to reduced Poiseuille Reynolds number was 51.21 and compressibility number, 135.09, for the low pressure and high rotating speed. For the high pressure and high rotating speed, the ratio of the reduced Couette Reynolds number to reduced Poiseuille Reynolds number was 24.35 and compressibility number, 4.03. For the low pressure and high rotating speed case, and high pressure and high speed case, the centrifugal inertia terms dominated the flow. For the low pressure and high rotating speed case, the flow was laminar for all fluid film thicknesses employed. In the high pressure and high rotating speed case, the flow was fully turbulent for all fluid film thicknesses examined. For the high pressure and low rotating speed case, transition to turbulence began when the fluid film thickness was $3.92\,\mu m$ and the flow was fully turbulent when the fluid film thickness was $5.27\,\mu m$.

From the results shown in Figure 4.12(a) and (b), the high pressure and low rotating speed case generated the highest opening force for all fluid film thickness considered. It was observed that as the rotating speed was increased, the opening force decreases and the leakage (Figure 4.12(d)) also decrease. Also the gradient of the opening force - fluid film thickness curve possesses a steeper gradient for the high speed and high rotating speed case, and low pressure and high rotating speed case than the high pressure and low rotating speed case. This is evidence that the centrifugal inertia terms acts to improve the hydrodynamic

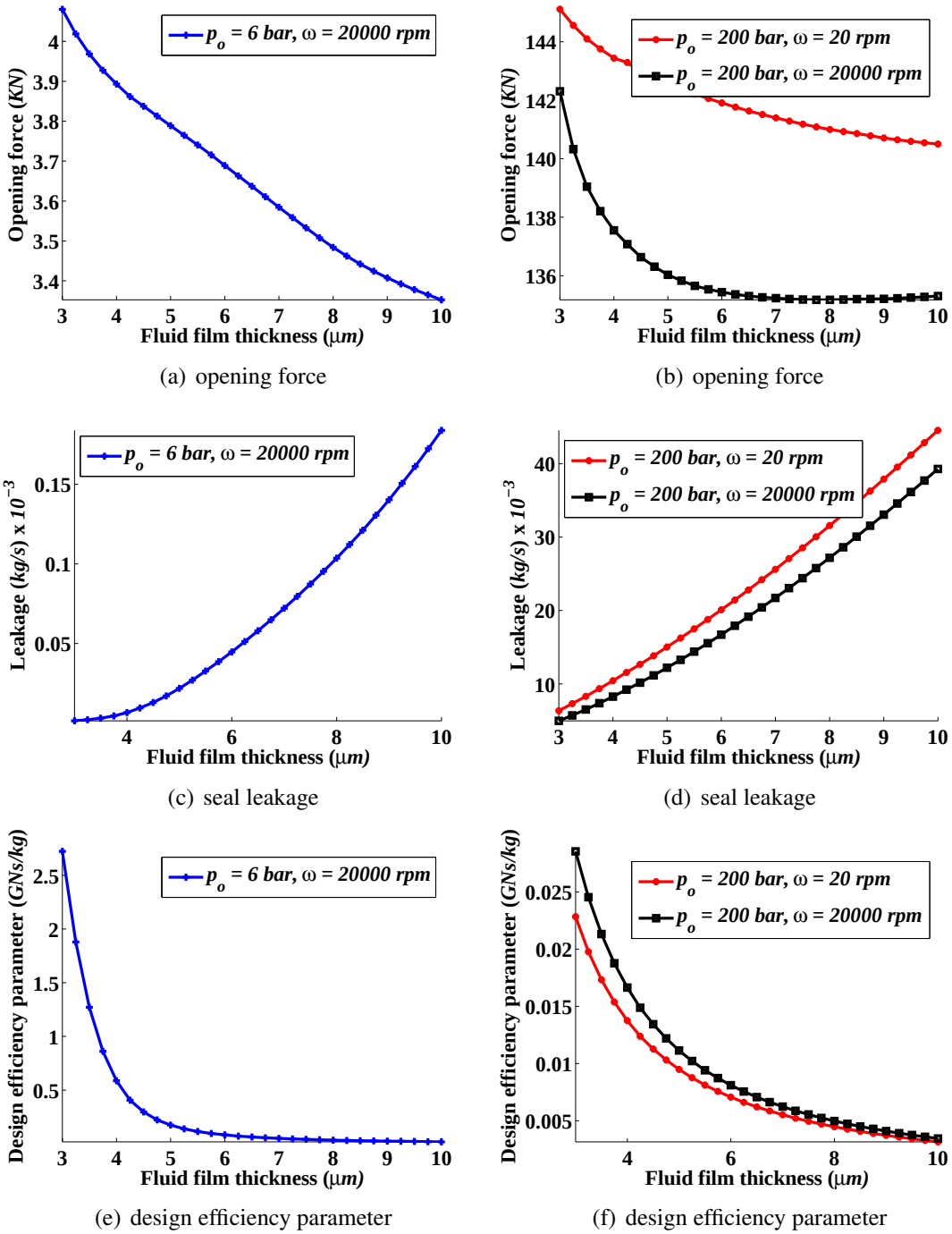

(a) opening force (b) opening force

(c) seal leakage (d) seal leakage

(e) design efficiency parameter (f) design efficiency parameter

Figure 4.12 Performance characteristics of a spiral groove seal operating at various combinations of sealed fluid pressure and rotating speed for the evaluations of the contributions of hydrostatic and hydrodynamic forces.

effectiveness of a seal at the expense of reducing the opening force. Also, the hydrodynamic load support is predominant at the low pressure and high rotating speed case so that the main consequence of increasing sealed fluid pressure is to increase the closing force on the floating face and consequently the film thickness diminishes with increasing pressure. Also, for the high pressure and low rotating speed case, the hydrostatic load support becomes

more significant so that the consequence of increasing sealed fluid pressure is to increase both the closing force and the opening force, leading to a minute variation in film thickness. The total closing force is supported by hydrostatic and hydrodynamic fluid pressures. For moderate to high pressure applications, the hydrostatic force component is predominant over the hydrodynamic force component.

The centrifugal effects play a significant role in seal performance at higher speeds. For an outside pressurized seal considered in this study, the regions of flow field may exist with radially inward flow along the stationary surface and outward along the rotating surface. Under certain circumstances, there can be net zero leakage if the pressure differential is very small. The existence of such a region is a direct consequence of centrifugal inertia effects. The resulting leakage component can be outward i.e. opposite to the direction of hydrostatic pressure drop) or inward i.e. in the same direction as the hydrostatic direction.

When the pressure-induced flows are small compared with the shear flow, the centrifugal terms dominate the flow as can be seen from the velocity contour plots shown in Figure A.22 in Appendix A. This will retard the flow thereby may produce instabilities in the seal operation, and if the shear flow is quite large may result in a significant amount of recirculation of flow leading to the fluid flow reversing its flow direction. When the pressure-induced flow is quite large compared with the shear flow, convective terms dominate the flow and enhance the seal stabilizing and increasing the opening force (Figure A.22 in Appendix A). The optimum operating condition of the seal is a balance between the pressure-induced flow and shear-induced flow whereby the negative effect of the centrifugal terms are canceled out by the positive effect of the convective terms.

In order to examine the temperature variations in the seal faces at different operating conditions, temperature contour plots were made from the CFD simulations at an XY planes at the middle of the fluid film thickness, $3\,\mu m$. Figure 4.13(a) and (b) show pressure and temperature contour plots of a low pressure differential and a high rotating speed case. Figure 4.13(c) and (d) also show pressure and temperature contour plots of a high pressure differential and a very low rotating speed case. Lastly, Figure 4.13(e) and (f) show pressure and temperature contour plots of a high pressure differential and high rotating speed case.

In the high pressure and low rotating speed case contour plots (Figure 4.13(d)), it can be seen that temperature only varies in the radial coordinate. There is no pronounced pressure variation for this case. For the cases of high pressure and high rotating speed (Figure 4.13(e) and (f)), and low pressure and high speed (Figure 4.13(a) and (b)), it can be clearly seen that pressure as well as temperature both varies in the radial and circumferential coordinates. The main causes of the temperature variation in both coordinates for the cases of high pressure and high rotating speed, and low pressure and high speed, is as a result of increase

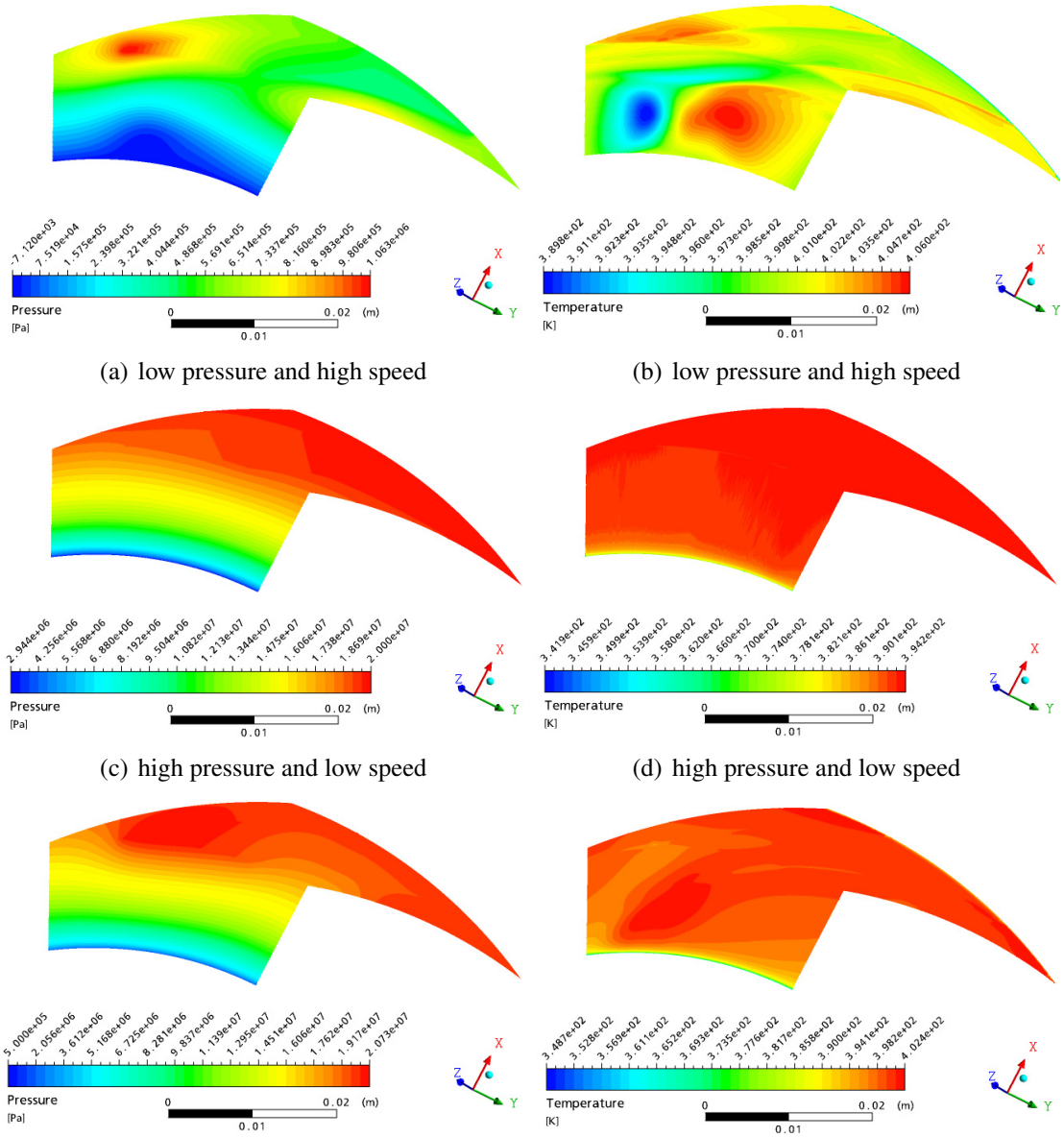

(a) low pressure and high speed

(b) low pressure and high speed

(c) high pressure and low speed

(d) high pressure and low speed

(e) combined high pressure and high speed

(f) combined high pressure and high speed

Figure 4.13 Pressure and temperature contour plots of a spiral groove seal operating at various combinations of sealed fluid pressure and rotating speed for the evaluations of the contributions of hydrostatic and hydrodynamic forces

compressibility number and centrifugal inertia terms dominating the flow.

The conclusions that can be made from the results presented in this section are the effects of convective and centrifugal inertia terms as well as compressibility effects significantly affect seal performance. The higher the ratio of the reduced Couette Reynolds number to reduced Poiseuille Reynolds number, the higher the compressibility number. When the convective inertia terms dominate the flow, the hydrodynamic effectiveness of a seal is reduced as seen from the pressure contour plots. The temperature only varies in the radial direction when

the flow is dominated by convective inertia terms and the isothermal flow condition can be made. For the case of high reduced Couette Reynolds number to reduced Poiseuille Reynolds number ratio, the temperature varies in the radial and circumferential coordinates and there is a significant pressure variation on both coordinates. This is an indication of improvements in terms of hydrodynamic effectiveness although at the expense of reduced opening force.

In order to determine the speed that will cause the seal to lift-off, the seal has to be pressurized only with spring load. That is the pressure at the outer and inner seal ring diameters are set to atmospheric. Also, to determine the pressure that will cause the seal to lift-off, the rotating speed is set to zero. In particular, one can evaluate at what speed the seal will completely lift-off. The other question is at what pressure the seal will completely lift-off at zero speed. These two parameters can give some idea of how well the seal might perform during start-up under certain operating conditions. The Reynolds equation model is employed for this analysis. The spiral groove face seal was used for this analysis and the dimensions of the geometrical parameters given in Table 4.1 were employed.

For the case of lift-off speed at a zero pressure differential, the rotating speed was varied from $5\,rpm$ to $230\,rpm$ while keeping the pressure at the seal ring inner and outer diameter at $1\,bar$ respectively. For the case of determination of the pressure required for the seal complete lift-off at a zero rotating speed, the pressure at the seal ring outer diameter was varied from $1.5\,bar$ to $20\,bar$ with $1\,bar$ assigned as the pressure at the seal ring inner diameter while a rotating speed of of $1\,rpm$ was considered. For both cases, the spring load corresponds to $100\,N$. A fixed fluid film thickness of $1\,\mu m$ was used for both cases. This value of fluid film thickness corresponds to a film thickness of a complete lift-off of a seal, which operates at full-film lubrication regime whereby $h/\sigma \gg 3$ assuming that the seal face material considered has a peak surface roughness amplitude that is not greater than $0.1\,\mu m$. The effects of face deformation resulting from coning and waviness were neglected for this analysis. The results obtained from this analysis for the opening force and closing force are shown in Figure 4.14 and for the leakage in Figure 4.15.

Figure 4.14(a) shows the results of the opening and closing forces for the case of varying the rotating speed at a zero pressure differential and Figure 4.14(b) corresponds to the opening and closing forces for the case of varying the sealed fluid pressure at $1\,rpm$ of rotating speed. The point at which the curves of the opening and closing forces as a function of either the rotating speed or sealed fluid pressure intersect corresponds to the complete lift-off of the seal. The lift-off speed corresponds to a value of $114.6\,rpm$ when the seal was only supported by the spring load and atmospheric pressure. The closing force is constant and does not depends on variation of the rotating speed (Figure 4.14(a)). The

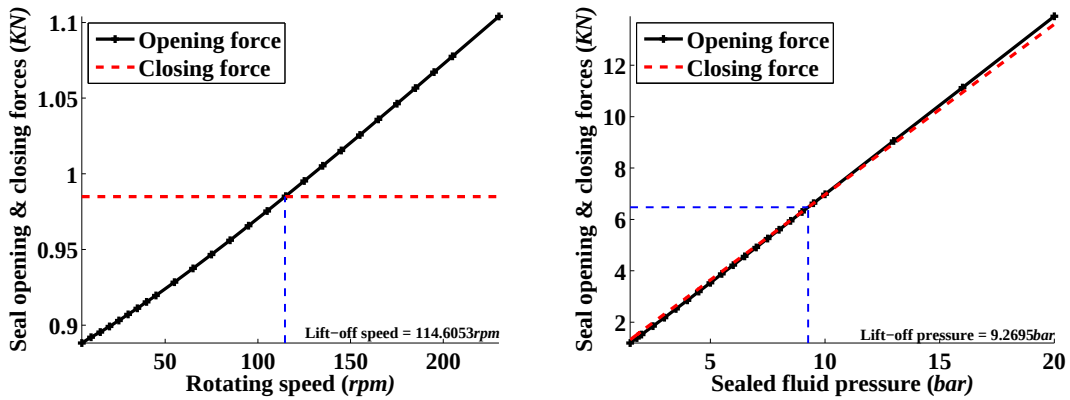

(a) Lift-off speed (b) Lift-off pressure

Figure 4.14 Lift-off speed and pressure at spiral groove seal start-up

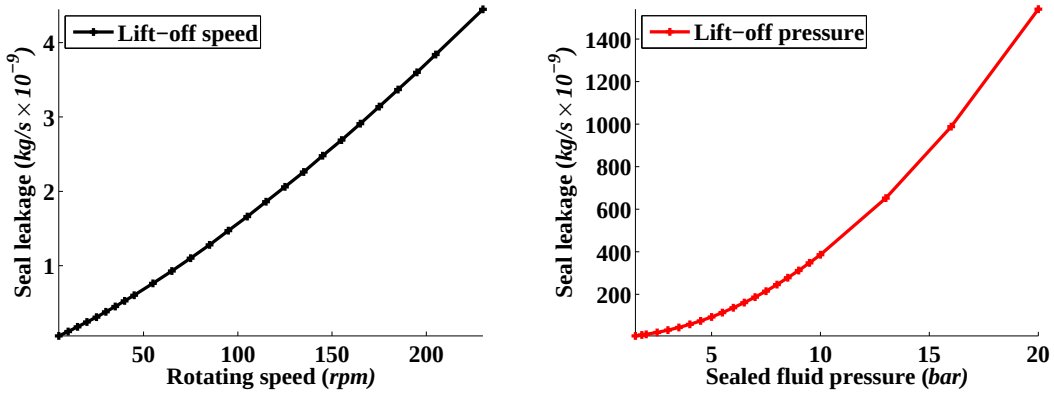

(a) Lift-off speed (b) Lift-off pressure

Figure 4.15 Seal leakage of a spiral groove seal as a function of increasing speed and pressure at seal start-up

sealed fluid pressure required for a complete lift-off of the seal corresponds to about 9.3 *bar* (Figure 4.14(b)). The closing force varies as the sealed fluid pressure is increased. Also, for both cases, the leakage increases as either the rotating speed or sealed fluid pressure is increased as shown in Figure 4.15(a) and (b) respectively.

4.6 Performance Comparison of Various Existing Geometrical Seal Face Profiles

A conventional face seal is a pressure balanced seal. The pressure drop occurs across a narrowly spaced sealing dam, and the force due to a pressure drop and the hydrodynamic force resulting from the relative tangential motion of the seal faces are balanced by a hydrostatic closing force and spring force. The different seal face profiles considered for this analysis include the plain face seal, orifice controlled seal, spiral groove, radial groove, T-groove and double spiral groove seal.

The operating conditions employed in this analysis consist of sealed fluid pressure of $6\,bar$, rotating speed of $10000\,rpm$ and sealed fluid temperature of 120^oC. The fluid film thickness considered ranges from $3\,\mu m$ to $10\,\mu m$. The dimensions of the geometrical parameters given in Table 4.1 were used for this analysis. There were some slight changes in the dimensions of the geometrical parameters for the T-groove seal and double spiral groove seal. The T-groove seal and the double spiral seal have two groove radii: the inner groove radius r_{g1} with a value of $64\,mm$ and the outer groove radius r_{g2} with a value of $68\,mm$. The T-groove seal has two groove widths: the inner groove width w_{g1} with a value of 65% of the total seal sector circumferential width and an outer groove width w_{g2} with a value of 35% of the total seal sector circumferential width. The grooves of the T-groove seal and radial groove face seal have an angle of 90^o. The double spiral seal has two groove widths: the inner groove width w_{g1} with a value of 50% of the total seal sector circumferential width and an outer groove width w_{g2} with a value of 35% of the total seal sector circumferential width. The double spiral groove seal has two groove angles: the inner groove angle α_1 with a value of 135^o and an outer groove angle α_2 with a value of 25^o. For the orifice controlled seal, the shape of the orifice is rectangular with side lengths of $1.08\,mm$ and the orifice is located at the groove radius given in Table 4.1. All the simulations carried out for this analysis assumed the faces to be parallel i.e., the radial taper in Table 4.1 is assigned a zero value. The geometrical face profiles of the T-groove seal and double spiral groove seal are shown in Figure 4.16 with the description of the geometrical parameters.

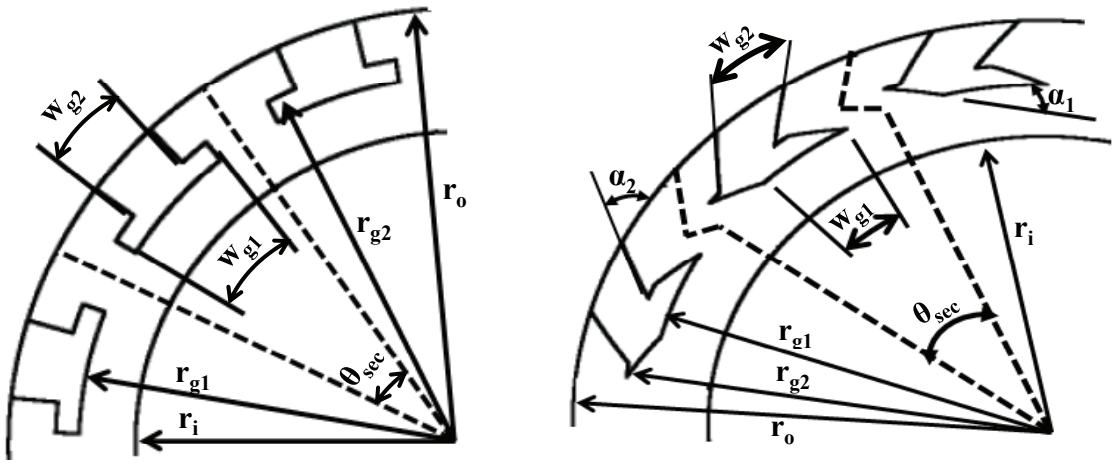

(a) T-groove

(b) Double spiral groove

Figure 4.16 Geometrical parameters descriptions of the T-groove and double spiral groove face seal profiles

The pressure contour plots for a plain face and orifice controlled seals are shown in Figure 4.17. It can be seen from Figure 4.17(a) for a plain face seal that the pressure variation is pronounced in the radial direction and fairly constant in the circumferential direction. This shows that plain face seal lack the ability to generate hydrodynamic force that can produce

positive axial film stiffness. In the case of the orifice controlled seal (Figure 4.17(b)), there is significant variation of pressure both in the radial and circumferential directions. A significant pressure variation in the radial and circumferential direction is an indication of pressure build-up in the seal interface that promotes the hydrodynamic effectiveness of a seal. A seal possesses a good hydrodynamic effectiveness is likely to produce positive axial film stiffness. The presence of a peak pressure in the seal interface is also an indication of pressure build-up in the seal interface.

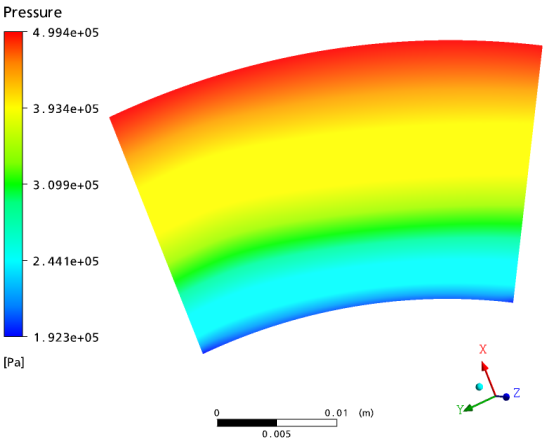

(a) Plain face seal pressure contour

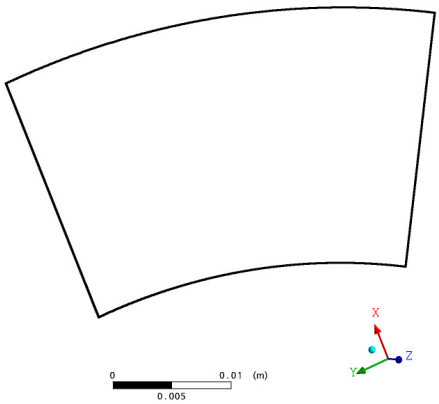

(c) Plain face seal geometry

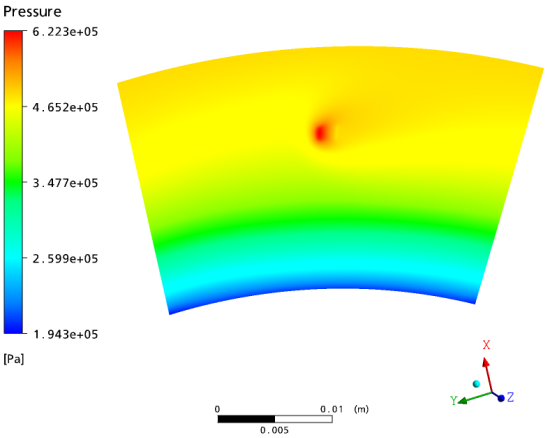

(b) Orifice controlled seal pressure contour

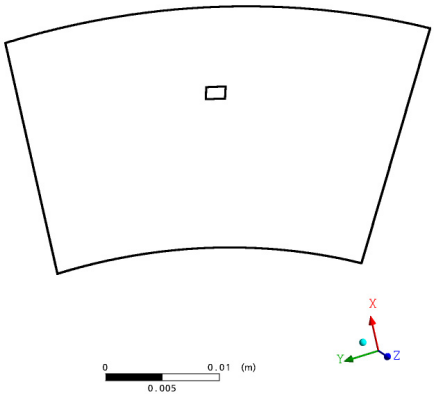

(d) Orifice controlled seal geometry

Figure 4.17 Pressure contour plots of plain face seal and orifice controlled seal operating at sealed fluid pressure of 6 bar, rotating speed of 10000 rpm and sealed fluid temperature of 120°C taken at an XY plane of fluid film thickness of 3 μm

Shown in Figure A.5 in Appendix A are plots of pressure distributions against the radial coordinate (Figure A.5(a)) and also against the circumferential coordinate (Figure A.5(b), (c), and (d)) for the plain face and orifice controlled seals. For the plain face case, there is no peak pressure in the radial direction; the pressure distributions curve is parabolic. Also, there are no peak pressures in the circumferential direction but very little variations

of pressures in the circumferential variation. These variations of pressure result from the compressibility effects of the sealing fluid medium. In the case of the orifice controlled seal, there is a large peak pressure in the radial coordinate. There is also a large peak pressure in the circumferential direction at the orifice radius. The peak pressure occurred at the location of the orifice slot.

The temperature and velocity contour plots as well as velocity vector plots for the plain face and orifice controlled seals are shown in Figures A.23, A.26 and A.29, respectively in Appendix A.

The results obtained for the plain face seal and orifice controlled seal are shown in Figure 4.18. For the plain face seal, there are regions of negative film stiffness as well as regions of zero film stiffness as can be seen in Figure 4.18(d). Although the classical theory states that the opening force is not dependent on the fluid film thickness, the results obtained for the plain face seal show that the opening force is dependent on the fluid film thickness at small values of fluid film thickness to about $6\,\mu m$. The variations in the results obtained for the plain face seal and the classical theory is as results of the inertia terms neglected in the classical theory which employs the Reynolds equation in its analysis. The opening force increases with the fluid film thickness up to about a fluid film thickness of $6\,\mu m$ and thereafter remains constant with increasing fluid film thickness for the plain face seal (Figure 4.18(a)). As in the case of the opening force for the plain face case, the axial film stiffness is negative up to about fluid film thickness of $6\,\mu m$ and thereafter has zero stiffness. The design efficiency parameter and power consumption of the plain face seal decreases with increasing the fluid film thickness as can be seen in Figure 4.18(c) and (e) respectively. The leakage increases with the fluid film thickness. Unlike the cubic dependence rate of the leakage on the fluid film thickness, the power dependence of the leakage rate on the fluid film thickness is about 1.0123.

Considering a fluid film thickness of $4\,\mu m$ for the purpose of results comparisons, the following can be deduced for the performance parameters of the plain face seal and orifice controlled seal shown in Figure 4.18.

- The orifice controlled seal generated the highest opening force with a value of $3.59\,KN$ and the lowest was computed for the plain face seal with an opening force of $3.32\,KN$.
- The plain face seal generated the lowest leakage with a value of $0.0060 \times 10^{-3}\,kg/s$ and the orifice controlled seal the highest leakage, $0.0082 \times 10^{-3}\,kg/s$.
- The plain face seal generated the highest design efficiency parameter with a value of $0.5502\,GNs/kg$ and the lowest was due to the orifice controlled seal with an opening force of $0.4355\,GNs/kg$.

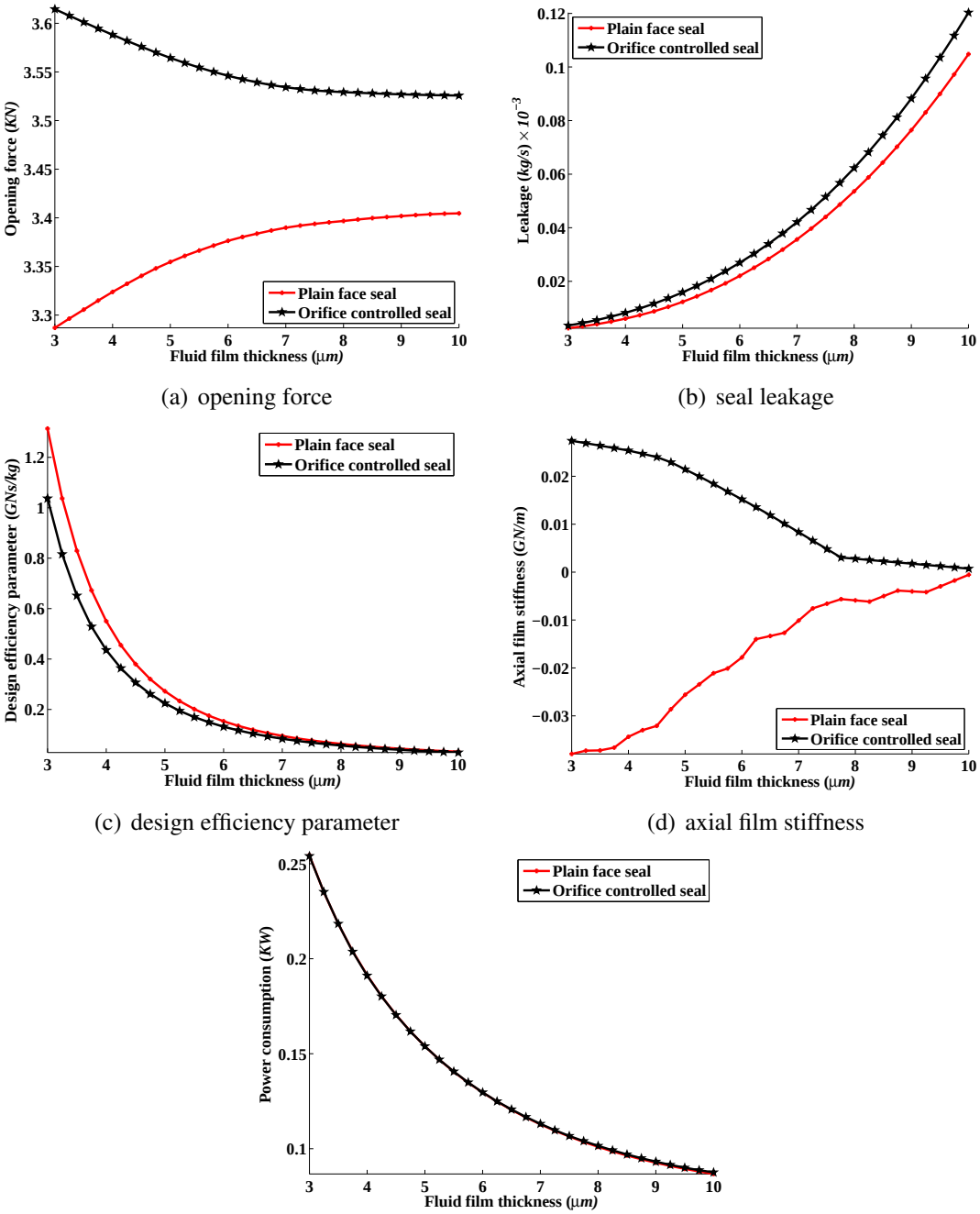

(a) opening force

(b) seal leakage

(c) design efficiency parameter

(d) axial film stiffness

(e) power consumption

Figure 4.18 Seal performance parameters of plain face seal and orifice controlled seal operating at sealed fluid pressure of 6 bar, rotating speed of 10000 rpm and sealed fluid temperature of 120°C

- The orifice controlled seal generated the highest axial film stiffness with a value of $0.0254\,GN/m$ and the lowest was calculated for the plain face seal with axial film stiffness of $-0.0344\,GN/m$.
- The orifice controlled seal generated the lowest power consumption with a value of $0.1911\,KW$ and the plain face seal the highest power consumption of $0.1913\,KW$.

The thermal density wedge has commonly been cited as the explanation for load support in parallel sliding (Lebeck, 1991). The idea is that as the fluid passes through the seal interface, the fluid is heated up due to viscous friction. As the fluid is heated up, its density decreases. Since continuity requires that the mass flow rate must be a constant, the volume flow rate must increase; the volume flow rate can increase only if there is an increasingly negative pressure gradient. From the results presented for the plain face seal, there is no way of maintaining preselected film thickness which will allow tolerable leakage and still have noncontact operation when the seal is perturbed. Since the plain face seal has negative and zero stiffness, the design lacks axial film stiffness that will be sufficient for dynamic tracking of the stationary nosepiece with the rotating seal seat. As a result of no positive axial film stiffness developing in plain face seal, some auxiliary devices such as grooves and orifice slots must be machined on one of the seal faces to provide positive axial film stiffness.

Adding orifice slots to the plain face seal significantly improves the performance of the plain face seal as illustrated with the results of the orifice controlled seal shown in Figure 4.18. The opening force-fluid film thickness curve has been improved from negative slope to positive slope (Figure 4.18(a)) which is an indication of positive axial film stiffness as shown in Figure 4.18(d). The power consumption of the orifice controlled seal and the plain face seal are both the same. Although the orifice controlled seal generated more leakage than the plain face seal, the positive axial film stiffness generated from the orifice controlled seal is not in any way comparable with the negative axial film stiffness generated by the plain face seal. Examining the pressure distributions as functions of seal face lengths (Figure A.5 in Appendix A) of the plain face seal and orifice controlled seal, it can be seen that there are significant fluid pressure variations both in the radial and circumferential directions of the orifice controlled seal. This is an indication of improvement on the hydrodynamic effectiveness of the plain face seal which has no significant pressure variations both in the radial and circumferential directions.

One important fact that needs to be pointed out here is the design efficiency parameter obtained from the plain face seal and the orifice controlled seal. From Figure 4.18(c), it can be seen that the plain face seal has a higher design efficiency parameter than the orifice controlled seal. It will be erroneous to conclude that the plain face seal has a better efficiency than the orifice controlled seal in terms of generating maximum opening force and less leakage. The reason is that the plain face seal has negative or zero axial film stiffness which makes it not hydrodynamic effective. Precaution must be taken in reviewing the weight of the design efficiency as a design objective for seal optimization. It is advisable to first carry out a numerical simulation on the geometrical seal face profile in order to ascertain that it generates positive axial film stiffness before selecting it as a design objective for seal optimization. If the results from the numerical simulations do not produce a positive steep

gradient (positive axial film stiffness) when the opening force is plotted against the fluid film thickness, then there is no way it can be considered as a design objective.

A technique of preserving a preselected film thickness and attaining axial film stiffness is to add a self-acting gas bearing, such as grooves to traditional plain face seals. Both the sealing dam force due to the pressure drop across the sealing dam and the self-acting lift force are balanced by the hydrostatic and spring closing forces. The gas bearing has a desirable characteristic whereby the force increases with decreasing film thickness. If the seal is upset in such a way as to decrease the gap, the additional force generated by the gas bearing will open the gap to the initial equilibrium position. In a related manner, if the gap becomes larger, the gas bearing force drop-offs and the closing force will induce the seal gap to revert it to the equilibrium position.

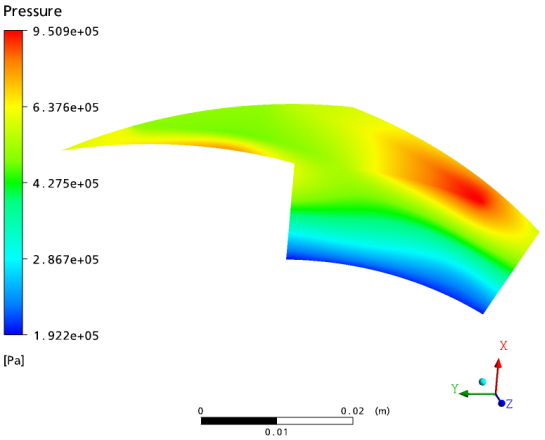

(a) Spiral groove face seal pressure contour

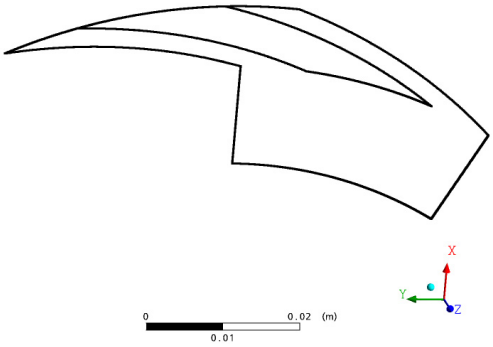

(c) Spiral groove face seal geometry

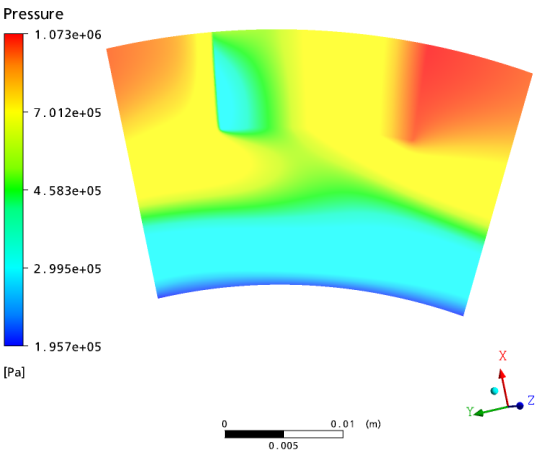

(b) Radial groove face seal pressure contour

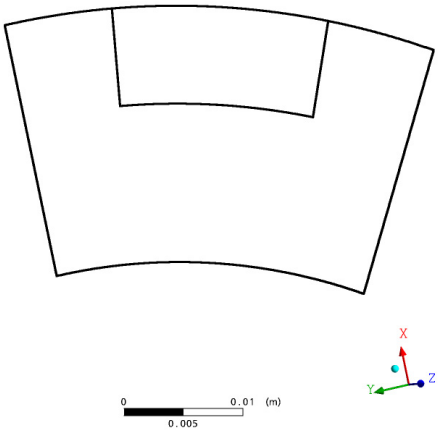

(d) Radial groove face seal geometry

Figure 4.19 Pressure contour plots of spiral and radial groove face seals operating at sealed fluid pressure of 6 bar, rotating speed of 10000 rpm and sealed fluid temperature of 120°C taken at an XY plane of fluid film thickness of 3 μm

The pressure contour plots for spiral groove, radial groove, T-groove and double spiral groove face seals for a sealing shaft rotating in the normal direction are shown in Figures 4.19 and 4.20. There are significant pressures variations in the radial and circumferential directions of the four grooved seals employed for this analysis. This significant pressures variation in both coordinates is evidence that grooved seals are better than the plain face and orifice controlled seals in terms of seal hydrodynamic effectiveness.

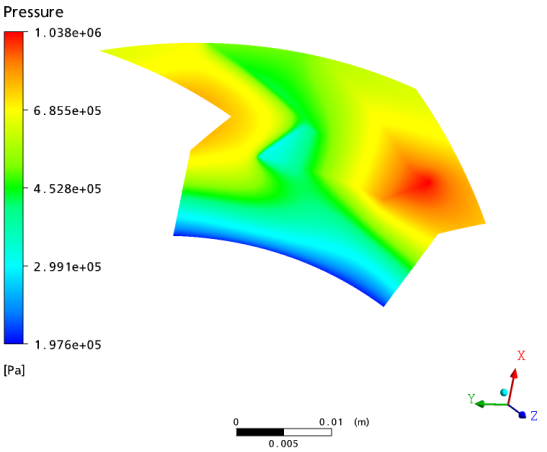

(a) Double spiral groove face seal pressure contour

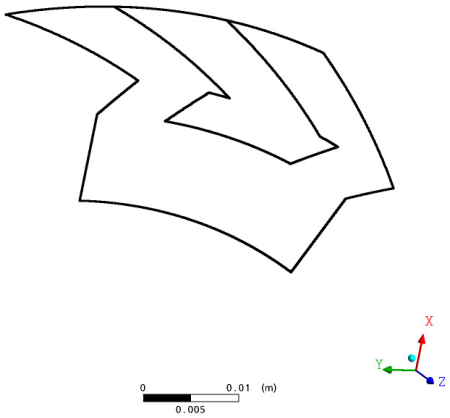

(c) Double spiral groove face seal geometry

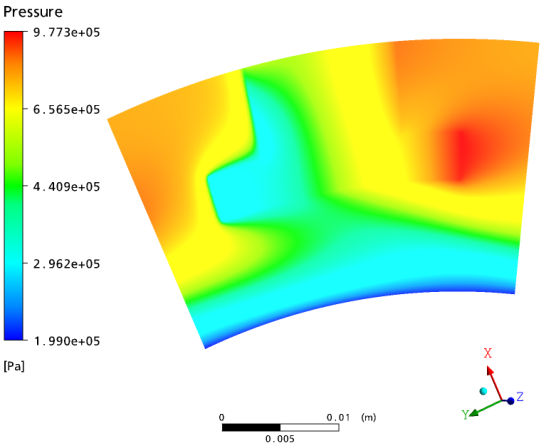

(b) T-groove face seal pressure contour

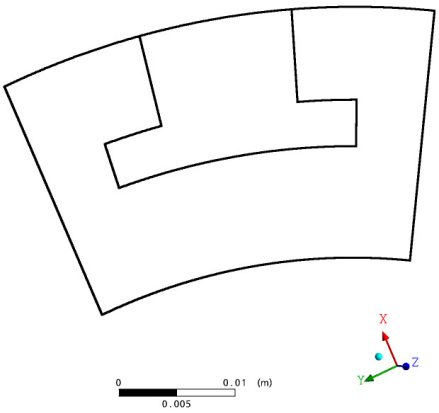

(d) T-groove face seal geometry

Figure 4.20 Pressure contour plots of double spiral groove and T-groove face seals operating at sealed fluid pressure of 6 bar, rotating speed of 10000 rpm and sealed fluid temperature of 120°C taken at an XY plane of fluid film thickness of 3 μm

Shown in Figure A.7 in Appendix A are plots of pressure distributions against the radial coordinate (Figure A.7(a)) and also against the circumferential coordinate (Figure A.7(b), (c), and (d)) for a sealing shaft rotating in the normal direction. Four different grooved seals were examined for this analysis. The grooved seals are spiral groove, radial groove, T-groove and double spiral groove face seals. Seals with asymmetrical groove patterns (spiral and double spiral groove seals) produced the largest peak pressures at the groove radius

both in the radial and circumferential coordinates. This is as a result of the spiral groove patterns pumping more fluid against the sealing dam translating to more pressure built-up at the groove - dam regions than the symmetrical groove patterns (radial and T-groove face seals). While the asymmetrical groove patterns generate axial film stiffness in three ways as already discussed in Subsection 2.2.1 in Chapter 2, the symmetrical groove patterns generate axial film stiffness in two ways as discussed in Subsection 2.2.2 in Chapter 2.

Shown in Figure A.9 in Appendix A are plots of pressure distributions against the radial coordinates (Figure A.9(a)) and also against the circumferential coordinates (Figure A.9(b), (c), and (d)) for a sealing shaft rotating in the reverse direction. For this reverse rotation of the sealing shaft, the asymmetrical groove patterns loose their peak pressures at the groove radius and eventually their opening force and positive axial film stiffness. This can be seen in Figure A.9(a) whereby, the peak pressures in the radial coordinate had vanished. Also the area under the pressure distributions curve as a function of the radial coordinate is so small that no appreciable amount of opening force can be obtained when the pressure distributions is integrated over the area. At the groove radius, the pressure variation in the circumferential direction of the asymmetrical groove patterns is insignificant. In the case of the symmetrical groove patterns, the pressure variations for the reverse rotation of the sealing shaft are the same as the normal rotation of the sealing shaft.

The temperature and velocity contour plots as well as velocity vector plots for the spiral and radial groove face seals are shown in Figures A.24, A.27 and A.30, respectively in Appendix A. Also the temperature and velocity contour plots as well as velocity vector plots for the double spiral groove and T-groove face seals are shown in Figures A.25, A.28 and A.31, respectively in Appendix A.

Shown in Figure 4.21 are the performance parameters obtained from the numerical simulations carried out when different geometrical seal face profiles were employed and the seal shaft is considered to rotate in the normal direction. Normal direction in this context is referred to the sealing shaft rotating in the clockwise direction and reverse rotation referred to the sealing shaft rotating in the anticlockwise direction. Considering a fluid film thickness of $4\,\mu m$ for the purpose of results comparisons, the following can be deduced for the performance parameters of the various geometrical face profiles shown in Figure 4.21 when the sealing shaft rotates in the normal direction.

- The highest opening force generated by the geometrical seal face profiles are: radial groove face seal with $4.91\,KN$, T-groove face seal with $4.81\,KN$, double spiral groove face seal with $4.59\,KN$ and the least was the spiral groove face seal with $4.21\,KN$.
- The least leakage generated by the geometrical seal face profiles are: spiral groove

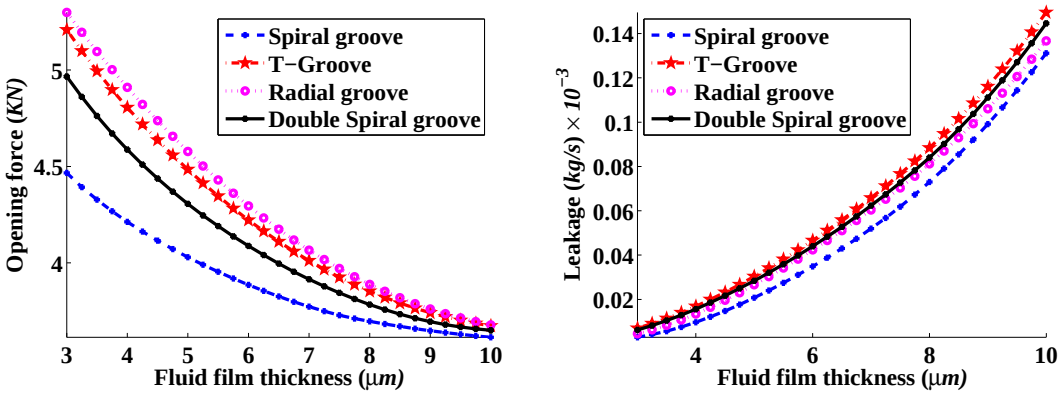

(a) opening force

(b) seal leakage

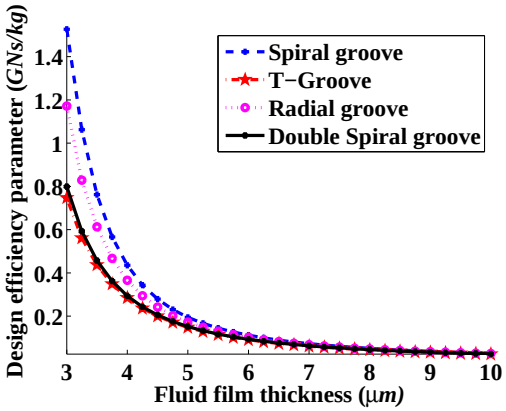

(c) design efficiency parameter

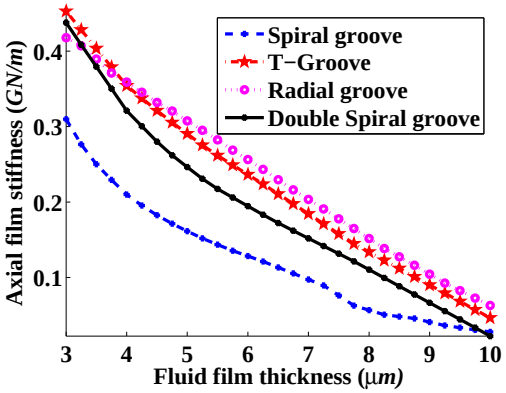

(d) axial film stiffness

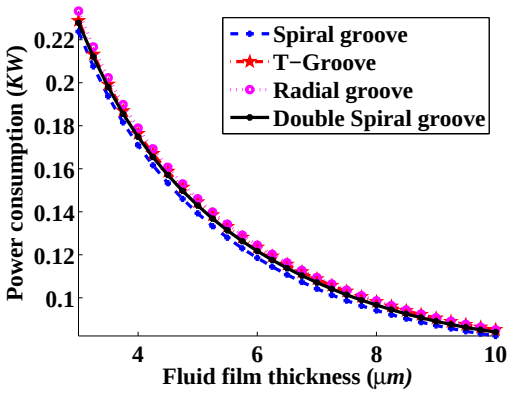

(e) power consumption

Figure 4.21 Seal performance parameters of various groove face profiles operating at sealed fluid pressure of 6 bar, normal rotating speed of 10000 rpm and sealed fluid temperature of 120°C

face seal with $0.0097 \times 10^{-3} kg/s$, radial groove face seal with $0.0134 \times 10^{-3} kg/s$, double spiral groove face seal with $0.0156 \times 10^{-3} kg/s$ and the highest been the T-groove face seal with $0.0169 \times 10^{-3} kg/s$.

- The highest design efficiency parameter generated by the geometrical seal face profiles are: spiral groove face seal with $0.4350\,GNs/kg$, radial groove face seal with

$0.3660\,GNs/kg$, double spiral groove face seal with $0.2936\,GNs/kg$ and the least was the T-groove face seal with $0.2845\,GNs/kg$.

- The highest axial film stiffness generated by the geometrical seal face profiles are: radial groove face seal with $0.3590\,GN/m$, T-groove face seal with $0.3542\,GN/m$, double spiral groove face seal with $0.3210\,GN/m$ and the least was the spiral groove face seal with $0.2100\,GN/m$.
- The least power consumption generated by the geometrical seal face profiles are: spiral groove face seal with $0.1709\,KW$, double spiral groove face seal with $0.1748\,KW$, T-groove face seal with $0.1763\,KW$ and the highest been the radial groove face seal with $0.1789\,KW$.

Considering a fluid film thickness of $4\,\mu m$ for the purpose of results comparisons, the following can be deduced for the performance parameters of the various geometrical face profiles shown in Figure 4.22 when the sealing shaft rotates in the reverse direction.

- The highest opening force generated by the geometrical seal face profiles are: radial groove face seal with $4.9107\,KN$, T-groove face seal with $4.8070\,KN$, double spiral groove face seal with $3.7647\,KN$ and the least was the spiral groove face seal with $3.4297\,KN$.
- The least leakage generated by the geometrical seal face profiles are: spiral groove face seal with $0.0041 \times 10^{-3}\,kg/s$, double spiral groove face seal with $0.0075 \times 10^{-3}\,kg/s$, radial groove face seal with $0.0134 \times 10^{-3}\,kg/s$ and the highest been the T-groove face seal with $0.0169 \times 10^{-3}\,kg/s$.
- The highest design efficiency parameter generated by the geometrical seal face profiles are: spiral groove face seal with $0.8273\,GNs/kg$, double spiral groove face seal with $0.5001\,GNs/kg$, radial groove face seal with $0.3663\,GNs/kg$ and the least was the T-groove face seal with $0.2842\,GNs/kg$.
- The highest axial film stiffness generated by the geometrical seal face profiles are: radial groove face seal with $0.3587\,GN/m$, T-groove face seal with $0.3550\,GN/m$, double spiral groove face seal with $0.0836\,GN/m$ and the least was the spiral groove face seal with $-0.0397\,GN/m$.
- The least power consumption generated by the geometrical seal face profiles are: spiral groove face seal with $0.1731\,KW$, double spiral groove face seal with $0.1761\,KW$, T-groove face seal with $0.1763\,KW$ and the highest been the radial groove face seal with $0.1789\,KW$.

As discussed earlier, the design efficiency parameter for the spiral groove face seal and double spiral groove face seal is not valid in judging how efficient a seal will perform when

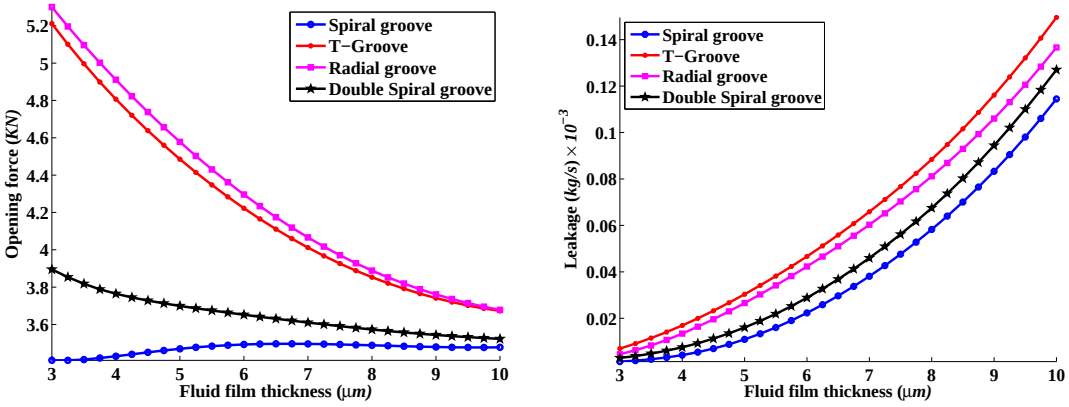

(a) opening force

(b) seal leakage

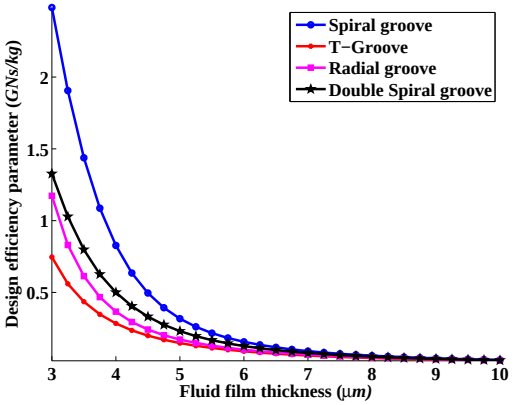

(c) design efficiency parameter

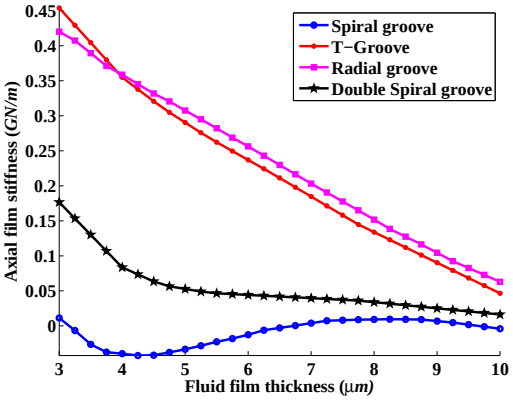

(d) axial film stiffness

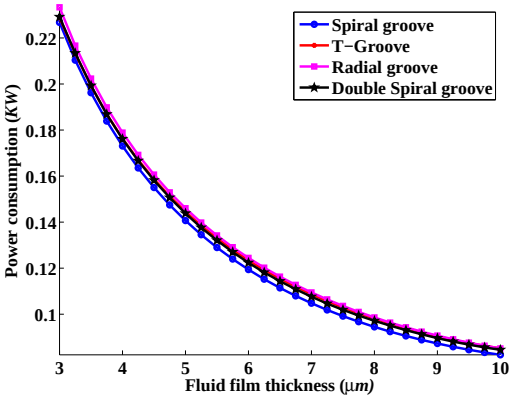

(e) power consumption

Figure 4.22 Seal performance parameters of various groove face profiles operating at sealed fluid pressure of 6 bar, reversed rotating speed of 10000 rpm and sealed fluid temperature of 120°C

the sealing shaft rotates in the reverse direction. This is true because in the reverse rotation of the sealing shaft, both the spiral groove and double spiral groove face seals generate either negative or zero axial film stiffness. It can be deduced that the spiral groove face seal and double spiral groove face seal cannot generate appreciable lift that will sustain the seal faces to remain apart upon reverse rotation of the sealing shaft. They are thus classified as unidirectional seals. The basic feature that makes them unidirectional seals is

the asymmetric groove face profiles they possess. The asymmetric groove face profiles limit these unidirectional seals from generating positive axial film stiffness upon reverse rotation of the sealing shaft. Seals that possess symmetric groove face profiles such as the radial groove and T-groove face seals are capable of generating positive axial film stiffness on both directions of sealing shaft rotation.

4.7 Effects of Face Deformation on Seal Performance

Since the film thickness is usually very small (of the order of a few microns), any local surface deformations due to the interfacial pressure and angular twist of the seal rings under pressure strongly influence the hydrostatic load support and hence the seal performance. For carbon rings with a relatively low modulus of elasticity, the distortions can easily be of the same order of magnitude as the nominal clearance of the seal. Thermal distortions can also occur due to both axial and radial temperature gradients in the seal rings caused by the frictional heat generated at the seal interface. These small tilts in the form of radial taper when added to the seal geometry can be used to include the effects of face deformation on seal performance analysis. Any radial taper in the direction of the flow changes the hydrostatic pressure distribution and the film stiffness. A diverging seals (in the leakage direction) exhibits a negative axial stiffness which may lead to seal collapse and high wear. With the availability of fast computers and necessary numerical tools, the Finite Element Analysis is commonly used for accurate predictions of pressure deformation and thermal distortion.

In order to evaluate the effects of face deformation on seal performance, various coning angles ranging from 0 to 0.0001 rad were added to the geometries of a plain face seal, spiral groove seal and radial groove seal. The 3D CFD model was employed for this analysis with the dimensions of the geometrical parameters stated in Table 4.1. Also, the operating conditions used are: sealed fluid pressure of $6\,bar$, rotating speed of $10000\,rpm$, sealed fluid temperature of $120^{o}C$ and fluid film thickness ranging from $3\,\mu m$ to $10\,\mu m$.

To operate without rubbing contact, the seal force balance had to be controlled within the load limits of the self-acting geometry. Therefore a necessary design goal is to minimize sealing face thermal and mechanical deformation. Generally, tapers in seals are small, but in some applications it is desirable to machine a converging taper in order to achieve positive stiffness.

Considering a fluid film thickness of $4\,\mu m$, for the purpose of results comparison, the performance parameters (Figure 4.23) obtained for two different radial tapers for plain face seal are presented as follows:

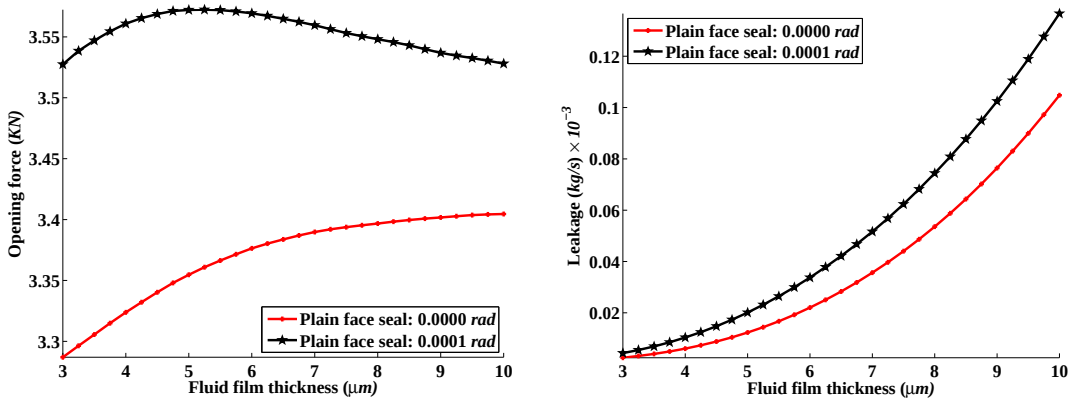

(a) opening force

(b) seal leakage

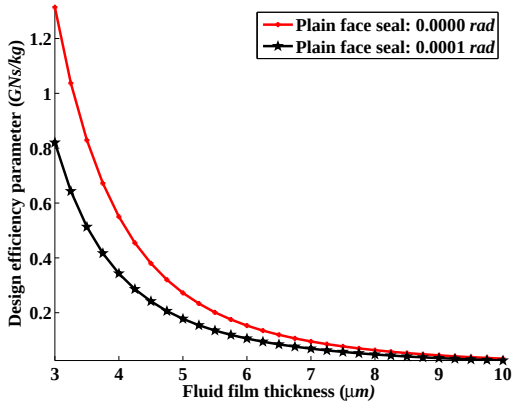

(c) design efficiency parameter

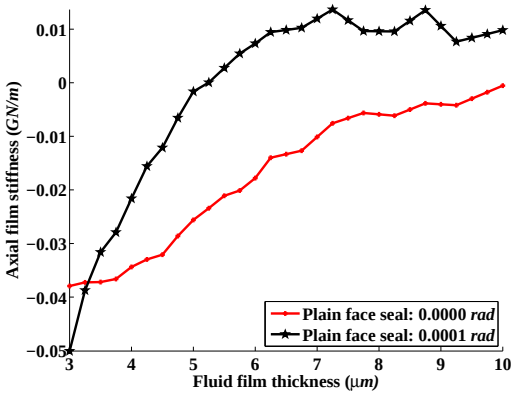

(d) axial film stiffness

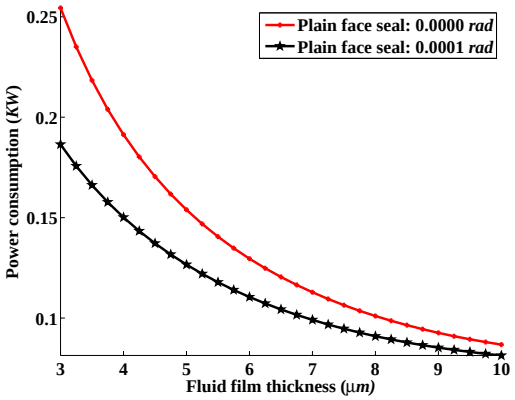

(e) power consumption

Figure 4.23 Seal performance parameters of a plain face seal with the considerations of face deformation, seal operating at sealed fluid pressure of 6 bar, rotating speed of 10000 rpm and sealed fluid temperature of 120°C

- The plain face seal with a radial taper of 0.0001 *rad* generated the highest opening force of 3.56 *KN* and the lowest was the plain face seal with a zero radial taper with a value of 3.32 *KN* opening force.
- The plain face seal with a zero radial taper generated the lowest leakage with a value of $0.0060 \times 10^{-3}\, kg/s$ and the plain face seal with a radial taper of 0.0001 *rad* generated the highest leakage of $0.0104 \times 10^{-3}\, kg/s$.

- The plain face seal with a zero radial taper generated the highest design efficiency parameter of $0.5502\,GNs/kg$ and the lowest been the plain face seal with a radial taper of $0.0001\,rad$ with a value of $0.3429\,GNs/kg$ design efficiency parameter.
- The plain face seal with a zero radial taper generated the highest negative axial film stiffness of $0.0344\,GN/m$ and the lowest been the plain face seal with a radial taper of $0.0001\,rad$ with a value of $0.0216\,GN/m$ negative axial film stiffness.
- The plain face seal with a radial taper of $0.0001\,rad$ generated the lowest power consumption of $0.150\,KW$ and the highest been the plain face seal with a zero radial taper with a value of $0.191\,KW$ power consumption.

As a results of the different regions of positive and negative axial film stiffness associated with the plain face seal, another fluid film thickness of $7\,\mu m$ is considered in order to further evaluate the effects of different radial tapers on plain face seal performance. The results obtained are presented as follows:

- The plain face seal with a radial taper of $0.0001\,rad$ generated the highest opening force of $3.56\,KN$ and the lowest was the plain face seal with a zero radial taper with a value of $3.39\,KN$ opening force.
- The plain face seal with a zero radial taper generated the lowest leakage with a value of $0.0356\times10^{-3}\,kg/s$ and the plain face seal with a radial taper of $0.0001\,rad$ generated the highest leakage of $0.0516\times10^{-3}\,kg/s$.
- The plain face seal with a zero radial taper generated the highest design efficiency parameter of $0.0951\,GNs/kg$ and the lowest been the plain face seal with a radial taper of $0.0001\,rad$ with a value of $0.0689\,GNs/kg$ design efficiency parameter.
- The plain face seal with a zero radial taper generated the lowest axial film stiffness of $-0.0101\,GN/m$ and the highest been the plain face seal with a radial taper of $0.0001\,rad$ with a value of $0.0120\,GN/m$ axial film stiffness.
- The plain face seal with a radial taper of $0.0001\,rad$ generated the lowest power consumption of $0.099\,KW$ and the highest been the plain face seal with a zero radial taper with a value of $0.113\,KW$ power consumption.

Considering a fluid film thickness of $4\,\mu m$, for the purpose of results comparison, the performance parameters (Figure 4.24) obtained for two different radial tapers for spiral groove face seal and radial groove face seal are presented as follows:

- The spiral groove face seal with a radial taper of $0.0001\,rad$ generated the lowest opening force of $4.11\,KN$ and the highest been the spiral groove face seal with a zero radial taper with a value of $4.21\,KN$ opening force. Also, the radial groove face seal

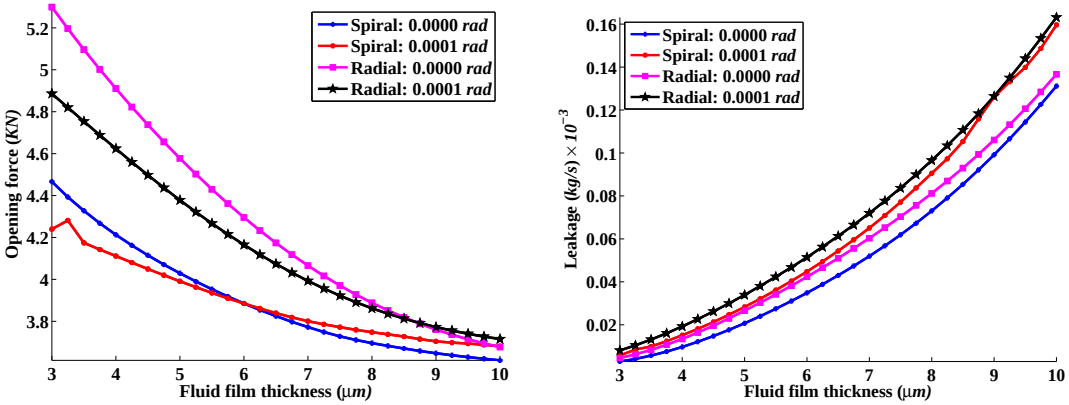

(a) opening force

(b) seal leakage

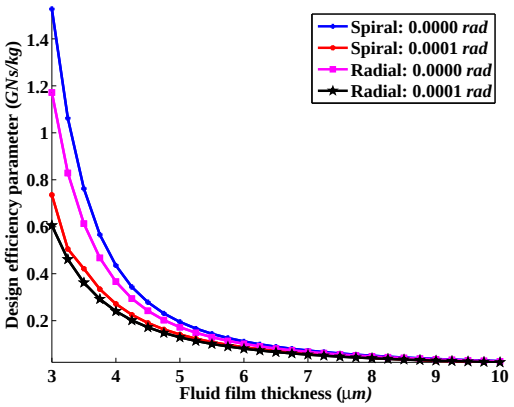

(c) design efficiency parameter

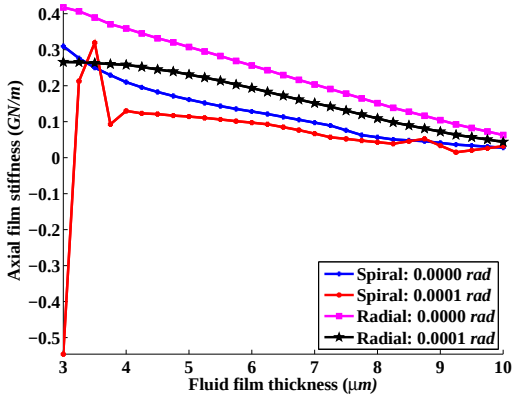

(d) axial film stiffness

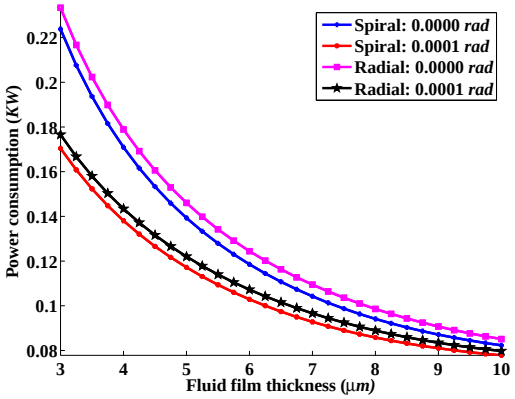

(e) power consumption

Figure 4.24 Seal performance parameters of a spiral groove seal and a radial groove seal with the considerations of face deformation, seal operating at sealed fluid pressure of 6 bar, rotating speed of 10000 rpm and sealed fluid temperature of 120°C

with a radial taper of 0.0001 *rad* generated the lowest opening force of 4.62 *KN* and the highest been the radial groove face seal with a zero radial taper with a value of 4.91 *KN* opening force.

- The spiral groove face seal with a zero radial taper generated the lowest leakage with a value of $0.0097 \times 10^{-3}\, kg/s$ and the spiral groove face seal with a radial taper of

$0.0001\,rad$ generated the highest leakage of $0.0151 \times 10^{-3}\,kg/s$. Also, the radial groove face seal with a zero radial taper generated the lowest leakage with a value of $0.0134 \times 10^{-3}\,kg/s$ and the radial groove face seal with a radial taper of $0.0001\,rad$ generated the highest leakage of $0.0193 \times 10^{-3}\,kg/s$.

- The spiral groove face seal with a zero radial taper generated the highest design efficiency parameter of $0.4350\,GNs/kg$ and the lowest been the spiral groove face seal with a radial taper of $0.0001\,rad$ with a value of $0.2715\,GNs/kg$ design efficiency parameter. Also, the radial groove face seal with a zero radial taper generated the highest design efficiency parameter of $0.3660\,GNs/kg$ and the lowest been the radial groove face seal with a radial taper of $0.0001\,rad$ with a value of $0.2401\,GNs/kg$ design efficiency parameter.
- The spiral groove face seal with a zero radial taper generated the highest axial film stiffness of $0.2100\,GN/m$ and the lowest been the spiral groove face seal with a radial taper of $0.0001\,rad$ with a value of $0.1299\,GN/m$ axial film stiffness. Also, the radial groove face seal with a zero radial taper generated the highest axial film stiffness of $0.3590\,GN/m$ and the lowest been the radial groove face seal with a radial taper of $0.0001\,rad$ with a value of $0.2581\,GN/m$ axial film stiffness.
- The spiral groove face seal with a radial taper of $0.0001\,rad$ generated the lowest power consumption of $0.138\,KW$ and the highest been the spiral groove face seal with a zero radial taper with a value of $0.171\,KW$ power consumption. Also, the radial groove face seal with a radial taper of $0.0001\,rad$ generated the lowest power consumption of $0.143\,KW$ and the highest been the radial groove face seal with a zero radial taper with a value of $0.179\,KW$ power consumption.

In Figure 4.24(a), at a fluid film thickness of about $3.25\,\mu m$, there is a sharp increase in opening force for the spiral groove with $0.0001\,rad$ convergent radial taper case. This is a numerical error since the actual opening force at this fluid film thickness would have been less than the opening force at $3\,\mu m$ fluid film thickness. Also, since the axial film stiffness is a function of the opening force, this numerical error has resulted in predicting inaccurate results of the axial film stiffness for the spiral groove with $0.0001\,rad$ in Figure 4.24(d).

The effects of positive radial taper on plain face seal is to improve the hydrodynamic effectiveness since more opening force is being generated as shown in Figure 4.23. For grooved seals, adding radial taper reduces the opening force resulting in a reduction of hydrodynamic effectiveness of the seal. This is illustrated by the results shown in Figure 4.25 and 4.24 that were obtained from the Reynolds equation model and 3D CFD model respectively. Adding convergent radial taper to plain face seal and grooved seal both increase the seal leakage. Adding convergent radial taper to plain face seal is beneficial but it is detrimental to seal performance of grooved seals.

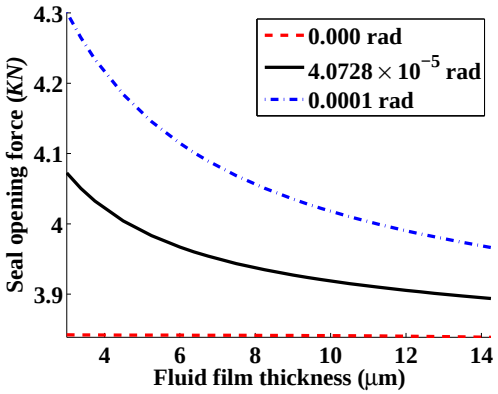

(a) plain face seal opening force

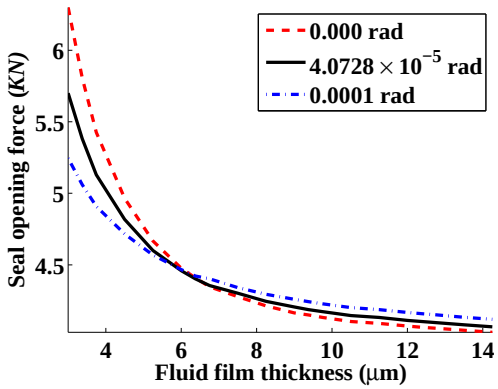

(b) spiral groove face seal opening force

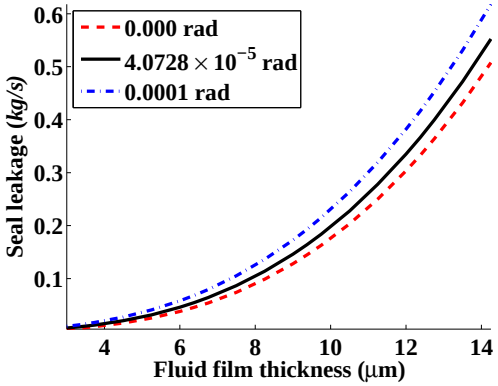

(c) plain face seal leakage

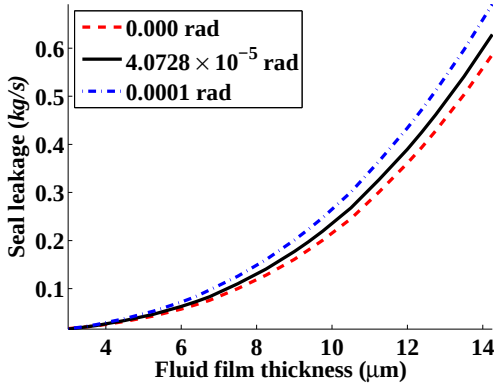

(d) spiral groove face seal leakage

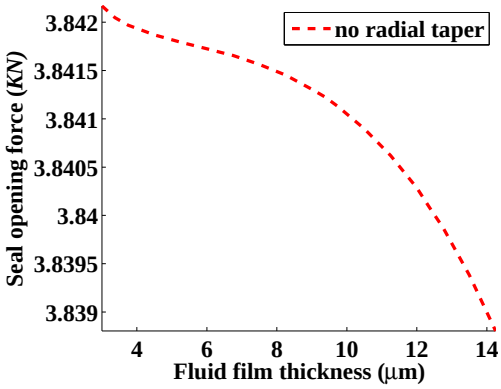

(e) opening force of a plain face seal without radial taper

Figure 4.25 Seal opening force and leakage of a plain face seal and spiral groove seal with the consideration of face deformation and utilising the Reynolds equation model for operating condition of sealed fluid pressure of 6 bar, rotating speed of 10000 rpm and sealed fluid temperature of 120°C

4.8 Presentation of a Novel Seal

A seal of innovative design is proposed here that has the capability of generating axial film stiffness on both directions of shaft rotation. Figure 4.26 shows the geometrical seal face

profile of the novel seal. Its working principle is the same as the spiral groove face profile already presented in Section 3.3.2.1 on page 96. The main difference between the novel seal and the spiral groove is that it has symmetrical face profile features which enable the seal to generate the same amount of lift on both directions of shaft rotation. Unlike the spiral groove face seal that has a logarithmic groove profile, the novel seal has a straight inclined groove profile. The two straight inclined groove edges of the novel seal are assigned the same groove angles, one of the groove edges angle (α_1) is assigned a positive value while the second groove edge angle (α_2) is assign a negative value. The groove angle may vary between 65^o to 135^o depending on choice of design or the optimal solution obtained from optimization. When the groove angle is 90^o, it can be likened to the parallel groove seal presented in Section 2.2.2 on page 20. The groove might take, a rectangular, trapezoidal, or triangular shape as shown in Figure 4.27.

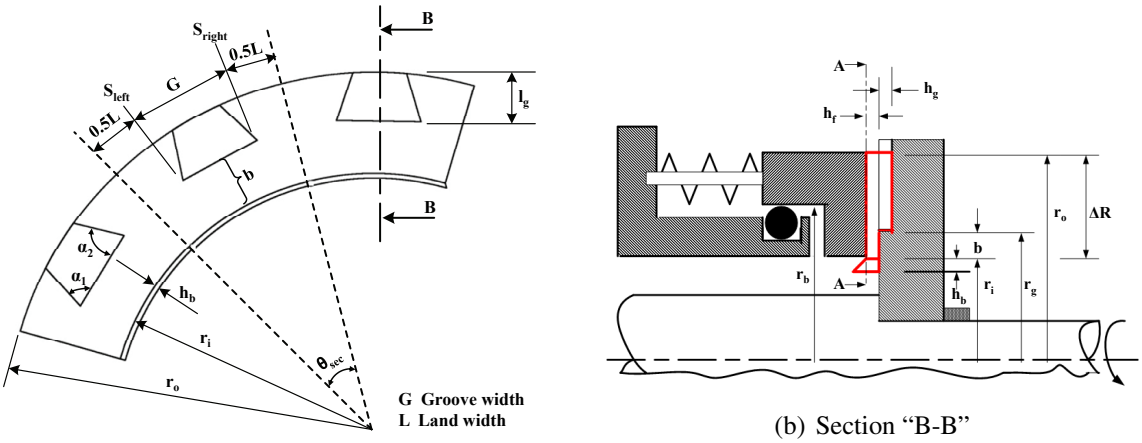

(a) Section "A-A" - Novel seal

(b) Section "B-B"

Figure 4.26 Sectional views of the novel seal geometry showing the extent of the computational domain

The results for the performance parameters of the novel seal were obtained by utilising the dimensions of the geometrical parameters given in Table 4.1 with the groove angle changed to 65^o and the coning angle set to zero. The operating conditions considered for this analysis are: sealed fluid pressure, $6\,bar$, rotating speed, $10000\,rpm$, sealed fluid temperature, 120^oC and a fluid film thickness that vary from $3\,\mu m$ to $10\,\mu m$.

The pressure contour plots for the novel seal for a sealing shaft rotating in the normal direction are shown in Figure 4.28. There are significant pressure variations both in the radial and circumferential directions. Shown in Figure A.15 in Appendix A are plots of pressure distributions against the radial coordinates (Figure A.15(a)) and also against the circumferential coordinates (Figure A.15(b), (c), and (d)) for a sealing shaft rotating in the normal and reverse directions. There is evidence of peak pressures in the radial and circumferential coordinates.

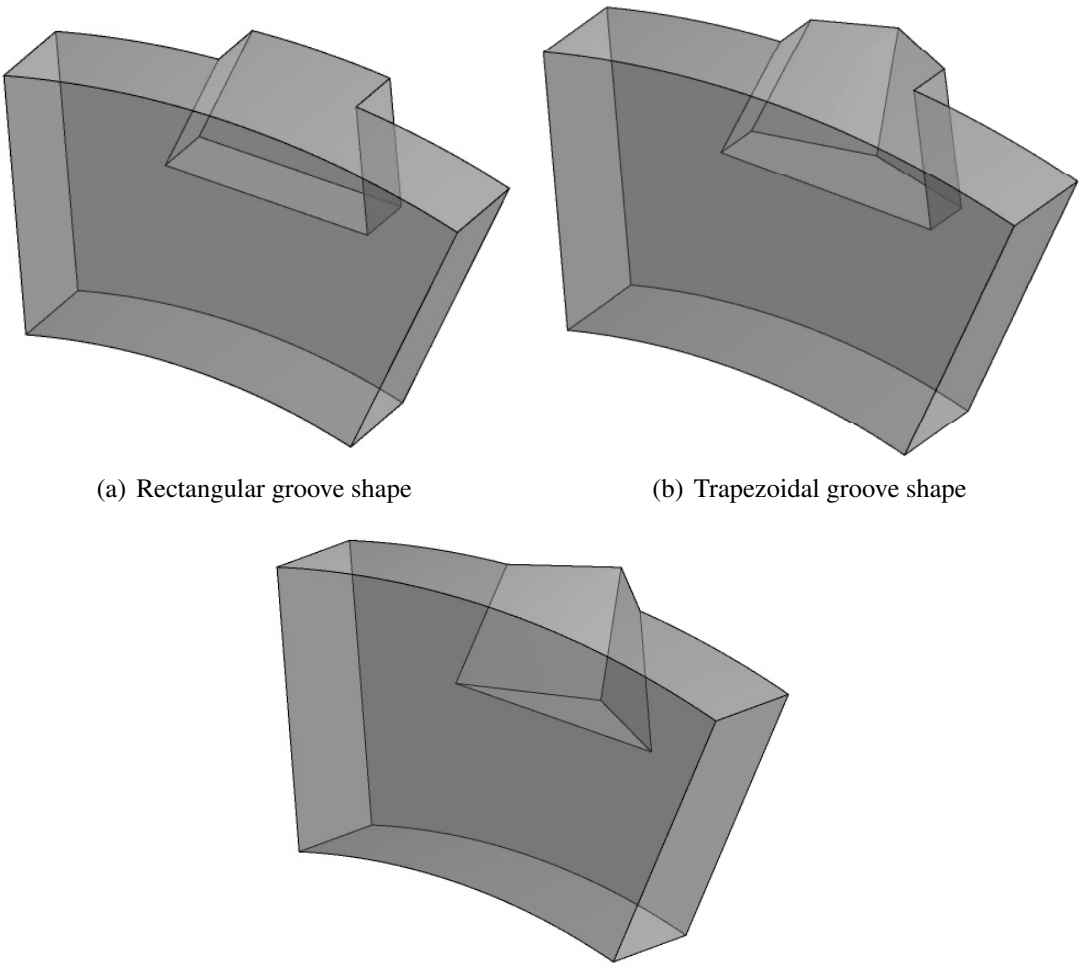

(a) Rectangular groove shape

(b) Trapezoidal groove shape

(c) Triangular groove shape

Figure 4.27 Different geometrical groove shapes of the proposed novel seal design

The temperature and velocity contour plots as well as velocity vector plots for a proposed novel seal are shown in Figures A.32 in Appendix A.

The results of the performance characteristics when the novel seal was analysed with the sealing shaft rotating in the reverse and normal directions are shown in Figure 4.29 and Figure 4.31, respectively. As is hardly surprising both cases generated the same amount of opening force, leakage, stiffness, power consumption as well as design efficiency parameter. The performance parameters of the novel seal are therefore not dependent on the direction of shaft rotation unlike the spiral groove face seal that is very sensitive to the direction of sealing shaft rotation in terms of lift generation. This has been shown in Figure 4.29 whereby the new seal and the spiral groove face seal performance parameters have been compared for reverse direction of shaft rotation.

In order to evaluate the best groove shape of the novel seal in terms of performance parameters, two groove profiles have been selected. The two groove shapes considered were

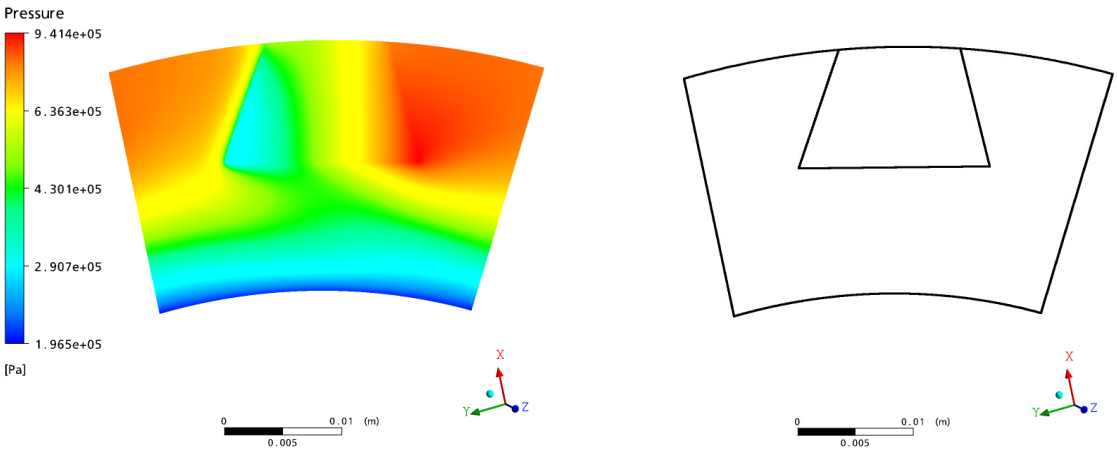

(a) Novel seal pressure contour

(b) Novel seal geometry

Figure 4.28 Pressure contour plots of a proposed novel seal operating at sealed fluid pressure of 6 bar, rotating speed of 10000 rpm and sealed fluid temperature of 120°C taken at an XY plane of fluid film thickness of 3 μm

the rectangular and the trapezoidal shapes as shown in Figure 4.27. The triangular groove shape was attempted in this analysis but due to the high skewness of its grid as a result of the structured meshing approach employed in this study, it was impossible to include the triangular groove shape in this analysis. Although there is not much difference in the results presented in Figure 4.30 for the rectangular and trapezoidal groove shapes, there are distinct differences in the plots of pressure distributions against seal face lengths as shown in Figure A.17 in Appendix A. The rectangular groove shape is associated with higher pressure generation in the radial direction than the trapezoidal groove shape. This suggests that the larger the area of the groove, the higher the opening force that will be generated. The increase in the pressure generation in the rectangular groove shape is an indication of a better hydrodynamic effectiveness of a seal.

Considering a fluid film thickness of $4\,\mu m$ for the purpose of results comparisons, the following observations can be made for the performance parameters of the rectangular and trapezoidal groove shapes of the novel seal shown in Figure 4.30.

- The rectangular groove shape generated the highest opening force of $4.70\,KN$ and the lowest was the trapezoidal groove shape with a value of $4.65\,KN$ of opening force.
- The rectangular groove shape generated the lowest leakage of $0.0140 \times 10^{-3}\,kg/s$ and the highest was the trapezoidal groove shape with a value of $0.0141 \times 10^{-3}\,kg/s$ of seal leakage.
- The rectangular groove shape generated the highest design efficiency parameter of $0.3363\,GNs/kg$ with the lowest being the trapezoidal groove shape with a value of $0.3303\,GNs/kg$ of design efficiency parameter.

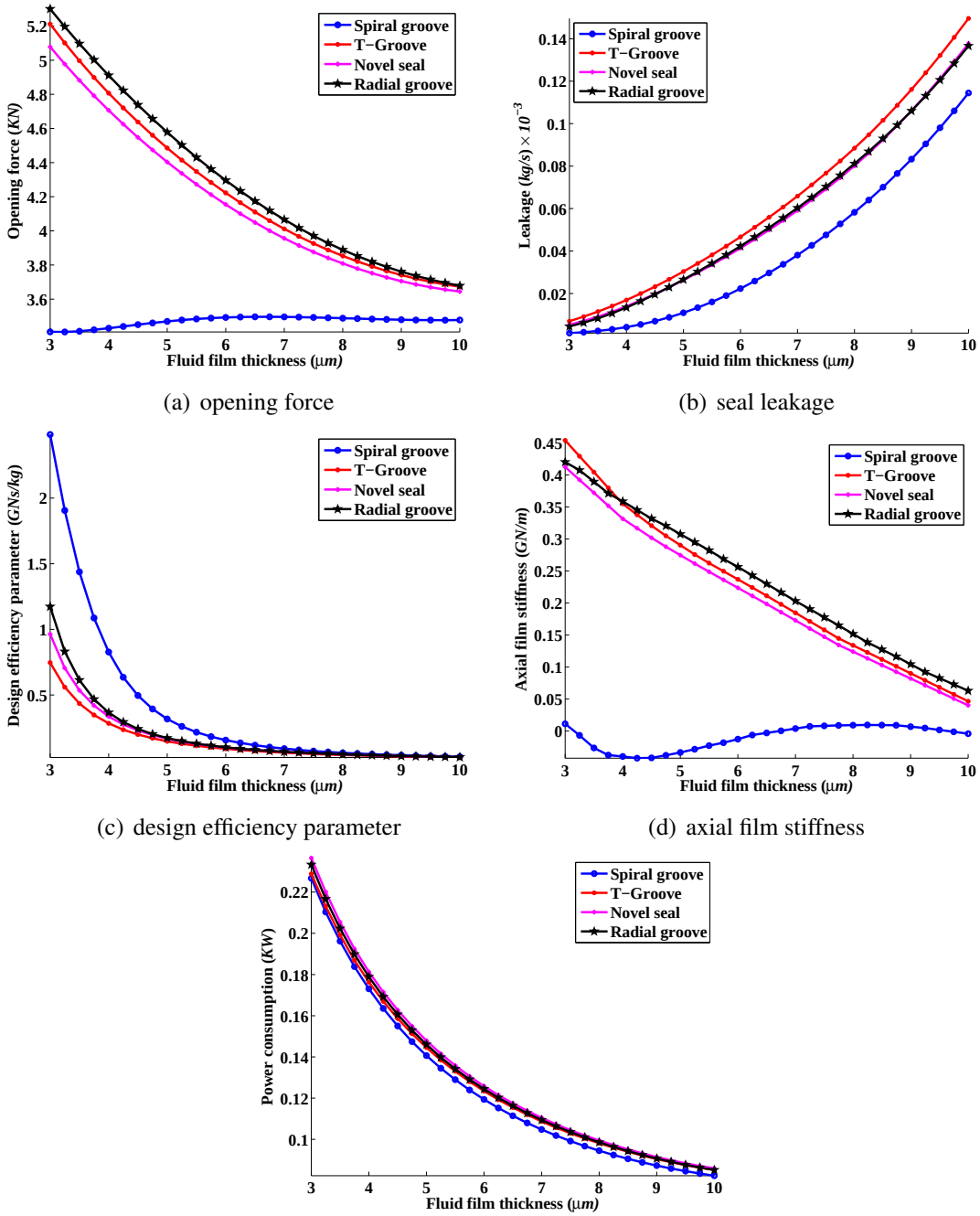

(a) opening force

(b) seal leakage

(c) design efficiency parameter

(d) axial film stiffness

(e) power consumption

Figure 4.29 Seal performance parameters of a novel seal compared with some existing geometrical seal face profiles, seal operating at sealed fluid pressure of 6 bar, reversed rotating speed of 10000 rpm and sealed fluid temperature of 120°C

- The rectangular groove shape generated the lowest axial film stiffness of $0.3306\,GN/m$ and the highest was the trapezoidal groove shape with a value of $0.3628\,GN/m$ of axial film stiffness.
- The rectangular groove shape generated the highest power consumption of $0.181\,KW$ and the lowest was the trapezoidal groove shape with a value of $0.181\,KW$ of power

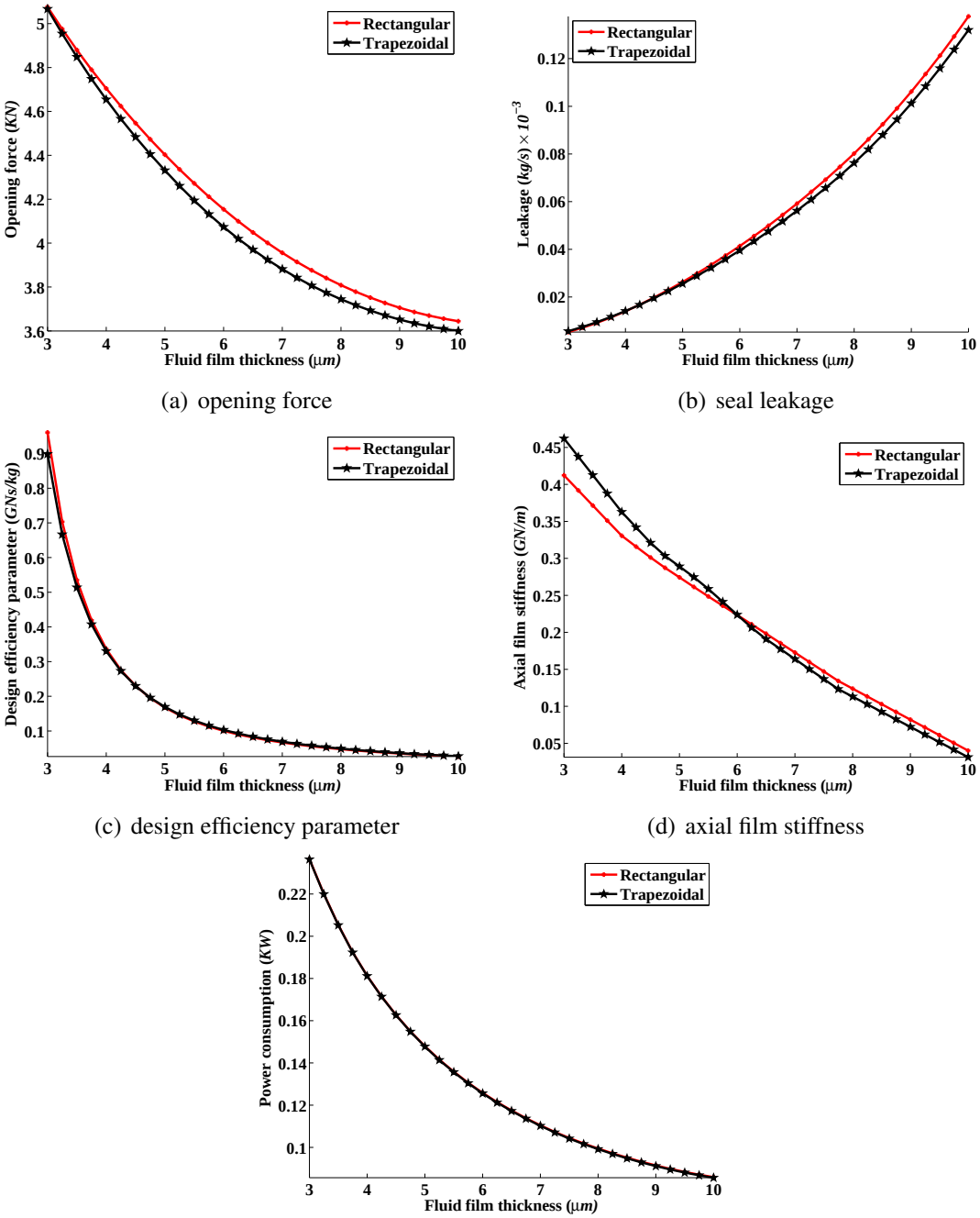

(a) opening force

(b) seal leakage

(c) design efficiency parameter

(d) axial film stiffness

(e) power consumption

Figure 4.30 Seal performance parameters of a novel seal with two different groove shapes, seal operating at sealed fluid pressure of 6 bar, rotating speed of 10000 rpm and sealed fluid temperature of 120°C

consumption.

Listed below are the deductions made from the comparisons of results shown in Figure 4.31 that were obtained from the comparison of the novel seal with other existing geometrical seal face profiles. This comparison was based on a fluid film thickness of $4\,\mu m$ with the sealing shaft rotating in the normal direction.

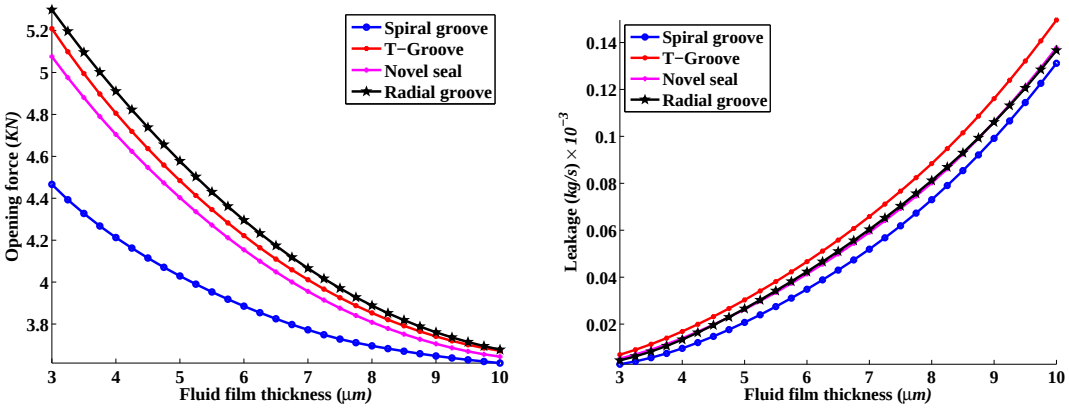

(a) opening force

(b) seal leakage

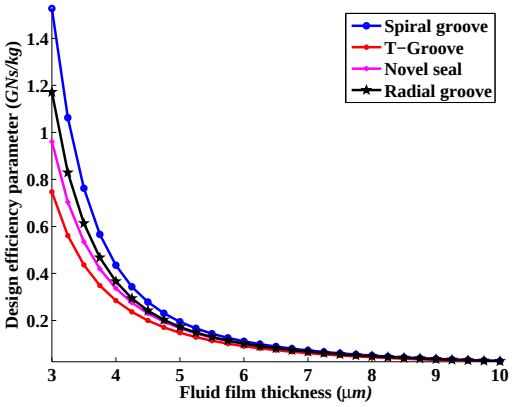

(c) design efficiency parameter

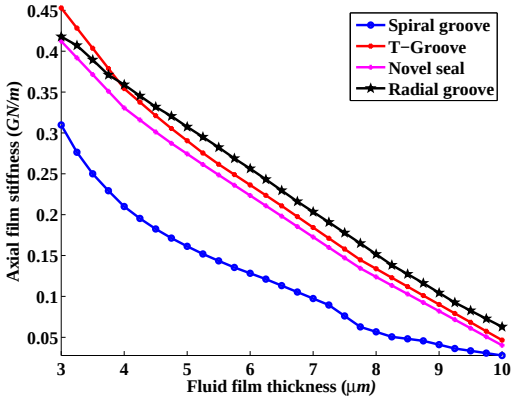

(d) axial film stiffness

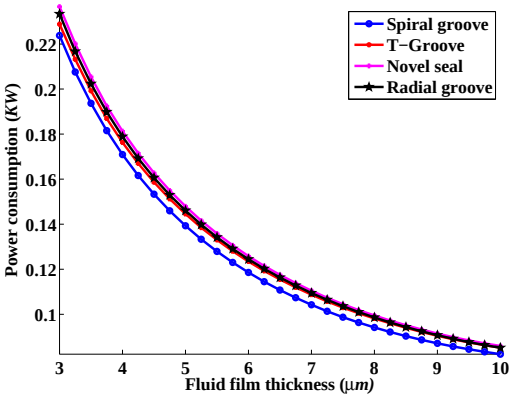

(e) power consumption

Figure 4.31 Seal performance parameters of a novel seal compared with some existing geometrical seal face profiles, seal operating at sealed fluid pressure of 6 bar, normal rotating speed of 10000 rpm and sealed fluid temperature of 120°C

- The highest opening force generated by the geometrical seal face profiles are: radial groove face seal, 4.91 KN, T-groove face seal, 4.81 KN, novel seal, 4.70 KN and the least performing was the spiral groove face seal with 4.21 KN.
- The least leakage generated by the geometrical seal face profiles are: spiral groove face seal, $0.0097 \times 10^{-3}\, kg/s$, radial groove face seal, $0.0134 \times 10^{-3}\, kg/s$, novel seal,

$0.0140 \times 10^{-3}\,kg/s$ and the highest is the T-groove face seal with $0.0169 \times 10^{-3}\,kg/s$.

- The highest design efficiency parameter generated by the geometrical seal face profiles are: spiral groove face seal, $0.4350\,GNs/kg$, radial groove face seal, $0.3660\,GNs/kg$, novel seal, $0.3363\,GNs/kg$ and the least was the T-groove face seal with $0.2845\,GNs/kg$.
- The highest axial film stiffness generated by the geometrical seal face profiles are: radial groove face seal, $0.3590\,GN/m$, T-groove face seal, $0.3542\,GN/m$, novel seal, $0.3306\,GN/m$ and the least was the spiral groove face seal with $-0.2100\,GN/m$.
- The least power consumption generated by the geometrical seal face profiles are: spiral groove face seal, $0.171\,KW$, T-groove face seal, $0.176\,KW$, radial groove face seal, $0.179\,KW$ and the highest is the novel seal with $0.181\,KW$.

4.9 Chapter Summary

In this chapter, various results for dry gas face seals that span across different operating conditions and geometrical seal face profiles, with the inclusion of convergent radial taper, have been presented and discussed. Also, a comparison and contrast of the results obtained from the Reynolds equation model and 3D CFD model have been carried out. The results from these two models were also validated against test data obtained from AESSEAL plc, the sponsor of this research.

The results of the Reynolds equation model and 3D CFD model follow the same trend for low operating conditions. The difference in the results from both models was essentially found in the predicted absolute values. At high operating conditions however, there are marked differences in results obtained from the two models which can be attributed to the limitations of the Reynolds equation model that neglected the effects of inertia and turbulence. The 3D CFD model predictions were generally in better agreement with the test data on the seal leakage than the results due to the Reynolds equation model. The leakage rates and fluid film thickness predictions illustrate how the 3D CFD model can be used for seal design while overcoming some of the shortcomings of the Reynolds equation based models. The major limitation of the 3D CFD model is that it is computationally rather expensive.

The results presented in this chapter have shown that a good dry gas face seal must possess a steep gradient of lift force against fluid film thickness also referred to as high gas film stiffness. This high gas film stiffness is advantageous in the sense that, the net resulting force (difference between closing and opening forces) is a closing force that increases rapidly when the opening force decreases. A small operating gas film thickness is therefore maintained and the high gas film stiffness forces the seal nosepiece to dynamically track the

run out motion of the seal face. Based on the reasoning above, the discussion of the results was based on performance parameters such as opening force, leakage, axial film stiffness, power consumption and design efficiency parameter.

The dry gas face seal is self-regulating during operation which depends on the proper balance of forces. The opening force is dependent on numerous variables. If the running gap increases, the opening force decreases. If the running gap decreases, the opening force will increase as a result of the grooves generating more lift. The closing force is more easily adjusted by manipulating the balance ratio. Increasing the balance diameter causes a decrease in the closing force; decreasing the balance diameter causes an increase in the closing force. To achieve optimum seal performance is to identify the running gap at which the opening force and closing force are exactly balanced. This is obtained from the force-film thickness curve. Since the seals must be pressure balanced, a proper balance of the opening and closing forces must be achieved with a leakage gap that has tolerable leakage. The gap must be small enough so that the leakage is minimal but it must be large enough so that power dissipation, due to shear in the film, and face deformation, are tolerable. Thus the design of the sealing gap is vital to seal performance and pressure distribution in the gap and mass leakage through the seal interface must be analyzed.

The rotational speed coupled with the seal face topography is responsible for the generation of the hydrodynamic force. At moderate rotating speed and high pressure differential, the groove effects do not have a significant impact on the seal performance in terms of the generation of high gas film stiffness. Increasing the sealed fluid pressure does not enhance the gas film stiffness rather it generates more opening and closing forces that will support the bulk of the load. The pressure differential is responsible for the generation of the hydrostatic forces. It is evident from the results presented that the hydrodynamic action impacts high gas film stiffness, particularly at small clearances and high rotating speeds.

Investigation of the contributions of the hydrostatic and hydrodynamic forces in the operation of a seal have shown that bulk of the opening forces comes from the hydrostatic force resulting from the sealed fluid pressure differential. Increasing the pressure differential does not improve the axial film stiffness of the seal but only increases the opening and closing forces. The hydrodynamic force is quite small compared to the hydrostatic force but it is the controlling mechanism of grooved seal which provides the positive axial film stiffness. The hydrodynamic force results from the relative motion of the sealing face. A high pressure generation at the groove section in the radial and circumferential directions is an indication of the presence of hydrodynamic forces in a seal.

Different geometrical seal face profiles were analyzed and their results compared. Adding an orifice slot to a plain face seal improves its performance from negative axial film stiffness

to positive axial film stiffness at the expense of increased leakage. It was found out that when the sealing shaft rotates in the normal direction, the spiral groove face profile is considered to be the best seal in terms of design efficiency parameter. Upon reverse direction of the sealing shaft rotation, the spiral groove face profile becomes a bad seal since it cannot produce positive axial film stiffness on reverse rotation. The radial groove and T-groove face profiles considered in this analysis showed that they can generate the same amount of lift on normal and reverse rotation of the sealing shaft. It was observed that seals with symmetrical groove face profiles do generate the same amount of lift on both directions of sealing shaft rotation. Based on the above discussion, a novel seal that is of bidirectional type is proposed. Even though the optimum geometrical values of the novel seal have not been found, the results obtained from utilising this novel seal are encouraging compared with the results of the existing geometrical seal face profiles. This novel seal which is believed to be unique and have not been designed elsewhere is easy to fabricate.

The results have shown that adding a positive radial taper to a plain face seal improves its performance in terms of higher opening force. Adding a positive radial taper to grooved seals reduces the opening force and positive axial stiffness. Adding positive radial taper to plain face seals and grooved seals increases their leakage. Therefore while positive radial taper in plain face seals is beneficial, its inclusion to grooved seal reduces its performance.

Chapter 5

Optimisation Techniques

5.1 Introduction

The minimization of seal leakage and maximization of seal opening force (or positive stiffness) are two of the greatest challenges in the design of dry gas face seals. Minimization of seal leakage or maximization of either the seal opening force or positive stiffness would usually be obtained at the expense of the other. The benefit of seals having minimal leakage, while maintaining maximum opening force or positive stiffness is that, contact between the seal faces would be avoided during operation. The importance of this issue should not be underestimated since in addition to improved seal performance, it delivers substantial cost savings to both the seal manufacturer and the end user.

A number of different methods have previously been applied to the optimization of mechanical face seals. Some of them used the parametric analysis approach (Liu et al. (2004), Zirkelback (2000), Salant and Homiller (1992), Feldman et al. (2007), Walowit and Pinkus (1982), Shellef and Johnson (1992), Kowalski and Basu (1995) and Feldman, Kligerman and Etsion (2006)) while a few chose some standard optimizers such as the complex method of nonlinear constrained optimization (Zhou et al. (2007), Leefe (2002) and Zheng (2005)). Depending on the seal face layout considered to be optimized, the design variables (geometrical parameters) vary from one seal face layout to another. The variation of these design variables will always have an effect on the seal performance parameters in different ways such as adequate film thickness, rate of leakage as well as stability. The four major performance parameters obtained from the analysis of seals are: opening force, leakage, stiffness and friction force (torque or power consumption). These performance parameters are chosen to be the objective function(s) in the optimization process. They can be considered as a single or multi-objective functions. These are tailored either with reference to a particular performance parameter, or combination of performance parameters,

or in some cases, a compromise between performance parameters must be considered.

Some previous research attempted to maximize opening force without consideration of leakage (Zheng, 2005); while another study aimed to maximize the opening force and treated the leakage as a constraint (Zhou et al., 2007). Kowalski and Basu (1995) and Shellef and Johnson (1992) tried to maximize the stiffness while others pioneered the use of a design efficiency parameter that depends on some performance parameters. Feldman, Kligerman and Etsion (2006) defined the design efficiency parameter as the ratio of average pressure to leakage, while Feldman et al. (2007) defined it as the ratio of stiffness to leakage. This parameter is useful when a single-objective function is considered since a leakage effect is included in the optimization. Maximization of stiffness is usually preferred to the opening force since a good seal must have a positive stiffness such that one of its faces will be able to dynamically track the run out motion of the other face when it is subjected to disturbances. Computing the stiffness is expensive since a single computation of stiffness will requires several calculations of the opening forces at different fluid film thicknesses for a single combination of design variables. As a result of its computational cost, a compromise has to be made by maximizing the opening force in place of the stiffness.

Most researchers have employed the Reynolds equation model (Liu et al. (2004), Zirkelback (2000), Salant and Homiller (1992), Basu (1992), Feldman, Kligerman, Etsion and Haber (2006), Feldman et al. (2007), Walowit and Pinkus (1982), Zhou et al. (2007), Shellef and Johnson (1992), Kowalski and Basu (1995) and Feldman, Kligerman and Etsion (2006)) while only a few have employed the 3D-CFD in their optimization (Zheng (2005) and Leefe (2002)). Although the Reynolds equation models are very fast in terms of computational requirements, they are inaccurate for computing flows that exist in highly loaded seals having complex geometries (Feldman, Kligerman, Etsion and Haber, 2006). Due to the limitations of the Reynolds equation models, 3D-CFD models are preferred for accuracy. Despite the rapid development of hardware and solver technology over recent years, the computational cost of many engineering simulations is still too high for 3D-CFD simulations to be directly linked with the available optimizers. For example, a 3D Reynolds Averaged Navier-Stokes CFD calculation for one-twelfth sector of a dry gas face seal (having about 3 million cells), may take in excess of 3 hours to run on a parallel high end compute node with 16 processors. This is a significant problem, since most types of standard optimizers may require, as a minimum, hundreds of function evaluations to obtain the optimum, but more typically thousands.

A possible way to reduce this excessive computational requirement is the coupling of Design and Analysis of Computer Experiments (DACE) methods with an optimizer that uses a meta-model(s) of the design space. DACE comprises a number of methods analogous to Design

of Experiments (DOE) methods used for physical experiments, and is used to "randomly" distribute sample points in the design space in which CFD simulations can be run. The results of these simulations can then be used to construct an approximation or meta-model of the design space. The optimization is then carried out using this meta-model to evaluate the objective function instead of performing expensive CFD calculations for each point.

This chapter presents an optimization tool that makes use of the results from either the 3D CFD model or Reynolds equation model for the optimization of a dry gas face seal. This tool implements a low-discrepancy sequence technique for sampling of points in the design space, makes use of approximate models (metamodels) in place of running a large number of numerical simulations of fluid flow in the seal interface. The metamodel algorithm produces fitness functions from a few numerical simulation runs and passes these fitness functions to an optimizer. The optimizer adopts a Genetic Algorithm that has the capability of optimizing both single and multiobjective function(s). The tool is used for obtaining the best possible solutions in the shortest time rather than depending directly on the results from numerical simulations runs, which is computationally expensive. With this numerical tool, optimal seal geometries with a minimum of human intervention can be generated.

5.2 The Optimization Model

The first step in carrying out the optimization process is the identification of the design variables and the most useful performance parameters needed for the optimization. This is achieved by carrying out a sensitivity analysis on the geometrical parameters at a particular operating condition. CFD simulation runs are carried out, varying the geometrical parameters one at a time. The performance parameters obtained from the CFD simulation runs of the variations of the geometrical parameters are compared with a "Base" case. Here, the "Base" case referred to one set of the CFD simulation runs of the varied geometrical parameters. The ones that produce most sensitive results are considered to be the design variables.

Quasi-random points are generated for the design variables using the Halton algorithm. The computational grids are then constructed based on the points generated from the Halton method. The CFD simulations are then carried out. The results obtained from the CFD simulations are passed to the metamodel algorithm. Fitness function(s) are then generated from the metamodel. The generality and accuracy of the metamodel is then tested. A limited number of predictions are carried out based on a number of design variables and these design variables are then used to generate a computational grid and a CFD simulation is run. If the predicted result from the metamodel is different from the result of the CFD simulation, more random points are added and the metamodel is fine tuned by varying some of the metamodel

input variables and the whole process is repeated until improved result is obtained. If the CFD simulation result is comparable to the results predicted from the metamodel, the fitness function is then passed to the genetic algorithm. A search is carried out to determine the optimum geometrical parameters that will produce the minimum leakage and maximum opening force. The optimization flow chart showing the flow process is shown in Figure 5.1. The stopping criteria in Figure 5.1 is a comparison between the predicted optimal values of the optimization tool and a 3D CFD simulated values at the predicted optimal values.

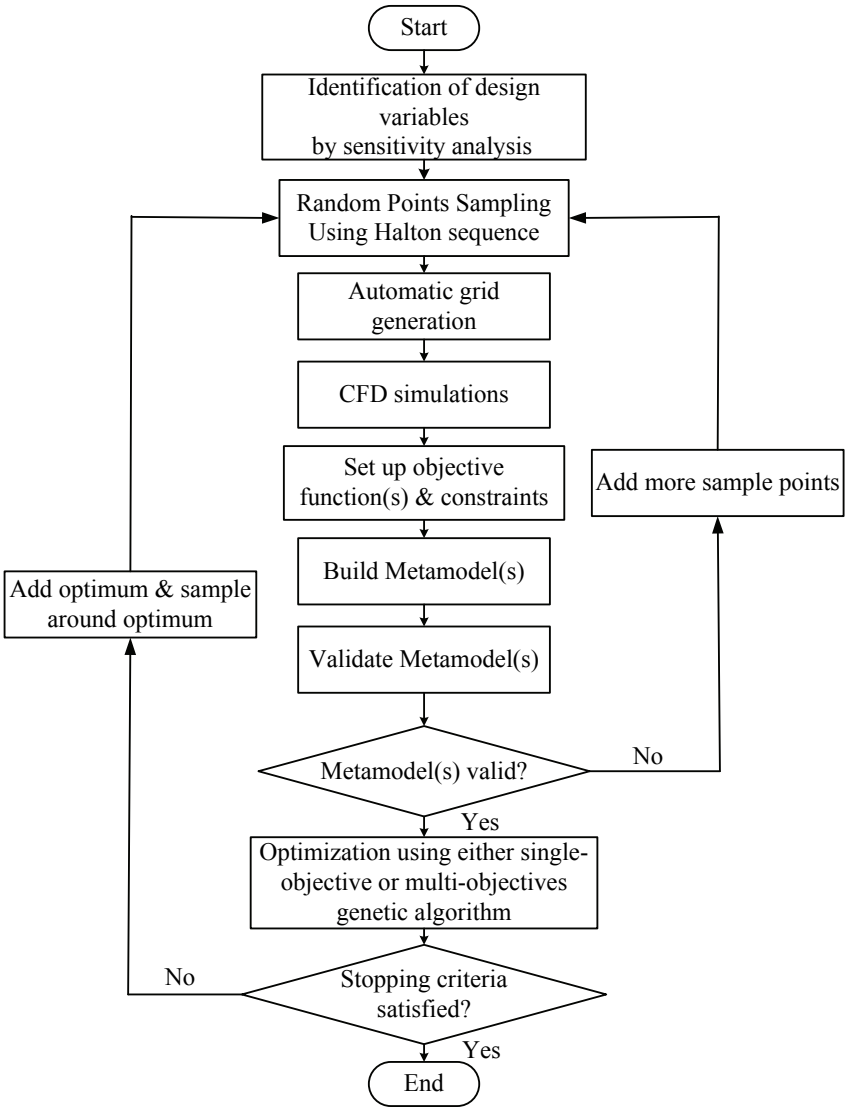

Figure 5.1 Optimization flow chart

5.3 The Basic Elements of the Optimization Tool

The basic elements of the optimization tool include an algorithm to generate Halton sequences, CFD simulation, a Kriging meta-model algorithm and a Genetic Algorithm

optimiser. Each of these will be explained in detail below.

5.3.1 Halton Sequence

DACE methods are similar to DOE methods in that they seek to maximise the amount of information that can be gleaned from a minimum number of experiments. Random points sampling arises in this context in deciding how to select the inputs at which to run the deterministic computer code (CFD simulations). This is to efficiently control or reduce the statistical uncertainty of the computed prediction. The main criteria for evaluating the suitability of this method are: how well it fills the design space, how extensible it is to high dimensional problems (many design variables), and how computationally expensive it is. To a certain extent, these criteria are found in a number of different techniques. They include:

- Latin Hypercube Sampling, LHS (McKay et al., 1979),
- Improved Distributed Hypercube Sampling, IDHS (Beachkofski and Grandhi, 2002),
- Centroidal Voronoi Tessellation, CVT (Du et al., 1999),
- Orthogonal Arrays, OA (Hedayat et al., 1999) and
- Low Discrepancy Sequences, LDS such as Hammersley, Halton, Faure, Sobol, Niederreiter, Van der Corput (Kocis and Whiten, 1997).

The IDHS has previously been regarded as the most appropriate choice for use in the optimization system as it provides very evenly distributed sample points throughout the design space. Its limitation is that it is computationally very expensive as the number of sample points, N, increases. The method chosen is the Halton method. Its sequences have a lesser cost of computation to the user. This is because there is no obvious difference in the time taken to find few points and several points irrespective of the number of dimensions. One of the good things about the Halton method is that, after the N members of a sequence are computed, it is possible to compute a sequence of length $N+i$ where, $i \in \Re$ without re-computing N. Simply put, an arbitrary number of points can be added to an existing Halton sequence and the result is also a valid Halton sequence. This quality is very attractive for choosing sample points in an optimization system since it is not often clear at the start how many points are needed to build a valid metamodel. If some measure of quality suggests that the metamodel needs more data points, then a specified number can be added, and these will still be distributed optimally.

The Halton sequence was first introduced by Halton (1960). It is derived from the one-dimensional van der Corput sequences to handle multi spatial dimensions. It is a quasi-random number generator in the sense that the points generated by this method are evenly distributed in the design space compared to the pseudo-random number generator. The

Halton sequence is built as a deterministic technique that utilizes a prime number as its base whereby each dimension uses a different prime number as the base of the calculation. The Halton formula is given in Equation (5.1).

$$x_n = \left(\Phi_{b1}(n), \ldots \Phi_{bj}(n), \ldots \Phi_{bs}(n)\right) \tag{5.1}$$

In Equation (5.1), $\Phi_{bj}(n)$ is the j^{th} radical inverse function as given in Equation (5.2). The summation is finite with the permutation coefficients $a_i(j,n)(0 \leq a_i(j,n) \leq b_j)$ coming from the digit expansion of the integer n in base b_j as shown in Equation (5.3).

$$\Phi_{bj}(n) = \sum_i a_i(j,n)\, b_j^{-i-1} \tag{5.2}$$

$$n = \sum_{i=0} a_i(j,n)\, b_j^i \tag{5.3}$$

In low dimensions ($s < 11$), the Halton sequence quickly "fills up" the design space in a well distributed pattern. However, in high dimensions, the points generated by the Halton sequence are very poorly distributed in the design space. The distribution of the points is only improved when the sequence elements N is large enough relative to the spatial dimension so that the points generated by the sequence can be evenly distributed in the design space. In order to improve the poor distributions of points in the design space at higher spatial dimensions, three approaches have been proposed. They are the generalized Halton sequence (Braaten and Weller, 1979), the reverse-radix algorithm (Kocis and Whiten, 1997) and the Halton sequence leaped (Kocis and Whiten, 1997).

The generalized Halton sequence utilizes a permutation coefficients in order to split the correlations between the inverse radical functions of various spatial dimensions by modifying Equation (5.2) to include the permutation coefficients as shown in Equation (5.4). The generalized Halton sequence is only limited to spatial dimensions $s \leq 16$. The generalized Halton sequence greatly depends on particular selected permutations but there is no technique which may result in optimal permutations of the coefficients $a_i(j,n)$.

$$\Phi_{bj}(n) = \sum_i \sigma\left(a_i(j,n)\right) b_j^{-i-1} \tag{5.4}$$

The reverse-radix algorithm is an extension of the generalized Halton sequence that provides permutations $\sigma\left(a_i(j,n)\right)$ for breaking the phases of the Halton sequence. This is achieved by permuting the values of $a_i(j,n)$ and reversing the binary digits of integers where a fixed number of base-2 digits are used and any values of $a_i(j,n)$ that are too large are removed

(Kocis and Whiten, 1997). The reverse-radix algorithm is not restricted to any number of spatial dimensions and its implementation of the permutations is simple. However, the reverse-radix algorithm brings in some extent of randomness.

The Halton sequence leaped reduces the apparent randomness associated with the reverse-radix algorithm and the generalized Halton sequence. This is attained by using only every L^{th} Halton number with the requirement that L is a prime that is distinct from all bases $b_1, \ldots, b_s$ used in the calculation. It is achieved by replacing n in Equation (5.2) with mL, where L is the leap and $m = 1, 2, 3, \ldots$. In the actual building of the Halton sequence leaped, one of the bases is skipped and is utilized as the leap value (Kocis and Whiten, 1997).

The MATLAB source codes used for the Halton sequence were developed by Burkardt (2007) and are available at `https://people.sc.fsu.edu/~burkardt/m_src/halton/halton.html`. The algorithm made use of the Halton sequence leaped approach. The inputs required by this algorithm are: number of the spatial dimension s, number of sample points N and the subsequence index of the first entry. The subsequence index is referred to as STEP in this study and it is used to restart the Halton sequence at a specific point. Also, the lower and upper limits of the design variables were also supplied to the algorithm as inputs. The Halton sequence algorithm made use of the inputs to select elements of a "leaped" subsequence of the Halton sequence. The successive jump in the Halton sequence is referred to as the LEAP and the default values provided by Burkardt (2007) has been utilized in this study. The Halton generated results in the form of $[0, 1]^s$ were multiplied by the lower and upper limits of the design variables as shown in Equation (5.5) in order to generate the exact values of evenly distributed design variables in the design space.

$$v_{ij} = v_{ij}^{l} + (v_{ij}^{u} - v_{ij}^{l})Hn_{ij} \tag{5.5}$$

In Equation (5.5), v is the design variable, l and u are the lower and upper limits of the design variables respectively. Also, i is the row position of the number of sample points generated, j is the column position of the number of dimensions (design variables) and Hn is the $m \times n$ Halton generated results.

5.3.2 Numerical Simulation

This section has been discussed in details in Sections 3.3.1 and 3.3.2 on pages 82 and 96 respectively and need not to be repeated here.

5.3.3 Metamodel Algorithm

Metamodels are typically curve fits of computer experiments. They are used in cases where computer model would otherwise have to be run a prohibitive number of times. Computer experiments provide the data for building the metamodel. Computer experiment refers to the collection of pairs of inputs and responses from a computer model. Both the input and the responses are high dimensional. These computer models are always deterministic meaning that responses from the model lack random error and that repeated runs for similar input parameters generate similar responses from the model. The advantage of the metamodel is that, once constructed, it can be executed in a small fraction of the time required for the full CFD simulation run.

There are three main types of metamodels. They are the Kriging metamodels, radial basis functions and the low-order polynomials. The Kriging metamodel is chosen because of its proven record as one of the best metamodels. It can perform very well under multiple modelling criteria (Jin et al. (2000), Guinta and Watson (1998), Daberkow and Marris (1998), Simpson et al. (2001) and Jeong et al. (2004)). The Kriging method employed here, adopts a model $\hat{y}$ that expresses the deterministic response $y(x) \in \Re^q$, for n dimensional input $x \in D \subseteq \Re^n$, as a realization of a regression model F and a random function (stochastic process) given in Equation (5.6).

$$\hat{y}(x) = F(\beta_{:,l}, x) + z_l(x), \qquad l = 1, ..., q \tag{5.6}$$

The regression model chosen is a linear combination of p chosen functions $f_j : \Re^n \longmapsto \Re$.

$$F(\beta_{:,l}, x) = \beta_{1,l} f_1(x) + ... \beta_{p,l} f_p(x)$$

Where, coefficients $\{\beta_{k,l}\}$ are regression parameters. The random process, z is assumed to have mean zero and covariance (Jin et al. (2000) and Meckesheimer et al. (2002)).

$$E[z_l(w), z_l(x)] = \sigma_l^2 R(\theta, w, x), \qquad l = 1, ..., q$$

The random process lies between $z(w)$ and $z(x)$. The process variance for the l^{th} component of the response is σ^2. The correlation model with parameter θ is $R(\theta, w, x)$. The number of basis functions in the regression is p and q is the dimensionality of responses. A variety of correlation functions can be used but the widely used correlation functions is the Gaussian correlation function proposed by Sacks et al. (1989).

The detailed formulation of the Kriging model can be found in Lophaven et al. (2002*b*) and Lophaven et al. (2002*a*). MATLAB source codes are available at `http://www2.imm.dtu.dk/~hbn/dace/`. The model comprises various MATLAB programs but the ones that are required by the optimization tool are the "dacefit" and "predictor". The dacefit computes the elements of the Kriging model. The correlation parameter θ is computed by the dacefit through a method of nonlinear optimization as discussed in detail in Lophaven et al. (2002*a*). One of the advantages of the dacefit is that it allows multiple responses. The predictor estimates the responses and errors at untried sites. The main inputs to the metamodel algorithm are the design variables and responses that are obtained from the numerical simulation of dry gas face seals. Other inputs that need to be specified prior to the simulation are the starting point *theta*, lower bounds *lob* and upper bounds *upb* of the correlation parameters θ. It is recommended that the starting point should be close to the upper bounds of the design variables (Lophaven et al., 2002*a*). Different regression models and correlation functions shown in Table 5.1 are used in the metamodel algorithm. Only one regression model and one correlation model are selected to carry out the simulation. The metamodel algorithm is used in the format given below:

$$[dmodel1,\ perf] = dacefit\,(S, Y, @regpoly2, @corrgauss, theta, lob, upb)$$

Table 5.1 Various regression and correlation models used in the metamodel algorithm

Syntax	Description
Regression models	
*regpoly*0	Zero order polynomial
*regpoly*1	First order polynomial
*regpoly*2	Second order polynomial
Correlation models	
correxp	Exponential
correxpg	Generalized exponential
corrgauss	Gaussian
corrlin	Linear
corrspherical	Spherical
corrspline	Cubic spline

5.3.4 Genetic Algorithm

Optimizers are divided into two groups: the linear programming and the non-linear programming. Every optimizer has a set of problems for which it is best suited. A good knowledge of the nature of the problem is a requirement as this allows for the choice of a more suitable optimization tool. In the subsequent paragraphs, each of the tools, as well as the problems to which they are most efficiently applicable, shall be discussed briefly.

The linear programming tool provides optimal solutions to problems that are perfectly represented by a set of linear equations. The equations solved for in dry gas face seals are non-linear in nature hence the use of the simplex method, which is an example of the linear programming tool is not suitable for the optimization of dry gas face seals. The deterministic and stochastic methods are examples of non-linear programming. The deterministic method uses the concepts of successive search within an optimization space, based on the function gradient information. The objective is to find where the function gradient is null using the direction to where it points. In dry gas face seals, the problems are usually complex, non-linear, and are partly described by non-differentiable functions, which demand more efficient numerical methods for their solutions. In these types of problems, the stochastic method, searches for the optimal value through probability rules, working in an oriented random manner. The main advantage of using this method is that it only makes use of the information from the objective function without requiring knowledge of its derivatives or possible discontinuities. Overviews of all the optimization tools have been reported by Garcia et al. (2006).

The most widely used stochastic techniques include: Evolutionary strategies (ESs), Genetic algorithms (GAs) and the Simulated Annealing (SA). ESs and GAs emulate nature's evolutionary behaviour, while the SA is based on the physical processes of annealing a material. There are many differences and similarities among these three methods. The SA searches from a single initial point while the ESs and GAs use a population of possible solutions. Solutions from one population are used to form the next solutions. This is caused by the expectation that the new generation (through the use of genetic operators) may be better than the previous one. Solutions that will give new solutions are chosen by evaluating their fitness, such that, their chances of reproduction is proportional to their suitability. This is carried out until the best solution is improved or the number of generations is attained.

Genetic Algorithms are well known and widely used in optimization. They overcome the major draw backs of simple deterministic optimizers, that is, they are more efficient when the main objective is to obtain an estimated optimum for multimodal functions in the best possible way. One of the positive aspects of GAs is that they can optimize with continuous or discrete parameters while not requiring gradient information. The likely lack of continuity in the fitness functions has little consequence on the whole performance of the optimization. The genetic algorithm are opposed to be confined in logical optima as well as are able to handle large number of parameters and are very suitable for parallel computing. Additionally, the genetic algorithm give a record of semi-optimum parameters rather than a single solution; and they can also be used for a range of optimization problems.

The MATLAB genetic algorithm (MathWorks, 2008) is used in this study. The algorithm is

divided into two parts, single objective optimization and multi objectives optimization. The two parts are discussed in the subsequent sections.

5.3.4.1 Single Objective Optimization

The single objective optimization involves two approaches based on the performance parameter chosen as the objective. In the first approach, the opening force is maximized without any consideration of the seal leakage. In the second approach, a performance parameter referred to as design efficiency parameter (E_P) is maximized. The design efficiency parameter is a function of the opening force and seal leakage and it is defined as the ratio of the opening force to seal leakage. The advantage of maximizing the design efficiency parameter rather than the opening force is that, varying the geometrical parameters does not only affect the opening force but as well affect the seal leakage.

The objective function in any of the two methods is defined in Equation (5.7). The objective to be maximized is y, x is the independent parameter having n design variables. The fitness function $mod1$, is built from the metamodel algorithm and relates the design variables to the seal performance parameters. For the maximization of only the opening force, the metamodel used the design variables with only the opening force while for the maximization of the design efficiency parameter, the metamodel used the design efficiency parameter, (E_P) with the design variables for generating the fitness function. The negative sign in Equation (5.7) indicates that the objective is being maximized. The lower and upper limits of the design variables are used as the constraints for the optimization process.

$$y = -predictor(x, mod1) \tag{5.7}$$

The algorithm begins by creating a random initial population based on a specified size. A sequence of new populations is then created by the algorithm. At each generational step, the algorithm uses the individuals in the current generation to create the next population. In order to create the new population, the algorithm performs the following steps:

- scores each member of the current population by computing its fitness value.
- Scales the raw fitness scores to convert them into a more usable range of values.
- Selects members, called parents based on their fitness.
- A certain number of individuals in the existing population that have lower fitness are chosen as elite. These elite individuals are sent on to the subsequent population.
- Produces children from the parents. Children are brought into being either by effecting random changes to a single parent-mutation or by combining the vector entries of a pair of parents known as crossover.

- Replaces the current population with the children to form the next generation.

The following conditions are used in determining when the genetic algorithm will stop. The algorithm stops as soon as any of the following criteria is met.

1. When the number of generations reaches a specified value. The higher the number, the longer the simulation will take. It is advisable to set an appreciable number and check after some iterations to see that the solution converges towards the set value else the number might be increase to reduce error in the simulation.
2. After a given clock time equal to time limit that is set. It is recommended that this be set to a very large figure in order to avoid an early termination of the process.
3. At the point where the highest value of the fitness function in the current population is less than or equal to the fitness limit.
4. When the weighted average variation in the fitness function value in excess of stall generations is less than function tolerance.
5. The function tolerance is an important parameter that determines the accuracy of the simulation. The default value of 1e-006 is chosen. The algorithm runs until the weighted average change in the fitness value over stall generation is less than the function tolerance.
6. When there is no improvement in the objective function through a time interval (in seconds) equal to stall time limit. It is advisable to set this value to infinity.
7. The nonlinear constraint tolerance is used to ascertain the practicability with respect to nonlinear constraints. The default value of 1e-006 is chosen.

5.3.4.2 Multi-Objective Optimization

The essence of optimizing dry gas face seals is to maximize the opening force and minimize the seal leakage as the geometrical parameters are varied. This assigns a vector character to the optimization problem. Two large groups of solution arise. The dominated solutions group, in which there will be solutions in all aspects worse than others. The second solutions set, the non-dominated or Pareto-optimal solutions in which there will be solutions which are better than others in some aspects and worse in others. In these cases, a comparison among results cannot be made, neither can one set of results be said to be better than other. These Pareto-optimal solutions form a set of infinite solutions within a finite space. Determining this set is the main purpose of the multi-objectives genetic algorithm approach. Making an effective choice of solution requires additional knowledge of the main problem such as the relative importance of different objectives. Again, the design efficiency parameter will be used in selecting the best result from the pool of the Pareto-optimal solutions.

The objective functions for this optimization problem are given in Equation (5.8). It consists of two objectives that returns a vector y of size 2-by-1 and x independent parameters of n design variables. The first objective $y(1)$, is the opening force being maximized and the second objective, $y(2)$ is the seal leakage being minimized. The fitness function relating the opening force with the design variables is $mod1$ and $mod2$ is the fitness function relating the seal leakage with the design variables. Both fitness functions are built by the metamodel algorithm.

$$\begin{aligned} y(1) &= -predictor(x, mod1) \\ y(2) &= predictor(x, mod2) \end{aligned} \tag{5.8}$$

The multiobjective genetic algorithm used in this study is the NSGA-II (Fast Non-dominated Sorting Genetic Algorithm). It is an improved version of the traditional NSGA that lacks elitism and has the difficulties of choosing the optimal parameter value for sharing parameter. This improved version has a better sorting algorithm that incorporates elitism and sharing parameter needs not to be chosen a priori.

It used the controlled elitist genetic approach. This controlled elitist genetic approach favours individuals with better fitness value (rank). It also favours individuals which can help increase the diversity of the population even though they have a lower fitness value. This is achieved by controlling the elite members of the population while the optimization is in progress. The two options used in controlling the elitism are the Pareto fraction and the distance crowding respectively. Maintaining the diversity of population is very important in order to obtain a good convergence to an optimal Pareto front. The Pareto fraction regulates the number of individuals by the Pareto front (elite members) while the distance crowding helps to maintain diversity on a front by favouring individuals that are relatively far away on the front.

The algorithm begins by creating a random initial population based on the population size that is chosen. The next generation of the population is computed using the non-dominated rank and a distance measure of the individuals in the current generation. The initialized population is sorted based on non-domination. An individual is said to dominate another if the objective functions of it is no worse than the other and at least in one of its objective functions it is better than the other. This is done by assigning a non-dominated rank to each individual using the relative fitness. Individual p is said to dominate q when p has a lower rank than q. Also, individual p is said to dominate q if p is strictly better than q in at least one objective and p is no worse than q in every one of the objectives. Two individuals p and q are considered to have equal ranks if neither dominates the other.

Once the population has been initialized, a crowding distance is assigned to each individual. The distance measure of an individual is used to evaluate individuals that have equal rank. It is basically a measure of how far an individual is with respect to the other individuals having the same rank. The individuals are selected using a crowded-comparison-operator ($\prec_n$). The comparison is carried out based on the following:

1. non-domination rank p_{rank}, that is individuals in front F_i will have their rank as $p_{rank} = i$
2. crowding distance $F_i(d_j), \quad p \prec_n q$, if
   (a) $p_{rank} \prec q_{rank}$ or
   (b) If p and q belong to the same front F_i, then $F_i(d_p) > F_i(d_q)$ that is the crowding distance should be more.

The offspring population is combined with the current generation population and selection is performed to set up the individuals for the next generation. Since all the previous and current best individuals are included in the population, elitism is ensured. Population is sorted based on non-domination. The fresh generation is filled by each front subsequently until the population size goes beyond the current population size. If the population exceeds N by adding all the individuals in front F_i, then individuals in front F_i are selected based on their crowding distance in the descending order until the population size is N. The process is repeated to generate the subsequent generations. Detailed formulation of the NSGA-II can found in Deb et al. (2002) and Konak et al. (2006).

The genetic operators used in the optimization tool are of two types. The simulated binary crossover operator and the polynomial mutation. The simulated binary crossover operator simulates the binary crossover as observed in nature and expressed in Equation (5.9)

$$\begin{aligned} c_{1,k} &= \frac{1}{2}[(1-\beta_k)p_{1,k} + (1+\beta_k)p_{2,k}] \\ c_{2,k} &= \frac{1}{2}[(1+\beta_k)p_{1,k} + (1-\beta_k)p_{2,k}] \end{aligned} \tag{5.9}$$

Where $c_{i,k}$ is the i^{th} child with k^{th} component, $p_{i,k}$ is the selected parent and β_k is always greater than or equal to zero and it is the sample from a random number generated having the density given in Equation (5.10).

$$\begin{aligned} p(\beta) &= \frac{1}{2}(\eta_c + 1)\beta^{\eta_c}, \qquad if \qquad 0 \leq \beta \leq 1 \\ p(\beta) &= \frac{1}{2}(\eta_c + 1)\frac{1}{\beta^{\eta_c+2}}, \qquad if \qquad \beta > 1 \end{aligned} \tag{5.10}$$

The distribution index for crossover is η_c and it determines how well spread the children will be from their parents.

The polynomial mutation is expressed in Equation (5.11).

$$c_k = p_k + (p_k^u - p_k^l)\delta_k \tag{5.11}$$

Where c_k is the child, p_k is the parent with p_k^u being the upper bound on the parent component, p_k^l is the lower bound and δ_k is the small variation calculated from a polynomial distribution using Equation (5.12).

$$\begin{aligned} \delta_k &= (2r_k)\frac{1}{\eta_m + 1} - 1, \qquad if \qquad r_k < 0.5 \\ \delta_k &= 1 - [2(1 - r_k)]^{\frac{1}{\eta_m + 1}} \qquad if \qquad r_k \geq 0.5 \end{aligned} \tag{5.12}$$

The uniformly sampled random number, r_k that lies between 0 and 1 and η_m is the mutation distribution index.

There are three different criteria for determining when the algorithm has to stop. The algorithm stops when any one of the following stopping criteria given below is met.

1. When the maximum number of generations is reached; the default value is 200 times the number of variables (design variables).
2. When the average change in the spread of the Pareto front over the stall generations is less than function tolerance specified. The default value is 100.
3. The third criterion is the upper time limit given in seconds. The default value is infinity.

5.4 Optimization Tool Testing

5.4.1 Illustrative Use of the Halton Sequence

To illustrate the advantage of using the Halton sequence, three cases with different subsequence index numbers were considered. All three cases used the same number of sample points in order to evaluate how well the generated sample points fill in the design space when one case is considered one at a time. The first case used a subsequence index number that is equal to zero; the second case considered a subsequence index number equal to 20 and the third case used a subsequence index number equal to 40. The number of sample points used for each case is 20. Shown in Figure 5.2 is a scattered plot from sample points

generated from the first case. It can be seen from Figure 5.2 that the points are somehow uniformly distributed in the design space. Figure 5.3 is a scattered plot for two cases - zero and twenty subsequence index numbers respectively. It can be seen from Figure 5.3 that by adding the second case, more areas of the design space are covered. None of the points overlay one another. Also, adding the third case to the other two cases in the design space will indicate that using another subsequence index number higher than the other two cases will fill in more areas of the design space as shown in Figure 5.4. Combining these three cases together is like generating sample points in a design space with 60 sample points and a subsequence number equal to zero. Figure 5.5 shows a scattered plot of the Halton generated points from the three cases above and a fourth case having 60 sample points and a zero subsequence index number. It can be seen from Figure 5.5 that the generated sample points from the three cases lay on top of the generated sample points from the fourth case which validates the above claim.

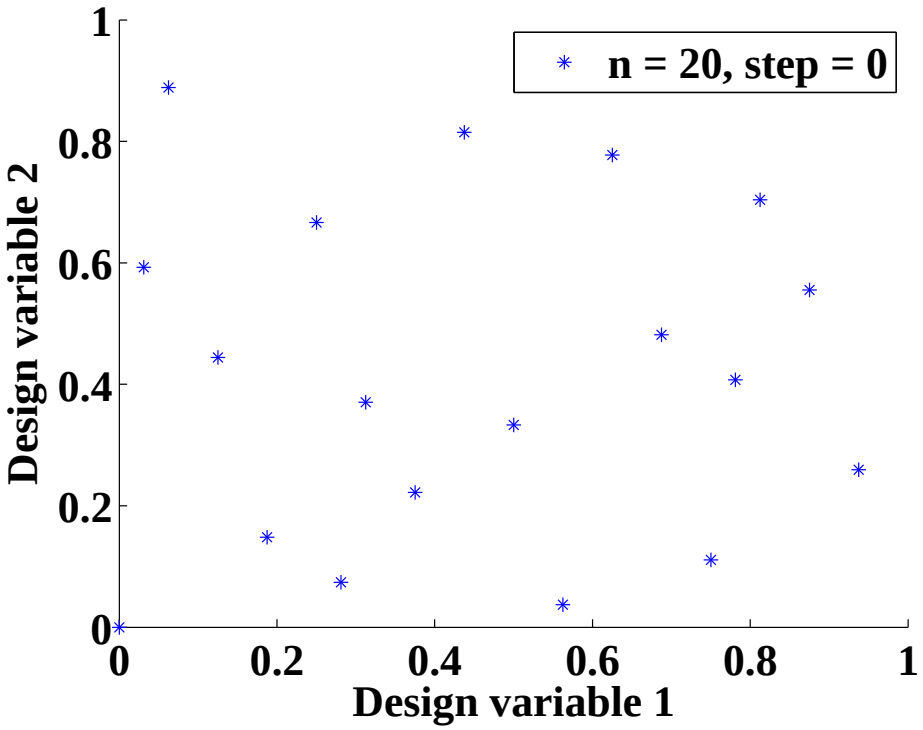

Figure 5.2 Halton generated points with 20 sample points and zero subsequence index number

5.4.2 Single & Multi Objective Optimization Examples

In order to test the applicability of the optimization tool, two examples comprising of two set of equations have been used herein. The two equations considered are expressed in Equation 5.13 (from page 6-27 in MathWorks (2009)) for a single objective optimization problem and Equation 5.14 (from page 8-7 in MathWorks (2009)) for a multi objective

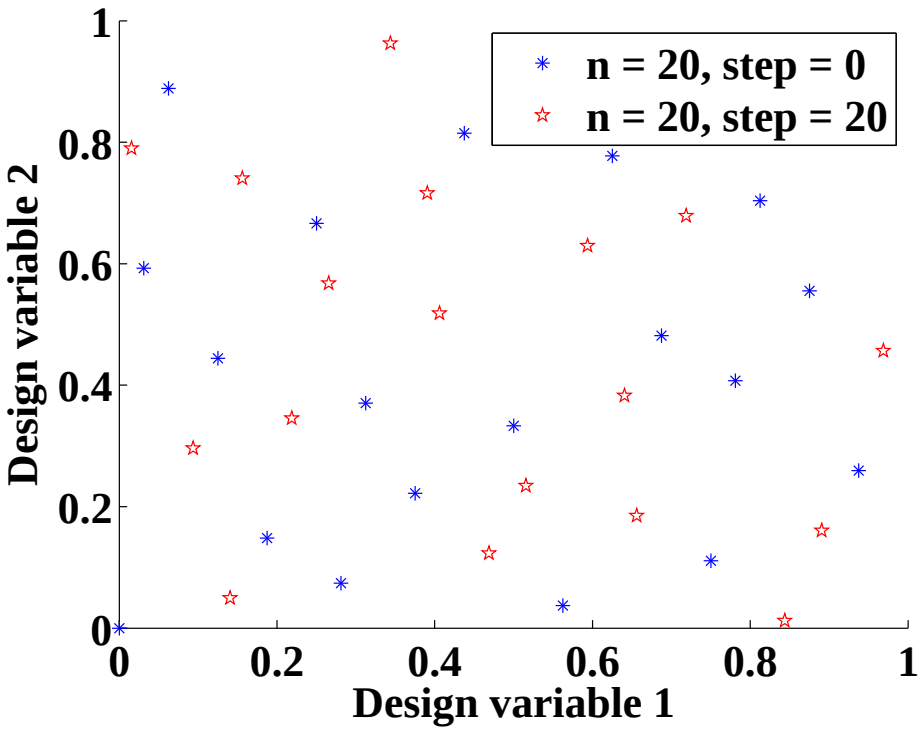

Figure 5.3 **Halton generated points with 20 sample points for a zero and twenty subsequence index numbers**

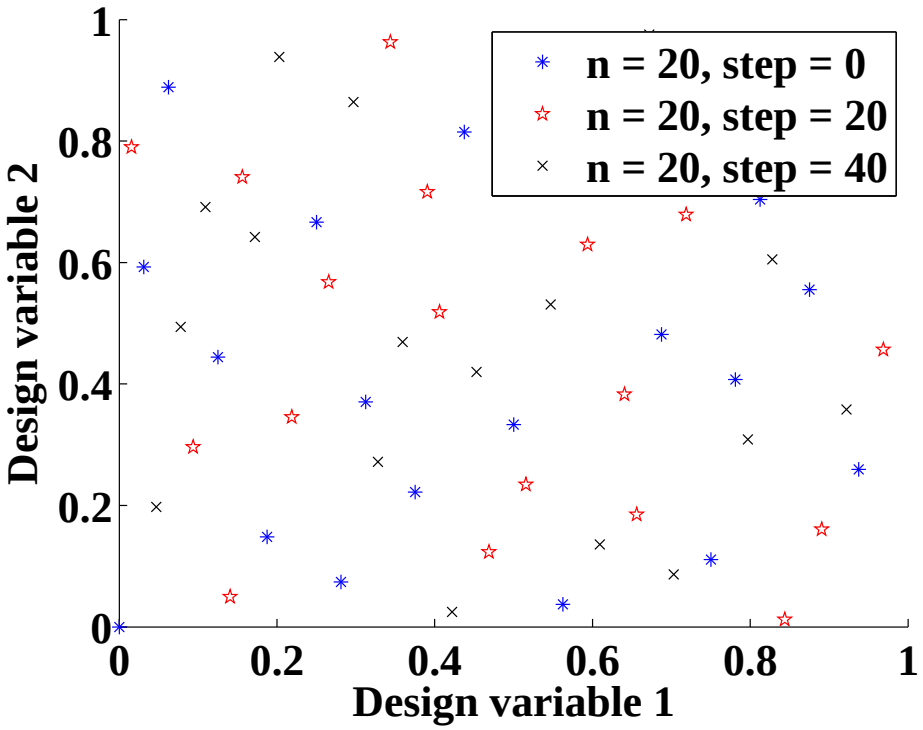

Figure 5.4 **Halton generated points with 20 sample points for a zero, twenty and forty subsequence index numbers**

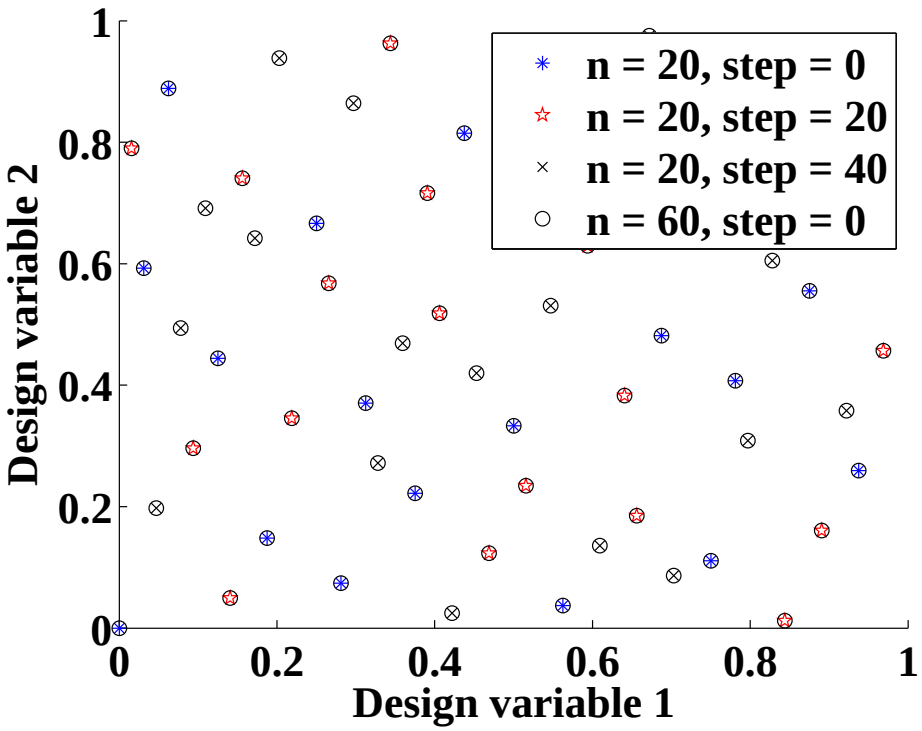

Figure 5.5 **Halton generated points with 20 sample points for a zero, twenty and forty subsequence index numbers and 60 sample points for a zero subsequence index number**

optimization problem.

$$f(x) = \frac{x_1^2}{2} + x_2^2 - x_1 x_2 - 2x_1 - 6x_2 \tag{5.13}$$

$$\begin{aligned} y_1 &= x_1^4 - 10x_1^2 + x_1 x_2 + x_2^4 - x_1^2 x_2^2 \\ y_2 &= x_2^4 - x_1^2 x_2^2 + x_1^4 + x_1 x_2 \end{aligned} \tag{5.14}$$

Equation 5.13 is a quadratic expression which is a MATLAB inbuilt function called "lincontest6.m" (MathWorks, 2008). The response $f(x)$ in Equation 5.13 depends on two independent variables (design variables) x_1 and x_2 respectively. Equation 5.14 has two responses - y_1 and y_2 both depending on two design variables x_1 and x_2. Equation 5.13 is an example of a constrained nonlinear optimization and used herein for a single objective optimization. The inequality constraints used for the single objective optimization is given in Equation 5.15 and the lower bounds used are $x_1 \geq 0$ and $x_2 \geq 0$.

$$\begin{aligned} x_1 + x_2 &\leq 2, \\ -x_1 + 2x_2 &\leq 2, \\ 2x_1 + x_2 &\leq 3 \end{aligned} \tag{5.15}$$

Equation 5.14 is used for a multi objective optimization whose population size is 60 with a population type of double vector. A crowding distance for distance measure function and a Pareto front population fraction of 0.7 were used for the multi objective optimization. The lower and upper limit bounds used for the multi objective optimization are $[-5, -5]$ and $[5, 5]$ respectively.

For the single objective and multi objective optimization, the inputs used for the metamodel algorithm are: $lob = [1e-1\ 1e-1]$, $upb = [20\ 20]$ and $theta = [10\ 10]$, where lob and upb are the lower and upper bounds for the correlation parameters, θ and $theta$ is the starting point of the correlation parameters. The number of sample points chosen for the Halton sequence algorithm is 90 for the single and multi objective optimization. Instead of coding these equations into a MATLAB function handles to be called directly by the genetic algorithm, the metamodel algorithm is used in evaluating these equations based on sample points generated by the Halton sequence algorithm. The fitness functions generated by the metamodel algorithm are called by the optimizer - genetic algorithm. This approach is comparable to how a dry gas face seal can be optimized by optimization tool.

Table 5.2 Optimal solutions of a single objective optimization of a nonlinear constraints problem

	Design variable 1 (x_1)		Design variable 2 (x_2)		Response ($f(x)$)	
	Exact	Model	Exact	Model	Exact	Model
*regpoly*0	0.6815	0.6853	1.3193	1.3157	-8.2054	-8.2011
% Diff.		-0.5576		0.2729		0.0524
*regpoly*2	0.6815	0.6815	1.3193	1.3193	-8.2054	-8.2054
% Diff.		0		0		0

For the single objective optimization, Equation 5.13 was minimized in two cases. One of the cases employed the optimization tool whereby the optimizer used the fitness function generated by the metamodel algorithm and its solutions referred to as "Model". In the second case, Equation 5.13 is held in the MATLAB inbuilt function, "lincontest6.m" and called directly by the optimizer and its solutions referred to as "Exact". The solutions obtained from both cases are given in Table 5.2.

It is observed that variation of the regression model greatly affects the optimal solutions obtained from the optimization tool. This can be seen in Table 5.2 and Figures B.1, B.2, B.3 and B.4 in Appendix B whereby the zero order and second order polynomials were employed as the regression models respectively. Selecting the zero order polynomial significantly affected the optimal solutions and variations of all other inputs to the metamodel algorithm and number of sample points in the Halton sequence algorithm. In the case of the second order polynomial selected, it was observed that variations of the other inputs to the metamodel algorithm and number of sample points in the Halton sequence

algorithm only have little effects on the optimal solutions, provided the bounds of the correlation parameters satisfy $0 < lop \leq upb$. Variations of the correlation models do not affect the optimal solutions for the single objective optimization problem considered herein.

The optimal solutions obtained from the optimization tool and from the exact optimization of Equation 5.13 are comparable for the zero order polynomial regression model since the percentage differences between the two cases are quite small. For the second order polynomial regression model, the "Exact" and "Model" optimal solutions are the same. Shown in Figure 5.6, are population plots showing the linear inequalities, bound constraints and level curves of the fitness function of a single objective optimization. In Figure 5.6, the red dashed lines represent the inequalities of $x_1 + x_2 \leq 2$, the blue dashed lines show the the inequalities of $-x_1 + 2x_2 \leq 2$ and the black dashed lines show the inequalities of $2x_1 + x_2 \leq 3$. Also, in Figure 5.6, the magenta dashed lines represent the lower bound variable x_1 and the green dashed lines show the the lower bound variable x_2 while the contour lines are level curves of the objective function. It can be seen in Figure 5.6 that the star point which is the optimum response, falls within the bound constraints.

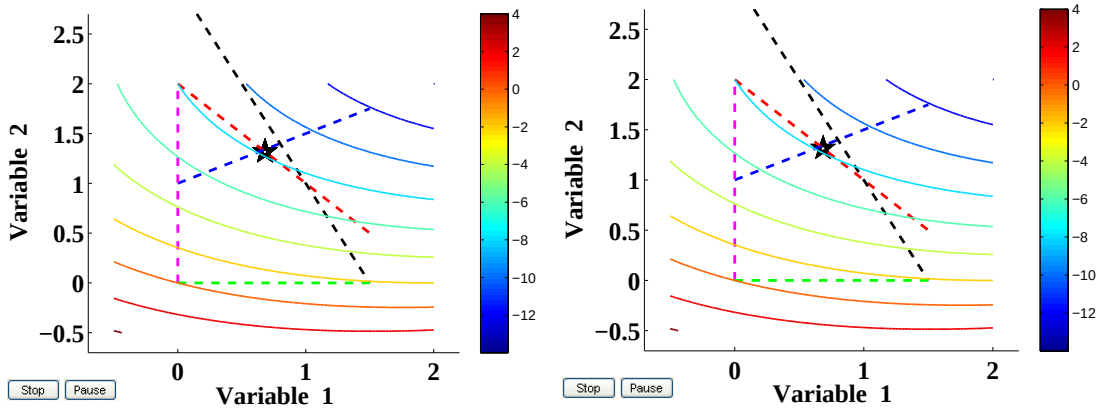

(a) Exact (b) Model

Figure 5.6 A population plot showing the linear inequalities, bound constraints and level curves of the fitness function of a single objective optimization

For the multi objective optimization, Equation 5.14 was also minimized in consideration of two cases. The two cases considered are the "Exact" and "Model" as previously stated for the single objective optimization. The results of the multi objective optimization are presented in the form as shown in Figure 5.7 containing both objectives values (Figure 5.7(a)) and design variables values (Figure 5.7(b)). The plot shown in Figure 5.7(a) is plotted in the objective function space and represents the trade off between the two objectives.

Since the regression model chosen is very sensitive to the optimal solutions, selecting a regression model that is not appropriate for a particular optimization problem makes it

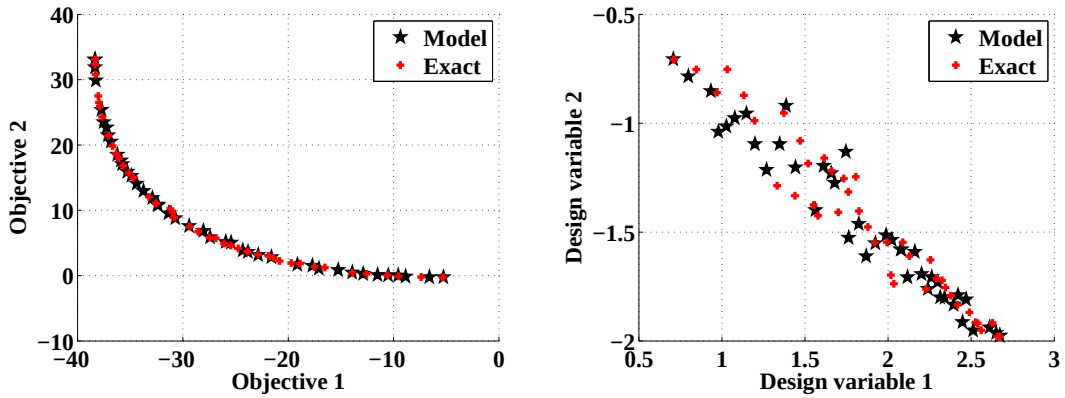

(a) Responses (b) Design variables

Figure 5.7 A Pareto front solution of the multi objective optimization showing the responses and design variables

difficult in selecting all other inputs to the metamodel algorithm and number of sample points in the Halton sequence algorithm. From the analysis carried, the regression model with polynomial of order 2 and the Gaussian correlation model will be appropriate for the optimization of dry gas face seals. The time taken to execute the Halton sequence algorithm in MATLAB was 0.08s, the metamodel execution time was 0.21s and the optimizer execution time was 14.77s for the single objective optimization when the population size was set to 200. Also, the time taken to execute the Halton sequence algorithm in MATLAB was 0.08s, the metamodel execution time was 0.43s and the optimizer execution time was 159.9845s for the multi objective optimization when the population size was set to 60.

It can be deduced from the optimization of the single and multi objective optimizations that the optimization tool presented herein is an appropriate tool for carrying out optimization of any machine or machine parts provided the design variables and the responses can be identified.

5.5 Chapter Summary

In this chapter, an automatic optimization tool that can be used for the optimization of dry gas face seal has been presented and illustrated with examples and MATLAB codes on how it can be implemented. The optimization tool comprises the Halton sequence algorithm, metamodel algorithm and an optimizer capable of handling either single objective function or multi objective functions. Once the design variables and objective function(s) have been identified, it can be used for any mechanical face seal optimization. It can also be used for any generic optimization such as machine components or elements optimization. The developed tool requires little human attention.

The optimization of a dry gas face seal that employs the optimization tool presented is accomplished in four sequential steps. The first step is the generation of uniformly distributed points for the geometrical parameters (in this context referred to as design variables) of the seal. The second step involves carrying out numerical simulations of the fluid flow in the seal interface based on the selected design variables to obtain performance parameters (in this context referred to as responses). The third step consists of using the design variables and responses as inputs to the metamodel algorithm to generate fitness function(s) which are surrogates of the entire seal design system. The forth step entails searching for the design variables that will produce the optimal solutions (responses) by the optimizer based on the generated fitness function(s) from the metamodel algorithm. In essence, with this approach, the optimizer does not directly depends on the results from the numerical simulations of the fluid flow in the seal interface but rather depends on the fitness function(s) generated by the metamodel algorithm.

Chapter 6

Parametric Analysis and Optimization Tool Application

6.1 Introduction

This chapter covers the sensitivity analysis of a spiral groove face seal and the design and study of a novel seal as well as the parametric analysis of a spiral groove face seal. Also covered in this chapter is the design of a generic seal face profile employing the optimization tool presented in Chapter 5. The sensitivity analysis was carried out in order to identify the appropriate design variables that more directly affect the seal performance parameters. In order to highlight the limitations of employing the parametric analysis in predicting optimal values of a seal, a parametric analysis was carried out on a spiral groove face seal. The design of a seal utilising the optimization tool is carried out in order to demonstrate the application of automated optimization to the design of a spiral groove face seal. Three design objectives have been selected in the optimization of the dry gas face seal in this chapter. They are: maximization of the opening force alone without consideration of the leakage, maximization of the design efficiency parameter which is the ratio of the opening force to the leakage and maximization of the opening force and minimization of the seal leakage. The first two design objectives employed a single objective optimization formulation while the last design objective employed the multi objectives optimization approach. The predicted optimal values from the optimization tool are compared against a 3D CFD simulated values at the predicted optimal values.

6.2 Parametric Analysis of a Seal Face Profile Geometry

A parametric design study is carried out on a face seal with spiral grooves geometry. The load carrying capacities and leakage, as well as design efficiency parameter of the

seal geometry are calculated for different values of groove radius, and depth, number of grooves, groove angle and groove-land width ratio. The seal outer and inner ring diameters were fixed by the space available between the sealing shaft and the seal housing of either a pump or compressor that utilises these seals. The geometrical parameters considered were varied one at a time in order to evaluate their optimum values with regards to seal performance parameters such as opening force, seal leakage and design efficiency parameter. This analysis employed the Reynolds equation model and the operating conditions given in Table 6.1. Also considered in this analysis are the dimensions of the geometrical parameters of the "Base" case given in Table 6.3.

Table 6.1 Operating parameters for optimum design of seals employing parametric analysis

Parameter	Value
Sealed fluid pressure	$5\,bar$
Sealed fluid temperature	120^oC
Rotating speed	$5000\,rpm$
Peak surface roughness amplitude	$0.000001\,\mu m$
Initial waviness amplitude	$0\,\mu m$
Radial taper	$0\,rad$
Sealing fluid	Air - Ideal gas

In order to examine the effects of varying the hydrostatic dam width, different groove radius ranging from $60\,mm$ to $69\,mm$ were considered while maintaining a constant fluid film thickness of $4\,\mu m$. The dimensions of the geometrical parameters apart from the groove radius of the "Base" case in Table 6.3 and operating conditions given in Table 6.1 were utilised in this analysis. The results obtained in terms of seal opening force, seal leakage and design efficiency parameter, while varying the groove radius are shown in Figure 6.1. As can be seen in Figure 6.1, the lower the hydrostatic dam width (i.e., smaller groove radius), the higher the opening force (Figure 6.1(a)) as well as higher leakage (Figure 6.1(b)). The larger the hydrostatic dam width, the lower the leakage that is produced at the expense of less opening force which is required to keep the sealing faces apart. Examining Figure 6.1(c) shows that the larger the hydrostatic dam, the higher the design efficiency that is generated. The maximum opening force, corresponding to a value of $4.48\,KN$, occurred when the groove radius was $60\,mm$, the minimum leakage, $7.79 \times 10^{-6}\,kg/s$, occurred when the groove radius was $68.4\,mm$ and the maximum design efficiency parameter, $0.50\,GNs/kg$ occurred when the groove radius was $68.4\,mm$.

The hydrostatic dam width presents a restriction to the fluid flow in the seal interface and most of the frictional pressure drop occurs at this section. Also most of the gas expansion occurs at the hydrostatic dam (Zuk, 1976). It is known that the cooling effect associated with the expansion is sometimes several times more than the heating effect due

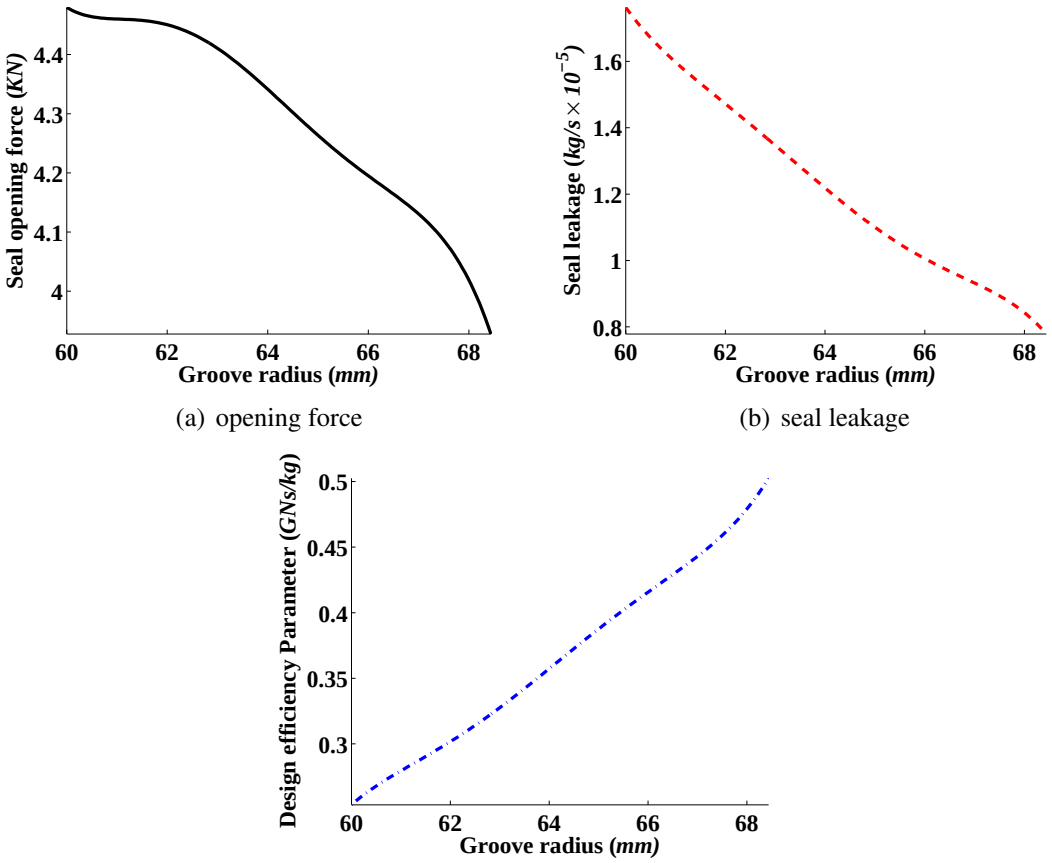

(a) opening force

(b) seal leakage

(c) design efficiency parameter

Figure 6.1 Performance parameters of a spiral groove seal as a function of groove radius

to viscous dissipation. The net effect is the cooling of the gas near the hydrostatic dam and consequently a considerable amount of heat conduction takes place from the seal rings to the gas in the vicinity of the hydrostatic dam. The temperature gradient thus set up in the seal rings tends to distort the seal faces in a way as to produce a divergent flow passage. This effect causes stability problems and sometimes causes seal face contact at the seal ring outer diameter. A wider hydrostatic dam design may overcome this effect since a wider dam may cause a higher heat generation which may result in neutralizing the cooling effect due to gas expansion. A compromise has to be made in selecting the optimum hydrostatic dam width that will produce maximum positive stiffness and minimum leakage since the wider the hydrostatic dam the less stiffness the seal may produce.

In order to examine the effects of varying the groove depth, different groove depths ranging from $3\,\mu m$ to $30\,\mu m$ were considered while maintaining a constant fluid film thickness of $4\,\mu m$. The dimensions of the geometrical parameters apart from the groove depth of the "Base" case in Table 6.3 and operating conditions given in Table 6.1 were utilised in this analysis. The results obtained in terms of seal opening force, seal leakage and

design efficiency while varying the groove depth are shown in Figure 6.2. The maximum opening force with a value of $4.13\,KN$ occurred when the groove depth was $10.38\,\mu m$, the minimum leakage, $6.82 \times 10^{-6}\,kg/s$, occurred when the groove depth was $3\,\mu m$ and the maximum design efficiency parameter with a value of $0.54\,GNs/kg$ occurred when the groove depth was $3\,\mu m$. As can be seen in Figure 6.2, there exist a certain groove depth where there is a maximum opening force (Figure 6.2(a)) as well as a maximum seal leakage (Figure 6.2(b)). This value of groove depth, where there is maximum opening force and leakage corresponds to about $10.38\,\mu m$. At this optimum groove depth ($10.38\,\mu m$), the minimum design efficiency parameter is obtained as shown in Figure 6.2(c).

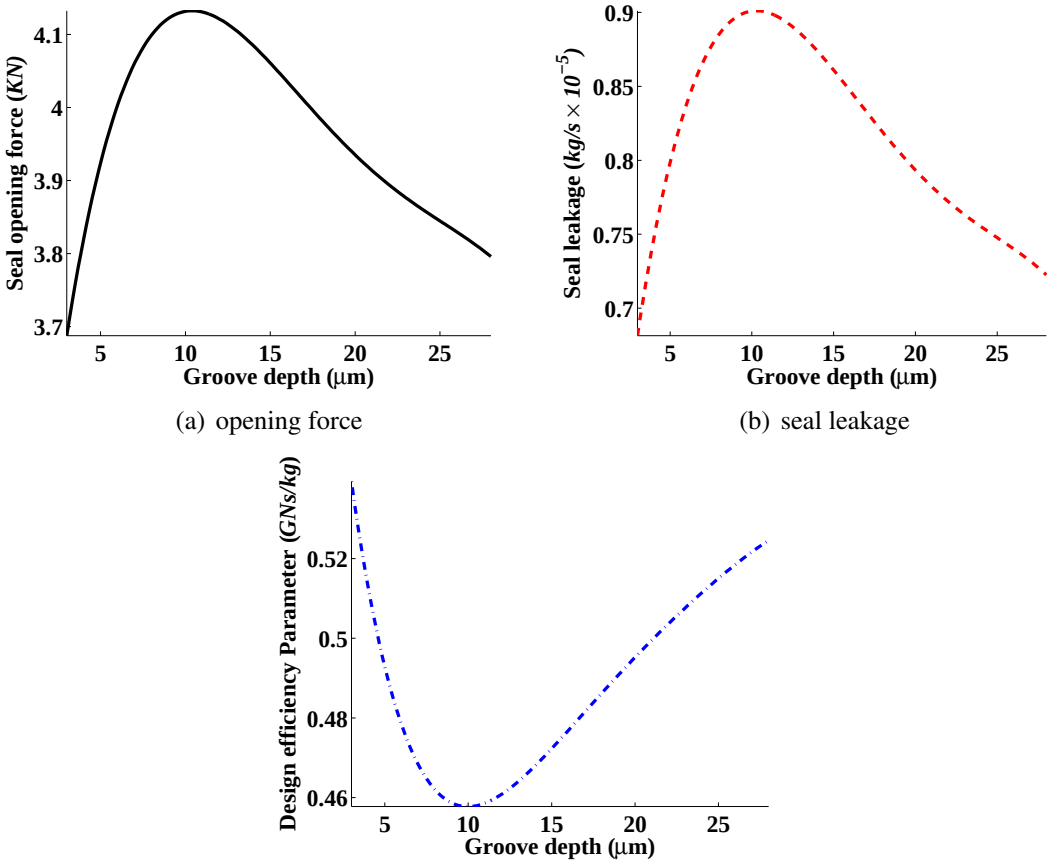

(a) opening force

(b) seal leakage

(c) design efficiency parameter

Figure 6.2 Performance parameters of a spiral groove seal as a function of groove depth

Examining the results obtained from the analysis, it can be seen that the deeper the groove depth, provided it is not greater than the optimum value ($10.38\,\mu m$), the greater the load capacity that is generated. Beyond the optimum value of $10.38\,\mu m$, the deeper the groove, the less load capacity that is generated. The shallow grooves up to the point of the optimum groove depth have higher film stiffness than the deeper grooves. Since the higher the film stiffness, the better its performance in tracking the seal nose piece, the shallow groove

is preferable but for consideration of wear effects, the seal is usually designed to have appreciable groove depth. The physical importance of the seal having a higher film stiffness is that if the seal tends to open, the self-acting force drops off rapidly and the closing force increases rapidly. Also, if the seal tends to close, the opposite effect occurs hence the seal will always operate in the non-contacting mode.

In order to investigate the effects of varying the number of grooves, different numbers of grooves ranging from 7 to 40 were considered while maintaining a constant fluid film thickness of $4\,\mu m$. The dimensions of the geometrical parameters, apart from the number of grooves, of the "Base" case in Table 6.3 together with the operating conditions given in Table 6.1 were utilised in this analysis. The results obtained in terms of seal opening force, seal leakage and design efficiency parameter while varying the number of grooves are shown in Figure 6.3.

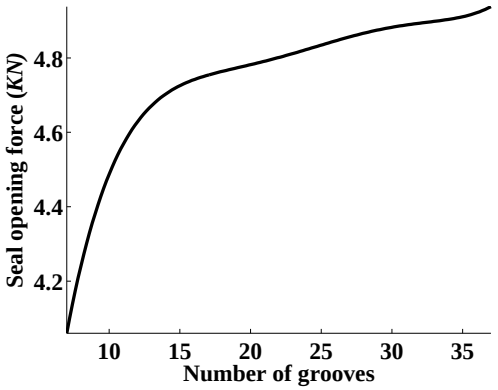

(a) opening force

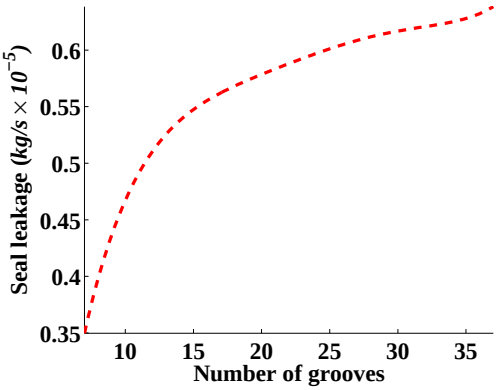

(b) seal leakage

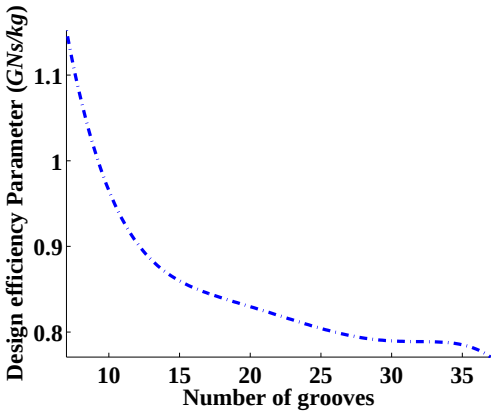

(c) design efficiency parameter

Figure 6.3 Performance parameters of a spiral groove seal as a function of number of grooves

As can be seen in Figure 6.3, as the number of grooves increases to about 15, there is a gradual increase in opening force (Figure 6.3(a)) as well as gradual increase in seal leakage (Figure 6.3(b)). As number of grooves increases beyond about 15, increasing the number of

grooves does not have any significant increase in the opening force and seal leakage. The reverse is observed for the case of the design efficiency parameter (Figure 6.3(c)) whereby increasing the number of grooves to about 15, sharply decreases the design efficiency parameter. Also, increasing the number of grooves beyond 15 does not have any significant decrease on the design efficiency parameter. Increasing the number of grooves reduces the circumferential length of each groove thereby reducing the area available for the sealing pressure to act on. The maximum opening force, $4.94\,KN$, occurred when the number of grooves was 37, the minimum leakage with a value of $3.50 \times 10^{-6}\,kg/s$ occurred when the number of grooves was 7 and the maximum design efficiency parameter , $1.15\,GNs/kg$, occurred when the number of grooves was 7. It can be deduced therefore that a compromise must be made while selecting the number of grooves which will give maximum opening force and minimum leakage since both opening force and seal leakage increases as number of grooves is increased.

The effects of varying the groove-to-land width ratio are investigated next. Different groove-to-land width ratios ranging from 0.3 to 0.7 were examined while maintaining a constant fluid film thickness of $4\,\mu m$. Once again the dimensions of the geometrical parameters, apart from the groove-to-land width ratio of the "Base" case in Table 6.3, and the operating conditions given in Table 6.1, were utilised in this analysis. The results obtained in terms of seal opening force, seal leakage and design efficiency parameter, while varying the groove-to-land width ratios, are shown in Figure 6.4.

As can be observed in Figure 6.4, the higher the groove-to-land width ratio, the higher the opening force (Figure 6.4(a)) as well as higher leakage (Figure 6.4(b)). The reverse is found for the case of the design efficiency parameter (Figure 6.4(c)) whereby increasing the groove-to-land width ratio, decreases the design efficiency parameter. The maximum opening force, $4.09\,KN$, occurred when the groove-to-land width ratio was 0.64, the minimum leakage, $7.13 \times 10^{-6}\,kg/s$, occurred when the groove-to-land width ratio was 0.25 and the maximum design efficiency parameter, with a value of $0.53\,GNs/kg$, occurred when the groove-to-land width ratio was 0.25. It can be deduced therefore that a compromise has to be made in selecting the groove-to-land width ratio which will give maximum opening force and minimum leakage since both opening force and seal leakage increases as groove-to-land width ratio is increased.

The final parametric analysis concerned the effects of varying the groove angle, different groove angles ranging from 12^o to 89^o were tested while once again maintaining a constant fluid film thickness of $4\,\mu m$. As done before, the dimensions of the geometrical parameters, apart from the groove angle of the "Base" case in Table 6.3 and operating conditions given in Table 6.1, were utilised in this analysis. The results obtained in terms of seal opening

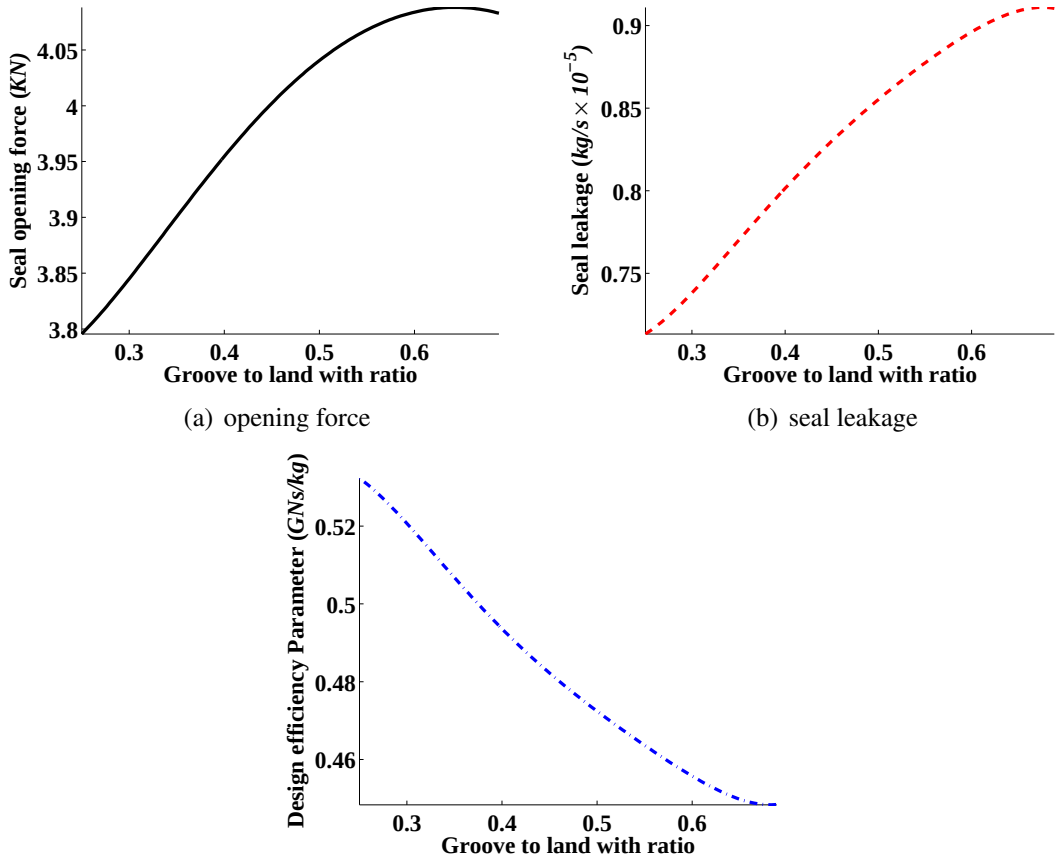

(a) opening force

(b) seal leakage

(c) design efficiency parameter

Figure 6.4 Performance parameters of a spiral groove seal as a function of groove to land width ratio

force, seal leakage and design efficiency parameter, while varying the groove angles, are shown in Figure 6.5.

As will be seen in Figure 6.5, the smaller the groove angle, the higher the opening force (Figure 6.5(a)) as well as higher leakage (Figure 6.5(b)). The reverse trend is observed in the case of the design efficiency parameter (Figure 6.5(c)) whereby increasing the groove angle, increases the design efficiency parameter. The maximum opening force, $4.03\,KN$, occurred when the groove angle was 12^o, the minimum leakage, $5.40 \times 10^{-6}\,kg/s$, occurred when the groove angle was 82^o and the maximum design efficiency parameter, with a value of $0.64\,GNs/kg$, occurred when the groove angle was 68.4^o. Once again a compromise has to be made in selecting the groove angle which will give a maximum opening force and minimum leakage since both opening force and seal leakage decrease as the groove angle is increased.

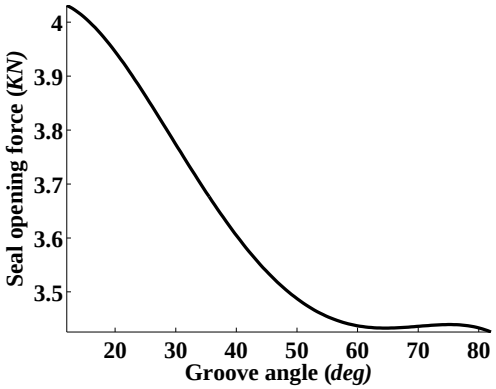

(a) opening force

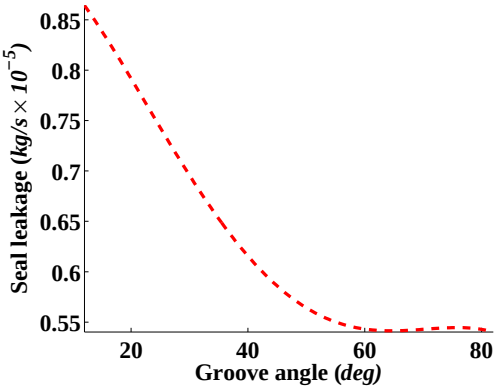

(b) seal leakage

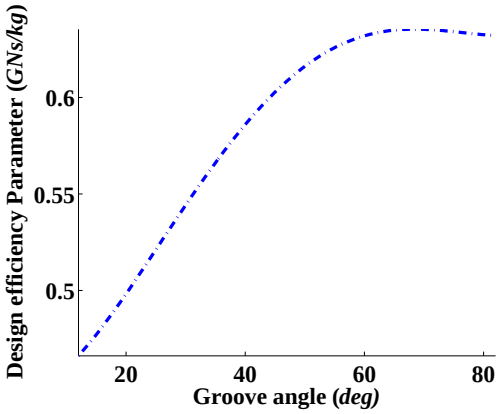

(c) design efficiency parameter

Figure 6.5 Performance parameters of a spiral groove seal as a function of groove angle

6.3 Sensitivity Analysis

A sensitivity analysis is carried out on two different face seals with grooves geometry. One of the groove geometries is a spiral groove and the other, the novel seal, has straight inclined grooves. The load carrying capacities (opening force), leakage, stiffness and friction force of the seal were calculated for different combinations of design variables employing the 3D CFD model. The design variables include: groove radius (r_g), groove depth (h_g), number of grooves (n_g), groove spiral angle (α) and groove width percentage (γ). The design variables were varied one at a time in order to determine the sensitivities of the performance parameters to the variation of the individual design variables. The operating condition parameters and their values considered for this analysis are given in Table 6.2.

For the examination of the spiral groove face seal, a fluid film thickness of $4.4\mu m$ and the "Base" case given in Table 6.3, for the purpose of results comparison, have been considered. The discussion of the sensitivity analysis for the spiral groove face seal is presented as follows:

Table 6.2 Operating condition parameters used for sensitivity analysis

Parameter	Value
Sealed fluid pressure	$6\,bar$
Sealed fluid temperature	120^oC
Rotating speed	$10000\,rpm$
Fluid film thickness	$3-10\,\mu m$
Sealing fluid	Air - Ideal gas

Table 6.3 Spiral groove face seal design variables used for sensitivity analysis

Cases	r_g (mm)	h_g (μm)	n_g	γ	α (deg)
Base	67.75	6.50	12	0.5	15.00
1 - r_g varied	67.50	6.50	12	0.5	15.00
2 - h_g varied	67.75	12.0	12	0.5	15.00
3 - n_g varied	67.75	6.50	8	0.5	15.00
4 - γ varied	67.75	6.50	12	0.7	15.00
5 - α varied	67.75	6.50	12	0.5	45

- Reducing the groove radius by 0.4% will result in a 5.6% increase of the stiffness (K_z), 0.0024% decrease of the power dependence of the leakage rate ($\dot{m}$) on the fluid film thickness, 3.7% decrease of the design efficiency parameter (E_P) and a 0.8% decrease of the friction coefficient (f_r).
- Increasing the groove depth by 84.6% will result in a 50.84% increase of the stiffness, 0.0081% decrease of the power dependence of the leakage rate on the fluid film thickness (h_f), 20.3% decrease of the design efficiency parameter and about 10.92% decrease of the friction coefficient.
- Reducing the number of groove by 33.3% will result in a 48.6% increase of the stiffness, 0.0278% decrease of the power dependence of the leakage rate on the fluid film thickness, 17.42% decrease of the design efficiency parameter and a 6% decrease of the friction coefficient.
- Increasing the groove width percentage by 40% will result in a 8.92% decrease of the stiffness, 0.0053% increase of the power dependence of the leakage rate on the fluid film thickness, 9.14% decrease of the design efficiency parameter and a 6.74% decrease of the friction coefficient.
- Increasing the spiral angle by 200% will result in a 98.15% increase of the stiffness, 0.0271% decrease of the power dependence of the leakage rate on the fluid film thickness, 20.5% decrease of the design efficiency parameter and a 11.03% decrease of the friction coefficient.

Considering a fluid film thickness of $4.68\mu m$, operating condition parameters in Table 6.2 and the "Base" case in Table 6.4 for the purpose of results comparison, the sensitivity analysis utilising the novel seal is presented as follows:

Table 6.4 Novel seal design variables used for sensitivity analysis

Cases	r_g (mm)	h_g (μm)	n_g	γ	α (deg)
Base	67.75	6.50	12	0.5	65.00
1 - r_g varied	70.00	6.50	12	0.5	15.00
2 - h_g varied	67.75	15.0	12	0.5	15.00
3 - n_g varied	67.75	6.50	20	0.5	15.00
4 - γ varied	67.75	6.50	12	0.7	15.00
5 - α varied	67.75	6.50	12	0.5	110

- Increasing the groove radius by 3.32% will result in a 1.21% increase of the stiffness (K_z), 0.012% increase of the power dependence of the leakage rate ($\dot{m}$) on the fluid film thickness, 10.04% increase of the design efficiency parameter (E_P) and a 0.32% decrease of the friction coefficient (f_r).
- Increasing the groove depth by 130.8% will result in a 39.07% decrease of the stiffness, 0.018% increase of the power dependence of the leakage rate on the fluid film thickness (h_f), 6.80% decrease of the design efficiency parameter and a 2.62% decrease of the friction coefficient.
- Increasing the number of groove by 66.67% will result in a 57.31% decrease of the stiffness, 0.030% increase of the power dependence of the leakage rate on the fluid film thickness, 31.96% increase of the design efficiency parameter and a 16.25% increase of the friction coefficient.
- Increasing the groove width percentage by 40% will result in a 13.28% increase of the stiffness, 0.0013% decrease of the power dependence of the leakage rate on the fluid film thickness, 8.81% decrease of the design efficiency parameter and a 9.03% decrease of the friction coefficient.
- Increasing the groove angle by 69.23% will result in a 20.80% increase of the stiffness, 0.0011% increase of the power dependence of the leakage rate on the fluid film thickness, 9.63% decrease of the design efficiency parameter and a 11.72% decrease of the friction coefficient.

The results shown in Figure 6.6 for the spiral groove face seal and Figure 6.7 for the novel seal and the discussion above show that varying any of the design variables (r_g, h_g, n_g, γ and α) significantly affects the seal performance parameters. Even where an automatic optimization method is employed the performance parameters to be used as objectives remains a designer's choice. However the designer must ensure that the performance parameters chosen as a design objective are also representative of the performance of the ones not employed directly in the optimization routine so that the optimal results generated are generally acceptable.

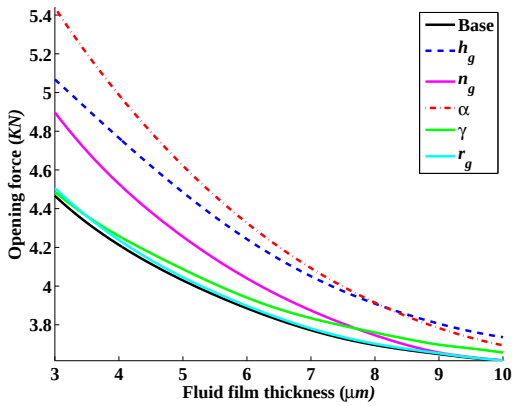

(a) opening force

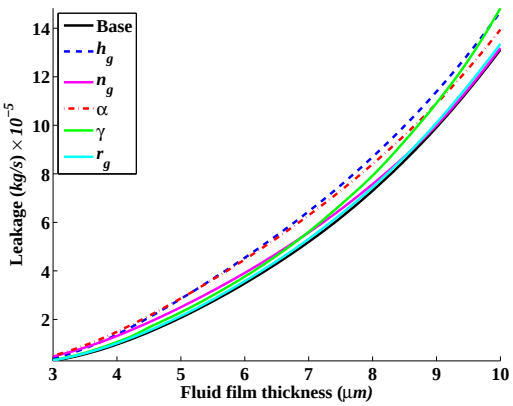

(b) Seal leakage

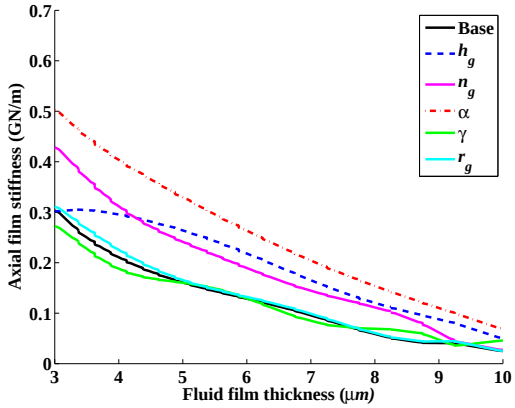

(c) Axial film stiffness

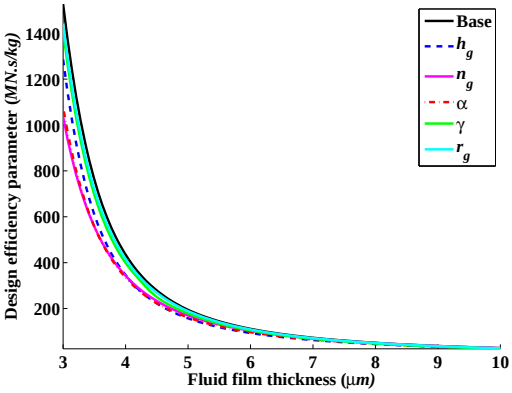

(d) Design efficiency parameter

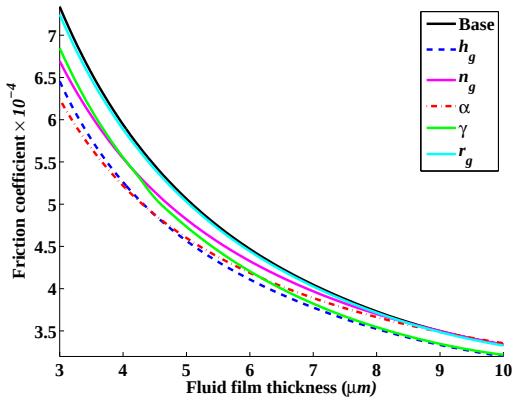

(e) Friction coefficient

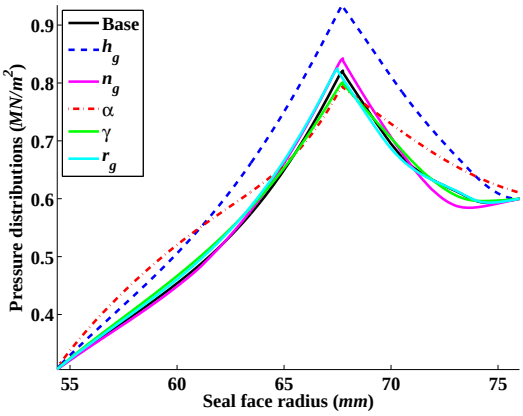

(f) Pressure distributions as a function of seal face radial length

Figure 6.6 Performance parameters of a spiral groove face seal for a sensitivity analysis, seal operating at sealed fluid pressure of 6 bar, rotating speed of 10,000 rpm and sealed fluid temperature of 120°C

6.4 Design of a Geometrical Seal Face Profile Utilising the Optimization Tool

Three cases have been analyzed using three different objective function(s), one at a time. The first of the cases required the maximization of the opening force without taking into

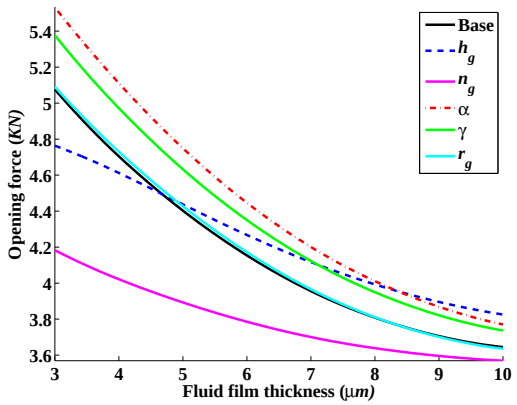

(a) opening force

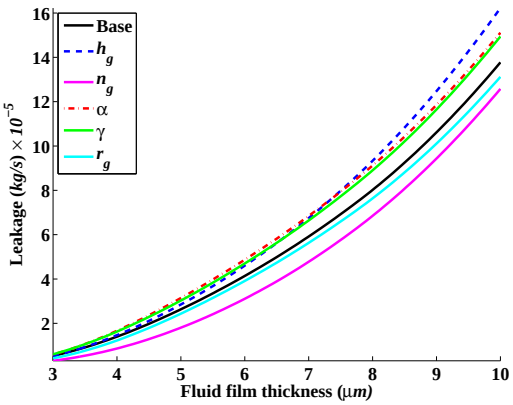

(b) Seal leakage

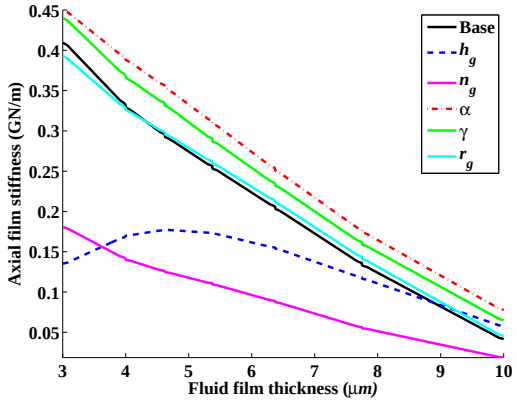

(c) Axial film stiffness

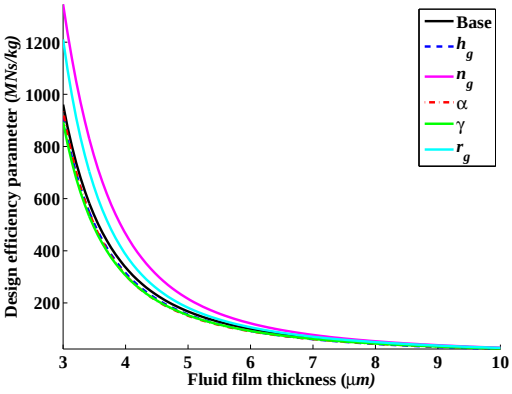

(d) Design efficiency parameter

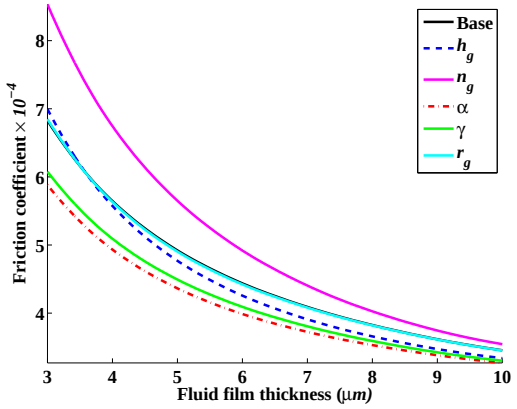

(e) Friction coefficient

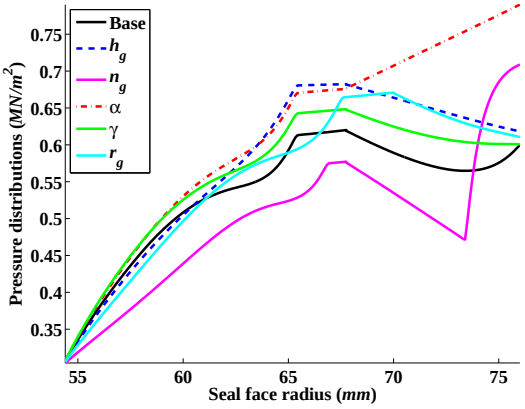

(f) Pressure distributions as a function of seal face radial length

Figure 6.7 Performance parameters of a novel seal for a sensitivity analysis, seal operating at sealed fluid pressure of 6 bar, rotating speed of 10,000 rpm and sealed fluid temperature of 120°C

account the seal leakage. The second case consisted of the maximization of the design efficiency parameter, defined as the ratio of the opening force to the seal leakage. For the third case the maximization of the opening force as well as minimization of the seal leakage was specified. The first two cases used a single objective genetic algorithm while in the third case a multiobjective genetic algorithm was employed. The number of CFD runs was

56; population size used for all cases was 1000 while the number of generations was fixed at 1000.

A spiral groove face seal is optimized and the geometrical parameters set as design variables, with their upper and lower limit values used as constraints, are given in Table 6.5. Other geometrical parameters that were kept as fixed parameters are: seal outside radius of 76mm, seal inside radius of 54.4mm and coning angle of $4.2785 \times 10^{-5}\,rad$. The operating conditions used in this study are given in Table 6.6. Air - ideal gas was used as the sealing fluid. A constant fluid film thickness was used in all cases.

Table 6.5 Design variables with lower and upper constraints for optimum design of seals employing optimization tool

Constraints	$\mathbf{r_g}$ (mm)	$\mathbf{h_g}$ (μm)	$\mathbf{n_g}$	γ	α (deg)
Lower	60.0000	3.00	8	0.3	12.00
Upper	66.7812	11.78	20	0.7	86.53

Table 6.6 Operating parameters for optimization

Parameter	**Value**
Sealed fluid pressure	$100\,bar$
Sealed fluid temperature	120^oC
Rotating speed	$10000\,rpm$
Fluid film thickness	$3.98\,\mu m$
Sealing fluid	Air - Ideal gas

The results of the optimized seal are given in Table 6.7. From the results presented in Table 6.7, the optimum groove angle of the spiral groove face seal is about 52^o for all three design objectives. The single objective optimization with design efficiency parameter and multi objective optimization produced similar optimal results. The optimal results produced by these two design objectives are: groove radius of about $66.6\,mm$, number of grooves, 9, and groove-to-land width ratio of 0.37. A significant difference is observed for the optimum groove depth between the single objective optimization with design efficiency parameter and the multi objective optimization. The multi objective optimization generates a groove depth 36% greater than the single objective optimization with design efficiency parameter. For the single objective optimization with maximization of opening force, the optimum values produced are: groove radius, $62.4\,mm$, number of grooves, 10, groove-to-land width ratio 0.61 and groove depth $11.7\,\mu m$.

Table 6.7 Optimal solutions obtained using different objective functions

Cases	CFD runs	r_g (mm)	h_g (mm)	n_g	γ	α (deg)	F_o (N) $\times 10^4$	$\dot{m}$ (kg/s) $\times 10^{-3}$	E_p (Ns/kg) $\times 10^7$
Single Objective F_o	56	62.4	11.7	10	0.61	52.82	7.94	4.94	1.61
Single Objective E_p	56	66.6	5.31	9	0.37	52.31	7.32	3.31	2.21
Multi Objective F_o & $\dot{m}$	56	66.6	7.2	9	0.37	52.32	7.32	3.31	2.21

6.5 Optimization Tool validation

The predicted optimal values from the optimization tool presented in Section 6.4 are compared with 3D CFD simulations. The CFD simulations were carried out based on the optimized parameters of the three cases considered in Section 6.4. The outputs of the optimization runs such as opening force, leakage and design efficiency parameter were compared with performance parameters obtained from the CFD simulations, which are given in Table 6.7. The same operating conditions used in Section 6.4 were applied to the CFD simulations for comparison. The results are presented in Table 6.8. The results show that maximizing the design efficiency parameter produces the best results since this method has the least percentage difference between the CFD results and optimized results. The comparison shows a 0.07% difference of the design efficiency parameter, 0.03% difference of the opening force and 0.09% difference of the leakage.

Table 6.8 Comparison of optimization results with 3D CFD results based on the predicted optimal results using a spiral groove face seal

Objective	Leakage			Opening Force			Design efficiency parameter		
	Optimized (kg/s) $\times 10^{-3}$	CFD (kg/s) $\times 10^{-3}$	% Diff.	Optimized (N)	CFD (N)	% Diff.	Optimized (Ns/kg) $\times 10^7$	CFD (Ns/kg) $\times 10^7$	% Diff.
Single Objective F_o	4.94308	4.6847	5.23	79447.8	80578.6	1.42	1.60723	1.72004	7.02
Single Objective E_p	3.31423	3.3111	0.09	73225.4	73203.8	0.03	2.20940	2.21085	0.07
Multi Objective F_o & $\dot{m}$	3.31421	3.3988	2.55	73224.4	73968.2	1.02	2.20939	2.17633	1.50

The closest result to the maximization of the design efficiency parameter is the multi-objective optimization method whereby the opening force is maximized and the leakage minimized. This method shows a 1.50% difference of the design efficiency parameter, 1.02% difference of opening force and 2.55% difference of the leakage. The maximization of the opening force without taking into account the leakage method produces the highest percentage difference in the results comparison. This method shows a 7.02% difference of the design efficiency parameter, 1.42% difference of the opening force and 5.23% difference of the leakage.

The parameters that corresponded to the maximization of the design efficiency parameter term were selected to carry out a further set of CFD simulations where the fluid film thickness was varied from $3\,\mu m$ to $10\,\mu m$ while still using the operating conditions stated in Table 6.2. The CFD results are compared with the "Base" case stated in Table 6.3. Figure 6.8 presents the results of the "Base" case and of the "optimized" seal. The "optimized" seal produced higher stiffness and opening force than the "Base" case. Also, the "optimized" seal produced less leakage and a lower power consumption than the "Base" case. Shown in Figure 6.9 are the schematic diagram of the geometrical seal face profiles before and after the optimization process. It can be deduced therefore that the "optimized" seal will be more stable in operation since the results produced by the "optimized" seal are in all ways better than the "Base" case.

6.6 Chapter Summary

The traditional method of optimizing mechanical face seal is based on the management of conflicting trends performance and requires extensive experience since it is very difficult to select the optimum values of the design variables from the pool of results produced from a parametric analysis study. This happen since in some cases, increasing a certain design variable may increase both the opening force and seal leakage while in some other cases increasing another design variable may increase the opening force and decrease the leakage. An efficient solution to the conflicting problem can be obtained by employing a genetic algorithm that is incorporated in the optimization tool and will conduct the searching for the optimum values of the design variables in an automated manner.

Results presented in this chapter show that good fitness functions can be generated by the metamodel from Fifty six CFD simulation runs and sufficient for an optimization process. Optimization of dry gas face seal is a nonlinear bound constraints optimization; hence the lower and upper limits of the design variables must be specified as inputs to the optimizer.

The most important performance parameters to be considered in the optimization of dry

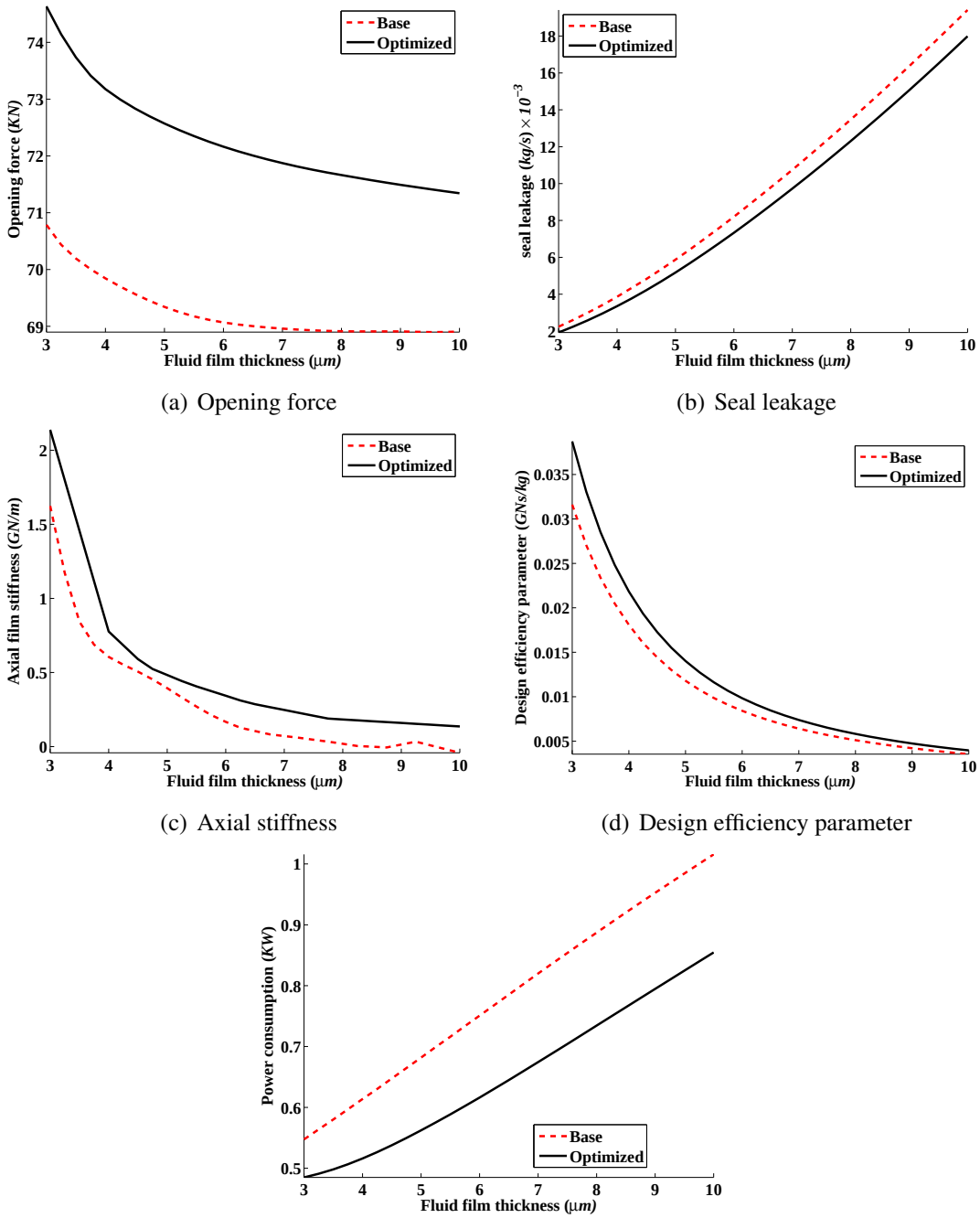

(a) Opening force

(b) Seal leakage

(c) Axial stiffness

(d) Design efficiency parameter

(e) Power consumption

Figure 6.8 Comparison plots of performance parameters as a function of fluid film thickness before and after optimization

gas face seal, which can in general represent all the seal performance parameters, are seal leakage, opening force and design efficiency parameter. Three cases of objective function(s) were tested. They were maximization of the opening force, maximization of the design efficiency parameter both representing single objective cases and the multi objective situation of maximization of the opening force and minimization of the leakage. The maximization of the design efficiency parameter returned the best results when compared against CFD simulation results based on the predicted optimal results.

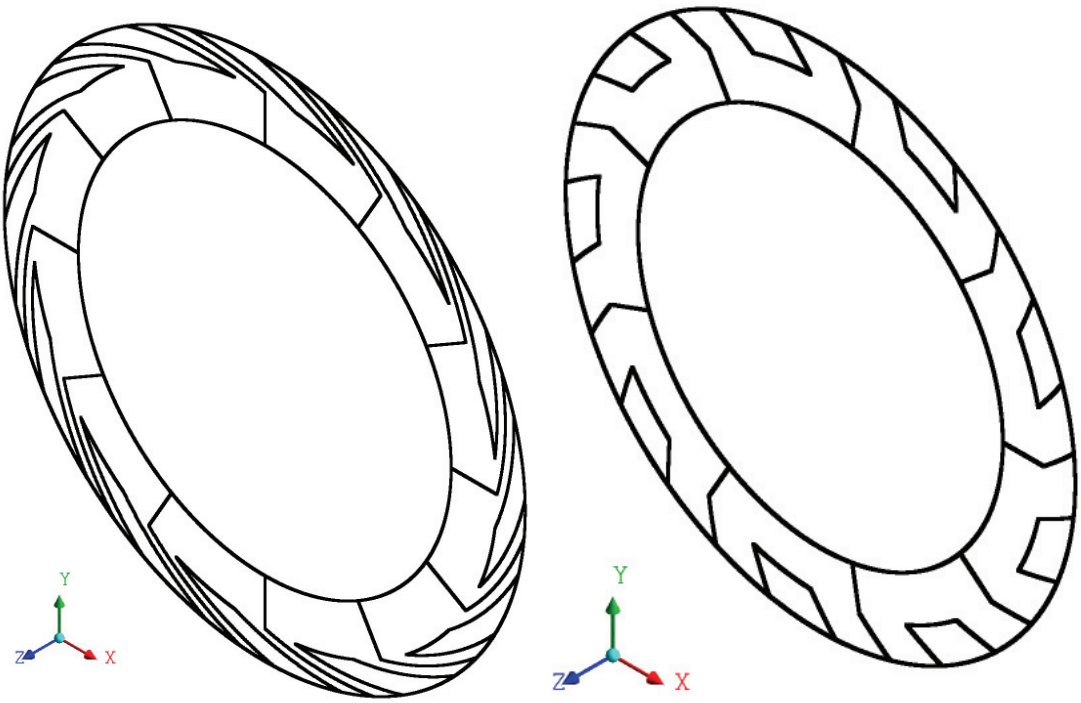

(a) Before optimization (b) After optimization

Figure 6.9 Geometrical seal face profiles before and after optimization

The improvements achieved from the optimization of the spiral groove face seal utilising the optimization tool are very significant. For a fluid film thickness of $4\,\mu m$, the following observations are made by comparing the results of the seal before and after optimization of the spiral groove face seal:

- The opening force generated for the "Base" case has a value of $69.85\,KN$ while for the "optimized" seal has a value of $73.18\,KN$ which amount to about 4.77% increase of opening force.
- The leakage generated for the "Base" case has a value of $3.86 \times 10^{-3}\,kg/s$ while for the "optimized" seal has a value of $3.35 \times 10^{-3}\,kg/s$ which amount to about 13.19% reduction of seal leakage.
- The design efficiency parameter generated for the "Base" case has a value of $0.018\,GNs/kg$ while for the "optimized" seal has a value of $0.022\,GNs/kg$ which amount to about 20.69% increase of design efficiency parameter.
- The axial film stiffness generated for the "Base" case has a value of $0.61\,GN/m$ while for the "optimized" seal has a value of $0.78\,GN/m$ which amount to about 28.28% increase of axial film stiffness.
- The power consumption generated for the "Base" case has a value of $0.61\,KW$ while for the "optimized" seal has a value of $0.52\,KW$ which amount to about 15.92% reduction of power consumption.

Chapter 7

Conclusion & Further Work

7.1 Work Summing-up and Overall Conclusions

Dry gas face seals are self-regulating during operation. However for this to occur a proper balance of forces must be established. The seal opening force is dependent on numerous variables. If the running gap increases, the opening force decreases. If the running gap decreases, the opening force will increase as a result of the grooves generating more lift. The closing force is more easily adjusted by manipulating the balance ratio. Increasing the balance diameter causes a decrease in the closing force whilst decreasing the balance diameter causes an increase in the closing force. To achieve optimum seal performance is to identify the running gap at which the opening and closing forces are exactly balanced. This is obtained from the force-film thickness curve. Since the seals must be pressure balanced, a proper balance of the opening and closing forces must be achieved with a leakage gap that has tolerable leakage. The gap must be small enough so that the leakage is minimal but it must be large enough so that power dissipation, due to shear in the film, and face deformation, are tolerable. Therefore the design of the sealing gap is vital to seal performance and the pressure distribution in the gap and the mass leakage through the seal interface must be analyzed.

The opening force which is obtained from the integration of the pressure distribution over the surface area of the seal interface is difficult to compute when the seal geometrical face profile is complex. The opening force is a function of rotational speed, gas pressures and temperatures, groove geometry and the running gap. Therefore, the opening force must be calculated by employing a numerical model. The numerical model in general computes the pressure, velocities and temperature distributions at every point within the seal interface. Since a numerical model is needed to compute the opening force and seal leakage with other performance parameters, two numerical models have been developed to analyse the

performance of dry gas face seals. A judicious employment of these models would permit to distinguish and discern the causes of seal failures and malfunctions, with far less testing than would be the case with strictly empirical means. The two seal models employed in this study are succinctly described in the next two paragraphs.

The Reynolds equation model numerically integrates the compressible Reynolds equation. For this study, the finite difference discretization was not directly applied to the compressible Reynolds equation, rather the mass flow rates for the radial and circumferential components were numerically integrated over the control area around each finite difference grid point. The grid was applied to a constant meshing space. The film thickness and the pressure gradient were evaluated at the control volume boundary, which is a point half way between nodes. The set of the discretized compressible Reynolds equations are nonlinear in terms of pressure. The nonlinear discretized compressible Reynolds equations were linearized using the Newton method and solved by a Gauss-Seidel iterative method. The rotational speed, sealed fluid temperature and the fluid film thickness were implemented directly into the discretized compressible Reynolds equation. This model considered the effects of surface roughness and face deformation (radial taper and waviness) but neglected the effect of inertia and turbulence. It assumed isothermal conditions, continuum flow and also considered choking and entrance losses effects. The model computational time is fast. It is associated with problems of fluid film thickness and pressure discontinuities between the groove-land interface and groove-dam interface for the case of the spiral groove seal face profile.

The 3D CFD model numerically integrates the Favre-averaged Navier-Stokes equations by employing a commercial CFD package (ANSYS CFX version 11). The Favre-averaged Navier-Stokes equations include the momentum, total energy and continuity equations. The effects of rotation are accounted for by adding Coriolis and centrifugal forces to the momentum equations and also replacing the total enthalpy in the energy equation with rothalpy. The computational domain was set as rotating and the value of the rotating shaft speed was assigned to the computational domain. The seal faces were assumed to be adiabatic. The computational domain was constructed with ANSYS Gambit (Gambit 2.3.16) by means of a user-specified subroutine. The user-specified subroutine is a Perl script that generates a journal file required by the Gambit software in generating the mesh. The geometrical parameters dimensions as well as the geometrical seal face profile are specified in the user-specified subroutine. Also prescribed in the user-specified subroutine are the coning angle and meshing parameters (number and spacing of nodes along particular edges). The computational domain is constructed as a topology of hexahedral blocks that yields a structured mesh. A representative value for the number of cells used is in the range of 3 million, for a one-twelfth sector of a seal face. The 3D CFD model is a very good tool for predicting seal flow behaviour at both low and high operating conditions. It includes

the effects of choking and inertia as well as turbulence. It is capable of handling complex geometries but it is computationally expensive as a result of keeping the mesh aspect ratio below a value of 200. The effect of waviness as a means of face deformation was not considered in this model.

A large number of results spanning across different operating conditions and geometrical variations, including seal face profiles as well as convergent radial taper, have been presented and are discussed in this thesis. The results of the Reynolds equation model and 3D CFD model follow the same trend for low pressure and velocity operating conditions. The differences in the results from both models were in the absolute predicted values. At high operating conditions, there were marked differences in the results obtained from the two models which can be attributed to the limitations of the Reynolds equation model that neglected the effects of inertia and turbulence. The 3D CFD model predictions showed a better agreement with the seal leakage test data than the results due to the Reynolds equation model. The leakage rates and fluid film thickness predictions illustrate how the 3D CFD model can be used for seal design while overcoming some of the shortcomings of the Reynolds equation based models. The major limitation of the 3D CFD model is that it is inherently computationally expensive.

In order to investigate the effects of varying the operating conditions on seal performance, the 3D CFD model was employed. At moderate rotating speeds and high pressure differentials, the groove effects do not have a significant impact on the seal performance in terms of the generation of high gas film stiffness. Increasing the sealed fluid pressure does not enhance the gas film stiffness rather it generates more opening and closing forces that will support the bulk of the load. The pressure differential is responsible for the generation of the hydrostatic forces. It is evident from the results presented that the hydrodynamic action impacts high gas film stiffness, particularly at small clearances and high rotating speeds.

In addition, the 3D CFD model was used in investigating the contributions of the hydrostatic and hydrodynamic forces with regards to seal performance. The results obtained from this analysis have shown that the bulk of the opening forces come from the hydrostatic force resulting from the sealed fluid pressure differential. Increasing the pressure differential does not improve the axial film stiffness of the seal but only increases the opening and closing forces. The hydrodynamic force is quite small compared to the hydrostatic force but it is the controlling mechanism of grooved seals, which provides the positive axial film stiffness. The hydrodynamic force results from the relative motion of the sealing face. A high pressure generation at the groove section in the radial and circumferential directions is an indication of the presence of hydrodynamic forces in a seal.

Different groove geometry employing the 3D CFD model were analyzed in order to evaluate

their performances as well as how much positive axial film stiffness each geometrical seal face profile can generate when the sealing shaft rotates in the normal and reverse directions. The different geometrical seal face profiles investigated in this study include the plain face, orifice controlled, spiral groove, double spiral groove, radial groove and T-groove seals. Adding an orifice slot to a plain face seal improves its performance from negative axial film stiffness to positive axial film stiffness at the expense of increased leakage. It was found out that when the sealing shaft rotates in the normal direction, the spiral groove face seal produces the best seal performance in terms of design efficiency parameter. Upon reverse rotation of the sealing shaft, the spiral groove face seal produces the worst seal performance since it does not produce positive axial film stiffness on reverse rotation. The radial groove and T-groove face seals considered in this analysis showed that they can generate the same amount of lift on normal and reverse rotation of the sealing shaft. The main mechanism responsible for the generation of positive axial film stiffness in terms of the direction of shaft rotation is the geometrical groove pattern. Seals with asymmetric groove face patterns fall into the unidirectional seal type while seal having symmetric groove face pattern fall into the bidirectional seal type.

Based on the knowledge gained from the analysis described in the preceding paragraph, a bidirectional seal of a novel type has been proposed in this thesis. Various analyses employing the 3D CFD model were carried out on the proposed novel seal and its results were compared with some existing seal face profiles. The results obtained from these predictions are encouraging when compared with the results of existing geometrical seal face profiles. This novel seal is easy to fabricate and has a strong commercial potential.

The results obtained from the Reynolds equation model and 3D CFD model, utilising different geometrical seal face profiles, and taking account of face deformation, have shown that convergent radial taper can affect the performance of seals in different ways depending on the geometrical seal face profile. Adding a positive radial taper to a plain face seal improves its performance in terms of higher opening force. Consequently, adding a positive radial taper to grooved seals reduces their opening forces and positive axial stiffness. Also, adding positive radial to plain face seal and grooved seals increases their leakage. While positive radial taper in plain face seal is beneficial, its inclusion to grooved seals reduces their performances.

The results presented in this thesis have shown that a good dry gas face seal must possess a steep gradient of lift force against fluid film thickness also referred to as high gas film stiffness. This high gas film stiffness is advantageous in the sense that, the net resulting force (difference between closing and opening forces) is a closing force that increases rapidly when the opening force decreases. A small operating gas film thickness is therefore

maintained and the high gas film stiffness forces the seal nosepiece to dynamically track the run out motion of the seal face. The analysis of the results were based on performance parameters such as opening force, leakage, axial film stiffness, power consumption and design efficiency parameter. Also, the good agreement between the test data and the 3D CFD model calculations of the leakage serves as a useful validation of the model. The acceptable leakage rates, as well as the predictions of the equilibrium film thickness exemplify how the numerical model could contribute to the development of a seal design while surmounting the limitations of the usage of the Reynolds equation models.

Optimization of the geometrical parameters of the hydrodynamic lift-off features and the analysis of the fluid flow in the seal interface are inter-twined. Any small changes in the geometrical parameters of the hydrodynamic lift features significantly affect the performance of a non-contacting gas face seals. For a non-contacting gas face seals to function properly, the optimum geometrical parameters are thus needed for seal to have an optimum performance. An automatic optimization tool has been presented for the optimization of dry gas face. The optimization tool comprises of the Halton sequence algorithm, metamodel algorithm and an optimizer capable of handling either single or multi objective functions. The optimization of a dry gas face seal employing the automatic optimization tool is carried out in four sequential steps. The first step is generating uniformly distributed points for the geometrical parameters (design variables) of the seal. The second step is carrying out numerical simulations of the fluid flow in the seal interface based on the selected design variables to obtain the seal performance parameters (responses). The third step is using the design variables and responses as inputs to the metamodel algorithm to generate fitness function(s) which are surrogates of the entire seal design system. The fourth step is searching for the design variables that will produce the optimal solutions (responses) by the optimizer based on the generated fitness function(s) from the metamodel algorithm.

In order to explore the advantages resulting from the use of the automatic optimization tool, the spiral groove face seal was optimized employing the 3D CFD model. Three cases of objective function(s) were considered. They are maximization of the opening force in isolation, maximization of the design efficiency parameter and the multi objective case of maximization of the opening force and minimization of the leakage. The maximization of the design efficiency parameter yielded the best results when compared against CFD simulation results based on the predicted optimal results. The improvements achieved by the automated optimization of the spiral groove face seal are:

4.77% increase in opening force.

13.19% reduction in seal leakage.

20.69% increase in the design efficiency parameter.

28.28% increase in axial film stiffness.

15.92% reduction in power consumption.

It is therefore clear that employing the optimization tool developed as part of this work, different geometrical seal face profiles with optimal performance characteristics can be designed in an automated manner with little human attention.

7.2 Research Contribution

The central aim of this research was to investigate the use of an advanced numerical method as a design tool for both uni and bidirectional dry gas face seals. The investigation covered seals functioning over a wide range of operating conditions in terms of sealed fluid pressure, temperature and sealing shaft speed.

The amount of previously reported work on the numerical modelling of dry gas face seals employing CFD is not extensive. Only a few papers (Wu and Clark (2000), Kudriavtsev et al. (2001), Leefe (2002), Zheng (2005), Luan and Khonsari (2006) and feng Zhang et al. (2006)) have been published on the analysis of dry gas face seals.

The present work therefore is believed to have provided a significant contribution to the field of dry gas face seal technology. The feasibility and practicability of using CFD in the gas face seal design loop, for seals operating over a wide range of operating conditions, has been proved through the detailed seal analyses presented in Chapter 4 and elsewhere.

The extent of the CFD investigations of both uni and bidirectional seal types having complex groove patterns is new as is some the information obtained through these studies. This work enabled also the identification of the impact of the variation of groove layouts on seal performance with emphasis on the understanding of the factors that condition bidirectional performances and the way that hydrodynamic lift is generated.

The traditional method of optimizing the hydrodynamic lift features of a mechanical face seal is the parametric analysis method. Most of the published work on mechanical face seal optimization employed that technique. In the current study the geometrical parameters of the seal are varied one at a time in order to identify the optimum performance parameters.

An additional contribution is in the form of the usage of an automatic optimization scheme employing a combination of high and low fidelity models for the design of dry gas face seals. This method enables the seal designer to concentrate on the selection of seals from a

pool of optimal results produced by the optimiser routine.

7.3 Recommendations for Future Work

Although the numerical models that have been employed in this study produce appreciable results in terms of performance prediction, there remains significant room for improvements.

Presented in the subsequent paragraphs are some recommendations for further work.

The Reynolds equation used in the Reynolds model could be discretized with the finite element method rather than the finite difference method employed in this study. This will reduce the pressure and fluid film thickness discontinuities associated with the finite difference method of discretization when complex geometries are employed. Also, implementation of the eddy viscosity model presented in Subsection 2.4.1 into the Reynolds equation model is necessary in order to cater for the effect of turbulence for seals operating in the turbulent regime.

There is a need to carry out instability analysis with the results obtained from the CFD simulations in order to analyse the dynamic response of a seal when it is perturbed. Discussed in the subsequent paragraphs is a suggested approach that can be used in analysing the dynamic response of a seal that is perturbed and using the solutions obtained from a CFD simulation.

In the past, two methods have been employed for the instability analysis. The two methods are the full numerical model and semi-analytical model. In the full numerical model, the lubrication analysis and kinetic analysis are coupled together into a single state space form. The equations representing the single state space form are solved with a linear multi-step ordinary differential equation solver (Miller and Green, 2001). Another approach of the full numerical model consists of coupling the lubrication analysis and seal dynamics into an inverse problem whereby it is solved iteratively at each time step to obtain the history of the sealing characteristics during the entire operation cycle of the seal including start-up and shut-down (Ruan, 2002*a*). In the semi-analytical model, the instability analysis is decoupled from the lubrication analysis and the fluid film is treated as an equivalent of a spring-damper system. The stiffness and the damping are obtained numerically from the perturbation method applied to the unsteady Reynolds equation. With this approach, the instability analysis is achieved by simply solving the dynamics equation analytically (Ruan, 2002*b*).

$$M\ddot{h} + c_s\dot{h} + k_s h = F_o - F_c \tag{7.1}$$

As a result of the computational cost of employing CFD for the analysis of dry gas face seal been expensive, the above methods are not applicable to instability analysis of dry gas face seals when CFD is employed. The best approach in solving the instability analysis with the solutions obtained from the 3D CFD model is to apply the method presented by Liu et al. (2007). In this approach, the instability analysis is carried out by solving the dynamics equation of a stator assembly with the expression given in Equation (7.1). In Equation (7.1), h is the fluid film thickness, M is the mass of stator, c_s is the damping of the flexible support (usually from the elastomeric O-ring), k_s is the combined axial stiffness of the spring and the O-ring, F_o is the opening force and F_c is the closing force. Liu et al. (2007) presented that the opening force (first term on the right hand side of Equation (7.1)) is a function of four operating parameters. These four operating parameters include the sealed fluid pressure, sealing shaft rotational speed, fluid film thickness and stator axial speed. The opening force is usually obtained from solving the fluid flow in the seal interface employing either the steady state Reynolds equation based methods or solving the full steady state Navier-Stokes equations. In order to establish relationships between the opening force and the four operating parameters, four sets of numerical simulations are carried out. These four sets of simulation include running several simulations by:

1. Varying fluid film thickness at fixed sealed fluid film pressure and sealing shaft rotational speed.
2. Varying sealed fluid pressure at fixed fluid film thickness and sealing shaft rotational speed.
3. Varying sealing shaft rotational speed at fixed fluid film thickness and sealed fluid pressure.
4. Varying stator axial speed at fixed sealed fluid pressure and sealing shaft rotational speed.

In this study, number 1 to number 3 has been done. There is a need to carry out CFD simulation for number 4. This can be achieved by assigning a velocity that is normal to the direction of the fluid flow to one of the walls (seal face) and a moving mesh approach be adopted.

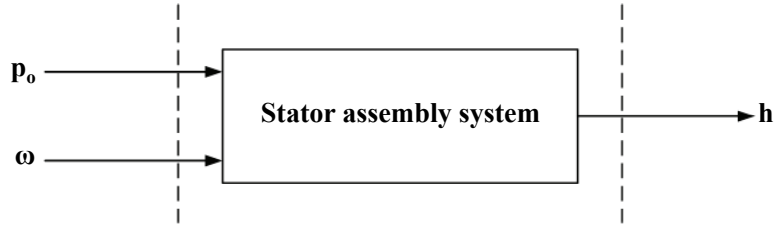

Figure 7.1 Control system of stator assembly

The Liu et al. (2007) approach statistically fit data of the opening force and the four operating parameters using a multivariate least square fitting. The fitness function generated from the multivariate least square fitting is used in place of the opening force in Equation (7.1). Liu et al. (2007) presented that the stator assembly can be represented as a control system with input signals and output signal as shown in Figure 7.1. The input signals consist of the sealed fluid pressure and sealing shaft rotation speed while the output signal is the fluid film thickness. Once the fitness function for the opening force and the four operating parameters has been generated by the multivariate least square fitting, a model can be built in MATLAB SIMULINK and employed for the instability analysis.

References

Almqvist, T. and Larsson, R. (2004), 'Some remarks on the validity of reynolds equation in the modeling of lubricant film flows on the surface roughness scale', *Journal of Tribology, Transactions of the ASME* **126**(4), 703–710.

Arkilic, E. B., Schmidt, M. A. and Breuer, K. S. (1997), 'Gaseous slip flow in long micro-channels', *Journal of Micro-Electro-Mechanical Systems* **6**(2), 167–178.

Barber, R. W. and Emerson, D. R. (2002), *The influence of Knudsen number on the hydrodynamic development length within parallel plate micro-channels*, Advances in Fluid Mechanics IV, Wessex Institute of Technology, Southampton, UK, pp. 207–216.

Bardina, J. E., Huang, P. G. and Coakley, T. J. (1997), Turbulence modeling validation, testing, and development, Technical Report TM-110446, NASA.

Bassani, R. and Piccigallo, B. (1992), 'Hydrostatic lubrication', *Tribology Series, Elsevier* **22**.

Basu, P. (1992), 'Analysis of a radial groove gas face seal', *Tribology Transactions* **35**(1), 11–20. Compilation and indexing terms, Copyright 2006 Elsevier Inc. All rights reserved.

Beachkofski, B. and Grandhi, R. (2002), 'Improved distributed hypercube sampling', *American Institute of Aeronautics and Astronautics* **1274**, 1–7.

Becker, K. M. (1963), 'Measurement of convective heat transfer from a horizontal cylinder rotating in a tank of water', *International journal of Heat Mass Transfer* **6**, 1053–1062.

Braaten, E. and Weller, G. (1979), 'An improved low-discrepancy sequence for multidimensional quasi-monte carlo integration', *Journal of Computational Physics* **33**(2), 249–258.

Brunetière, N. (2005), 'A modified turbulence model for low reynolds numbers: Application to hydrostatic seals', *Journal of Tribology, Transactions of the ASME* **127**(1), 130–140.

Brunetière, N. and Tournerie, B. (2006), 'The effect of inertia on radial flows-application to hydrostatic seals', *Journal of Tribology, Transactions of the ASME* **128**(3), 566–574.

Brunetière, N., Tournerie, B. and Frêne, J. (2002), 'Influence of fluid flow regime on performances of non-contacting liquid face seals', *Journal of Tribology, Transactions of the ASME* **124**(3), 515–523.

Burkardt, J. (2007), 'The halton quasirandom sequence'. Available at: `https://people.sc.fsu.edu/~burkardt/m_src/halton/halton.html`.

Cheng, H. S., Chow, C. Y. and Wilcock, D. F. (1968), 'Behavior of hydrostatic and hydrodynamic noncontacting face seals', *Journal of Lubrication Technology, Transactions of ASME* **90**, 510–519.

Christensen, H. (1972), 'A theory of mixed lubrication', *Proceedings of the Institution of Mechanical Engineers* **186**, 421–427.

Christensen, H. and Tonder, K. (1971), 'The hydrodynamic lubrication of rough bearing surfaces of finite width', *Journal of Lubrication Technology, Transactions of ASME* **93**, 324–330.

Constantinescu, V. N. (1962), 'Analysis of bearings operating in turbulent regime', *ASME Journal of Basic Engineering* **84**(1), 139–151.

Constantinescu, V. N. and Galetuse, S. (1982), 'Operating characteristics of journal bearings in turbulent inertial flow', *Journal of Lubrication Technology, Transactions of ASME* **104**(1), 173–179.

Daberkow, D. D. and Marris, D. N. (1998), New approaches to conceptual and preliminary aircraft design: A comparative assessment of a neural network formulation and response surface methodology, *in* 'World Aviation Conference', AIAA.

Daily, D. W. and Neece, R. E. (1960), 'Chamber dimension effects on induced flow and frictional resistance of enclosed rotating disks', *Journal of Basic Engineering, Transactions of ASME* **82**, 217–232.

Deb, K., Pratap, A., Agarwal, S. and Meyarivan, T. (2002), 'A fast and elitist multiobjective genetic algorithm: NSGA-II', *IEEE Transaction on Evolutionary Computation* **6**(2), 182–197. Available at: `http://www.mathworks.com/matlabcentral/fileexchange/loadAuthor.do?objectType=author&objectId=1094923`.

Debuchy, R., Dyment, A., Muhe, H. and Micheau, P. (1998), 'Radial inflow between a rotating and a stationary disc', *European Journal of Mechanics - B/Fluids* **17**(6), 791–810.

Du, Q., Faber, V. and Gunzburger, M. (1999), 'Centroidal voronoi tessellations: Applications and algorithms', *Society for Industrial and applied Mathematics Review* **41**(4), 637–676.

Elrod, H. G. and Ng, C. W. (1967), 'A theory for turbulent films and its application to bearings', *Journal of Lubrication Technology, Transactions ASME* **89**, 346–362.

Etsion, I. (2004), 'Improving tribological performance of mechanical components by laser surface texturing', *Tribology Letters* **17**(4), 733–737.

Etsion, I. and Burstein, L. (1996), 'A model for mechanical seals with regular microsurface structure', *Tribology Transactions* **39**(3), 677–683.

Etsion, I. and Front, I. (1994), 'A model for static sealing performance of end face seals', *Tribology Transactions* **37**, 111–119.

Etsion, I. and Halperin, G. (2002), 'A laser surface textured hydrostatic mechanical seal', *Tribology Transactions* **45**(3), 430–434.

Feldman, Y., Kligerman, Y. and Etsion, I. (2006), 'A hydrostatic laser surface textured gas seal', *Tribology Letters* **22**(1), 21–28.

Feldman, Y., Kligerman, Y. and Etsion, I. (2007), 'Stiffness and efficiency optimization of a hydrostatic laser surface textured gas seal', *Journal of Tribology, Transactions of the ASME* **129**, 407–410.

Feldman, Y., Kligerman, Y., Etsion, I. and Haber, S. (2006), 'The validity of the reynolds equation in modeling hydrostatic effects in gas lubricated textured parallel surfaces', *Journal of Tribology, Transactions of the ASME* **128**, 345–350.

feng Zhang, J., qi Yuan, S., hong Fu, Y. and jian Fang, Y. (2006), 'A numerical simulation of 3-d inner flow in up-stream pumping mechanical seal', *Journal of Hydrodynamics* **18**(5), 572–577.

Frêne, J. (1977), 'Tapered land thrust bearing operating in both turbulent and laminar regimes', *ASLE Transactions* **21**(3), 243–249.

Frêne, J., Arghir, M. and Constantinescu, V. (2006), 'Combined thin-film and navierstokes analysis in high reynolds number lubrication', *Tribology International* **39**(8), 734–747.

Fukui, S. and Kaneko, R. (1990), 'A database for implementation of poiseuille flow rates for high knudsen number lubrication problem', *Journal of Tribology, Transactions of the ASME* **112**(1), 78–83.

Gad, A. M., Nemat-Alla, M. M., Khalil, A. A. and Nasr, A. M. (2006), 'On the optimum groove geometry for herringbone grooved journal bearings', *Journal of Tribology, Transactions of the ASME* **128**, 585–593.

Guardino, C., Chew, J. W. and Hills, N. J. (2004), 'Calculation of surface roughness effects on air-riding seals', *Journal of Engineering for Gas Turbines and Power* **126**(1), 75–82.

Guinta, A. A. and Watson, L. (1998), A comparison of approximation modelling techniques: polynomial versus interpolating models, *in* 'Symposium on Multidisciplinary Analysis and Optimization', American Institute of Aeronautics and Astronautics.

Halton, J. H. (1960), 'On the efficiency of certain quasi-random sequences of points in evaluating multi-dimensional integrals', *Numerische Mathematik* **2**(1), 84–90.

Hedayat, A. S., Sloane, N. J. A. and Stufken, J. (1999), *Orthogonal Arrays: Theory and Applications*, Springer, Berlin, Heidelberg, New York.

Hirs, G. G. (1973), 'Bulk flow theory for turbulence in lubricant films', *Journal of Lubrication Technology, Transactions of ASME* **95**, 137–146.

Hoppermann, A. and Kordt, M. (2002), *Oelhydraulik und Pneumatik*, Vereinigte Fachverlage Mainz.

Hsing, F. C. and Malanoski, S. B. (1969), 'Mean free path effect in spiral grooved thrust bearings', *Journal of Lubrication Technology, Transactions of ASME* **91**.

Jeong, S., Murayama, M. and Yamamoto, K. (2004), Efficient optimization design method using kriging model, *in* '42nd AIAA Aerospace Sciences Meeting and Exhibit', pp. 1–10.

Jin, R., Chen, W. and Simpson, T. W. (2000), 'Comparative studies of metamodeling techniques under multiple modeling criteria', *American Institute of Aeronautics and Astronautics* **4801**, 1–11.

Kligerman, Y. and Etsion, I. (2001), 'Analysis of the hydrodynamic effects in a surface textured circumferential gas seal', *Tribology Transactions* **44**(3), 472–478.

Kocis, L. and Whiten, W. J. (1997), 'Computational investigations of low-discrepancy sequences', *ACM Transactions on Mathematical Software* **23**(2), 266–294.

Konak, A., Coit, W. D. and Smith, E. A. (2006), 'Multi-objective optimization using genetic algorithms: A tutorial', *Reliability Engineering and System Safety* **91**, 992–1007.

Kowalski, C. A. and Basu, P. (1995), 'Reverse rotation capability of spiral-groove gas face seals', *Tribology Transactions* **38**(3), 549–556.

Kudriavtsev, V., Braun, M. J. and Hendricks, R. C. (2001), Computational analysis of 3d fluid flow and pressure forces in a spiral groove seal, *in* '2001 ASME Pressure Vessels and Piping Conference, Jul 22-26 2001', Vol. 424 2, American Society of Mechanical Engineers, New York, NY 10016-5990, United States, Atlanta, GA, United States, pp. 261–267.

Laurenson, I. T. and O'Donoghue, J. P. (1978), Preliminary experiments with slot fed hydrostatic face seals, *in* 'In Proceedings of the Eighth International Conference on Fluid Sealing, BHRA', pp. 41–52.

Lebeck, A. O. (1981), 'Hydrodynamic lubrication in wavy contacting face seals: A two dimensional model', *Journal of Lubrication Technology, Transactions of ASME* **103**, 578–586.

Lebeck, A. O. (1991), *Principles and Design of Mechanical Face Seals*, Wiley, New York ; Chichester. Bibliography included; "A Wiley-Interscience publication." Includes bibliographical references and index; HL: Birmingham ; Oxford ; Sheffield ; Trinity College Dublin Record 7 of 45.

Lebeck, A. O., Teale, J. L. and Pierce, R. E. (1978), Hydrodynamic lubrication with wear and asperity-contact in mechanical face seals, Technical Report ME-86(78)ONR-414-1 for ONR Contract N00014-76-C-0071, Bureau of Engineering Research, The University of New Mexico, Albuquerque, New Mexico.

Leefe, S. E. (2002), *Use of CFD in the Design of a Shaft Seal for High-performance Turbomachinery*, Advances of CFD in Fluid Machinery Design, John Wiley & Sons Inc., New York, chapter 12, pp. 211–227.

Lin, J. F. and Yao, C. C. (1996), 'Hydrodynamic lubrication of face seal in a turbulent flow regime', *Journal of Tribology, Transactions of the ASME* **118**(3), 589–601.

Liu, K., Liu, Y. and Liu, X. (2007), Opening force analytical model for dynamic response analysis of hydrodynamic face seal, *in* '12th IFToMM World Congress'. June18-21, Besançon, France.

Liu, Y., Shen, X., Xu, W. and Wang, Z. (2004), 'Performance comparison and parametric study on spiral groove gas film face seals', *Science in China Series, G Physics, Mechanics & Astronomy* **47**, 29–36.

Lophaven, S. N., Nielsen, H. B. and Søndergaard, J. (2002*a*), Aspects of the matlab toolbox DACE, Technical report, Informatics and Mathematical Modelling, Technical University of Denmark, DTU, Richard Petersens Plads, Building 321, DK-2800 Kgs. Lyngby. Availabe at: `http://www2.imm.dtu.dk/pubdb/p.php?1050`.

Lophaven, S. N., Nielsen, H. B. and Søndergaard, J. (2002*b*), DACE - a matlab kriging toolbox, Technical Report IMM-TR-2002-12, Informatics and Mathematical Modelling, Technical University of Denmark, DTU, Richard Petersens Plads, Building 321, DK-2800 Kgs. Lyngby. Availabe at: `http://www2.imm.dtu.dk/pubdb/p.php?1049`.

Loschmidt, J. (1995), 'On the size of the air molecules', *Journal of Chemical Education* **72**(10), 870–875.

Luan, Z. and Khonsari, M. M. (2006), 'Numerical simulations of the flow field around the rings of mechanical seals', *Journal of Tribology, Transactions of the ASME* **128**, 559–565.

Lubbinge, H. (1999), On the Lubrication of Mechanical Face Seals, PhD thesis, Universiteit Twente, Enschede.

MathWorks (2008), 'Matlab 7.7.0 software, version r2008b', The MathWorks, Inc.

MathWorks (2009), *Genetic Algorithm and Direct Search Toolbox 2: Users Guide*, The MathWorks, Inc., 3 Apple Hill Drive, Natick, MA 01760-2098. Revised for Version 2.4.2 (Release 2009b). Available at: `http://www.mathworks.com/access/helpdesk/help/pdf_doc/gads/gads_tb.pdf`.

Mayer, E. (1969), Thermohydrodynamic in mechanical seals, *in* 'Proceedings of the 4th International Conference On Fluid Sealing BHRA Fluid Engineering', pp. 48–54.

McKay, M. D., Beckman, R. J. and Conover, W. J. (1979), 'A comparison of three methods for selecting values of lnput variables in the analysis of output from a computer code', *Technometrics* **21**, 239–245.

McNikel, A., I. and Etsion (2004), 'Near-contact laser surface textured dry gas seals', *Journal of Tribology, Transactions of the ASME* **126**(4), 788–794.

Meckesheimer, M., Barton, R. R., Simpson, T. W. and Booker, A. (2002), 'Computationally inexpensive metamodel assessment strategies', *Journal of American Institute of Aeronautics and Astronautics* **40**(10), 2053–2060.

Menter, F. R. (1992), 'Influence of freestream values on $k-\omega$ turbulence model predictions', *AIAA Journal* **30**, 1651–1659.

Menter, F. R. (1994), 'Two-equation eddy-viscosity turbulence models for engineering applications', *AIAA Journal* **32**, 1598–1605.

Menter, F. R. and Rumsey, L. C. (1994), Assessment of two-equation turbulence models for transonic flows, Technical Report 94-2343, AIAA Paper.

Miller, B. A. and Green, I. (2001), 'Numerical formulation for the dynamic analysis of spiral-grooved gas face seals', *Journal of Tribology* **123**(2), 395–403. Compilation and indexing terms, Copyright 2006 Elsevier Inc. All rights reserved.
URL: *http://dx.doi.org/10.1115/1.1308015*

Missimer, J. R. and Thomas, L. C. (1983), 'Analysis of transitional and fully turbulent plane couette flow', *Journal of Lubrication Technology, Transactions of ASME* **105**(2), 364–368.

Muijderman, E. A. (1967), 'Analysis and design of spiral-groove bearings', *Journal of Lubrication Technology, Transactions ASME* **89**, 291–306.

Murphy, H. D., Chambers, F. W. and Mceligot, D. M. (1983), 'Laterally converging flow. part 1. mean flow', *Journal of Fluid Mechanics* **127**, 379–401.

Mutama, K. R. and Iacovides, H. (1993), 'The investigation of developing flow and heat transfer in a long converging duct', *Journal of Heat Transfer* **115**(4), 897–903.

Ng, C. W. (1964), 'Fluid dynamic foundation of turbulent lubrication theory', *ASLE Transactions* **7**, 311–321.

Ng, C. W. and Pan, C. H. T. (1965), 'A linearized turbulent lubrication theory', *Journal of Basic Engineering* **87**, 675–688.

Pape, J. G. (1968), 'Fundamental research on a radial face seal', *ASLE Transactions* **11**, 302309.

Patel, V. C. and Head, M. R. (1969), 'Some observations on skin friction and velocity profiles in fully developed pipe and channel flows', *Journal of Fluid Mechanics* **38**, 181–201.

Patir, N. and Cheng, H. S. (1978), 'An average flow model for determining effects of three-dimensional roughness on partial hydrodynamic lubrication', *Journal of Lubrication Technology* **100**, 12–17.

Polycarpou, A. A. and Etsion, I. (1998), 'Static sealing performance of gas mechanical seals including surface roughness and rarefaction effects', *Tribology Transactions* **41**(4), 531–536.

Robertson, J. M. (1959), On turbulent plane-couette flow, *in* 'Proceedings of 6th Midwestern Conference of Fluid Mechanics', pp. 169–182.

Ruan, B. (2000), 'Finite element analysis of the spiral groove gas face seal at the slow speed and the low pressure conditions - slip flow consideration', *Tribology Transactions*

43(3), 411–418. Compilation and indexing terms, Copyright 2006 Elsevier Inc. All rights reserved.

Ruan, B. (2002*a*), 'Numerical modeling of dynamic sealing behaviors of spiral groove gas face seals', *Journal of Tribology* **124**(1), 186–195. Compilation and indexing terms, Copyright 2006 Elsevier Inc. All rights reserved.
URL: *http://dx.doi.org/10.1115/1.1398291*

Ruan, B. (2002*b*), 'A semi-analytical solution to the dynamic tracking of non-contacting gas face seals', *Journal of Tribology* **124**(1), 196–202. Compilation and indexing terms, Copyright 2006 Elsevier Inc. All rights reserved.
URL: *http://dx.doi.org/10.1115/1.1398292*

Sacks, J., Welch, W. J., Mitchell, T. J. and Wynn, H. P. (1989), 'Design and analysis of computer experiments', *Journal of Statistical Science* **4**(4), 409–423.

Salant, R. F. and Homiller, S. J. (1992), 'The effects of shallow groove patterns on mechanical seal leakage', *Tribology Transactions* **35**(1), 142–148.

Saxena, N. N. (2003), 'Dry gas seals and support systems: benefits and options'. Available at: `http://www.globalmachineryconsultants.com/resources/HP1103_Dry_gas_seals_eprint1.pdf`.

Schaaf, S. A. and Chambre, P. L. (1961), *Flow of Rarefied Gases*, Princeton University Press.

Sedy, J. (1980), 'Improved performance of film-riding gas seals through enhancement of hydrodynamic effects', *ASLE Transactions* **23**(1), 35–44. Compilation and indexing terms, Copyright 2006 Elsevier Inc. All rights reserved.

Shapiro, W., Walowit, J. and Jones, H. F. (1984), 'Analysis of spiral-groove face seals for liquid oxygen', *ASLE Transactions* **27**(3), 177–188.

Shellef, R. A. and Johnson, R. P. (1992), 'Bi-directional gas face seal', *Tribology Transactions* **35**(1), 53–58. Compilation and indexing terms, Copyright 2006 Elsevier Inc. All rights reserved.

Simpson, T. W., Mauery, T. M., Korte, J. J. and Mistree, F. (2001), 'Kriging models for global approximation in simulation-based multidisciplinary design optimization', *American Institute of Aeronautics and Astronautics Journal* **39**(12), 2233–2241.

Singh, A., Vyas, B. D. and Powle, U. S. (1999), 'Investigation on inward flow between two stationary parallel disks', *International Journal of Heat and Fluid Flow* **20**(4), 395–401.

Souchet, D. (1991), Comportement Thermohydrodynamique des Butées à Patins Oscillants en Règime Laminaire et Turbulent, PhD thesis, University of Poitiers, France.

Stanghan-Batch, B. A. (1971), Face lubrication in mechanical seals, *in* 'Tribology Conventions', Vol. C59/71, Institution of Mechanical Engineers, pp. 54–59.

Szeri, A. Z. (1998), *Fluid Film Lubrication - Theory & Design*, Cambridge University Press, Cambridge, UK.

Trytek, J. J. (1983), 'High pressure rotary mechanical seal', Patent number: 277/961 ed., F16J 1516; F16J 1540; United States. Available at: `http://www.freepatentsonline.com/4407512.html`.

van Odyck, D. E. A. and Venner, C. H. (2003), 'Compressible stokes flow in thin films', *Journal of Tribology, Transactions of the ASME* **125**, 543–551.

Versteeg, H. and Malalasekra, W. (1996), *An Introduction to Computational Fluid Dynamics: The Finite Volume Method*, Addison-Wesley, Upper Saddle River, NJ.

Wallace, N. M. (1992), *Basic Concepts of Seal Function and Design*, Mechanical Seal Practice for Improved Performance (IMechE Guides for the Process Industries), second revised edn, Mechanical Engineering Publications Limited for The Institution of Mechanical Engineers, London, pp. 3–35.

Walowit, J. A. and Pinkus, O. (1982), 'Analysis of face seals with shrouded pockets', *Journal of Lubrication Technology, Transactions of ASME* **104**, 262–270.

Wilcox, D. C. (1988), 'Reassessment of the scale-determining equation for advanced turbulence models', *AIAA Journal* **26**, 1299–1310.

Wilcox, D. C. (1993), *Turbulence Modeling for CFD*, DCW Industries, Inc., La Canada, California, USA.

Wu, S. and Clark, R. (2000), 'Positioning of hydrodynamic lift features on non-contacting mechanical gas seal rings', *Tribology Transactions* **43**(3), 498–506. Compilation and indexing terms, Copyright 2006 Elsevier Inc. All rights reserved.

Yasuna, J. A. and Hughes, W. F. (1994), 'Squeeze film dynamics of two-phase seals: Part ii - turbulent flow', *Journal of Tribology, Transactions of the ASME* **116**(3), 479–488.

Young, L. A. and Lebeck, A. O. (1982), 'Experimental evaluation of a mixed friction hydrostatic mechanical face seal model considering radial taper,thermal taper and wear', *Journal of Lubrication Technology, Transactions ASME* **104**, 439–448.

Zheng, X. (2005), Parametrical study of hydrodynamic seal using a 2d design code and comparing with a 3d cfd model, *in* 'GT2005 ASME Turbo Expo 2005: Power for Land, Sea and Air', Vol. 3 PART B of *Proceedings of the ASME Turbo Expo*, Centurion Mechanical Seals, PerkinElmer Fluid Sciences, Warwick, RI 02888, United States, pp. 1173–1180. Compilation and indexing terms, Copyright 2006 Elsevier Inc. All rights reserved.

Zheng, X. and Berard, G. (2001), Development of non-contacting, film-riding face seals for large-diameter gas engines, *in* '37th AIAA/ASME/SAE/ASEE Joint Propulsion Conference', Vol. AIAA 01-3624, American Institute of Aeronautics & Astronautics.

Zhou, J., Gu, B. and Chen, Y. (2007), 'An improved design of spiral groove mechanical seal', *Chineese Journal of Chemical Engineering* **15**(4), 499–506.

Zirkelback, N. (2000), 'Parametric study of spiral groove gas face seals', *Tribology Transactions* **43**(2), 337–343. Compilation and indexing terms, Copyright 2006 Elsevier Inc. All rights reserved.

Zuk, J. (1976), Fundamentals of fluid sealing, Technical Report NASA TN D-8151, National Aeronautics and Space Administration (NASA).

Bibliography

Abernethy, R. B. (2006), *The New Weibull Handbook*, Abernethy Robert B, 536 Oyster Road, North Palm Beach, Florida.

Aksit, M., Bagepalli, B., Demiroglu, M., Dinc, S., Kellock, I. and Farrell, T. (1999), 'Advanced flexible seals for gas turbine shroud applications', **AIAA Paper**, 1999–2827. NR: 11.

Andrés, L. S. (2000), 'Bulk-flow analysis of hybrid thrust bearings for process fluid applications', *Journal of Tribology, Transactions of the ASME* **122**, 170–180.

Arghir, M. and Frêne, J. (2004), 'A bulk-flow analysis of static and dynamic characteristics of eccentric circumferentially-grooved liquid annular seals', *Journal of Tribology, Transactions of the ASME* **126**, 316–325.

Arghir, M., Lez, S. L. and Frêne, J. (2006), Finite-volume solution of the compressible reynolds equation: linear and non-linear analysis of gas bearing, *in* 'Proceedings of the IMECHE Part J Journal of Engineering Tribology', Vol. 220, Professional Engineering Publishing, pp. 617–618–627.

Artiles, A., Shapiro, W. and Jones, H. F. (1984), 'Design analysis of rayleigh-step floating-ring seals', *ASLE Transactions* **27**(4), 321–331.

Atkin, R. J., Ellam, D. J. and Bullough, W. A. (2002), 'Electro-structured fluid seals', *Journal of Intelligent Material Systems and Structures* **13**(7-8), 459–464.

Aydin, E. M. and Leutheusser, H. J. (1991), 'Plane-couette flow between smooth and rough walls', *Experimental Fluids* **11**, 302–312.

Azibert, H. and Clark, R. (2003), Using cfd to improve performance and extend life of mechanical seals in slurry applications, *in* '17th International Symposium on Fluid Sealing', BHR Group, pp. 447–467.

Baheti, S. K., Ramesh, K. and Kirk, R. G. (1996), 'Effect of axially grooved oil seals on the leakage flow and stability of a centrifugal compressor', *Tribology Transactions*

39(2), 398–406. Compilation and indexing terms, Copyright 2006 Elsevier Inc. All rights reserved.

Barber, R. W. and Emerson, D. R. (2003), Numerical simulation of low reynolds number slip flow past a confined microsphere, *in* A. D. Ketsdever and E. P. Muntz, eds, 'Rarefied Gas Dynamics: 23rd International Symposium', American Institute of Physics.

Bayada, G., Martin, S. and Vazquez, C. (2005), 'An average flow model of the reynolds roughness including a mass-flow preserving cavitation model', *Journal of Tribology, Transactions of the ASME* **127**, 793–802.

Bech, K. H., Tillmark, N., Alfredsson, P. H. and Andersson, H. I. (1995), 'An investigation of turbulent plane couette flow', *Journal of Fluid Mechanics* **286**, 291–325.

Bhagat, S. K., Sinhasan, R. and Singh, D. V. (1982), 'Analysis of a hydrodynamic seal with helical grooves', *Wear* **80**, 15–25. Compilation and indexing terms, Copyright 2006 Elsevier Inc. All rights reserved.
URL: *http://dx.doi.org/10.1016/0043-1648(82)90084-9*

Bhushan, B. (2001), *Modern tribology handbook*, CRC Press, Boca Raton, FL ; London. ill ; 27 cm; Includes bibliographical references; HL: Imperial College ; Sheffield ; Trinity College Dublin Record 6 of 85.

Billy, F., Arghir, M. and Pineau, G. (2006), 'Navier-stokes analysis of a requlr two-dimensional roughness pattern under turbulent flow regime', *Journal of Tribology, Transactions of the ASME* **128**, 122–130.

Blazek, J. (2001), *Computational Fluid Dynamics: Principles and Application*, Elservier, Oxford, England.

Bloch, H. P. and Budris, A. R. (2005), *Pump User's Handbook Life Extension*, Fairmont Press, Inc., 700 Indian Trail, Lilburn, GA 30047.

Bloch, H. P. and Elliott, H. G. (1985*a*), Mechanical seals in medium-pressure steam turbines, *in* 'Preprints presented at the ASLE 1985 Annual Meeting.', ASLE Preprints, Exxon Chemical Co, Baytown, TX, USA, ASLE, Park Ridge, IL, USA, Las Vegas, NV, USA, p. 6. Compilation and indexing terms, Copyright 2006 Elsevier Inc. All rights reserved.

Bloch, H. P. and Elliott, H. G. (1985*b*), 'Mechanical seals in medium-pressure steam turbines', *Lubrication Engineering* **41**(11), 653–658. Compilation and indexing terms, Copyright 2006 Elsevier Inc. All rights reserved.

Bonneau, D., Huitric, J. and Tournerie, B. (1993), 'Finite element analysis of grooved gas thrust bearings and grooved gas face seals', *Journal of Tribology, Transactions of the*

ASME **115**(3), 348–354. Compilation and indexing terms, Copyright 2006 Elsevier Inc. All rights reserved.

Booker, J. F. and Huebner, K. H. (1972), 'Application of finite element methods to lubrication: An engineering approach', *Lubrication Technology, Transaction of the ASME* pp. 313–323.

Bouard, L., Fillon, M. and Frne, J. (1996), 'Comparison between three turbulent models - application to thermohydrodynamic performances of tilting-pad journal bearings', *Tribol.Int.* **29**(1), 11–18.

Boyson, S. (2006), 'Gas up your sealing knowledge', *Chemical Processing* **69**(12), 20–25.

Brajdic-Mitidieri, P., Gosman, A. D., Ioannides, E. and Spikes, H. A. (2005), 'Cfd analysis of a low friction pocketed pad bearing', *Journal of Tribology, Transactions of the ASME* **127**(4), 803–812.

Bratley, P., Fox, B. L. and Niederreiter, H. (1992), 'Implementation and tests of low-discrepancy sequences', *ACM Transactions on Modeling and Computer Simulation* **2**(3), 195–213.

Brunetière, N., Galenne, E., Tournerie, B. and Pierre-Danos, I. (2008), 'Modelling of non-laminar phenomena in high reliability hydrostatic seals operating in extreme conditions', *Tribology International* **41**(4), 211–220.

Buck, G. S. and Volden, D. (1990), 'Upstream pumping. a new concept in mechanical sealing technology', *Lubrication Engineering* **46**(4), 213–217. Compilation and indexing terms, Copyright 2006 Elsevier Inc. All rights reserved.

Burkardt, J. (2007), 'The halton quasirandom sequence'. Available at: `http://people.sc.fsu.edu/~burkardt/m_src/halton/halton.html`.

Burkardt, J., Gunzburger, M. and Lee, H.-C. (2006), 'Centroidal voronoi tessellation-based reduced-order modeling of complex systems', *SIAM Journal on Scientific Computing* **28**(2), 459–484.

Cao, Y., Hu, G. and Wang, J. (2000), 'Numerical simulation of gas seal flowfield in an axially staggered configuration', *Aircraft Engineering and Aerospace Technology* **72**(5), 447–451.

Chen, Z. and Li, J.-M. (2005), 'Mathematical simulation of flow in gas face seals', *Journal of Sichuan University: Engineering Science Edition* **37**(3), 133–137. IL: Graphs; NR: 12.

Clark, R., Azibert, H. and Oshinowo, L. (2002), 'Computer simulation of mechanical seal leads to design change that improves coolant circulation', *Journal of Materials and Design* **23**, 113–117.

Coello, C. A. C. (1999), 'A comprehensive survey of evolutionary-based multiobjective optimization techniques', *Knowledge and Information Systems: An International Journal* **1**(3), 269–308.

Coello, C. A. C. and Romero, C. E. M. (2002), *Evolutionary algorithms and multiple objective optimization*, Multiple Criteria Optimization, State of the Art, Annotated Bibliographic Surveys, Kluwer Academic.

Constantinescu, V. N. and Galetuse, S. (1987), 'On the dynamic stability of the spiral-grooved gas-lubricated thrust bearing', *Journal of Tribology, Transactions of the ASME* **109**(1), 183–188. Compilation and indexing terms, Copyright 2006 Elsevier Inc. All rights reserved.

Corne, D. W., Knowles, J. D. and Oates, M. J. (2000), The pareto envelope-based selection algorithm for multiobjective optimization, *in* 'Proceedings of sixth international conference on parallel problem solving from nature', Springer.

Cupillard, S., Cervantes, M. J. and Glavatskih, S. (2008), 'Pressure buildup mechanism in a textured inlet of a hydrodynamic contact', *Journal of Tribology, Transactions of the ASME* **130**(2), 021701–1–021701–10.

Dean, R. B. (1974), 'Reynolds number dependence of skin friction and other bulk flow variables in two-dimensional duct flow', *Journal of Fluids Engineering, ASME* **100**, 215–223.

Deb, K. (2001), *Multi-Objective Optimization using Evolutionary Algorithms*, John Wilet & Sons, Ltd, West Sussex, England.

Dhagat, S. K. (1982), 'Suitability of grooved configurations for bearings and seals', *Wear* **82**(1), 37–44. Compilation and indexing terms, Copyright 2006 Elsevier Inc. All rights reserved.
URL: *http://dx.doi.org/10.1016/0043-1648(82)90125-9*

DiRusso, E. (1983), Design analysis of a self-acting spiral-groove ring seal for counter-rotating shafts, Technical Report NASA TP 2142, National Aeronautics and Space Administration. Compilation and indexing terms, Copyright 2006 Elsevier Inc. All rights reserved.

DiRusso, E. (1984*a*), Dynamic behaviour of spiral-groove and rayleigh-step self-acting face seals, Technical Report NASA TP 2266, National Aeronautics and Space Administration.

DiRusso, E. (1984*b*), 'Feasibility analysis of a spiral groove ring seal for counter-rotating shafts', *Journal of Aircraft* **21**(8), 618–622. Compilation and indexing terms, Copyright 2006 Elsevier Inc. All rights reserved.

DiRusso, E. (1985), Dynamic response of film thickness in spiral-groove face seals, Technical Report NASA TP 2544. Compilation and indexing terms, Copyright 2006 Elsevier Inc. All rights reserved.

el Hak, M. G. (1999), 'The fluid mechanics of microdevices - the freeman scholar lecture,', *Journal of Fluids Engineering, ASME* **121**, 5–33.

Elaoud, S., Loukil, T. and Teghem, J. (2007), 'The pareto fitness genetic algorithm: Test function study', *European Journal of Operational Research* **177**, 1703–1719.

Etsion, I. (2000), Improving tribological performance of mechanical seals by laser surface texturing, *in* '17th International Pump Users Symposium', p. 17.

Etsion, I. (2004), 'Improving tribological performance of mechanical components by laser surface texturing', *Tribology Letters* **17**(4), 733–737.

Faria, M. T. C. (2001), 'An efficient finite element procedure for analysis of high-speed spiral groove gas face seals', *Journal of Tribology* **123**(1), 205–210. Compilation and indexing terms, Copyright 2006 Elsevier Inc. All rights reserved.
URL: *http://dx.doi.org/10.1115/1.1331276*

Faria, M. T. C. (2004), 'Finite element analysis of the misalignment effects on the dynamic force coefficients of spiral groove gas face seals', *JSME International Journal, Series C (Mechanical Systems, Machine Elements and Manufacturing)* **47**(1), 289–96.
URL: *http://dx.doi.org/10.1299/jsmec.47.289*

Feng, X. and Peng, X. (2006), 'Effect of surface roughness on performance of a spiral groove gas seal', *Run Hua Yu Mi Feng/Lubrication Engineering* (1), 20–22. Compilation and indexing terms, Copyright 2006 Elsevier Inc. All rights reserved.

Fonseca, C. M. and Fleming, P. J. (1993), Multiobjective genetic algorithms, *in* 'Genetic Algorithms for Control Systems Engineering, IEE Colloquium'.

Gabriel, R. P. (1994), 'Fundamentals of spiral groove noncontacting face seals', *Lubrication Engineering* **50**(3), 215–224. Compilation and indexing terms, Copyright 2006 Elsevier Inc. All rights reserved.

Gamble, W. L. (1985), 'Counterrotating intershaft seals for advanced engines', *Journal of Propulsion and Power* **1**(6), 437–440. Compilation and indexing terms, Copyright 2006 Elsevier Inc. All rights reserved.

Garcia, J. S. D., Ávila, S. L. and Carpes, W. P. (2006), 'Introduction to optimization methods: A brief survey of methods', IEEE Multidisciplinary Engineering Education Magazine.

Gardner, J. F. (1973), 'Recent development on non-contacting face seals', *Journal of Lubrication Technology, Transactions of ASME* **29**(9), 406–412.

Gardner, J. F. (1997), Testing of pressure balanced compliant seal in air, Vol. AIAA Paper 1997-2873. NR: 5.

Gilding, B. H. (1988), 'Numerical grid generation technique', *Computers & Fluids* **16**(1), 47–58. Compilation and indexing terms, Copyright 2006 Elsevier Inc. All rights reserved.
URL: *http://dx.doi.org/10.1016/0045-7930(88)90038-2*

Gould, P. (1971), 'Flow instability induced by viscosity variation in high pressure two-dimensional laminar flow between parallel plates', *Journal of Lubrication Technology, Transactions of ASME* pp. 465–469.

Hajela, P. and Lin, C. Y. (1992), 'Genetic search strategies in multicriterion optimal design', *Structural and Multidisciplinary Optimization* **4**(2), 99–107.

Hämäläinen, J. P., Mäkinen, R. A. E., Tarvainen, P. and Toivanen, J. (2000), Evolutionary shape optimization in cfd with industrial applications, *in* 'European Congress on Computational Methods in Applied Sciences and Engineering ECCOMAS'.

Helene, M., Arghir, M. and Frêne, J. (2003), 'Numerical three-dimensional pressure patterns in a recess of a turbulent and compressible hybrid journal bearing', *Journal of Tribology, Transactions of the ASME* **125**, 301–308.

Hendricks, R. C. and Liang, A. D. (1993), Seals flow code development-92, Technical Report NASA CP-10124, National Aeronautics and Space Administration.

Hendricks, R. C. and Liang, A. D. (1996), Seals code development workshop, *in* 'Proceedings of a workshop held at NASA Lewis Research Center, Cleveland, Ohio, June 14-15, 1995', NASA CP-10181, Washington, D.C.

Hernandez, P. and Boudet, R. (1995), 'Modelling of the behavior of dynamical gas seals: Calculation with a finite element method implicitly assuring the continuity of flow', *Proceedings of the Institution of Mechanical Engineers - Part J: Journal of Engineering Tribology* **209**, 195–201.

HimYu, T. and Sadeghi, F. (2001), 'Groove effects on thrust washer lubrication', *Journal of Tribology, Transactions of the ASME* **123**, 295–304.

Hiromu, H. and Masayuki, O. (2008), 'Optimization of groove geometry for thrust air bearing to maximize bearing stiffness', *Journal of Tribology, Transactions of the ASME* **130**(3), 031101.1–031101.11.

Horn, J., Nafpliotis, N. and Goldberg, D. E. (1994), A niched pareto genetic algorithm for multiobjective optimization, *in* 'First IEEE Conference on Evolutionary Computation, IEEE World Congress on Computational Intelligence', IEEE.

Hou, Y., Chen, C. and Wang, B. (2002), 'Design of gas-lubricated spiral grooved thrust bearings', *Run Hua Yu Mi Feng/Lubrication Engineering* (1), 2. Compilation and indexing terms, Copyright 2006 Elsevier Inc. All rights reserved.

Hsiao, C. K. (1971), 'A numerical method and higher approximations for a self-acting, gas-lubricated bearing of finite length', *Journal of Lubrication Technology, Transactions of ASME* pp. 87–92.

Hsing, F. C. (1972), 'Formulation of a generalized narrow groove theory for spiral grooved viscous pumps', *ASME Journal of Lubrication Technology* **94 Ser F**(1), 81–85. Compilation and indexing terms, Copyright 2006 Elsevier Inc. All rights reserved.

Huffman, G. D. and Bardshaw, P. (1972), 'A note on von karman's constants in low reynolds number turbulent flows', *Journal of Fluid Mechanics* **53**(1), 181–201.

Jeong, S., Murayama, M. and Yamamoto, K. (2004), Efficient optimization design method using kriging model, *in* '42nd AIAA Aerospace Sciences Meeting and Exhibit', p. 1.

Johnson, L. G. (1964), *The Statistical Treatment of Fatigue Experiments*, Elservier Publishing Company, New York.

Johnson, R. L. and Ludwig, L. P. (1969), Shaft face seal with self-acting lift augmentation for advanced gas turbine engines, Technical Report NASA TN D-5170, National Aeronautics and Space Administration.

Jürgen, B., Deb, K., Kaisa, M. and Steuer, R. E. (2004), '04461 abstracts collection: Practical approaches to multi-objective optimization', *Dagstuhl Seminar Proceedings 04461* .

Keane, A. and Nair, P. (2005), *Computational approaches for aerospace design: the pursuit of excellence*, John Wiley & Sons.

Keogh, P. S. and Khonsari, M. M. (2001), 'Influence of inlet conditions on the thermohydrodynamic state of a fully circumferentially grooved journal bearing', *Journal of tribology, Transactions of the ASME* **123**, 525–532.

Ketola, H. N. and McGrew, J. M. (1967), Pressure, frictional resistance, and flow characteristics of the partially wetted rotating disk, Technical Report ASME PAPER 67-WA/LUB-4, NASA.

Key, W. E., Salant, R. F., Payvar, P., Gopalakrishnan, S. and Vaghasia, G. (1989), 'Analysis of a mechanical seal with deep hydropads', *Tribology Transactions* **32**(4), 481–489.

Kim, J. H. and Kim, J.-H. (2005), 'Thermohydrodynamic analysis of surface roughness in the flow field', *Journal of Tribology, Transactions of the ASME* **127**, 293–301.

Knowles, J. and Corne, D. (1999), The pareto archived evolution strategy: A new baseline algorithm for pareto multiobjective optimisation, *in* 'Proceedings of the 1999 Congress on Evolutionary Computation-CEC99', Vol. 1, IEEE, p. 98.

Konak, A., Coit, W. D. and Smith, E. A. (2006), 'Multi-objective optimization using genetic algorithms: A tutorial', *Reliability Engineering and System Safety* **91**, 992–1007.

Laurenson, I. T. and O'Donoghue, J. P. (1978), 'Hydrostatic seal design', *Journal of Mechanical Engineering Science* **20**(3), 159–167. Compilation and indexing terms, Copyright 2006 Elsevier Inc. All rights reserved.

Li, W., Song, P., Zhao, Y. and Cao, D. (2006), 'Influence of waviness and taper of seal faces on the operating performance of slow speed gas face seal', *Run Hua Yu Mi Feng/Lubrication Engineering* (5), 93–97. Compilation and indexing terms, Copyright 2006 Elsevier Inc. All rights reserved.

Liang, A. D. (1994), Seals flow code development workshop, *in* 'Proceedings of a workshop held at NASA Lewis Research Center, Cleveland, Ohio, November 3-4, 1993', NASA CP-10136, Washington, D.C.

Liepmann, H. W. and Roshko, A. (1957), *Elements of Gas Dynamics*, John Wiley and Sons, New York.

Lin, K.-L. and Shaw, H.-J. (1991), 'Two-dimensional orthogonal grid generation techniques', *Computers and Structures* **41**(4), 569–583. Compilation and indexing terms, Copyright 2006 Elsevier Inc. All rights reserved.
URL: *http://dx.doi.org/10.1016/0045-7949(91)90169-M*

Lipschitz, A., Basu, P. and Johnson, R. P. (1991), 'Bi-directional gas thrust bearing', *Tribology Transactions* **34**(1), 9–16. Compilation and indexing terms, Copyright 2006 Elsevier Inc. All rights reserved.

Liu, Y.-C., Xu, W.-F., Chen, G.-L. and Shen, X.-M. (2000), 'High-performance face configuration for a gas film face seal', *Acta Aeronautica et Astronautica Sinica* **21**(2), 187–190. NR: 11.

Liu, Y., Shen, X. and Xu, W. (2002), 'Numerical analysis of dynamic coefficients for gas film face seals', *Journal of Tribology* **124**(4), 743–754. Compilation and indexing terms, Copyright 2006 Elsevier Inc. All rights reserved.
URL: *http://dx.doi.org/10.1115/1.1472459*

Liu, Z., Liu, Y. and Liu, X. (2007), 'Optimization design of main parameters for double spiral grooves face seal', *Science in China Series E: Technological Sciences* **50**(4), 448–453.

Lu, H. and Yen, G. G. (2003), 'Rank-density-based multiobjective genetic algorithm and benchmark test function study', *Evolutionary Computation, IEEE Transactions* **7**(4), 325–343.

Mathé, P. (2000), 'Hilbert space analysis of latin hypercube sampling', *Proceedings of the American Mathematical Society* **129**(5), 1477–1492.

Menendez, R. P. and Cunningham, M. D. (1999), Development of liftoff seal technology for air/oil axial sealing applications, *in* 'AIAA/ASME/SAE/ASEE Joint Propulsion Conference and Exhibit, 35th, Los Angeles, CA; UNITED STATES; 20-24 June 1999', Vol. AIAA Paper 1999-2822, EG&G Centurion Mechanical Seals, Warwick, RI. NR: 5.

Miller, B. A. and Green, I. (2002), 'Numerical techniques for computing rotordynamic properties of mechanical gas face seals', *Journal of Tribology* **124**(4), 755–761. Compilation and indexing terms, Copyright 2006 Elsevier Inc. All rights reserved.
URL: *http://dx.doi.org/10.1115/1.1467635*

Miller, B. A. and Green, I. (2003), 'Semi-analytical dynamic analysis of spiral-grooved mechanical gas face seals', *Journal of Tribology* **125**(2), 403–413. Compilation and indexing terms, Copyright 2006 Elsevier Inc. All rights reserved.
URL: *http://dx.doi.org/10.1115/1.1510876*

Molyneaux, A. K. and Leonhard, M. (1989), 'Use of spiral groove gas bearings in a 350,000 rpm cryogenic expander', *Tribology Transactions* **32**(2), 197–204. Compilation and indexing terms, Copyright 2006 Elsevier Inc. All rights reserved.

Mtisuya, Y., Ohkubo, T. and Ota, H. (1989), 'Averaged reynolds equation extended to gas lubrication possessing surface roughness in the slip flow regime: Approximate method and confirmation experiments', *Journal of Tribology, Transactions of the ASME* **111**, 495–503.

Mundt, C., Keraus, R. and Fischer, J. (1991), 'New, accurate, vectorized approximations of state surfaces for the thermodynamic and transport properties of equilibrium air', *Zeitschrift für Flugwissenschaften und Weltraumforschung* **15**(Springer Verlag), 179–184.

Murata, T. and Ishibuchi, H. (1995), Moga: Multi-objective genetic algorithm, *in* 'IEEE international conference on evolutionary computation', IEEE.

Nassab, S. A. G. and Moayeri, M. S. (2002), 'Three-dimensional thermohydrodynamic analysis of axially grooved journal bearings', *Proceedings of the Institution of Mechanical Engineers, Part J: Journal of Engineering Tribology* **216**(1), 35–48. Compilation and indexing terms, Copyright 2006 Elsevier Inc. All rights reserved.
URL: *http://dx.doi.org/10.1243/1350650021543870*

Nelson, W. (1985), 'Weibull analysis of reliability data with few or no failures', *Journal of Quality Technology* **17**(3), 140–146.

Nelson, W. (2004), *Accelerated Testing: Statistical Models, Test Plans, and Data Analysis*, John Wiley and Sons Ltd, New York.

Owen, A. B. (1992), 'Orthogonal arrays for computer experiments, integration and visualization', *Statistica Sinica* **2**, 439–452.

Pan, C. H. T. (1998), 'Compressible narrow groove analysis - part 2: Computation of pressure field in a spherical device rotating in either direction', *Journal of Tribology, Transactions of the ASME* **120**(4), 765–771. Compilation and indexing terms, Copyright 2006 Elsevier Inc. All rights reserved.

Pan, C. H. T. and Andrés, L. S. (2005), The narrow groove analysis revisited, *in* '2005 World Tribology Congress III, Sep 12-16 2005', Proceedings of the World Tribology Congress III - 2005, Engineering Consultant, Millbury, MA 01527, United States, American Society of Mechanical Engineers, New York, NY 10016-5990, United States, Washington, D.C., United States, pp. 121–122. Compilation and indexing terms, Copyright 2006 Elsevier Inc. All rights reserved.

Papavassiliou, D. V. and Hanratty, T. J. (1997), 'Interpretation of large-scale structures observed in a turbulent plane couette flow', *International Journal of Heat Fluid Flow* **18**, 55–69.

Patir, N. and Cheng, H. S. (1978), 'An average flow model for determining effects of three-dimensional roughness on partial hydrodynamic lubrication', *Journal of Lubrication Technology* **100**, 12–17.

Pecht, G. G. and Carter, D. (1990), 'System design and performance of a spiral groove gas seal for hydrogen service', *Lubrication Engineering* **46**(9), 607–612. Compilation and indexing terms, Copyright 2006 Elsevier Inc. All rights reserved.

Pennink, H. (1985), Gas lubricated spiral grooved face seal in the process industry, *in* 'Proceedings of the Fourteenth Turbomachinery Symposium.', Proceedings of the Turbomachinery Symposium, Atlas Copco Comptec Inc, Voorheesville, NY, USA, Texas A&M Univ, College Station, TX, USA, Houston, TX, USA, pp. 59–64. Compilation and indexing terms, Copyright 2006 Elsevier Inc. All rights reserved.

Pinkus, O., Szeri, A. Z. and Shapiro, W. (1987), 'The reynolds centennial : a brief history of the theory of hydrodynamic lubrication', *American society of mechanical engineers/American society of lubrification engineers tribology conference, Pittsburg (1986)* **109**(1), 2–20.

Rasaei, M. and Winoto, S. H. (1997), 'Visualization in the interface of a noncontacting mechanical face seal with spiral groove pattern', *Journal of Flow Visualization and Image Processing* **4**, 141–148.

Razzaque, M. M. and Faisal, M. T. R. (2007), 'Performance of mechanical face seals with surface micropores', *Journal of Mechanical Engineering, Transaction of the Mech. Eng. Div., The Institution of Engineers, Bangladesh* **ME37**, 77–80.

Roberts, M. G. (1996), Comparison of spiralg performance predictions with a spread sheet solution, *in* 'Proceedings of the 1995 Workshop of NASA Lewis Research Center, Jun 14-15 1995', NASA Conference Publication, Rolls-Royce, Inc, Atlanta, GA, USA, NASA, Cleveland, OH, USA, Cleveland, OH, USA, pp. 139–143. Compilation and indexing terms, Copyright 2006 Elsevier Inc. All rights reserved.

Rogers, G. F. C. and Mayhew, Y. R. (1995), *Thermodynamic and Transport Properties of Fluids: S. I. Units*.

Romero, V. J., Burkardt, J. V., Gunzberger, M. D. and Peterson, J. S. (2003), Initial application and evaluation of a promising new sampling method for response surface generation: Centroidal voronoi tessellation, *in* 'Fourth International Symposium on Uncertainty Modeling and Analysis', IEEE, p. 174.

Ruan, B. (2001), 'Numerical modeling of dynamic sealing behaviors of spiral groove gas face seals', *American Society of Mechanical Engineers, Tribology Division, TRIB* (52), 1–10. Compilation and indexing terms, Copyright 2006 Elsevier Inc. All rights reserved.

Sahlin, F., Glavatskih, S. B., Almqvist, T. and Larsson, R. (2005), 'Two-dimensional cfd-analysis of micro-patterned surfaces in hydrodynamic lubrication', *Journal of Tribology, Transactions of the ASME* **127**(1), 96–102.

Salant, R. F. (2003), 'The use of modeling to understand malfunction and failure in mechanical seals', *Elsevier Science Journal of sealing technology* **203**, 8–12.

Salant, R. F. and Cao, B. (2005), 'Unsteady analysis of a mechanical seal using duhamel's method', *Journal of Tribology, Transactions of the ASME* **127**(3), 623–631.

Salant, R. F. and Homiller, S. J. (1991), Behavior of upstream pumping seals, *in* 'Winter Annual Meeting of the American Society of Mechanical Engineers, Dec 1-6 1991', Vol. 21 of *American Society of Mechanical Engineers, Bioengineering Division (Publication) BED*, Georgia Inst of Technology, Atlanta, GA, USA, Publ by ASME, New York, NY, USA, Atlanta, GA, USA, pp. 33–36. Compilation and indexing terms, Copyright 2006 Elsevier Inc. All rights reserved.

Salant, R. F. and Homiller, S. J. (1992), 'The effects of shallow groove patterns on mechanical seal leakage', *Tribology Transactions* **35**(1), 142–148.

Salant, R. F. and Wolff, P. J. (1994), 'Development of an electronically controlled mechanical seal for aerospace applications', *SAE Transactions* **103**(1), 331–336.

Sarker, R., Liang, K.-H. and Newton, C. (2002), 'Continous optimization: A new multiobjective evolutionary algorithm', *European Journal of Operational Research* **140**(1), 12–23.

Sawada, T. (1979), 'Vacuum sealing with a spiral grooved gas dynamic seal', *Bulletin of the JSME* **22**(169), 974–981. Compilation and indexing terms, Copyright 2006 Elsevier Inc. All rights reserved.

Sawada, T. and Morikawa, H. (1981), Performance of spiral grooved gas dynamic seals in the free molecule flow regime, *in* 'Vacuum Symposium Proceedings, 1980', Vol. 24 of *J. Vac. Soc. Jpn. (Japan)*, Mining Coll., Akita Univ., Akita, Japan, Kyoto, Japan, pp. 181–4.

Sayma, A. I., Breard, C., Vahdati, M. and Imregun, M. (2002), 'Aeroelasticity analysis of air-riding seals for aero-engine applications', *Journal of Tribology, Transactions of the ASME* **124**(3), 607–616.

Schaffer, J. D. (1985), Multiple objective optimization with vector evaluated genetic algorithm, *in* 'Proceedings of the 1st International Conference on Genetic Algorithms', L. Erlbaum Associates Inc., Hillsdale, NJ, USA.

Schmatz, M. A. (1989), Hypersonic three-dimensional navier-stokes calculations for equilibrium gas, *in* '7th annual applied aerodynamics conference in conjunction with the AIAA/AHS/ASEE aircraft design and operations meeting, Seattle, WA (USA), 31 Jul - 2 Aug 1989', number 89-2183.

Sedy, J. (1980), 'New self-aligning mechanism for the spiral-groove gas seal stability', *Lubrication Engineering* **36**(10), 592–598. Compilation and indexing terms, Copyright 2006 Elsevier Inc. All rights reserved.

Shapiro, W. and Athavale, M. M. (1995), Seal analysis computer codes, *in* 'SAE 1994 Transactions, Journal of Aerospace. Section 1 - Vol. 103 (A96-37718 10-31); UNITED STATES', Vol. SAE Paper 941206, Mechanical Technology, Inc., Latham, NY, Warrendale, PA: Society for Automotive Engineers, Inc. NU: Contract: NAS3-25644; NR: 18.

Simpson, T. W., Mauery, T. M., Korte, J. J. and Mistree, F. (2001), 'Kriging models for global approximation in simulation-based multidisciplinary design optimization', *American Institute of Aeronautics and Astronautics Journal* **39**(12), 2233–2241.

Smalley, A. J. (1972), 'Narrow groove theory of spiral grooved gas bearings: Development and application of a generalized formulation for numerical solution', *Journal of Lubrication Technology, Transactions of ASME* **94 Ser F**(1), 86–92. Compilation and indexing terms, Copyright 2006 Elsevier Inc. All rights reserved.

So, H. and Chen, C. H. (2004), 'Effects of micro-wedges formed between parallel surfaces on mixed lubrication part i: Experimental evidence', *Tribology Letters* **17**(3), 513–520.

Spear, M. (1990), 'Sealing the future', *Process Engineering (London)* **71**(5), 51–52. Compilation and indexing terms, Copyright 2006 Elsevier Inc. All rights reserved.

Srinivas, N. and Deb, K. (1994), 'Multiobjective optimization using nondominated sorting in genetic algorithm', *Evolutionary Computation* **2**(3), 221–248.

Srinivasan, S. and Weilmuenster, K. J. (1987), Simplified curve fits for the thermodynamic properties of equilibrium air, Technical Report RP-1181, NASA.

Stolarski, T. A. and Xue, Y. (1998), 'Performance study of a back-depression mechanical dry gas seal', *Proceedings of the Institution of Mechanical Engineers, Part J: Journal of Engineering Tribology* **212**(4), 279–290. http://dx.doi.org/10.1243/1350650981542092.

Strodtman, C. L. (1971), 'Optimization of clearance in a squeeze-film journal bearing', *Journal of Lubrication Technology, Transactions ASME* pp. 246–251.

Strom, T. N., Ludwig, L. P. and Allen, G. P. (1967), Spiral groove face seal concepts; comparison to conventional face contact seals in sealing liquid sodium (400^o to $1000^o f$), Technical Report TM X-52327, National Aeronautics and Space Administration.

Szeri, A. Z. (1980), *Turbulence, Inertia, and Thermal Effects in Fluid Film Bearings*, Tribology: Friction, Lubrication, and Wear, Mc Graw-Hill B.C., pp. 229–294.

Telbany, M. M. M. E. and Reynolds, A. J. (1980), 'Velocity distributions in plane turbulent channel flows', *Journal of Fluid Mechanics* **100**, 1–29.

Teo, K.-M. and Lafdi, K. (2002), 'Effect of thermal property variation on surface grooving', *Journal of Tribology, Transactions of the ASME* **124**, 274–280.

Theodorsen, T. and Reigier, A. (1944), Experiments on drag of revolving disk, cylinders, and streamline rods at high speeds, Technical Report NACA 793, National Advisory Committee for Aeronautics.

Thomas, S., Brunetière, N. and Tournerie, B. (2006), 'Numerical modelling of high pressure gas face seals', *Journal of Tribology, Transactions of the ASME* **128**(2), 396–405.

Thompson, J. F. (1984), 'Grid generation techniques in computational fluid dynamics', *AIAA Journal* **22**(11), 1506–23.

Tieu, A. K. and Kosasih, P. B. (1992), 'An expression of reynolds stresses in turbulent lubrication theory', *Journal of Tribology, Transactions of the ASME* **114**(1), 57–60.

Tonder, K. (1977), 'Lubrication of surfaces having area distributed isotropic roughness', *Journal of Lubrication Technology, Transactions of ASME* **99**, 323–330.

Tournerie, B., Huitric, J., Bonneau, D. and Frêne, J. (1994), Optimization and performance prediction of grooved face seals for gases and liquids, *in* '14th International Conference on Fluid sealing', BHR Group Limited, Cranfield, Bedford, UK, p. 351.

Wachmann, C., Malanoski, S. B. and Vohr, J. H. (1971), 'Thermal distortion of spiral-grooved gas-lubricated thrust bearings', *Journal of Lubrication Technology, Transactions of ASME* **93 Ser F**(1), 102–114. Compilation and indexing terms, Copyright 2006 Elsevier Inc. All rights reserved.

Wada, S. and Hashimoto, H. (1979), 'Turbulent lubrication theory using the frictional law i - derivation of turbulent coefficients and lubrication equation', *Bulletin of the JSME* **22**(164), 249–256.

Wang, X., Zhang, Z. and Sun, M. (2000), 'A comparison of flow fields predicted by various turbulent lubrication models with existing measurements', *Journal of Tribology, Transactions of the ASME* **122**(2), 475–477.

Wasser, J. R. (1994), 'Dry seal technology for rotating equipment', *Lubrication Engineering* **50**(3), 247–252. Compilation and indexing terms, Copyright 2006 Elsevier Inc. All rights reserved.

Weibull, W. (1951), 'A statistical distribution function of wide applicability', *ASME Journal of Applied Mechanics* **18**, 293–297.

Weibull, W. (1961), *Fatigue Testing and Analysis of Results*, Pergamon Press, Oxford, UK.

Whipple, R. T. P. (1958), The inclined groove bearing, Technical Report AERE Report T/T 622 (revised), United Kingdom Atomic Energy Authority, Research Group, Atomic Energy Establishment.

White, J. S. (1964), Weibull renewal analysis, Technical Report GMR-597, General Motors Corporation Research Report.

Wu, L. and Bogy, D. B. (2003), 'New first and second order slip models for the compressible reynolds equation', *Journal of Tribology, Transactions of the ASME* **125**, 558–561.

Xu, W., Chen, C., Guo, X. and Li, Y. (1990), The characteristics study of gas lubricated self-acting spiral grooved thrust bearings equipped on the expansion turbines, *in* 'Thirteenth International Cryogenic Engineering Conference ICEC 13, 24-27 April 1990', Vol. 30 of *Cryogenics (UK)*, Div. of Cryogenic Tech., Xi'an Jiaotong Univ., China, Beijing, China, pp. 93–7.

Xue, Y. and Stolarski, T. A. (1997), 'Numerical prediction of the performance of gas-lubricated spiral groove thrust bearings', *Proceedings of the Institution of Mechanical Engineers, Part J: Journal of Engineering Tribology* **211**(2), 117–128. Compilation and indexing terms, Copyright 2006 Elsevier Inc. All rights reserved.
URL: *http://dx.doi.org/10.1243/1350650971542363*

Yamada, Y. (1962), 'Resistance of a flow through an annulus with an inner rotating cylinder', *JSME International Journal* **5**(18), 302–310.

Yang, S. L. and Shih, T. I.-P. (1986), 'Algebraic grid generation technique for time-varying two-dimensional spatial domains', *International Journal for Numerical Methods in Fluids* **6**(5), 291–304. Compilation and indexing terms, Copyright 2006 Elsevier Inc. All rights reserved.

Yelma, S. S., Miller, B. A. and Landers, R. G. (2004), 'Automatic feedback control of mechanical gas face seals via clearance control', *Tribology Transactions* **47**(4), 500–507.

Yen, G. G. and Lu, H. (2003), 'Dynamic multiobjective evolutionary algorithm: adaptive cell-based rank and density estimation', *Evolutionary Computation, IEEE Transactions* **7**(3), 253–274.

Yin, X. and Peng, X. (2006*a*), 'Finite element analysis of a dry gas seal under slip flow conditions', *Run Hua Yu Mi Feng/Lubrication Engineering* (4), 55–56. Compilation and indexing terms, Copyright 2006 Elsevier Inc. All rights reserved.

Yin, X. and Peng, X. (2006*b*), 'Selection of a shape function in finite element analysis for a spiral groove dry gas seal', *Run Hua Yu Mi Feng/Lubrication Engineering* (3), 13–14. Compilation and indexing terms, Copyright 2006 Elsevier Inc. All rights reserved.

Zhang, H., Miller, B. A. and Landers, R. G. (2006), 'Nonlinear modeling of mechanical gas face seal systems using proper orthogonal decomposition', *Journal of Tribology, Transactions of the ASME* **128**, 817–827.

Zheng, X. (2005), Parametrical study of hydrodynamic seal using a 2d design code and comparing with a 3d cfd model, *in* 'GT2005 ASME Turbo Expo 2005: Power for Land, Sea and Air', Vol. 3 PART B of *Proceedings of the ASME Turbo Expo*, Centurion Mechanical Seals, PerkinElmer Fluid Sciences, Warwick, RI 02888, United States, pp. 1173–1180. Compilation and indexing terms, Copyright 2006 Elsevier Inc. All rights reserved.

Zhou, Z., Ong, Y. S., Nair, P. B., Keane, A. J. and Lum, K. Y. (2007), 'Combining global and local surrogate models to accelerate evolutionary optimization', *IEEE Transactions On Systems, Man and Cybernetics* **37**(1), 66–76.

Zhu, Q. and Zhang, W. J. (2000), 'A numerical procedure based on the boundary element method analysis of the archimedean spiral grooved thrust oil bearing', *Journal of Tribology, Transactions of the ASME* **122**, 565–572.

Zirkelback, N. (2000), 'Parametric study of spiral groove gas face seals', *Tribology Transactions* **43**(2), 337–343. Compilation and indexing terms, Copyright 2006 Elsevier Inc. All rights reserved.

Zirkelback, N. and Andrés, L. S. (1999), 'Effect of frequency excitation on force coefficients of spiral groove gas seals', *Journal of Tribology, Transactions of the ASME* **121**(4), 853–863. Compilation and indexing terms, Copyright 2006 Elsevier Inc. All rights reserved.

Zitzler, E., Laumanns, M. and Thiele, L. (2001), Spea2: Improving the strength pareto evolutionary algorithm, Technical Report TIK-Report 103.

Zitzler, E. and Thiele, L. (1999), 'Multiobjective evolutionary algorithms: a comparative case study and the strength pareto approach', *IEEE Transaction on Evolutionary Computation* **3**(4), 257–271.

Zobens, A. (1975), 'Noncontacting face seals application for sealing gas', *Journal of Lubrication Technology, Transactions of ASME* **31**(1), 16–19.

Appendix A

Results Figures for Application of Numerical Models

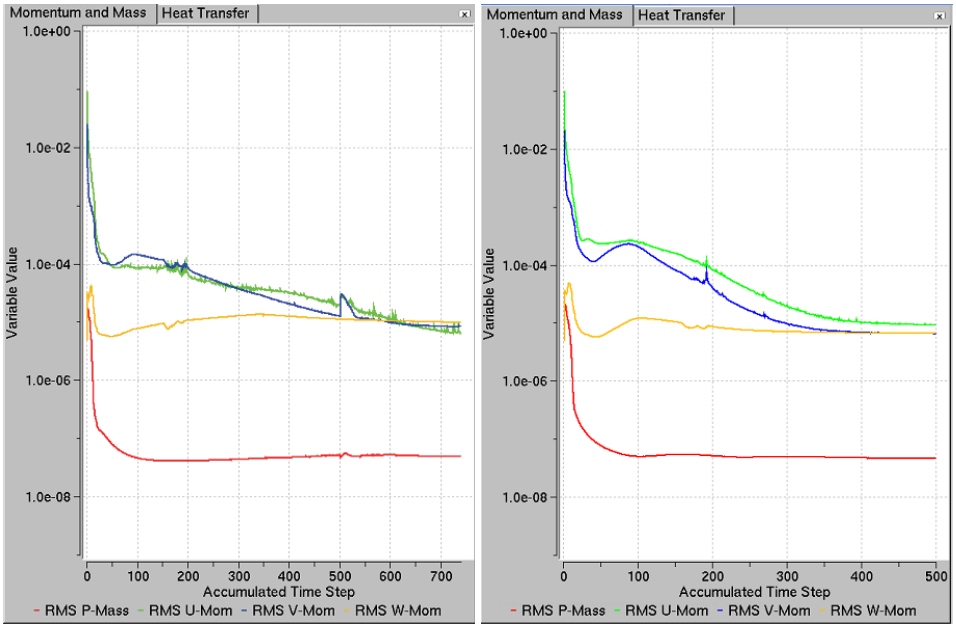

(a) fluid film thickness, $3\,\mu m$

(b) fluid film thickness, $5\,\mu m$

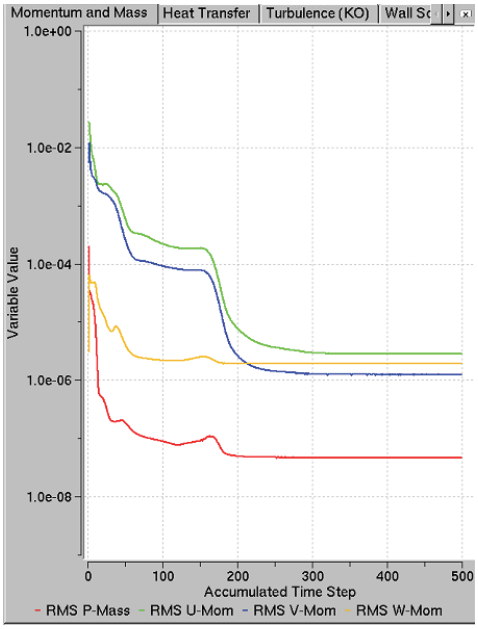

(c) fluid film thickness, $10\,\mu m$

Figure A.1 Convergence plots of the 3D CFD model simulations at seal operating conditions of sealed fluid pressure, 31.52 bar, rotating speed, 5052 rpm, and sealed fluid temperature, 23.9°C

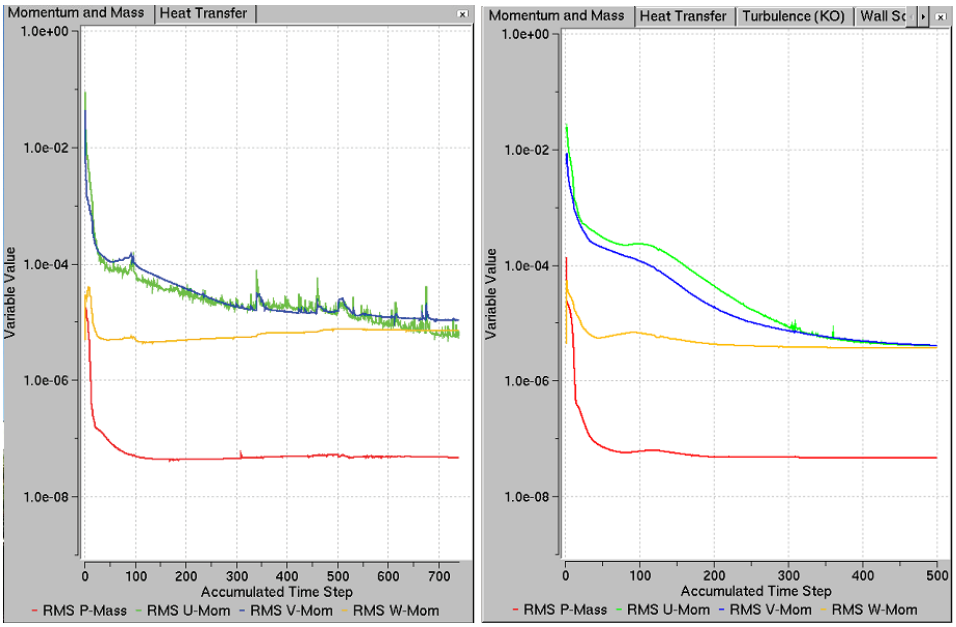

(a) fluid film thickness, $3\,\mu m$ (b) fluid film thickness, $5\,\mu m$

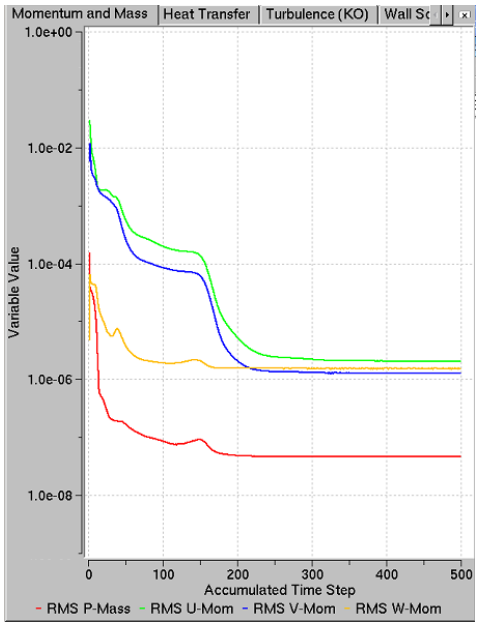

(c) fluid film thickness, $10\,\mu m$

Figure A.2 Convergence plots of the 3D CFD model simulations at seal operating conditions of sealed fluid pressure, 31.52 bar, rotating speed, 10104 rpm, and sealed fluid temperature, 48.9°C

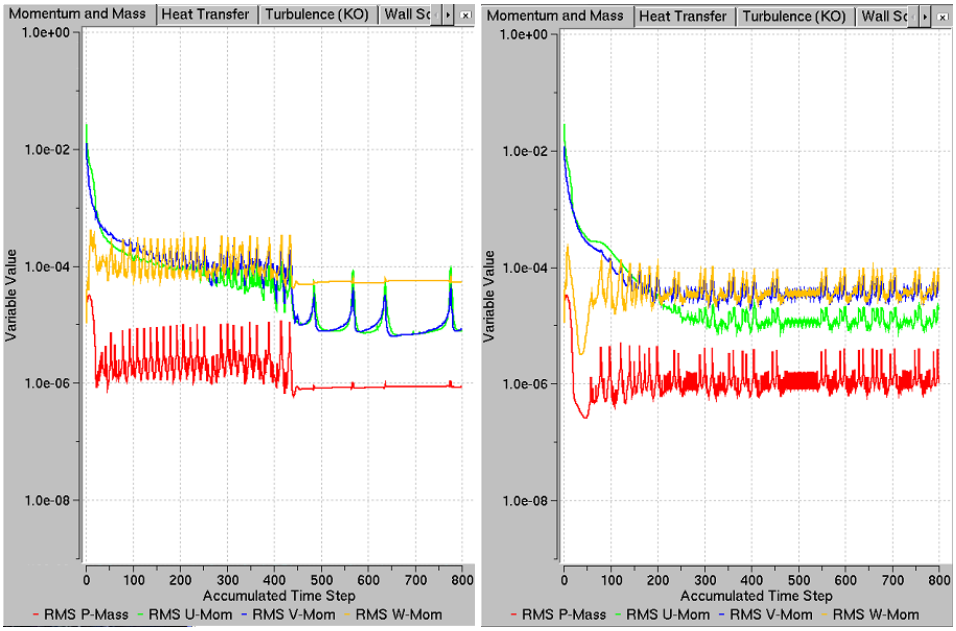

(a) fluid film thickness, $3\,\mu m$ (b) fluid film thickness, $5\,\mu m$

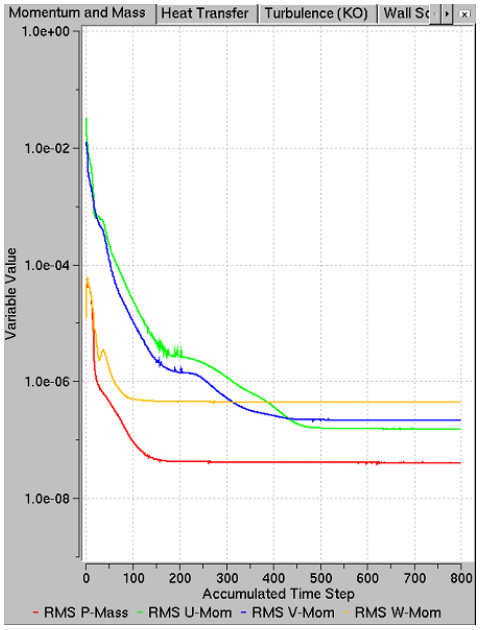

(c) fluid film thickness, $10\,\mu m$

Figure A.3 Convergence plots of the 3D CFD model simulations at seal operating conditions of sealed fluid pressure, 200 bar, rotating speed, 40000 rpm, and sealed fluid temperature, 120°C

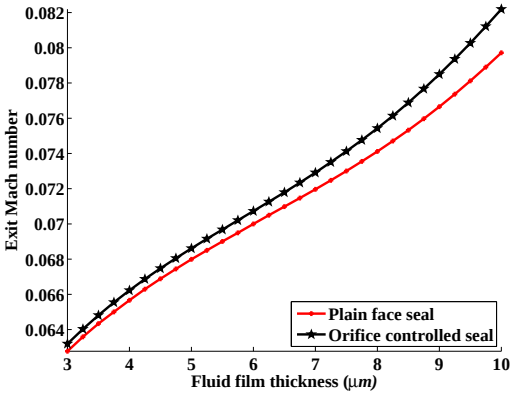

(a) Exit Mach number

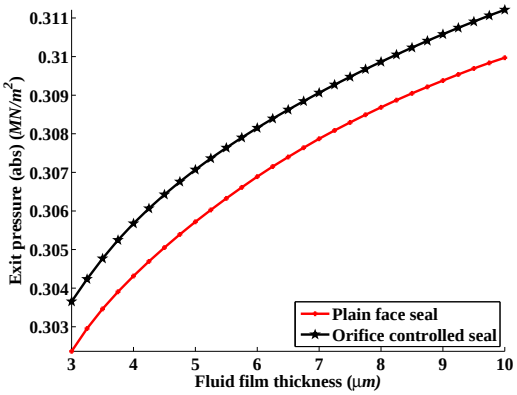

(b) Exit pressure

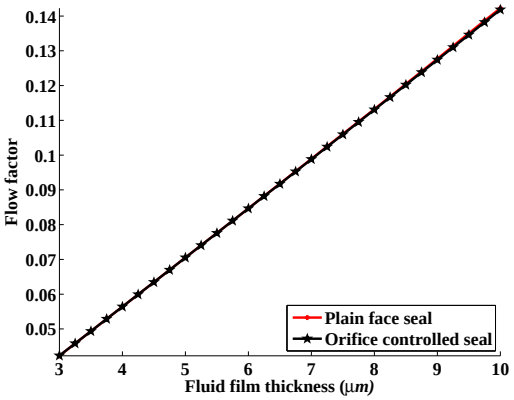

(c) Flow factor

Figure A.4 Flow characteristics as functions of fluid film thickness of plain face seal and orifice controlled seal operating at sealed fluid pressure of 6 bar, rotating speed of 10000 rpm and sealed fluid temperature of 120°C

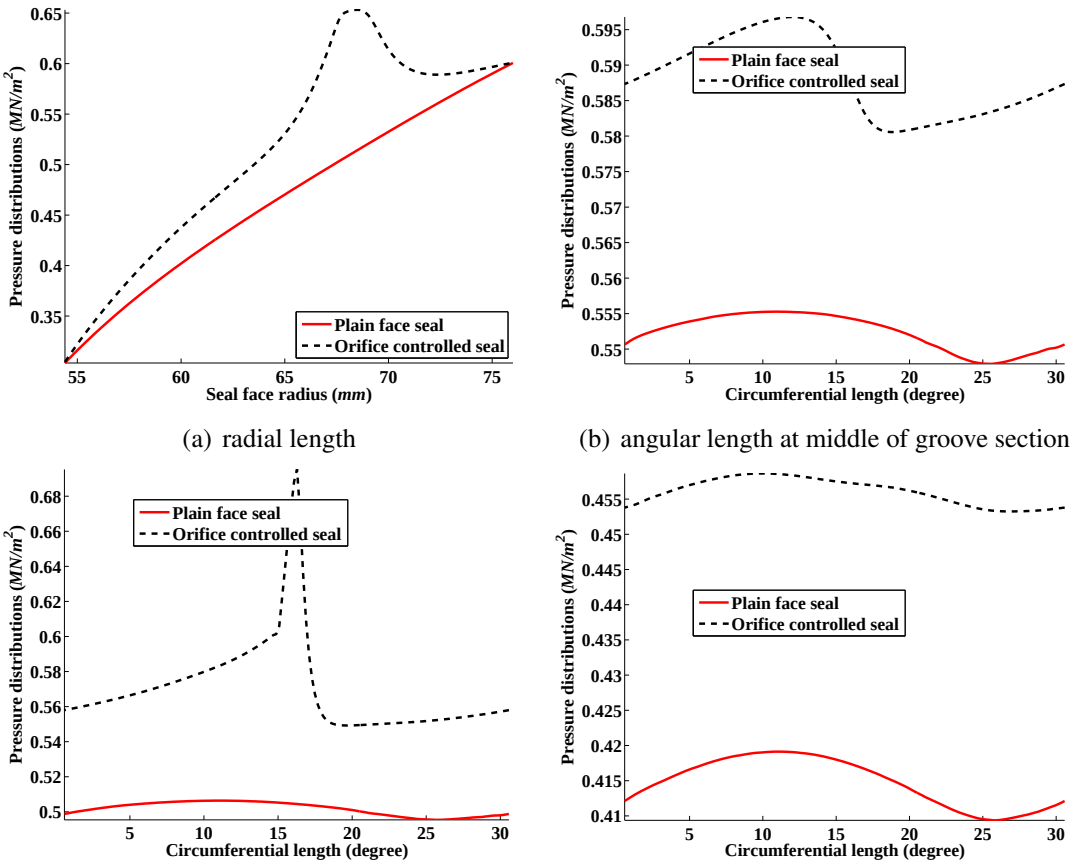

(a) radial length

(b) angular length at middle of groove section

(c) angular length at beginning of groove

(d) angular length at middle of dam section

Figure A.5 Seal pressure distributions as functions of seal face lengths of plain face seal and orifice controlled seal operating at sealed fluid pressure of 6 bar, rotating speed of 10000 rpm and sealed fluid temperature of 120°C taken at an XY plane of fluid film thickness of 3 μm

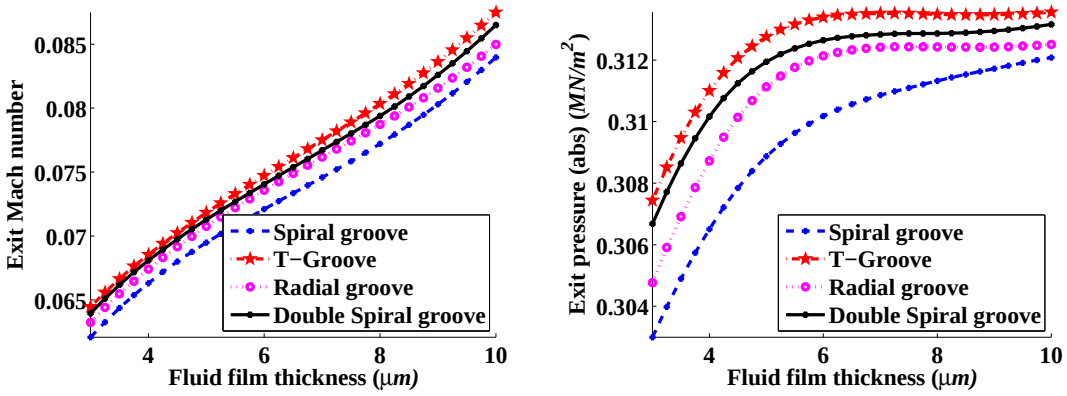

(a) Exit Mach number

(b) Exit pressure

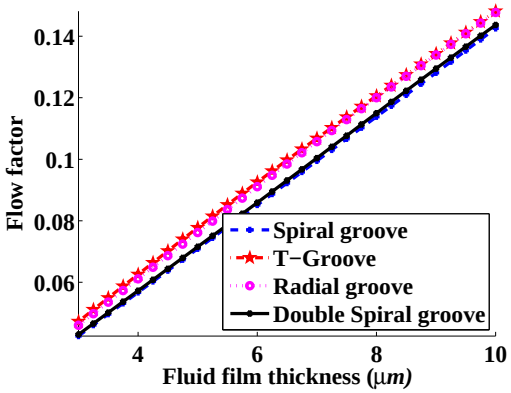

(c) Flow factor

Figure A.6 Flow characteristics as functions of fluid film thickness of various groove face profiles operating at sealed fluid pressure of 6 bar, normal rotating speed of 10000 rpm and sealed fluid temperature of 120°C

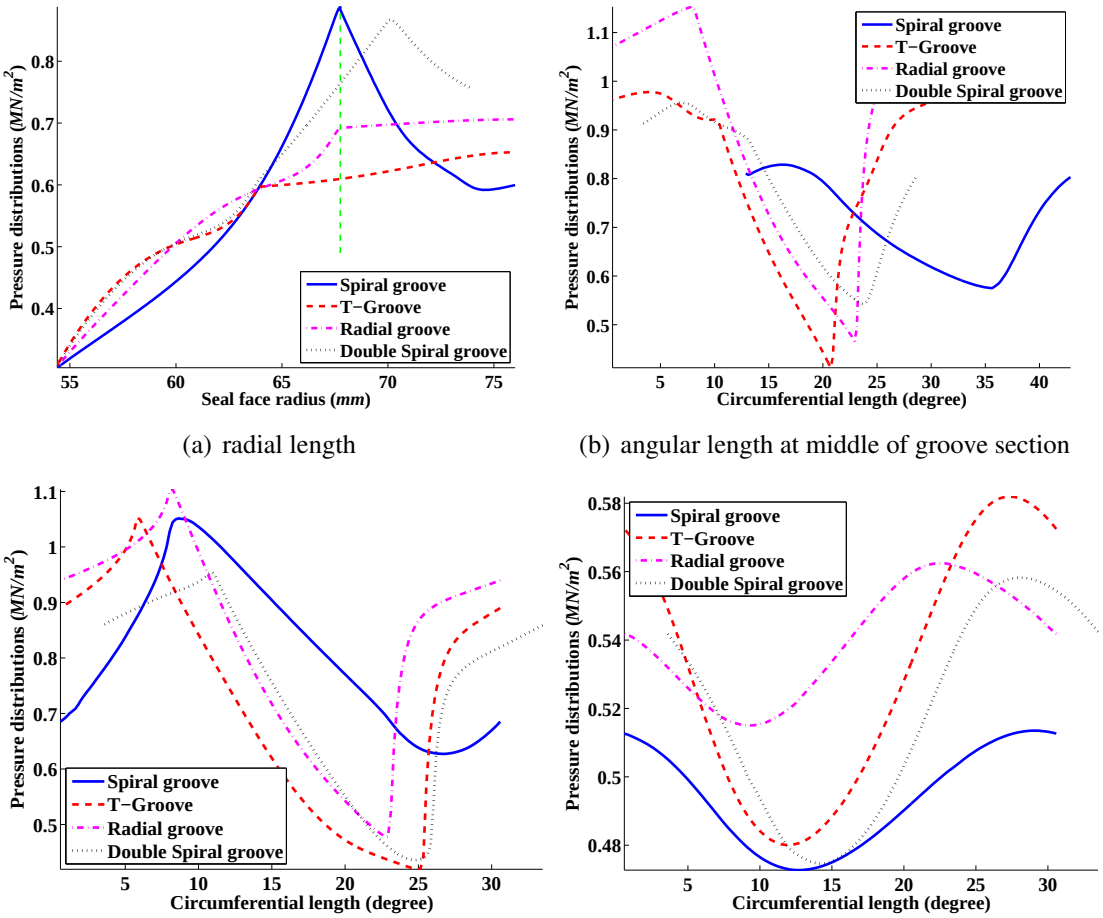

(a) radial length

(b) angular length at middle of groove section

(c) angular length at beginning of groove

(d) angular length at middle of dam section

Figure A.7 Seal pressure distributions as functions of seal face lengths of various groove face profiles operating at sealed fluid pressure of 6 bar, normal rotating speed of 10000 rpm and sealed fluid temperature of 120°C taken at an XY plane of fluid film thickness of 3 μm

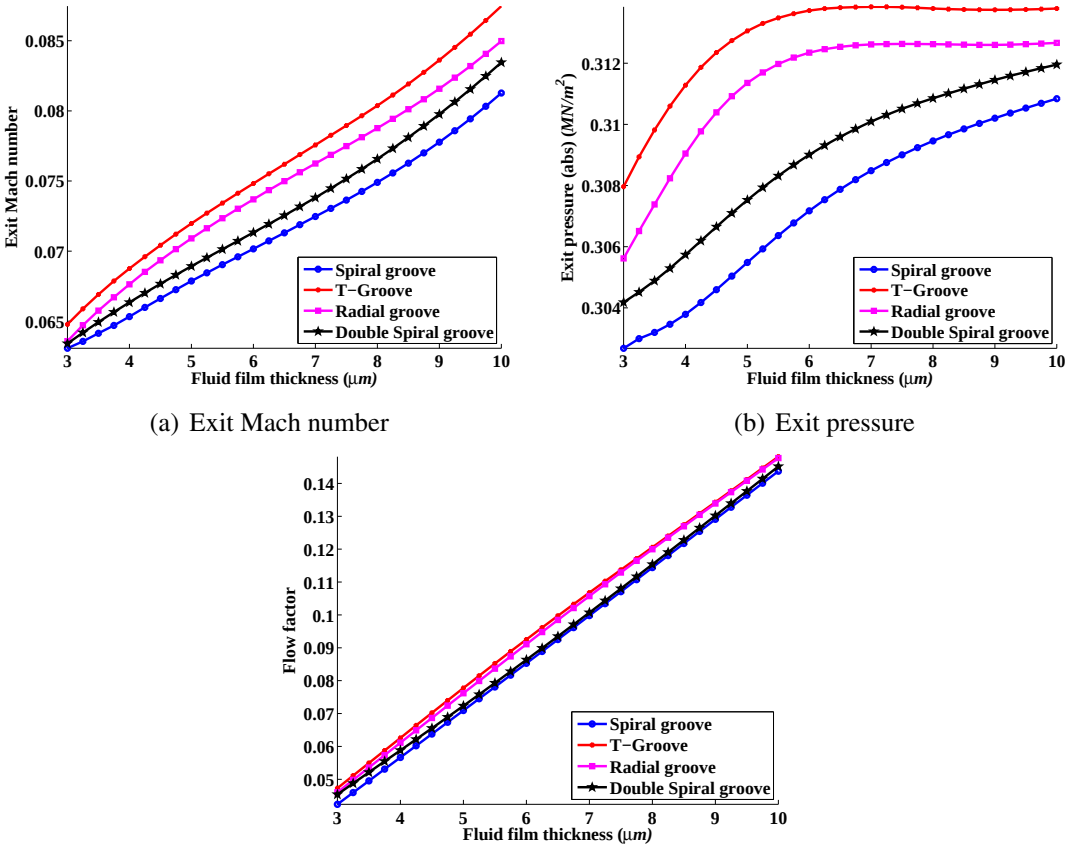

(a) Exit Mach number

(b) Exit pressure

(c) Flow factor

Figure A.8 Flow characteristics as functions of fluid film thickness of various groove face profiles operating at sealed fluid pressure of 6 bar, reversed rotating speed of 10000 rpm and sealed fluid temperature of 120°C

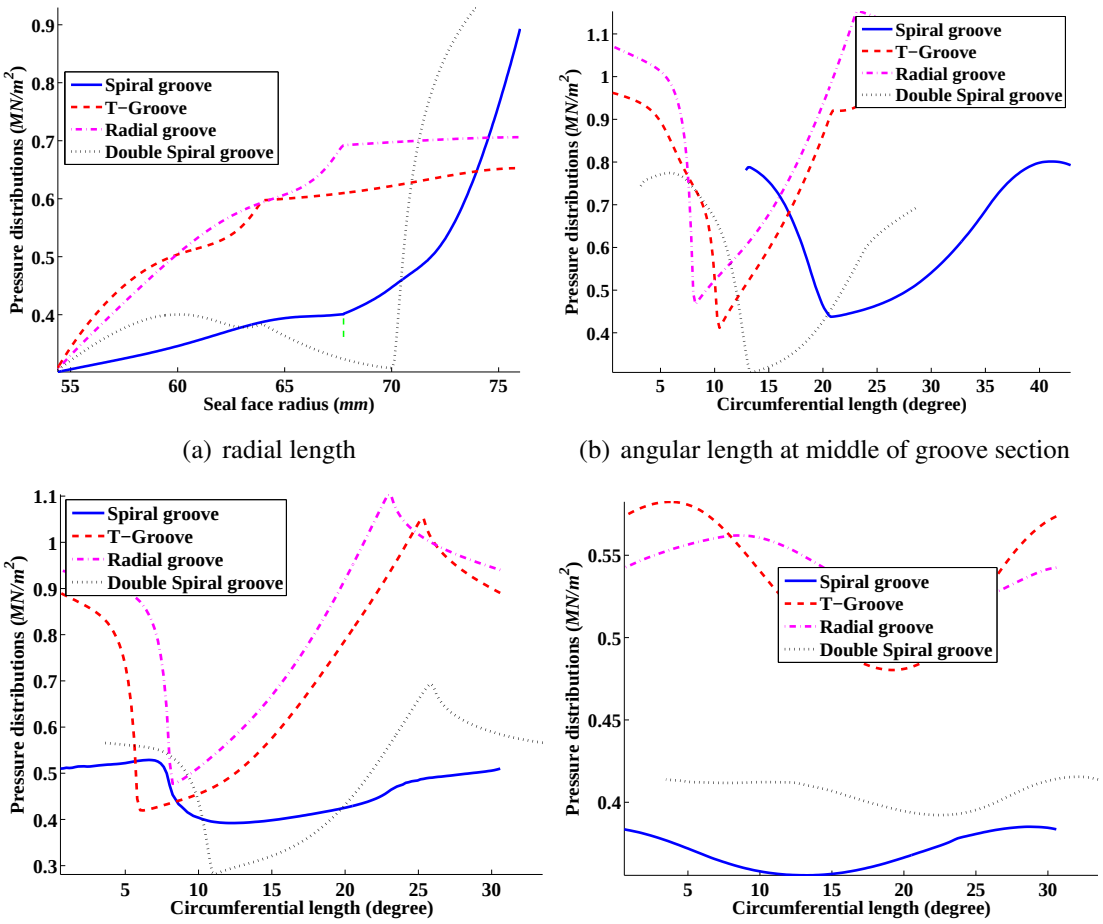

(a) radial length

(b) angular length at middle of groove section

(c) angular length at beginning of groove

(d) angular length at middle of dam section

Figure A.9 Seal pressure distributions as functions of seal face lengths of various groove face profiles operating at sealed fluid pressure of 6 bar, reversed rotating speed of 10000 rpm and sealed fluid temperature of 120°C taken at an XY plane of fluid film thickness of 3 μm

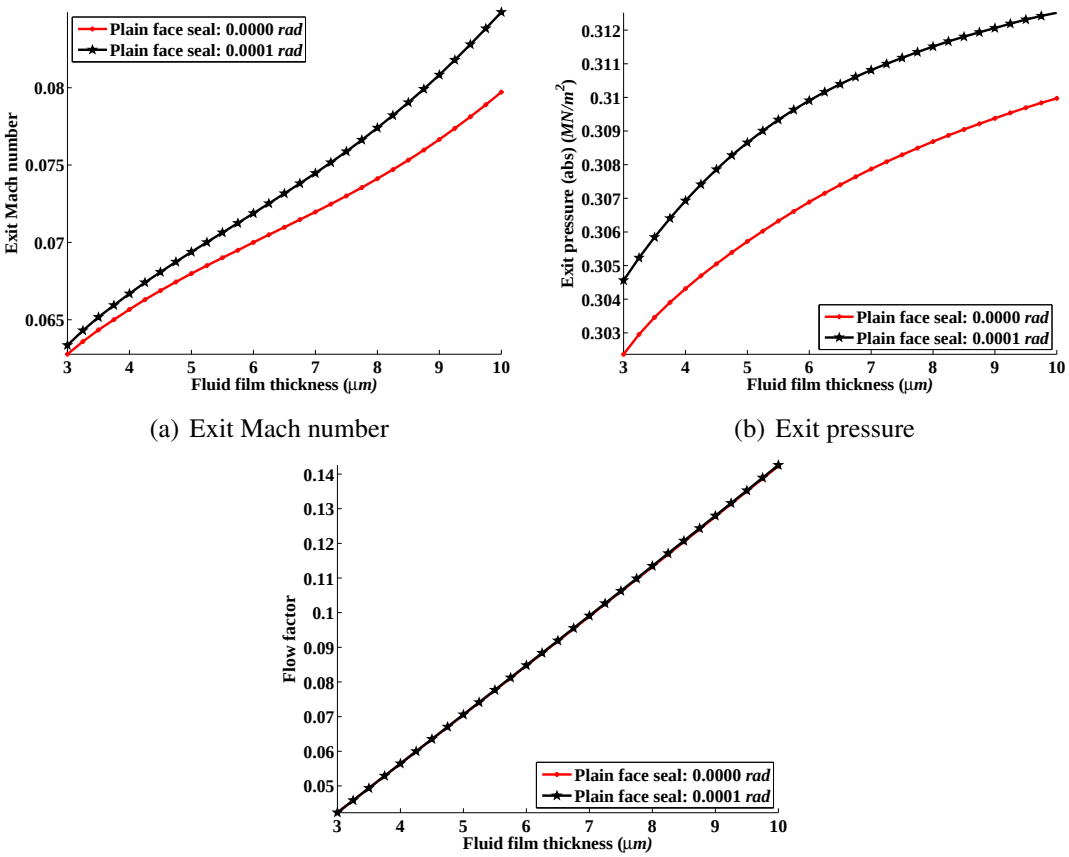

(a) Exit Mach number

(b) Exit pressure

(c) Flow factor

Figure A.10 Flow characteristics as functions of fluid film thickness of a plain face seal with the considerations of face deformation, seal operating at sealed fluid pressure of 6 bar, rotating speed of 10000 rpm and sealed fluid temperature of 120°C

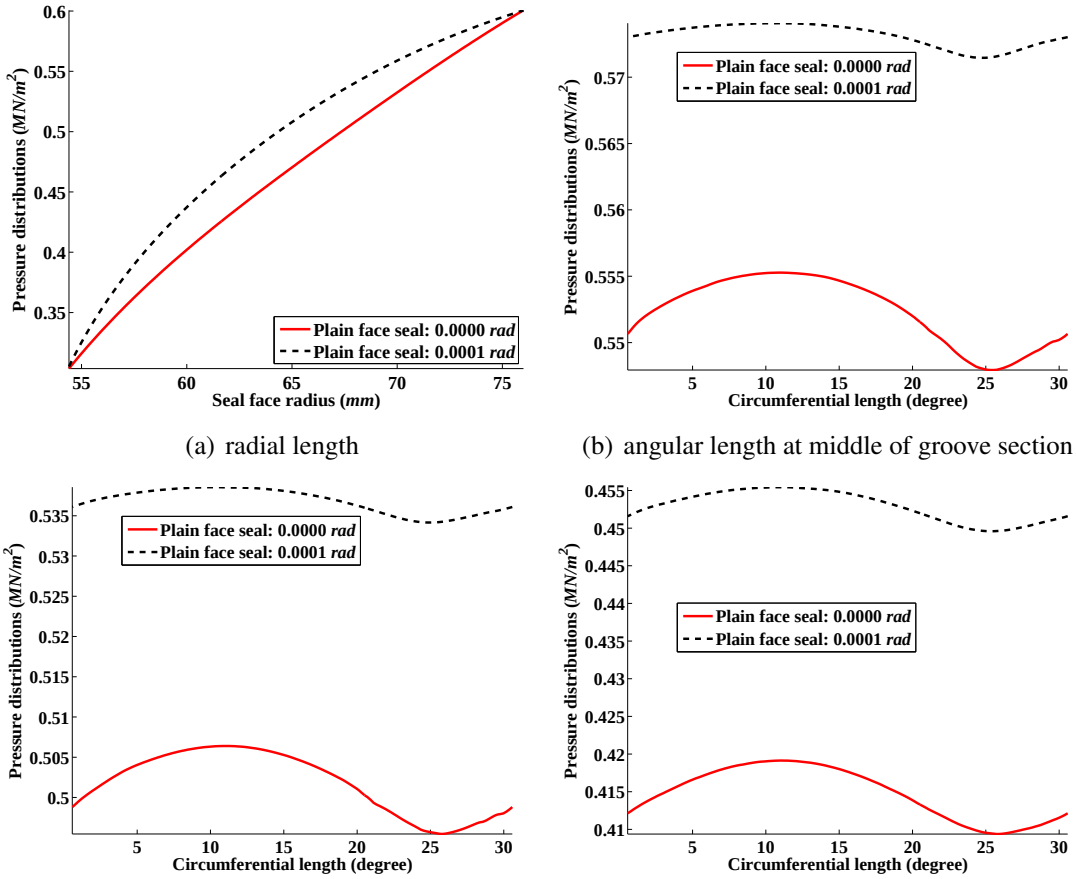

(a) radial length

(b) angular length at middle of groove section

(c) angular length at beginning of groove

(d) angular length at middle of dam section

Figure A.11 Seal pressure distributions as functions of seal face lengths of a plain face seal with the considerations of face deformation, seal operating at sealed fluid pressure of 6 bar, rotating speed of 10000 rpm and sealed fluid temperature of 120°C taken at an XY plane of fluid film thickness of 3 μm

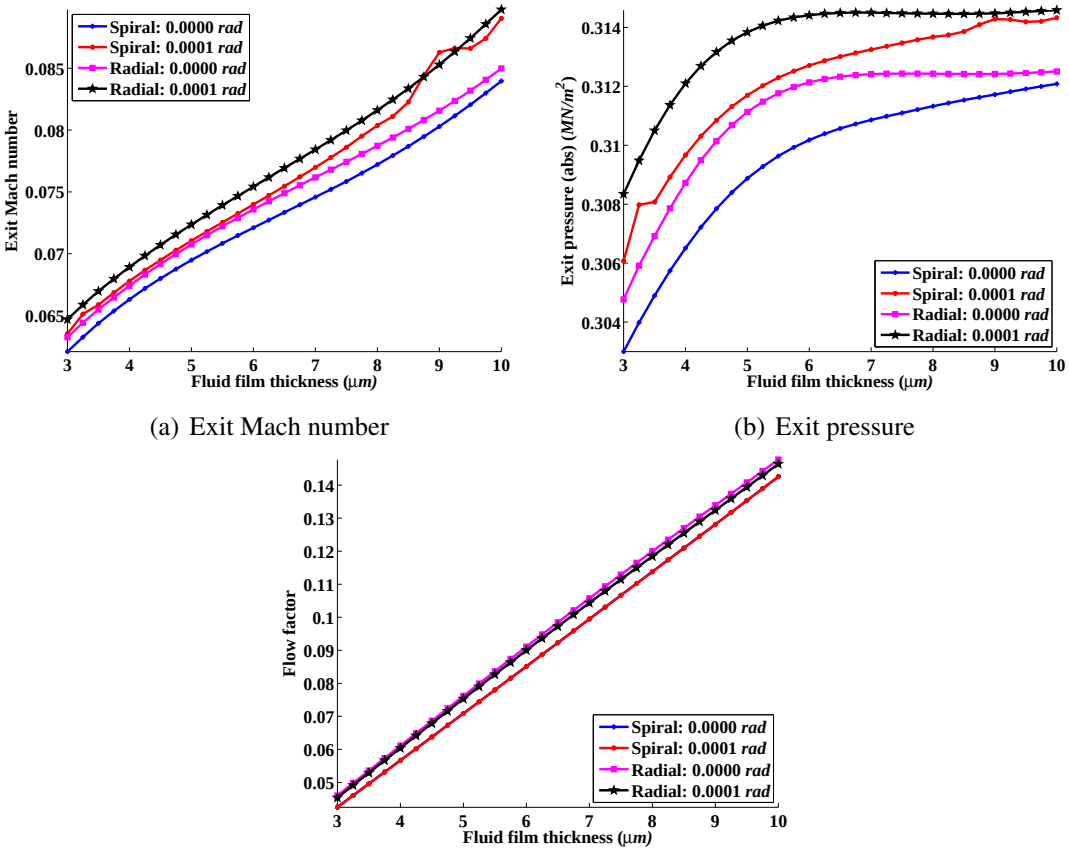

(a) Exit Mach number

(b) Exit pressure

(c) Flow factor

Figure A.12 Flow characteristics as functions of fluid film thickness of a spiral groove seal and a radial groove seal with the considerations of face deformation, seal operating at sealed fluid pressure of 6 bar, rotating speed of 10000 rpm and sealed fluid temperature of 120°C

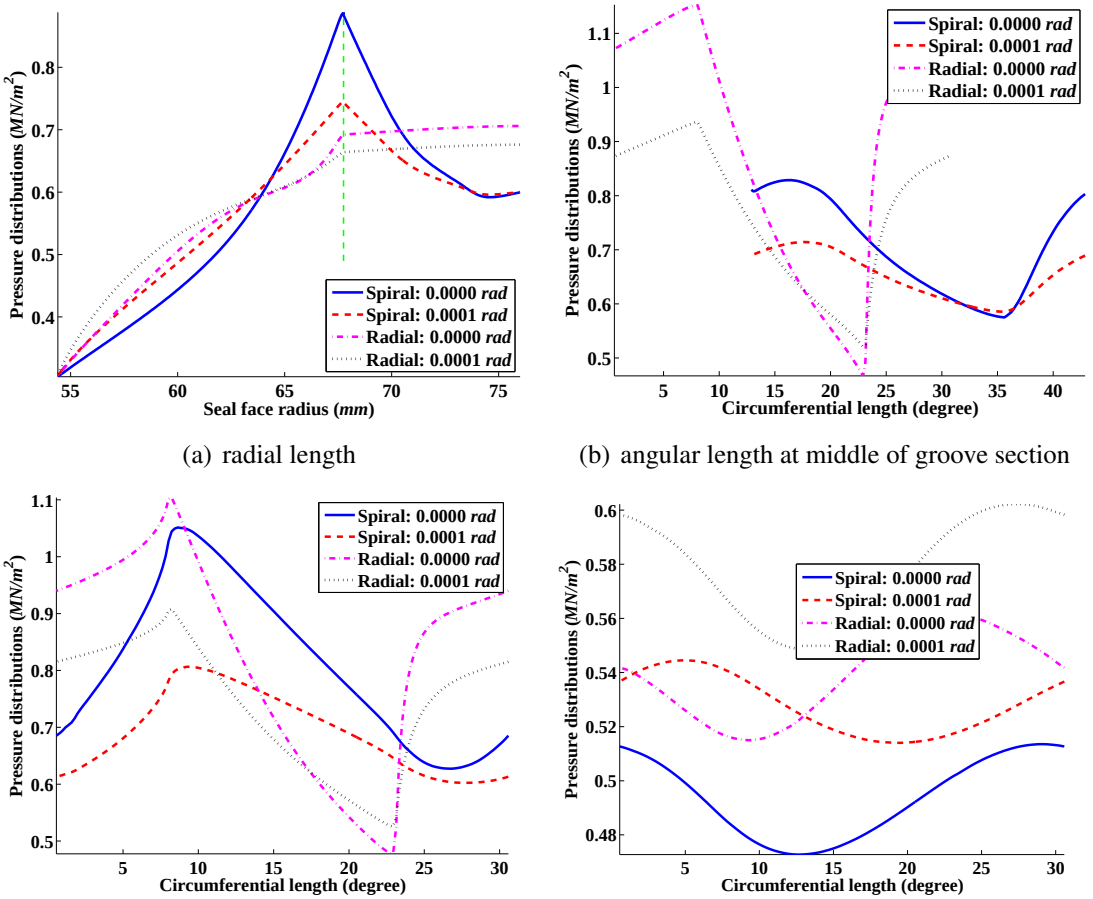

(a) radial length

(b) angular length at middle of groove section

(c) angular length at beginning of groove

(d) angular length at middle of dam section

Figure A.13 Seal pressure distributions as functions of seal face lengths of a spiral groove seal and a radial groove seal with the considerations of face deformation, seal operating at sealed fluid pressure of 6 bar, rotating speed of 10000 rpm and sealed fluid temperature of 120°C taken at an XY plane of fluid film thickness of 3 μm

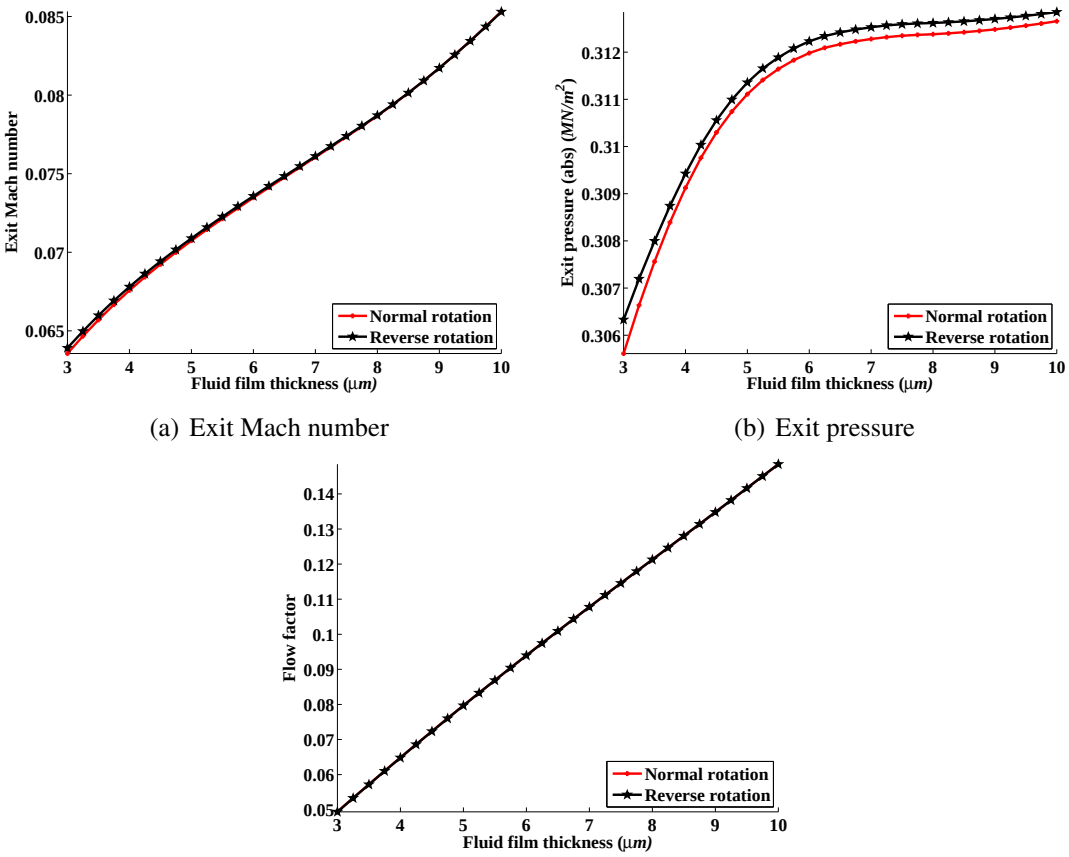

(a) Exit Mach number

(b) Exit pressure

(c) Flow factor

Figure A.14 Flow characteristics as functions of fluid film thickness of a novel seal operating at sealed fluid pressure of 6 bar, normal and reversed rotating speed of 10000 rpm and sealed fluid temperature of 120°C

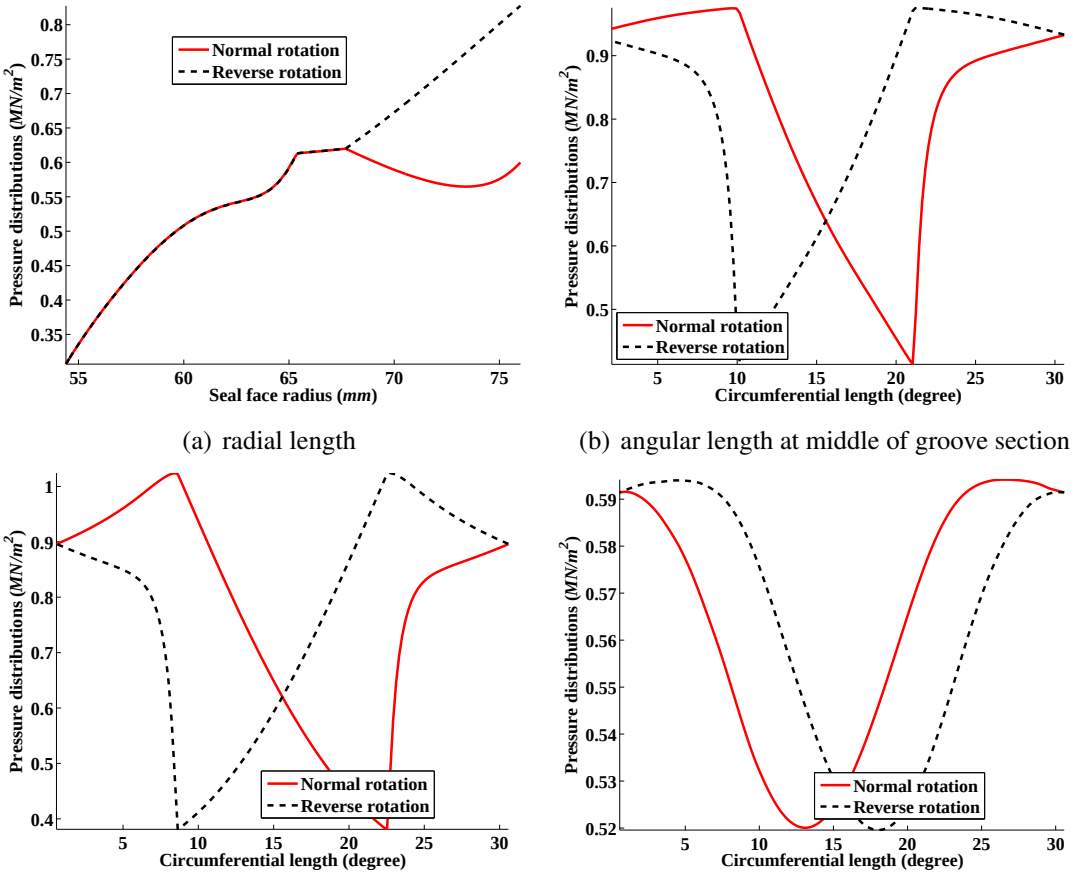

(a) radial length

(b) angular length at middle of groove section

(c) angular length at beginning of groove

(d) angular length at middle of dam section

Figure A.15 Seal pressure distributions as functions of seal face lengths of a novel seal operating at sealed fluid pressure of 6 bar, normal and reversed rotating speed of 10000 rpm and sealed fluid temperature of 120°C taken at an XY plane of fluid film thickness of 3 μm

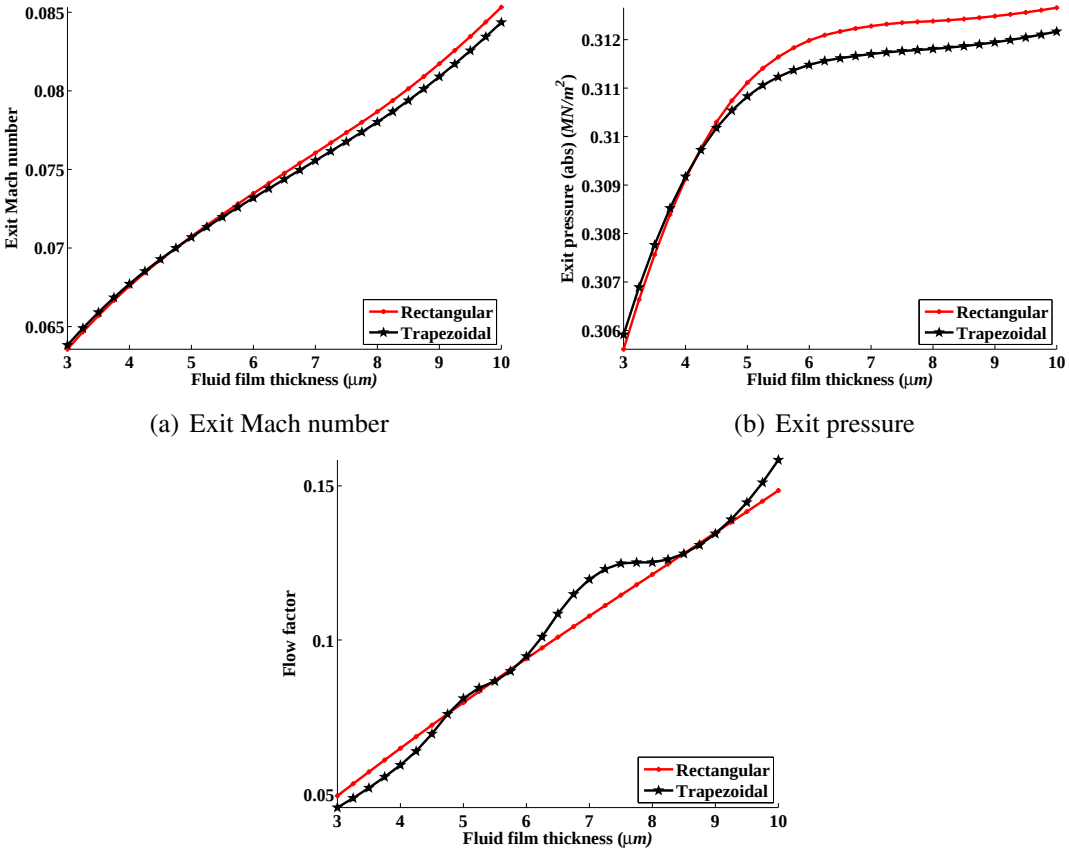

(a) Exit Mach number

(b) Exit pressure

(c) Flow factor

Figure A.16 Flow characteristics as functions of fluid film thickness of a novel seal with two different groove shapes, seal operating at sealed fluid pressure of 6 bar, rotating speed of 10000 rpm and sealed fluid temperature of 120°C

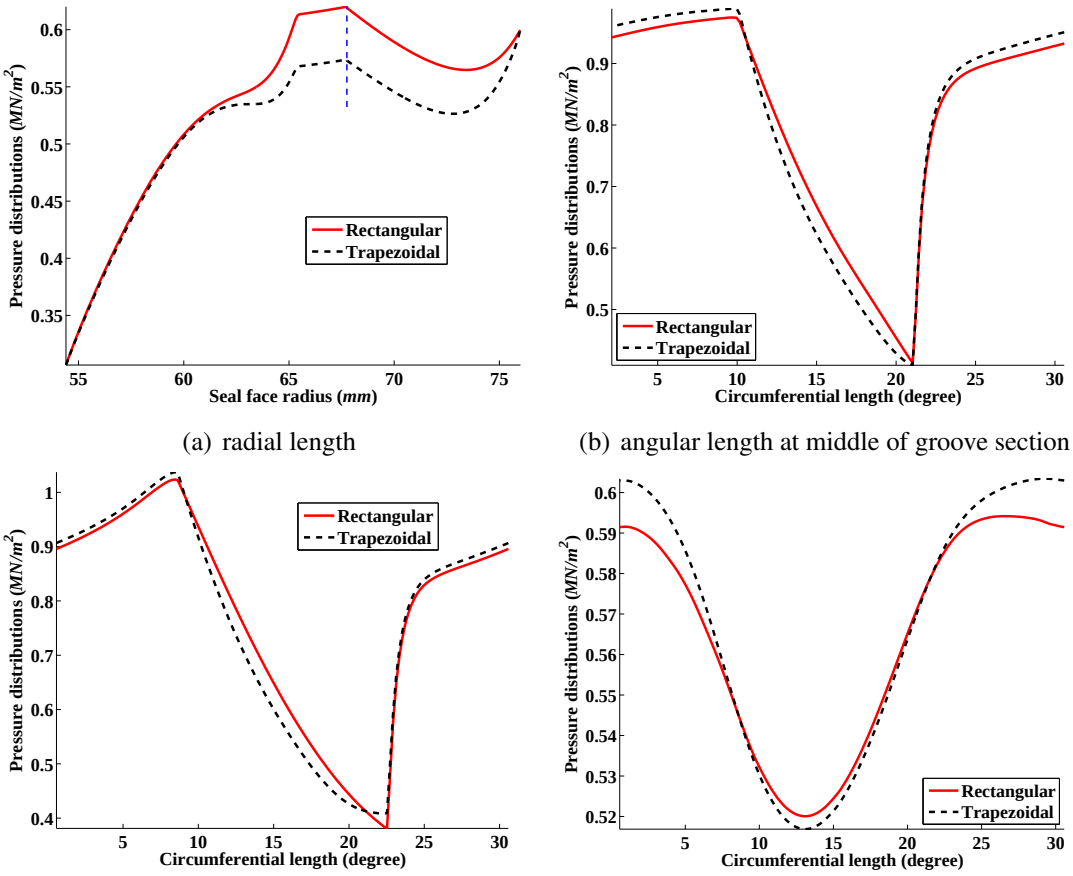

(a) radial length

(b) angular length at middle of groove section

(c) angular length at beginning of groove

(d) angular length at middle of dam section

Figure A.17 Seal pressure distributions as functions of seal face lengths of a novel seal with two different groove shapes, seal operating at sealed fluid pressure of 6 bar, rotating speed of 10000 rpm and sealed fluid temperature of 120°C taken at an XY plane of fluid film thickness of 3 μm

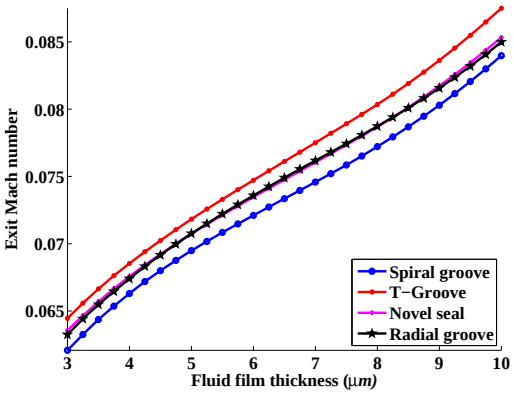

(a) Exit Mach number

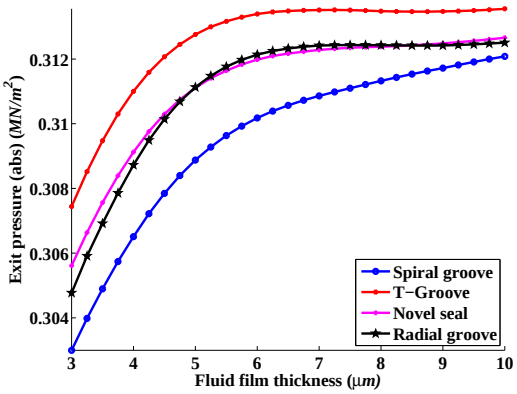

(b) Exit pressure

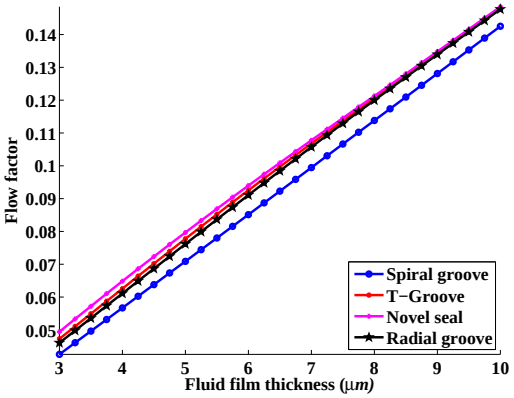

(c) Flow factor

Figure A.18 Flow characteristics as functions of fluid film thickness of a novel seal compared with some existing geometrical seal face profiles, seal operating at sealed fluid pressure of 6 bar, normal rotating speed of 10000 rpm and sealed fluid temperature of 120°C

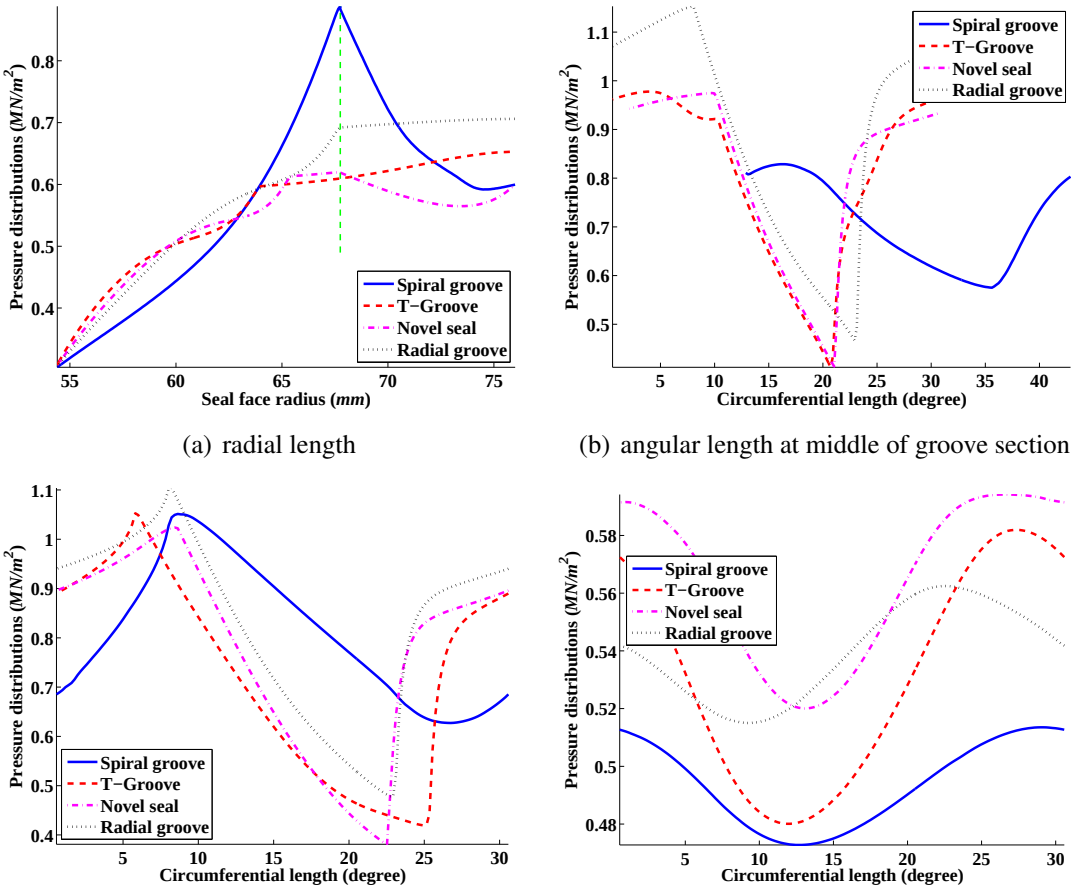

(a) radial length

(b) angular length at middle of groove section

(c) angular length at beginning of groove

(d) angular length at middle of dam section

Figure A.19 Seal pressure distributions as functions of seal face lengths of a novel seal compared with some existing geometrical seal face profiles, seal operating at sealed fluid pressure of 6 bar, normal rotating speed of 10000 rpm and sealed fluid temperature of 120°C taken at an XY plane of fluid film thickness of 3 μm

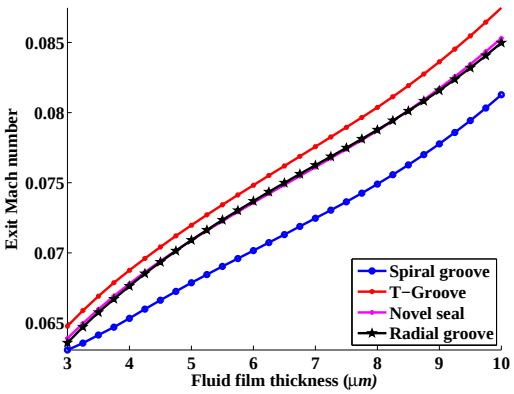

(a) Exit Mach number

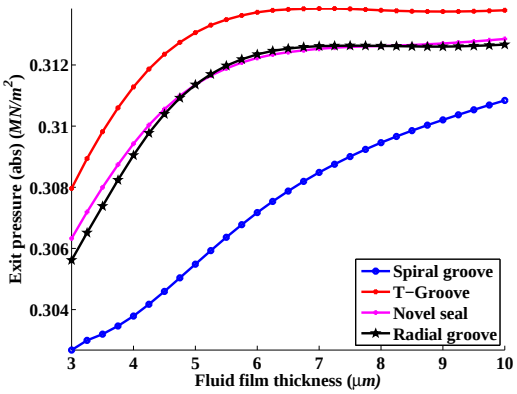

(b) Exit pressure

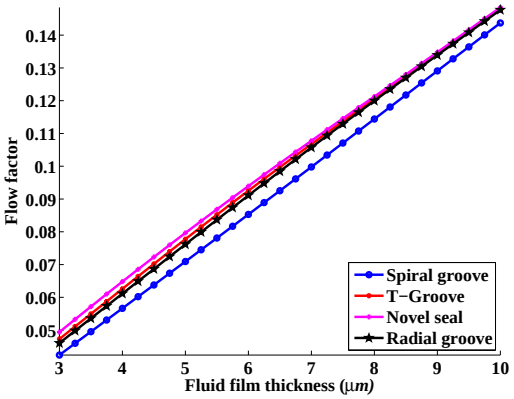

(c) Flow factor

Figure A.20 Flow characteristics as functions of fluid film thickness of a novel seal compared with some existing geometrical seal face profiles, seal operating at sealed fluid pressure of 6 bar, reversed rotating speed of 10000 rpm and sealed fluid temperature of 120°C

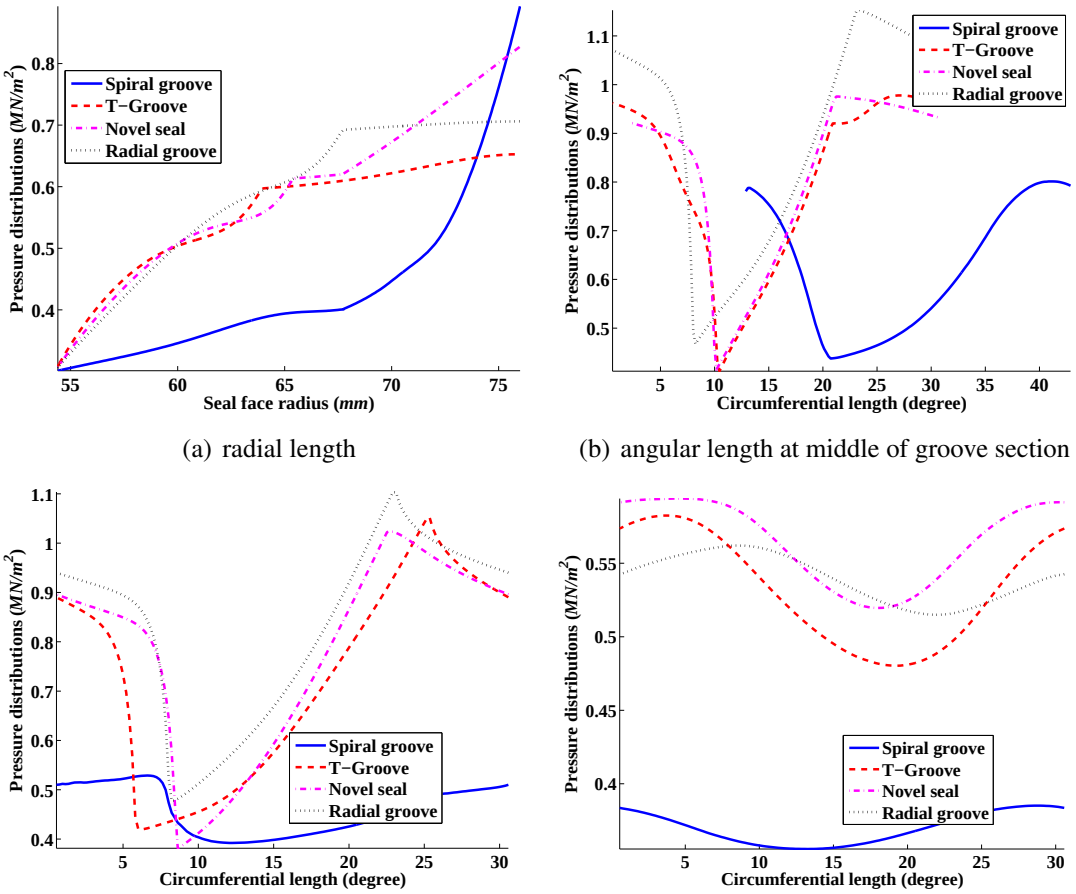

(a) radial length

(b) angular length at middle of groove section

(c) angular length at beginning of groove

(d) angular length at middle of dam section

Figure A.21 Seal pressure distributions as functions of seal face lengths of a novel seal compared with some existing geometrical seal face profiles, seal operating at sealed fluid pressure of 6 bar, reversed rotating speed of 10000 rpm and sealed fluid temperature of 120°C taken at an XY plane of fluid film thickness of 3 μm

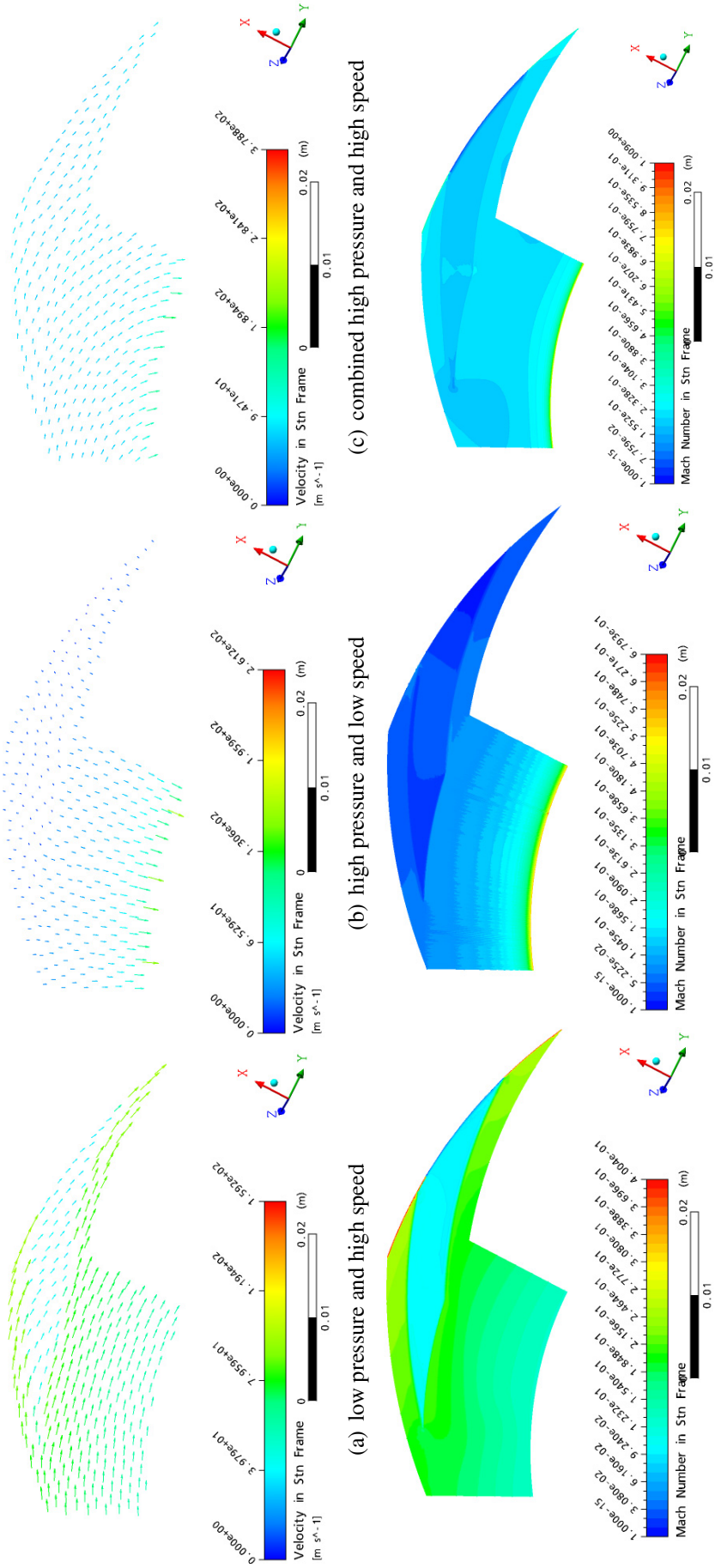

(a) low pressure and high speed (b) high pressure and low speed (c) combined high pressure and high speed

(d) low pressure and high speed (e) high pressure and low speed (f) combined high pressure and high speed

Figure A.22 Velocity vector plots and Mach number contour plots of a spiral groove seal operating at various combinations of sealed fluid pressure and rotating speed for the evaluations of the contributions of hydrostatic and hydrodynamic forces

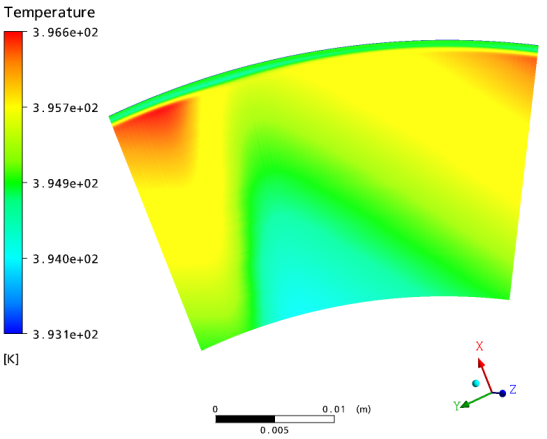

(a) Plain face seal temperature contour

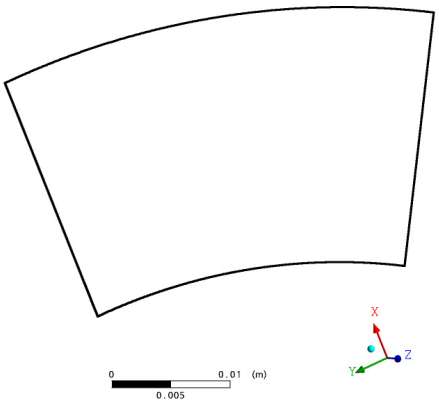

(c) Plain face seal geometry

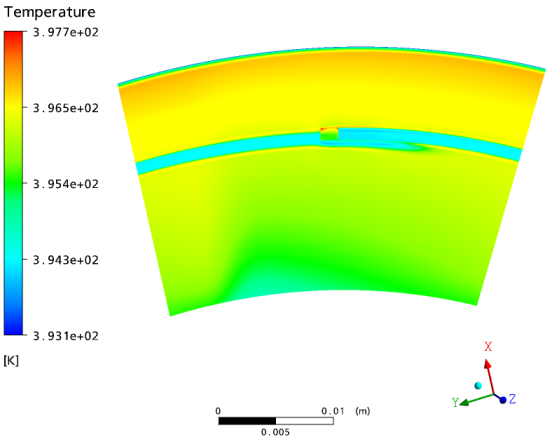

(b) Orifice controlled seal temperature contour

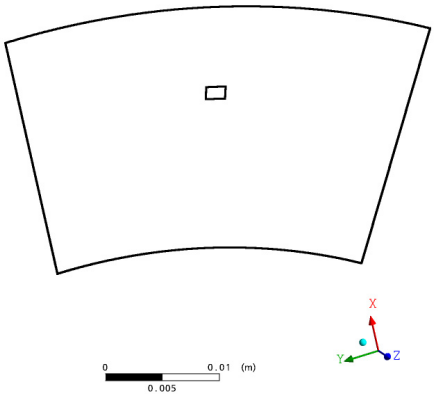

(d) Orifice controlled seal geometry

Figure A.23 Temperature contour plots of plain face seal and orifice controlled seal operating at sealed fluid pressure of 6 bar, rotating speed of 10000 rpm and sealed fluid temperature of 120°C taken at an XY plane of fluid film thickness of 3 μm

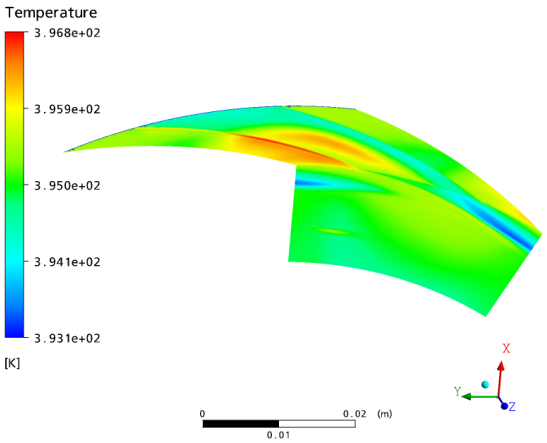

(a) Spiral groove face seal temperature contour

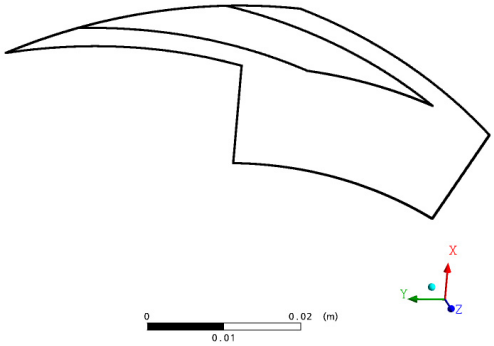

(c) Spiral groove face seal geometry

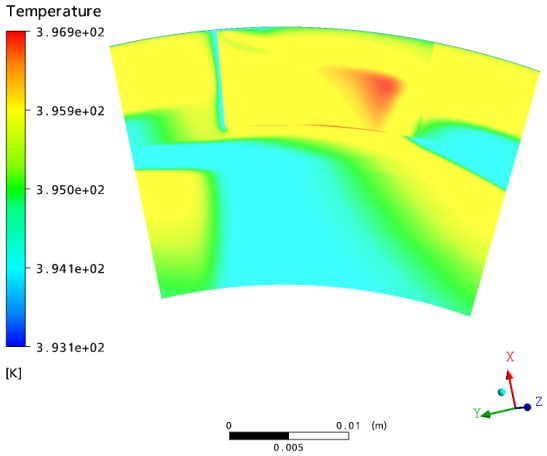

(b) Radial groove face seal temperature contour

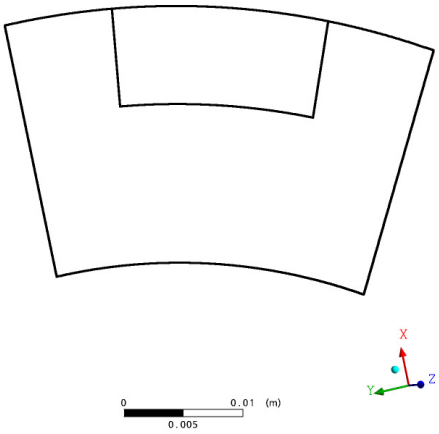

(d) Radial groove face seal geometry

Figure A.24 Temperature contour plots of spiral and radial groove face seals operating at sealed fluid pressure of 6 bar, rotating speed of 10000 rpm and sealed fluid temperature of 120°C taken at an XY plane of fluid film thickness of 3 μm

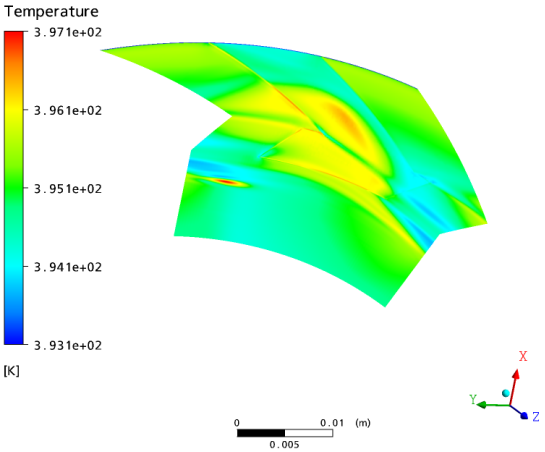

(a) Double spiral groove face seal temperature contour

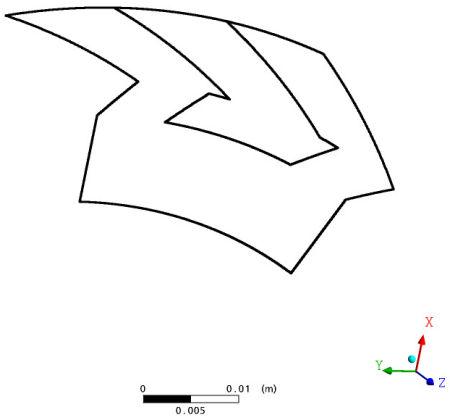

(c) Double spiral groove face seal geometry

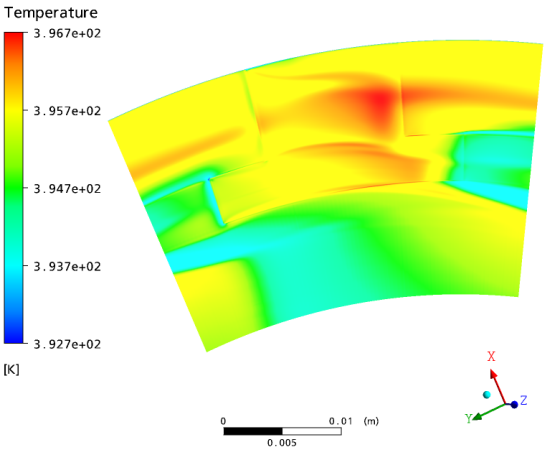

(b) T-groove face seal temperature contour

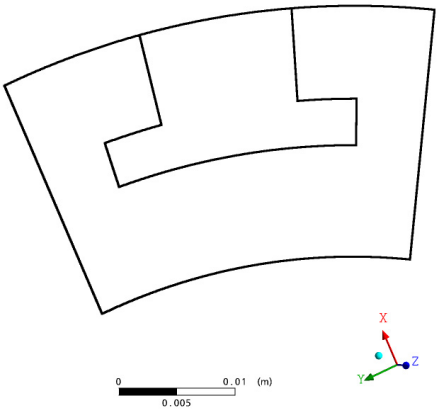

(d) T-groove face seal geometry

Figure A.25 Temperature contour plots of double spiral groove and T-groove face seals operating at sealed fluid pressure of 6 bar, rotating speed of 10000 rpm and sealed fluid temperature of 120°C taken at an XY plane of fluid film thickness of 3 μm

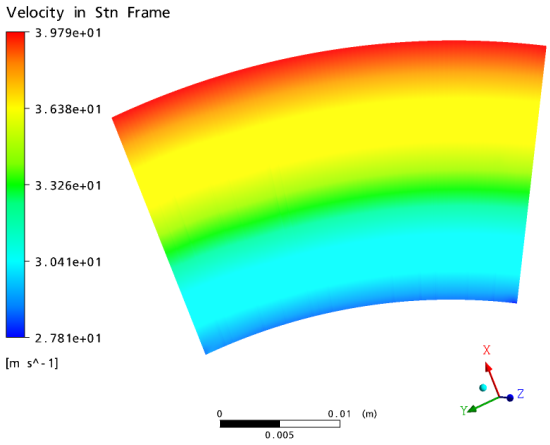

(a) Plain face seal velocity contour

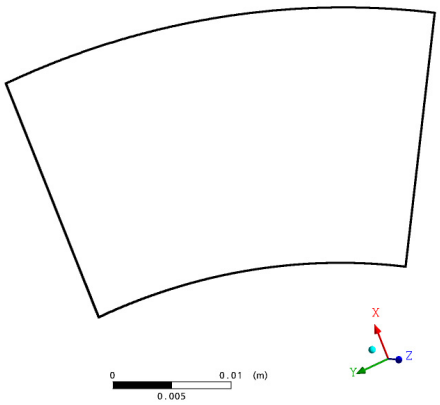

(c) Plain face seal geometry

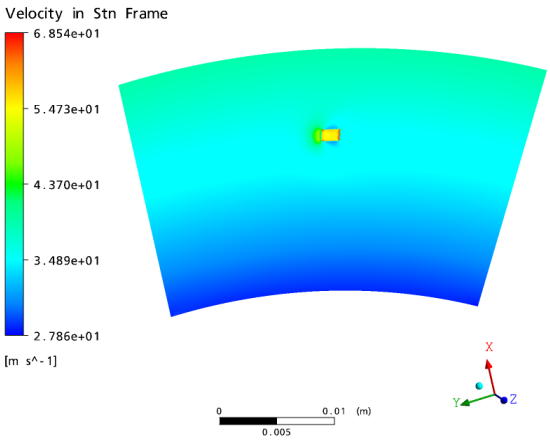

(b) Orifice controlled seal velocity contour

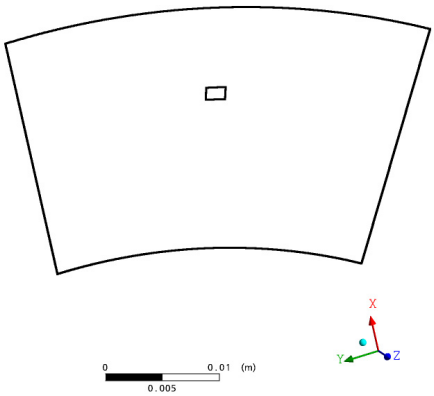

(d) Orifice controlled seal geometry

Figure A.26 Velocity contour plots of plain face seal and orifice controlled seal operating at sealed fluid pressure of 6 bar, rotating speed of 10000 rpm and sealed fluid temperature of 120°C taken at an XY plane of fluid film thickness of 3 μm

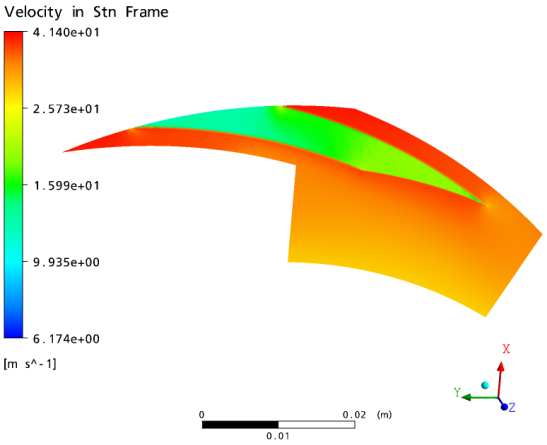

(a) Spiral groove face seal velocity contour

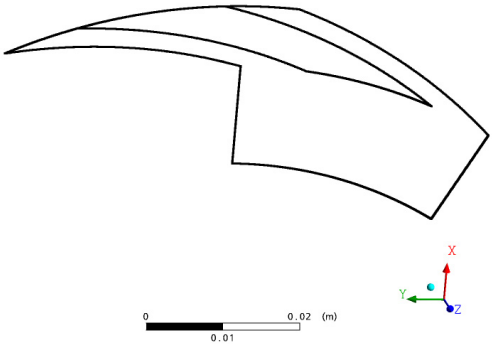

(c) Spiral groove face seal geometry

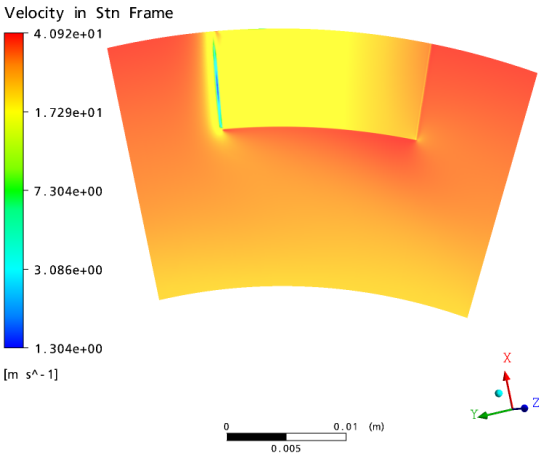

(b) Radial groove face seal velocity contour

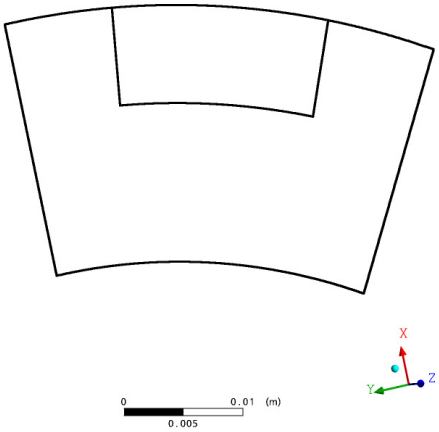

(d) Radial groove face seal geometry

Figure A.27 Velocity contour plots of spiral and radial groove face seals operating at sealed fluid pressure of 6 bar, rotating speed of 10000 rpm and sealed fluid temperature of 120°C taken at an XY plane of fluid film thickness of 3 μm

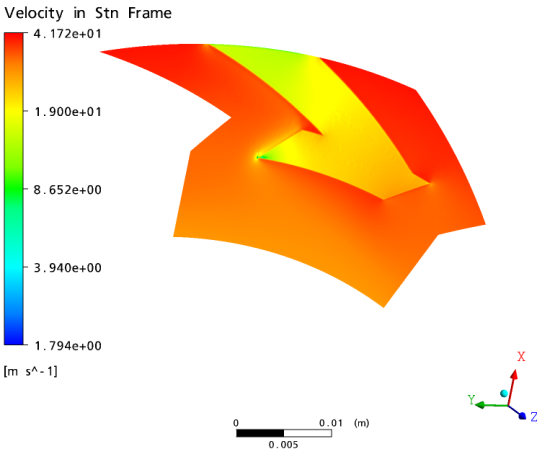

(a) Double spiral groove face seal velocity contour

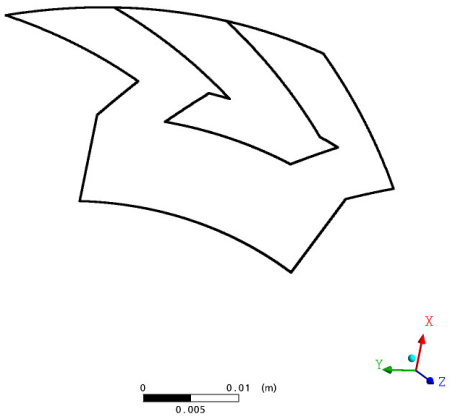

(c) Double spiral groove face seal geometry

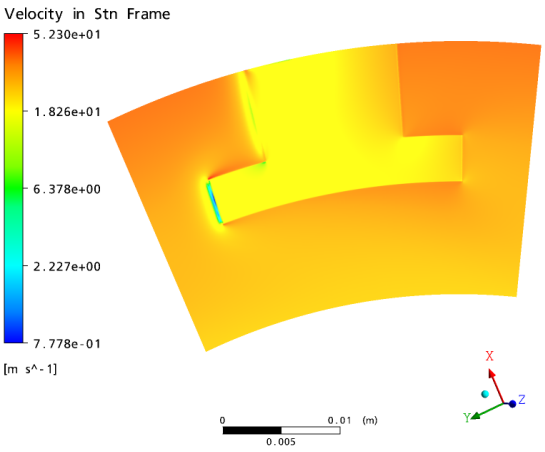

(b) T-groove face seal velocity contour

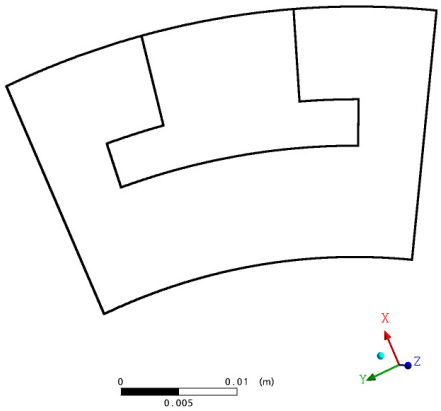

(d) T-groove face seal geometry

Figure A.28 Velocity contour plots of double spiral groove and T-groove face seals operating at sealed fluid pressure of 6 bar, rotating speed of 10000 rpm and sealed fluid temperature of 120°C taken at an XY plane of fluid film thickness of 3 μm

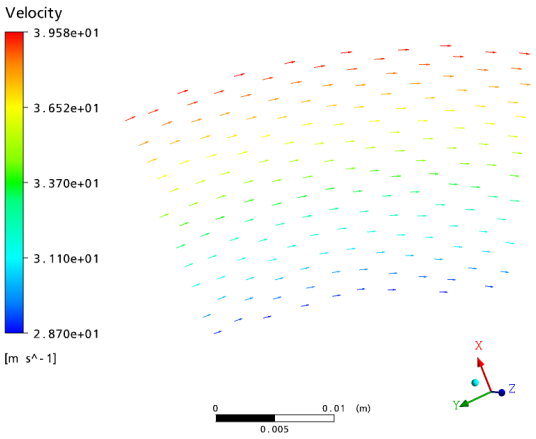

(a) Plain face seal velocity vector

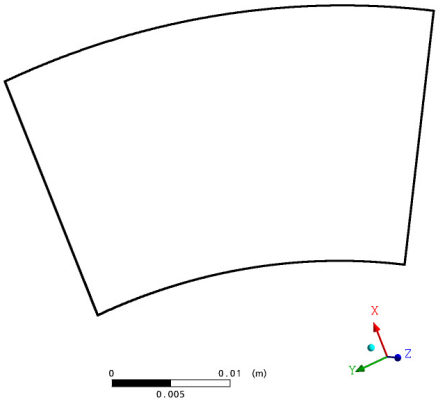

(c) Plain face seal geometry

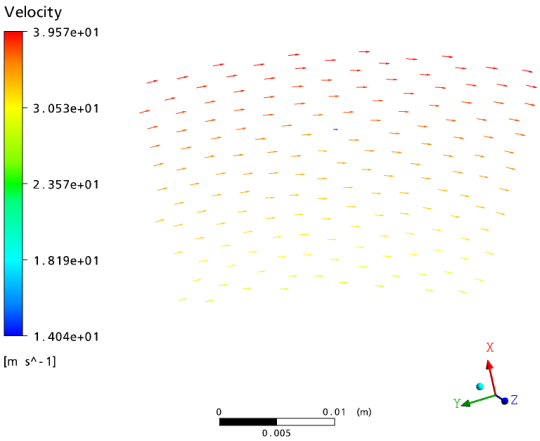

(b) Orifice controlled seal velocity vector

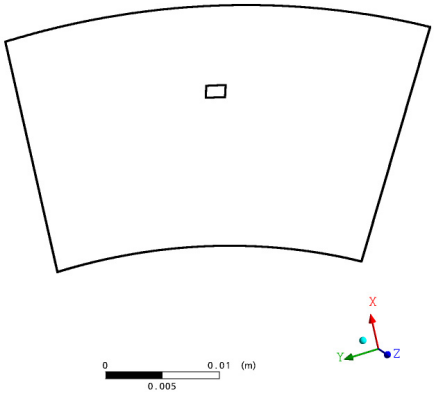

(d) Orifice controlled seal geometry

Figure A.29 Velocity vector plots of plain face seal and orifice controlled seal operating at sealed fluid pressure of 6 bar, rotating speed of 10000 rpm and sealed fluid temperature of 120°C taken at an XY plane of fluid film thickness of 3 μm

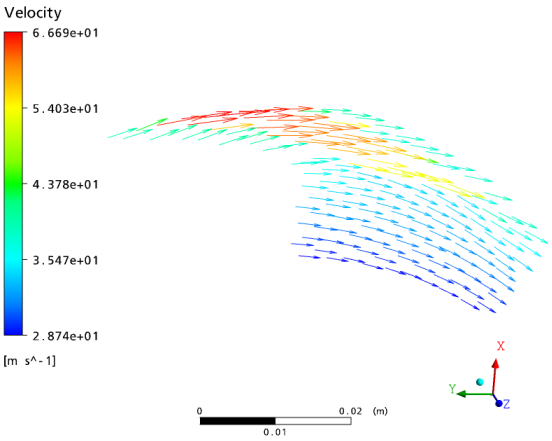

(a) Spiral groove face seal velocity vector

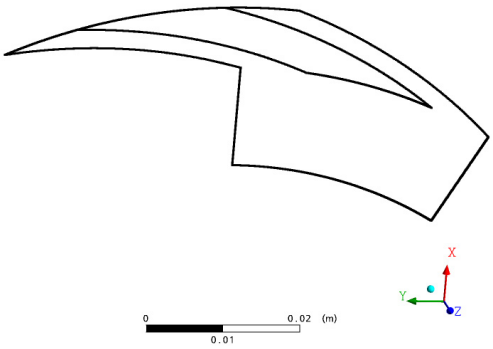

(c) Spiral groove face seal geometry

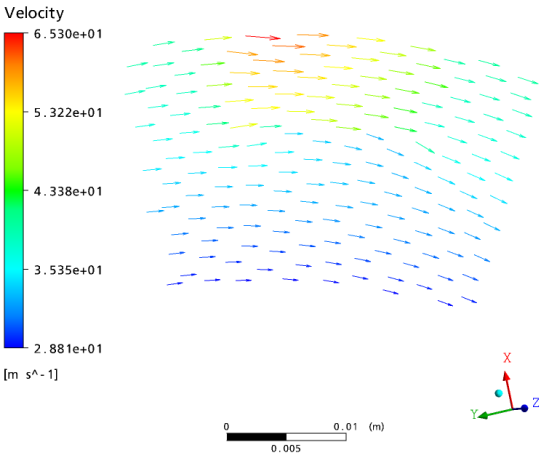

(b) Radial groove face seal velocity vector

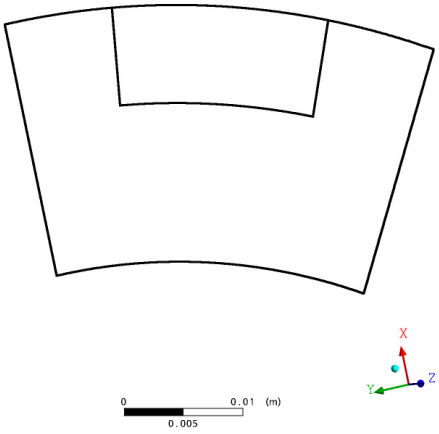

(d) Radial groove face seal geometry

Figure A.30 Velocity vector plots of spiral and radial groove face seals operating at sealed fluid pressure of 6 bar, rotating speed of 10000 rpm and sealed fluid temperature of 120°C taken at an XY plane of fluid film thickness of 3 μm

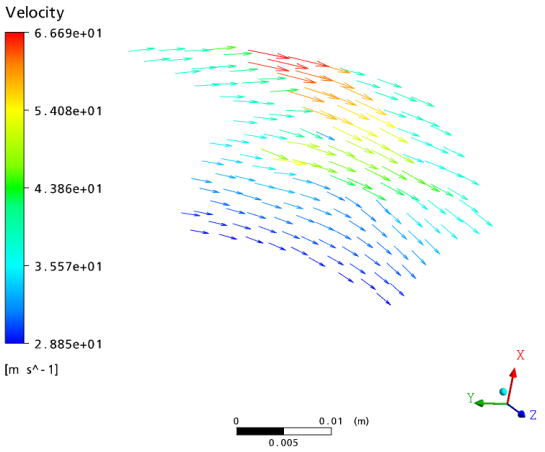

(a) Double spiral groove face seal velocity vector

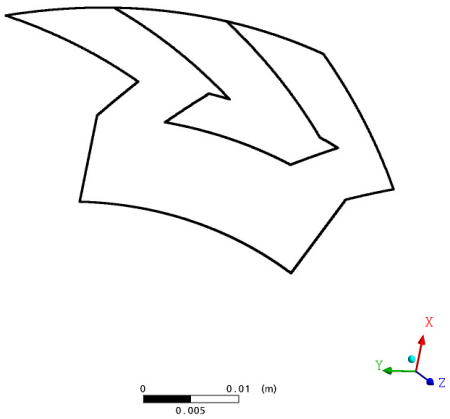

(c) Double spiral groove face seal geometry

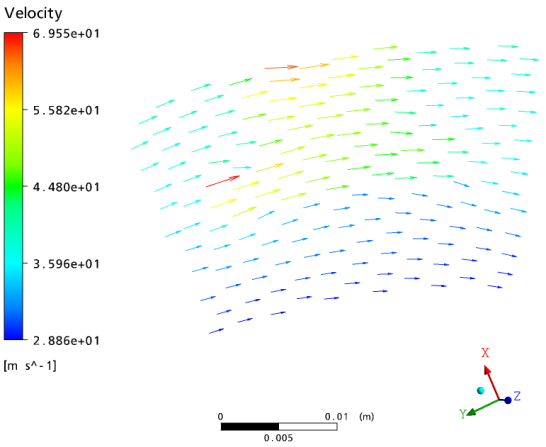

(b) T-groove face seal velocity vector

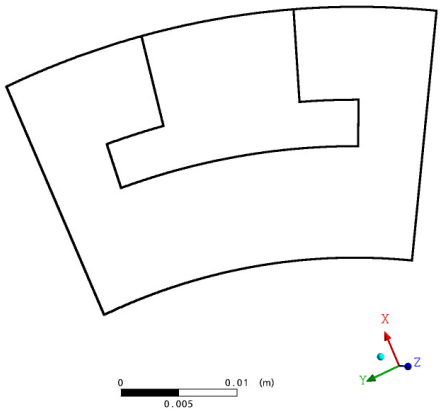

(d) T-groove face seal geometry

Figure A.31 Velocity vector plots of double spiral groove and T-groove face seals operating at sealed fluid pressure of 6 bar, rotating speed of 10000 rpm and sealed fluid temperature of 120°C taken at an XY plane of fluid film thickness of 3 μm

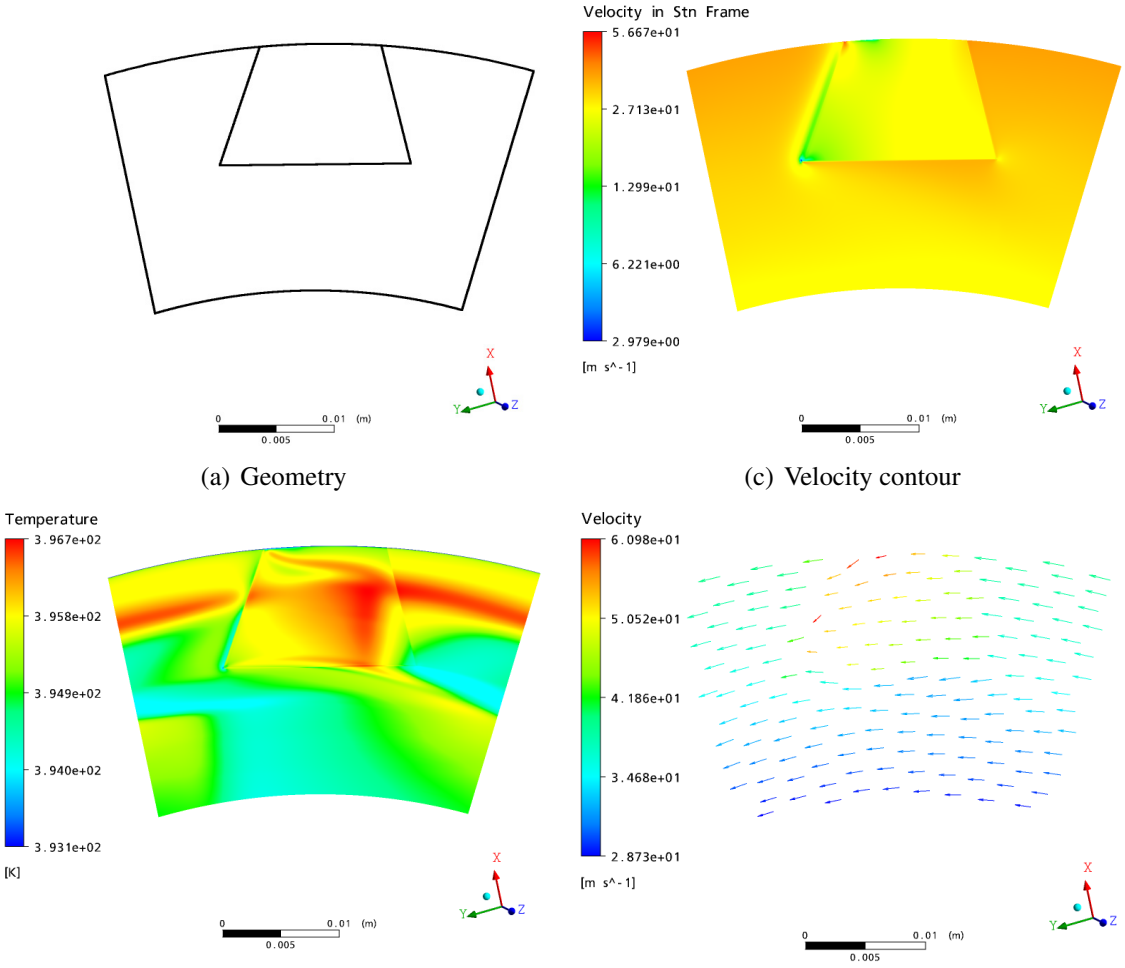

(a) Geometry

(c) Velocity contour

(b) Temperature contour

(d) Velocity vector

Figure A.32 Flow characteristics plots of a proposed novel seal operating at sealed fluid pressure of 6 bar, rotating speed of 10000 rpm and sealed fluid temperature of 120°C taken at an XY plane of fluid film thickness of 3 μm

Appendix B

Results Figures for Optimization Tool Testing

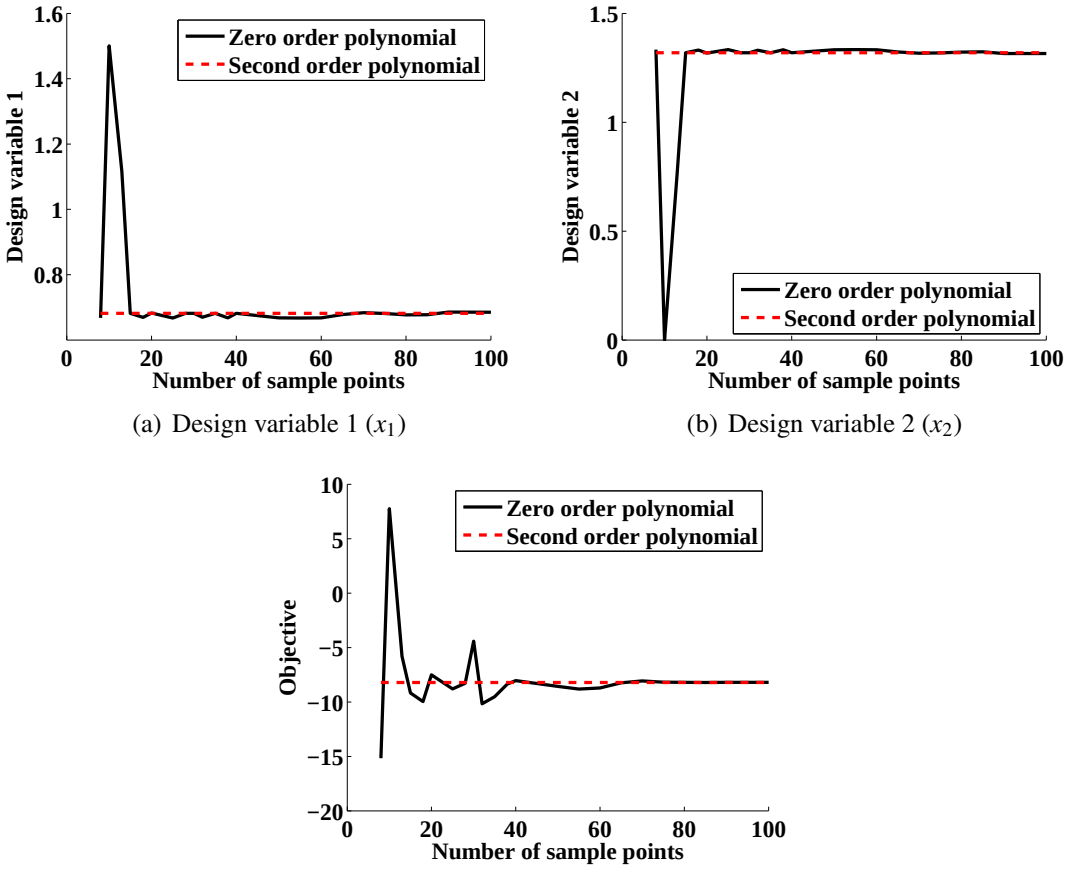

(a) Design variable 1 (x_1)

(b) Design variable 2 (x_2)

(c) Objective ($f(x)$)

Figure B.1 Plots of optimal solutions of a single objective optimization as a function of number of sample points using different regression models

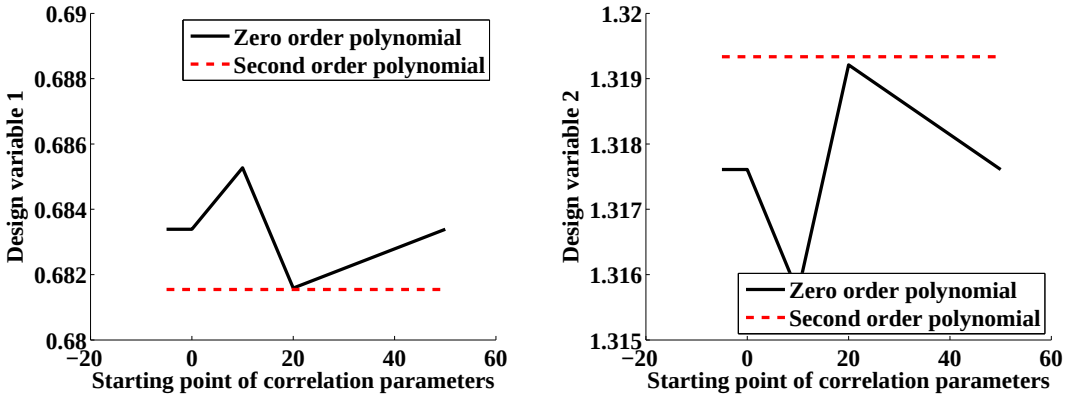

(a) Design variable 1 (x_1)

(b) Design variable 2 (x_2)

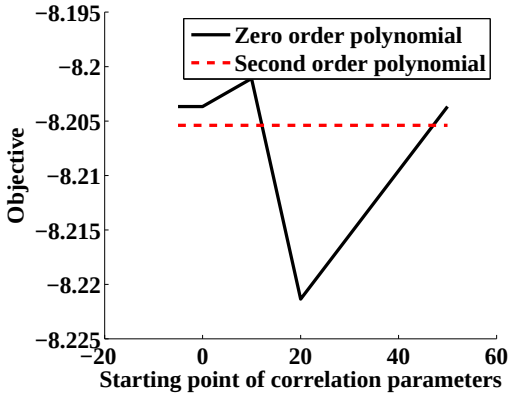

(c) Objective ($f(x)$)

Figure B.2 Plots of optimal solutions of a single objective optimization as a function of starting point of correlation parameters using different regression models

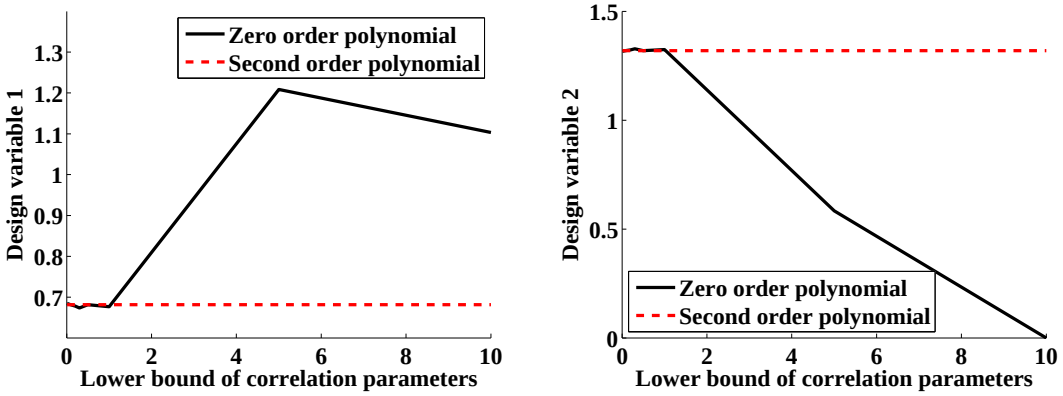

(a) Design variable 1 (x_1)

(b) Design variable 2 (x_2)

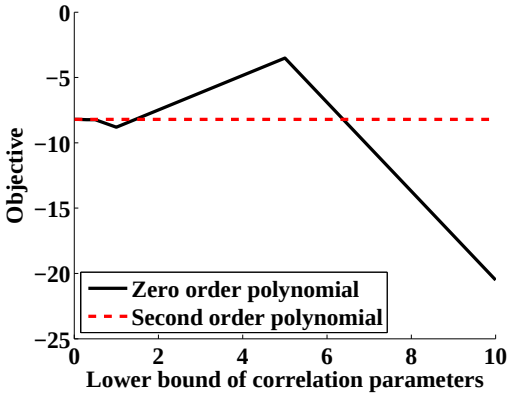

(c) Objective ($f(x)$)

Figure B.3 Plots of optimal solutions of a single objective optimization as a function of lower bound of correlation parameters using different regression models

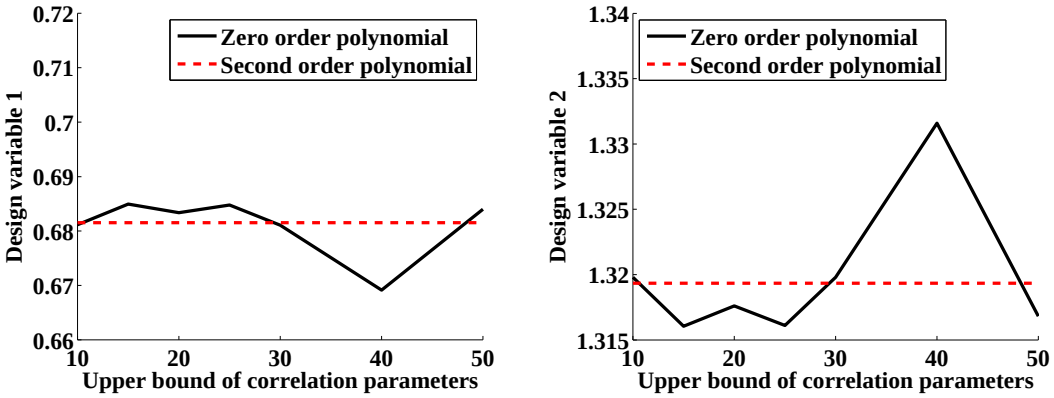

(a) Design variable 1 (x_1)

(b) Design variable 2 (x_2)

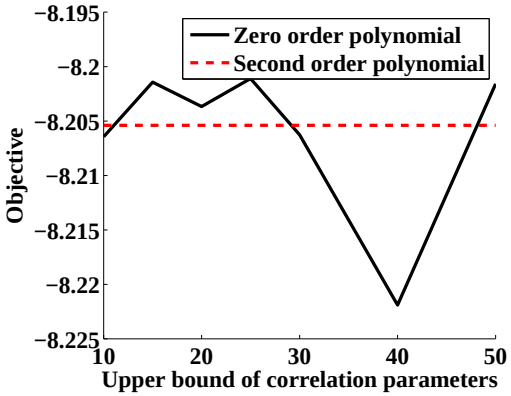

(c) Objective ($f(x)$)

Figure B.4 Plots of optimal solutions of a single objective optimization as a function of upper bound of correlation parameters using different regression models